Sensorless Temperature Measurements for Advanced Battery Management Systems

Raijmakers, Luc

DOI
10.4233/uuid:73aa76cf-d38a-49b0-b363-3a7c5ab9dc9b

Publication date
2018

Document Version
Final published version

Citation (APA)
Raijmakers, L. (2018). *Sensorless Temperature Measurements for Advanced Battery Management Systems*. [Dissertation (TU Delft), Delft University of Technology]. https://doi.org/10.4233/uuid:73aa76cf-d38a-49b0-b363-3a7c5ab9dc9b

Sensorless Temperature Measurements for Advanced Battery Management Systems

Sensorless Temperature Measurements for Advanced Battery Management Systems

Dissertation

for the purpose of obtaining the degree of doctor
at Delft University of Technology
by the authority of the Rector Magnificus prof. dr. ir. T.H.J.J. van der Hagen;
Chair of the Board for Doctorates
to be defended publicly on
Monday 24 September 2018 at 12:30 o'clock

by

Lucas Hermanus Johannes RAIJMAKERS

Master of Science in Automotive Technology,
Eindhoven University of Technology, Eindhoven, The Netherlands,
born in Boxmeer, The Netherlands.

This dissertation has been approved by the promotors.

Composition of the doctoral committee:

Rector Magnificus	chairperson
Prof. dr. E.H. Brück	Delft University of Technology, promotor
Prof. dr. P.H.L. Notten	Eindhoven University of Technology, promotor

Independent members:

Prof. dr. ir. W.A. Serdijn	Delft University of Technology
Prof. dr. F.M. Mulder	Delft University of Technology
Prof. dr. R.A. Eichel	RWTH Aachen
Dr. E.M. Kelder	Delft University of Technology

Other member:

Prof. dr. ir. H.J. Bergveld	Eindhoven University of Technology

The work described in this thesis is achieved by a collaboration between Delft University of Technology, Eindhoven University of Technology and NXP Semiconductors. I acknowledge financial support for this research from ADEM, A green Deal in Energy Materials of the Ministry of Economic Affairs of The Netherlands (www.adem-innovationlab.nl).

Keywords: Li-ion batteries, (non-)zero-intercept frequency, electrochemical impedance spectroscopy, battery temperature, sensorless temperature measurements.

Printed by: Drukkerij Knoops, Venlo

Front & Back: Frank Backhuijs, Venlo. The front cover illustrates impedance-spectra measured at various temperatures. From the impedance-spectra intercept frequencies can be determined which can be used for 'sensorless' temperature indication.

ISBN 978-94-6228-861-4

An electronic version of this dissertation is available at
http://repository.tudelft.nl/.

Our greatest weakness lies in giving up. The most certain way to succeed is always to try just one more time.

- Thomas Alva Edison

Contents

Summary

Li-ion batteries have drawn considerable attention in the last decades due to the fact that these devices have a relative high energy density, long cycle life and low self-discharge rate. Therefore, Li-ion batteries are highly suitable for stationary energy storage and for providing mobile devices with energy. Examples of mobile devices are portable phones, laptops, tablets, watches and (hybrid) electric vehicles ((H)EV). Especially the (H)EV market requires many batteries since it is to be expected that (H)EV sales will tremendously increase in the near future.

Despite the fact that Li-ion batteries offer many advantages, challenges are met in monitoring and controlling the states of a Li-ion battery, such as State of Charge (SoC), State of Health (SoH) and temperature. The consequences of poor monitoring and control can lead to a decrease in battery performance, rapid degradation and, even worse, fire or explosion. Therefore, it is of high importance to keep the battery states within their safe operating range, which is defined by voltage, temperature and current limits. A Battery Management System (BMS), including a Thermal Management System (TMS), is the critical component to monitor and control these states in order to guarantee safe and reliable battery operation.

The main goal of this thesis is to investigate whether impedance-based temperature measurements, sometimes referred to as sensorless temperature measurements, can be applied as method for monitoring the temperature of Li-ion batteries. Impedance-based temperature indication offers significant advantages with respect to conventional temperature measurements. For instance, no external or internal hardware temperature sensors are required, thermal measurement delay is short, it measures the integral temperature of the active material, and impedance measurements can also be used to determine additional states, such as SoC and SoH. In particular, the investigation of the suitability of the intercept frequency as temperature indicator is a central topic in this thesis. Investigations have been performed by both experiments and simulations on Li-ion batteries under various conditions. In the end, sensorless temperature measurements facilitate the design of an efficient BMS in terms of safety, performance and reliability.

In Chapter 2, the working principle of Li-ion batteries is explained. In Li-ion batteries, Li^+ ions shuttle between the positive and negative electrodes upon charging and discharging. Unfavorably, the processes during (dis)charging occur with certain inefficiencies and heat is therefore generated. This heat flows from the electrode materials to the battery surface at which it is dissipated to the environment. Since heat is generated internally, thermal gradients develop, resulting in temperature measurement complications and position-dependent aging. When the heat cannot be sufficiently dissipated, or when the battery is under abusive conditions, thermal runaway may occur, which leads to dangerous situations. In particular, if a battery inside a battery pack induces thermal runaway to adjacent batteries, it can propagate through the complete battery pack. Therefore, careful design considerations need to be taken on both single-battery, module, and pack level in order to prevent dangerous situations and to maximize performance and lifetime.

Due to the thermal gradients, which might quickly develop during operation, fast and accurate temperature measurements can be rather challenging. For a proper selection of a temperature measurement method, aspects such as measurement range, accuracy, resolution, and costs of the method are important. Chapter 3 gives a comprehensive overview of the various existing temperature measurement methods that can be used for temperature indication of Li-ion batteries. At present, traditional temperature measurement methods, such as thermistors and thermocouples, are extensively used. The more recent introduced methods, such as impedance-based temperature indication and fiber Bragg-grating techniques are under investigation in order to determine if those are suitable for large-scale introduction in sophisticated battery-powered applications.

In Chapter 4, a new impedance-based temperature indication method is proposed to measure the internal temperature of (Li-ion) batteries. Based on electrochemical impedance spectroscopy measurements, a zero-intercept frequency (ZIF) can be determined, which is exclusively related to the internal battery temperature. The ZIF is defined as the frequency at which the imaginary part of the impedance is zero ($Z_{im} = 0$), *i.e.* where the phase shift between the battery current and voltage is absent. Mathematical analysis of an equivalent electrical circuit, representing the battery performance, shows that the ZIF decreases with rising temperatures. Impedance measurements on rechargeable Li-ion batteries of various chemistries were conducted to verify the proposed method. These experiments revealed that the ZIF is clearly dependent on the temperature and, essentially independent on the Li-ion chemistry, SoC and aging. These impedance-based sensorless temperature measurements are therefore simple and convenient for application in a wide range of stationary, mobile and high-power devices, such as hybrid- and full electric vehicles. However, the presented measurement results in Chapter 4 are all measured under equilibrium conditions in the laboratory and further investigations are therefore required to investigate whether the proposed temperature indication method is also applicable to battery-powered applications outside the laboratory, such as in a (H)EV.

In Chapter 5, investigations are described in which the ZIF (proposed in Chapter 4) is applied in an EV to indicate the battery temperature. The measurement results reveal that ZIF measurements are heavily disturbed by interference, resulting from the current flowing through the battery (pack) and making an accurate temperature indication impossible. Therefore, a new impedance-based approach is introduced in which the integral battery temperature is related to other frequencies than the ZIF. The advantage of the proposed non-zero-intercept-frequency (NZIF) method is that measurement interference can be avoided at these frequencies. This gives a higher signal-to-noise ratio (SNR) and, consequently, more accurate temperature measurements. A theoretical analysis, using an equivalent circuit model of a Li-ion battery, shows that NZIFs are temperature dependent in a way similar to the ZIF and can therefore also be used as battery temperature indicator. To validate the proposed method, impedance measurements have been performed with individual $LiFePO_4$ batteries and with large $LiFePO_4$ battery packs tested in a full electric vehicle under driving conditions. The measurement results show that the NZIF is clearly dependent on the integral battery temperature and reveals a similar behavior to that of the ZIF method. However, in contrast to the ZIF method, the NZIF method makes it possible to optimally adjust the measurement frequencies such that the highest SNR can be obtained and, therefore, accurate temperature measurements are achieved.

In battery-powered applications, such as an EV, in which multiple batteries inside a pack are simultaneously monitored through the impedance, another disturbing phenomenon occurs. This phenomenon is called crosstalk and is described in Chapter 6. Performing impedance measurements simultaneously on each battery in a pack introduces crosstalk interference in the surrounding batteries. This causes impedance measurements in battery packs to be inaccurate. Experimental investigations on a battery pack showed that crosstalk is a linear phenomenon, which is dependent on the measurement frequency, the relative position of the batteries and the inter-battery spacing. However, it was found that crosstalk is independent of the battery temperature and SoC. Furthermore, it has been shown that the (N)ZIF is clearly dependent on crosstalk interference. Therefore, crosstalk interference should be carefully considered in the development of battery packs. Based on the experimental results and a proposed two-coil model with inductive coupling, a transfer-function description has been developed in order to simulate the crosstalk behavior. This model can be used as a supporting tool in the development of impedance-based measurement systems in battery packs.

In chapters 4 and 5, impedance-based temperature indication methods through the (N)ZIF have been presented. So far, these methods were only applied to (commercial) Li-ion batteries having two electrodes. For this reason, only the total battery impedance and, hence the (N)ZIF can be measured. However, to develop advanced BMS, and to investigate the underlying behaviour of the individual electrode impedances and (N)ZIF, it is of interest to distinguish between both electrodes with the use of (micro-)reference electrodes ((µ)REF). Favorably, (µ)REF make it possible to measure the electrochemical characteristics and, thus, the (N)ZIF of the individual electrodes. However, measuring the electrochemical impedance with respect to (µ)REF can lead to severe measurement artefacts, making a detailed analysis of the impedance spectra complicated. In Chapter 7, a new method is developed in which high-frequency measurement artefacts can be compensated for. A theoretical analysis, using equivalent circuit models of the measurement setups, shows that if two different impedance measurements are averaged, the impedance contributions from the measurement leads can be completely eliminated. The theoretical analysis is validated using Li-ion batteries with seven integrated µREF, all having different impedances. The measurement results show that artefacts are dominating for high-impedance µREF in the high-frequency range. However, these artefacts can be fully compensated by averaging two separate impedance measurements, as predicted by theory. This makes it easily possible to perform artefact-free impedance measurements, even at high frequencies.

The compensation method described in Chapter 7 is advantageously used in the study in Chapter 8 to accurately investigate the impedance and (N)ZIF behavior of the positive electrode (P) and the negative electrode (N). In Chapter 8, (N)ZIF values of the total battery (Bat), P and N are extracted from the corresponding impedance spectra in order to investigate what electrode is responsible for the (N)ZIF behavior of Bat. It has been found that the impedance of both electrodes are temperature dependent and that the (N)ZIF of Bat, P, and N all decrease with increasing battery temperature. It also has been found that both individual electrodes contribute to the Bat (N)ZIF and are therefore both responsible for its behavior. Since P and N (N)ZIF are temperature dependent, impedance-based temperature indication through (N)ZIF measurements essentially can also be performed on the individual electrodes. For the investigated batteries, (N)ZIF values of N are more sensitive to temperature changes in comparison to that of P, leading to steeper N (N)ZIF curves than that of P, which favors the temperature indication accuracy. Furthermore, the electrode revealing the highest imaginary value of the impedance in the inductive quadrant of the complex plane is the electrode that dominates the (N)ZIF magnitude of Bat. For the investigated batteries, it was

found that P revealed the highest imaginary values in the inductive area and the magnitude of the Bat (N)ZIF of these specific batteries is therefore dominated by P.

In summary, it can be concluded that impedance-based temperature indication, in particular the (N)ZIF method, is a valuable tool for temperature monitoring of Li-ion batteries. From the investigations described in this thesis, it can favorably be concluded that (N)ZIF values essentially are chemistry, SoC and aging independent. In addition, key challenges, such as interference from electric components in an EV and crosstalk interference in battery packs, which all considerably disturb the (N)ZIF measurements, have been described and resolved. This brings impedance-based temperature indication, in particular through the (N)ZIF, one step closer to the application of sophisticated battery management systems. Furthermore, a convenient and effective method has been developed to compensate dominating high-frequency artefacts which are encountered with impedance measurements on three-electrode Li-ion batteries. This method favorably enables accurate investigations of the individual electrode impedances and the underlying (N)ZIF behaviour. The (N)ZIF studies performed on the individual electrodes revealed that both electrodes are responsible for the (N)ZIF behavior of the total battery.

In this thesis, the (N)ZIF method is introduced, described and applied in a full electric vehicle. In the performed investigations, interference from electric components and crosstalk, are applied individually. Therefore, it is proposed to perform future research on (N)ZIF measurements under the influence of all different disturbing sources simultaneously. Furthermore, it would be valuable to further study the (N)ZIF behavior as a function of (thermal) gradients. Electric vehicles are perfect candidates on which these investigations can be performed because all disturbing phenomena are present in these applications.

Samenvatting

Door een relatief hoge energiedichtheid, lange levensduur en lage zelfontlading zijn Li-ion batterijen de laatste decennia erg aantrekkelijk geworden om te dienen als energie-opslag medium. Li-ion batterijen zijn daarom uiterst geschikt voor stationaire energie opslag en het voorzien van energie voor mobiele apparaten. Voorbeelden van mobiele apparaten zijn mobiele telefoons, laptops, tablets, horloges en (hybride) elektrische voertuigen ((H)EV). Vooral door de oplopende (H)EV verkoop wordt verwacht dat ook de verkoop van batterijen snel toeneemt.

Ondanks het feit dat Li-ion batterijen vele voordelen bieden, zijn er uitdagingen in het monitoren en regelen van belangrijke batterijeigenschappen, zoals de ladingstoestand (SoC), gezondheidstoestand (SoH) en temperatuur. De gevolgen van het niet goed monitoren en regelen van deze eigenschappen kan leiden tot prestatievermindering, snelle degradatie en, erger nog, tot brand en explosies. Daarom is het van belang dat de toestanden in een veilig werkgebied gehouden worden, welke gedefinieerd zijn door het voltage, de temperatuur en stroom. Een batterij management systeem (BMS), waaronder begrepen het thermisch management systeem (TMS), is de kritische component voor veilig en betrouwbaar batterijgebruik.

Het belangrijkste doel van dit proefschrift is om te onderzoeken of impedantie-gebaseerde temperatuurmetingen, soms ook *sensorless* temperatuurmetingen genoemd, kunnen worden toegepast als methode voor het monitoren van de temperatuur van Li-ion batterijen. Impedantie-gebaseerde temperatuurmetingen bieden aanzienlijke voordelen ten opzichte van conventionele temperatuurmetingen. Bijvoorbeeld, externe en/of geïntegreerde hardware temperatuur sensoren zijn niet vereist, er is geen thermische meetvertraging, de integrale temperatuur wordt gemeten van het actieve materiaal en impedantiemetingen kunnen bovendien gebruikt worden om andere toestanden te schatten, zoals SoC en SoH. In het bijzonder wordt in dit proefschrift onderzoek verricht naar de geschiktheid van de *intercept* frequentie als temperatuur indicator. De *intercept* frequentie is dan ook de rode draad in dit proefschrift. Dit werk is tot stand gekomen door experimenten en simulaties onder verschillende toestanden aan Li-ion batterijen uit te voeren. Uiteindelijk leiden *sensorless* temperatuur metingen tot een beter ontwerp van een efficiënt BMS op het gebied van veiligheid, prestaties en betrouwbaarheid.

In hoofdstuk 2 wordt het werkingsprincipe van Li-ion batterijen uitgelegd. In Li-ion batterijen bewegen Li^+ ionen tussen de positieve en negatieve elektroden tijdens laden en ontladen. De processen die plaatsvinden tijdens (ont)laden gaan gepaard met zekere inefficiënties en daarom wordt er warmte gegenereerd. De warmte, die intern gegenereerd wordt, verplaatst zich van de binnenkant van de batterij naar het buitenste batterijoppervlak waar het gedissipeerd wordt naar de omgeving. Omdat de warmte intern gegenereerd wordt, ontstaan thermische gradiënten, resulterende in temperatuur meet-complicaties en positie-afhankelijke oudering. Wanneer de warmte niet voldoende gedissipeerd kan worden, of wanneer batterijen misbruikt worden, kan *thermal runaway* ontstaan, wat leidt tot gevaarlijke situaties. Vooral als een batterij in een batterij pakket andere batterijen 'aansteekt' kan het *thermal runaway* effect zich door het hele pakket verspreiden. Om die redenen moeten zorgvuldige ontwikkelingsoverwegingen genomen worden op het gebied van batterijen, modules en batterijpakketten om te allen tijden gevaarlijke situaties te voorkomen en om de prestaties en levensduur te maximaliseren.

Vanwege de thermische gradiënten, die snel kunnen ontstaan tijdens gebruik, is het snel en nauwkeurig meten van temperatuur een grote uitdaging. Voor het selecteren van een goede temperatuurmeetmethode, zijn aspecten zoals meetbereik, nauwkeurigheid, resolutie en kosten belangrijk om te overwegen. In hoofdstuk 3 worden verschillende bestaande temperatuurmeetmethoden, die geschikt zijn voor Li-ion batterijen, uitgebreid aan de orde gesteld. Momenteel worden temperatuurmeetmethoden zoals thermistors en thermokoppels veel gebruikt. De meer recent geïntroduceerde methoden, zoals impedantie-gebaseerde temperatuur indicatie en door middel van *fiber Bragg* sensoren, worden momenteel onderzocht om te kijken of deze geschikt zijn voor applicaties die van energie worden voorzien door batterijen.

In hoofdstuk 4 is een nieuwe impedantie-gebaseerde temperatuurmeetmethode geïntroduceerd voor het meten van de interne (Li-ion) batterijtemperatuur. Door middel van elektrochemische impedantie metingen, kan een *zero-intercept* frequentie (ZIF) bepaald worden, die exclusief aan de temperatuur gerelateerd kan worden. De ZIF is gedefinieerd als de frequentie waarbij het imaginaire deel van de impedantie gelijk gesteld is aan nul ($Z_{im} = 0$), dat wil zeggen dat de fase tussen de stroom en het voltage ook nul is. Een wiskundige analyse van een elektrisch equivalent circuit, wat de prestaties van een batterij representeert, laat zien dat de ZIF daalt als de temperatuur stijgt. Impedantie metingen aan herlaadbare en verschillende soorten Li-ion batterijen zijn uitgevoerd om de voorgestelde temperatuurmeetmethode te verifiëren. De experimenten onthulden dat de ZIF een duidelijke afhankelijkheid laat zien als een functie van temperatuur en in principe onafhankelijk is van de chemie, SoC en oudering. Deze impedantie-gebaseerde *sensorless* temperatuurmetingen zijn daarom gemakkelijk en geschikt voor gebruik in een brede doelgroep van stationaire en mobile applicaties, zoals hybride en elektrische voertuigen. Echter, de gepresenteerde meetresultaten in hoofdstuk 4 zijn alle gemeten onder evenwichtsomstandigheden in het laboratorium. Daarom is vervolgonderzoek nodig of de voorgestelde temperatuur meetmethode ook geschikt is voor het gebruik in applicaties buiten het laboratorium, zoals (H)EV.

In hoofdstuk 5 worden onderzoeksresultaten beschreven waarin de in hoofdstuk 4 geïntroduceerde ZIF is gebruikt om de batterijtemperatuur te meten in een EV. De meetresultaten onthullen dat ZIF metingen ernstig verstoord worden door de batterijstroom die door het gehele batterijpakket stroomt. Deze verstoringen maken het onmogelijk om de batterijtemperatuur nauwkeurig te monitoren. Daarom is een nieuwe impedantie-gebaseerde temperatuurmeetmethode geïntroduceerd waarbij de integrale batterijtemperatuur gerelateerd wordt aan andere frequenties dan de ZIF. Het grote voordeel van de voorgestelde *non-zero intercept* frequentie (NZIF), is dat meetverstoringen vermeden kunnen worden. Dat resulteert in een hogere signaal-ruisverhouding (SNR) en derhalve nauwkeurigere temperatuurmetingen. Een theoretische analyse van een equivalent circuit van een Li-ion batterij, laat zien dat het NZIF temperatuur gedrag hetzelfde is als bij de ZIF. Om die reden kan de NZIF ook gebruikt worden voor het meten van de batterijtemperatuur. Om de voorgestelde NZIF methode te valideren zijn impedantiemetingen verricht aan individuele $LiFePO_4$ batterijen en aan grote $LiFePO_4$ batterijpakketten in een EV tijdens bedrijf. De meetresultaten laten zien dat de NZIF inderdaad temperatuur afhankelijk is op dezelfde manier als de ZIF. Echter, in tegenstelling tot de ZIF methode maakt de NZIF methode het mogelijk de meetfrequenties optimaal af te stellen zodat de hoogste SNR verkregen kan worden en derhalve ook meer nauwkeurige temperatuurmetingen.

In applicaties waarbij de energie wordt geleverd door meerdere batterijen in een pakket, kan zich nog een ander verstorend fenomeen voordoen. Dit fenomeen wordt overspraak genoemd en is beschreven in hoofdstuk 6. Als impedantiemetingen bij dezelfde frequentie en tegelijkertijd uitgevoerd worden aan batterijen in een batterijpakket, dan verstoort dat de metingen aan de aangrenzende batterijen. Dit resulteert in onnauwkeurige impedantiemetingen. Experimenteel onderzoek aan een batterijpakket onthulde dat overspraak een lineair verschijnsel is en afhankelijk is van de meetfrequentie, de relatieve positie van de batterijen en van de afstand tussen de batterijen. Echter, de experimenten lieten ook zien dat overspraak onafhankelijk van temperatuur en SoC is. Verder werd geconstateerd dat (N)ZIF waardes duidelijk beïnvloed worden door overspraak. De overspraak tussen batterijen moet daarom weloverwogen worden tijdens het ontwerp van een batterijpakket. Gebaseerd op de experimentele resultaten en een voorgesteld model met twee spoelen met inductieve koppeling, is een overdrachtsfunctie ontworpen die het mogelijk maakt het overspraak verschijnsel te simuleren. Het model kan vervolgens een ondersteunende functie bieden bij het ontwikkelen van impedantiemeetsystemen aan batterijpakketten.

In hoofdstukken 4 en 5 zijn impedantie-gebaseerde temperatuurmeetmethoden op basis van de (N)ZIF gepresenteerd. Tot op heden waren deze methoden slechts gebruikt op (commerciële) Li-ion batterijen met twee elektroden. Om die reden kan alleen de totale batterij impedantie en ook (N)ZIF gemeten worden. Echter, om een geavanceerde BMS te ontwikkelen en om het onderliggende gedrag van de individuele elektrode-impedanties en (N)ZIF te onderzoeken, is het interessant om beide individuele elektrodes te onderscheiden met behulp van (micro-)referentie elektrodes ((µ)REF). (µ)REF maken het mogelijk om de elektrochemische karakteristieken en ook de (N)ZIF van de individuele elektrodes te meten. Echter, impedantiemetingen aan batterijen met (µ)REF kunnen leiden tot ongewenste meetartefacten welke een gedetailleerde impedantie-analyse onmogelijk maken. In hoofdstuk 7 is daarom een methode ontwikkeld die het mogelijk maakt om ongewenste meetartefacten bij hoge meetfrequenties te compenseren. Een theoretische analyse van equivalente modellen van de meetopstelling laat zien dat als twee aparte metingen worden uitgemiddeld, de bijdrage van de impedantie van de meetkabels geheel geëlimineerd kan worden. De theoretische analyse is gevalideerd met Li-ion batterijen met zeven geïntegreerde µREF, die allen een andere impedantie hebben. De experimenten onthulden dat meetartefacten dominant zijn als hoog-impedante µREF gebruikt worden bij hoge meetfrequenties. Echter, de artefacten kunnen volledig gecompenseerd worden door twee separate impedantie metingen uit te middelen, zoals al voorspeld was op basis van de theoretische analyse. De voorgestelde methode maakt het mogelijk ongewenste artefacten bij hoge meetfrequenties volledig te compenseren.

De compensatiemethode beschreven in hoofdstuk 7 is gebruikt in hoofdstuk 8 om de impedantie en de (N)ZIF van de positieve elektrode (P) en de negatieve elektrode (N) nauwkeurig te analyseren. In hoofdstuk 8 zijn (N)ZIF waardes van de totale batterij (Bat), P en N verkregen van de corresponderende impedantiespectra om te bepalen welke elektrode verantwoordelijk is voor het gedrag van de (N)ZIF van Bat. Uit de metingen bleek dat de impedantie van beide elektrodes temperatuur-afhankelijk is en dat (N)ZIF waardes van Bat, P en N allemaal dalen bij stijgende batterij temperatuur. Ook bleek dat beide elektrodes bijdragen aan de Bat (N)ZIF en derhalve ook beiden verantwoordelijk zijn voor het gehele batterij-gedrag. Omdat P en N (N)ZIF waardes temperatuur-afhankelijk zijn, kunnen deze in principe ook gebruikt worden voor impedantie-gebaseerde temperatuurindicatie. Voor de onderzochte batterijen bleek dat (N)ZIF waardes van N gevoeliger zijn voor temperatuurveranderingen dan die van P. Daardoor zijn N (N)ZIF lijnen steiler, wat de nauwkeurigheid van temperatuur monitoren ten goede komt. Verder is de elektrode met de hoogste imaginaire waardes in het inductieve kwadrant van het complexe vlak de elektrode die de (N)ZIF amplitude van de Bat domineert. Voor de onderzochte batterijen had P de hoogste imaginaire waarde in het inductieve deel en daarom wordt de (N)ZIF amplitude in dit specifieke geval gedomineerd door P.

Samenvattend kan geconcludeerd worden dat impedantie-gebaseerde temperatuurindicatie, in het bijzonder de (N)ZIF methode, een waardevol middel is om de temperatuur van Li-ion batterijen te monitoren. Uit het onderzoek beschreven in dit proefschrift kan geconcludeerd worden dat (N)ZIF waardes chemie, SoC en oudering onafhankelijk zijn. Verder zijn uitdagingen, zoals verstoringen door elektrische componenten in een EV en overspraak, waardoor (N)ZIF metingen verstoord worden, beschreven en opgelost. Dit brengt impedantie-gebaseerde temperatuur metingen, in het bijzonder de (N)ZIF, een stap dichter bij het gebruik van geavanceerde batterij management systemen. Verder is een handige en effectieve methode ontwikkeld om ongewenste meetartefacten te compenseren welke verschijnen bij impedantiemetingen aan Li-ion batterijen met referentie elektrodes. Deze compensatiemethode maakt het mogelijk om nauwkeurig de impedantie en het (N)ZIF gedrag van de individuele elektrodes te bestuderen. Uit de studies van de (N)ZIF waardes van de individuele elektrodes bleek dat beide elektrodes verantwoordelijk zijn voor het (N)ZIF gedrag van Li-ion batterijen.

In dit proefschrift wordt de (N)ZIF als nieuwe methode geïntroduceerd, beschreven en toegepast in een volledig elektrisch voertuig. Hierbij zijn de verstoringen van elektrische componenten en overspraak, individueel onderzocht. Voorgesteld wordt vervolgonderzoek uit te voeren waarbij de invloed van diverse verstoringen op (N)ZIF metingen simultaan worden uitgevoerd. Ook is het waardevol om het (N)ZIF gedrag verder te onderzoeken onder invloed van (thermische) gradiënten. Elektrische voertuigen zijn perfecte kandidaten gebleken om dergelijk onderzoek aan te verrichten, omdat hierin alle verstoringen reeds aanwezig zijn.

List of abbreviations

AC	Alternating current
ARC	Accelerating rate calorimetry
Bat	Battery
BMS	Battery management system
CCCV	Constant current, constant voltage
CE	Counter electrode connection measurement device
DC	Direct current
EIS	Electrochemical impedance spectroscopy
EMF	Electromotive force
EQC	Equivalent circuit
ERT	Electrical resistance tomography
ETIS	Electrothermal impedance spectroscopy
EV	Electric vehicle
FBG	Fiber Bragg-grating
FFT	Fast Fourier transform
HEV	Hyrbid electric vehicle
IR	Infrared
Li-ion	Lithium ion
μREF	Micro-reference electrode
N	The negative electrode
NCA	LiNiCoAl-Oxide
NMC	LiNiMnCo-Oxide
N_r	Negative electrode measured with reversed connections
NTC	Negative temperature coefficient
NZIF	Non-zero-intercept frequency
OCP	Open circuit potential
OCV	Open circuit voltage
P	The positive electrode
PCB	Printed circuit board
PDM	Pulse density modulation
PEM	Proton exchange membrane
P_r	Positive electrode measured with reversed connections
PTC	Positive temperature coefficient
RC-circuit	Electric circuit containing resistors and capacitors
RE	Reference electrode connection measurement device
REF	Reference electrode
RMSE	Root-mean-square-error
RTD	Resistance temperature detector

S	Sense connection measurement device
SEI	Solid-electrolyte-interface
SNR	Signal-to-noise ratio
SoC	State-of-charge
SoH	State-of-health
TCR	Temperature coefficient of resistance
TLC	Thermochromic liquid crystals
TMS	Thermal management system
UV-light	Ultraviolet light
WE	Working electrode connection measurement device
ZIF	Zero-intercept frequency

List of symbols

Symbol	**Meaning**	**Unit**
A	Battery surface area	m^2
A_p	Pre-exponential factor in Arrhenius equation	1/Ω
a	Radius of circular coil	m
B	Magnetic field	T
C	Capacitance	F
C_d	Diffusion capacitance (capacitance to model diffusion)	F
C_{dl}	Double layer capacitance	F
C_{kin}	Capacitance capturing double layers and surface layers	F
C_p	Specific heat capacity of battery	J/(kg·K)
d	Axial distance between battery centers	m
dV/dQ	Differential voltage	V/Ah
E_a	Activation energy	J/mol
F	Faraday constant	As/mol
f	Frequency	Hz
f_0	Zero-intercept frequency	Hz
f_{int}	Intercept frequency	Hz
$\mathscr{g}$	Function for NZIF calculations	1/Ω
ΔG	Gibbs free energy change	J/mol
h	Heat transfer coefficient	W/(m^2·K)
$\mathscr{h}$	Function for NZIF calculations	-
$\mathcal{H}$	Implicit function for NZIF calculations	-
ΔH	Enthalpy change	J/mol
I	Current	A
I_{Bat}	Battery current flowing between CE and WE connections	A
I_c	Current flowing through capacitor bridge	A
j	Imaginary unit satisfying $j^2 = -1$	-
k	Coupling coefficient	-
K_1	Dimensionless modeling parameter	-
K_2	Dimensionless modeling parameter	-
k_c	Phase lag filter gain	-
L	Inductance	H
m	Mass	kg
M	Mutual inductance	H
n	Number of electrons involved in charge-transfer reaction	-
$\vec{n}$	Unit (outer) normal vector at boundary	-
N	Number of turns on coil	-
n_{eff}	Effective core index of refraction	-

p	Pressure	Pa
q_η	Irreversible heat power calculated by overpotential η	W
$\vec{q}_{cond}$	Heat flux	W/m^2
q_{conv}	Convective heat exchange power	W
Q_{in}	Volumetric heat power	W/m^3
q_{in}	Total heat generation power	W
q_{out}	Total heat dissipation power	W
q_R	Irreversible heat power calculated by resistance R	W
q_{rad}	Radiative heat exchange power	W
q_S	Reversible heat generation power	W
R	Resistance	Ω
R_g	Gas constant	J/(mol·K)
R_{kin}	Resistance capturing charge transfer and surface layers	Ω
R_s	Series resistance	Ω
s	Laplace transform variable	rad/s
ΔS	Entropy change	J/(mol·K)
T	Battery temperature	K
t	Time	s
T_a	Ambient temperature	K
$T_{Container}$	Battery container temperature	K
T_{EIS}	Temperature measured through the impedance	K
∇T	Temperature gradient	K/m
T_{Neg}	Temperature of negative battery terminal	K
V	Voltage	V
V_{bat}	Voltage at battery terminals	V
V_{bat}^{eq}	Battery EMF	V
ΔV	Voltage difference between V_+ and V_-	V
V_{im}	Imaginary part of complex voltage	V
V_{re}	Real part of complex voltage	V
V_+	Voltage measured at RE connection	V
V_-	Voltage measured at S connection	V
x	Stoichiometric coefficient of the positive electrode	-
y	Stoichiometric coefficient of the negative electrode	-
z	Axial distance from center of a coil	m
Z	Impedance	Ω
$Z_{\mu REF}$	Micro-reference electrode impedance	Ω
Z_{Bat}	Battery impedance	Ω
Z_{Bat}^m	Measured battery impedance	Ω
Z_C	Capacitor impedance	Ω
Z_{filter}	Phase-lag filter	-
Z_{im}	Imaginary part of impedance	Ω
Z_{in}	Input-impedance measurement device	Ω
Z_L	Inductor impedance	Ω
Z_l^i	Lead and connection impedance of the measurement setup, where i can be WE, CE, RE, or S	Ω

Z_N	Negative electrode impedance	Ω
Z_N^m	Measured negative electrode impedance	Ω
$\overline{Z_N^m}$	Averaged measured negative electrode impedance	Ω
$Z_{N,C}^m$	Measured negative electrode impedance in presence of capacitor	Ω
$Z_{N,r}^m$	Measured negative electrode impedance with reversed connections	Ω
Z_P	Positive electrode impedance	Ω
Z_P^m	Measured positive electrode impedance	Ω
$\overline{Z_P^m}$	Averaged measured positive electrode impedance	Ω
$Z_{P,C}^m$	Measured positive electrode impedance in presence of capacitor	Ω
$Z_{P,r}^m$	Measured positive electrode impedance with reversed connections	Ω
Z_R	Resistor impedance	Ω
Z_{Re}	Real part of impedance	Ω
ϵ	Emissivity of surface material	-
κ	Heat conductivity	W/(m·K)
Λ	Grating spacing	m
λ_B	Bragg wavelength	m
μ_0	Vacuum permeability	H/m
η_{bat}	Battery overpotential	V
η_{ct}	Charge-transfer overpotential	V
η_d	Diffusion overpotential	V
η_e	Overpotential due to electron transport	V
η_{el}	Electrolyte overpotential	V
η_{neg}	Overpotential negative electrode	V
η_Ω	Overpotential from Ohmic losses	V
η_{pos}	Overpotential positive electrode	V
ω	Angular frequency	rad/s
ω_0	Zero-intercept frequency	rad/s
ρ	Density	kg/m^3
σ	Real part of Laplace transform variable s	rad/s
ξ	Reaction progress or SoC	-

1

Introduction

This introductory chapter starts with an overview of various energy sources and explains the recent increasing demand for renewable energy. Subsequently, the history and evolution of the most important battery systems are described. It turns out that the lithium-ion battery is nowadays the technology of choice to power mobile applications and to serve as stationary energy storage devices. The chapter is concluded with the scope and overview of this thesis.

1.1. General introduction

Today's society is extremely dependent on energy. The supply and availability of energy is taken for granted by many people in the developed countries. For instance, in modern society it is easy to power electronic devices, heat up or cool down buildings and drive vehicles. A recent report from the U.S. Energy Information Administration [1] reveals that the world's energy consumption will increase in the coming decades. Countries with large economic growth, particularly Asian countries, are mainly responsible for this increase in energy consumption. Fig. 1.1 shows predictions up to the year 2040 for five different energy sources. So far, the fossil fuels, such as coal, oil and natural gas are dominating due to their long existence and to the scientific innovations that are based upon them. Although new fossil fuel resources certainly will be found with advanced techniques it is, however, inevitable that these non-renewable energy sources will deplete in the future [2, 3]. Moreover, fossil fuels contribute to global warming by generating greenhouse gases, which has a major environmental impact in the long term [2, 3].

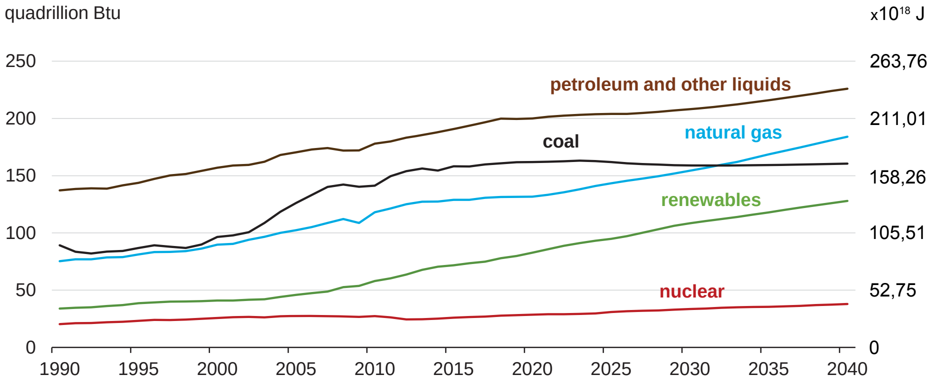

Fig. 1.1: World energy consumption by source from 1990 - 2040. Adapted from Ref. [1].

The emission of greenhouse gases from fossil fuels can be strongly reduced by using alternatives such as nuclear and renewable energy sources. However, both sources have their challenges. For instance, the waste of nuclear energy can be radioactive for thousands of years, and improper safety management can lead to disastrous consequences. In that respect, renewable energy sources are safer and cleaner. Examples of renewable energy sources are solar, wind, tidal and geothermal power. The challenge with renewable sources is that the energy output is often non-continuous and that energy generation (completely) lacks at required moments. The reason is that these sources are highly dependent on time, location and weather. Therefore, these systems would benefit from energy storage devices in order to stabilize the output. Energy can, for example, be stored in a mechanical, electrical, thermal or electrochemical way. The electrochemical methods, in particular batteries, have drawn considerable attention in the last decades due to the fact that these devices are highly efficient [4].

Batteries are currently popular devices to buffer energy that is generated from renewable sources. These battery systems are better known as stationary energy storage devices. In addition, batteries are also highly suitable for providing mobile devices with energy. Examples of mobile devices are portable phones, laptops, tablets, watches and (hybrid) electric vehicles ((H)EV). Especially the (H)EV market requires many batteries since it is to be expected that (H)EV sales will tremendously increase in the near future. The exact growth in market share of (H)EV is hard to predict since this depends on factors such as costs, technology, infrastructure, consumer acceptance and governmental regulations [5–7]. However, Bloomberg New Energy Finance [8] made a prediction of (H)EV sales. A projection of these sales is shown in Fig. 1.2.

If (H)EV batteries are charged with electricity generated by renewable energy sources, the environmental impact of a (H)EV is much lower than the impact of vehicles using combustion engines running on fossil fuels. In that respect, (H)EV are excellent candidates to reduce greenhouse gas emissions. Evidently, the battery plays a major role in the success of both stationary and mobile applications.

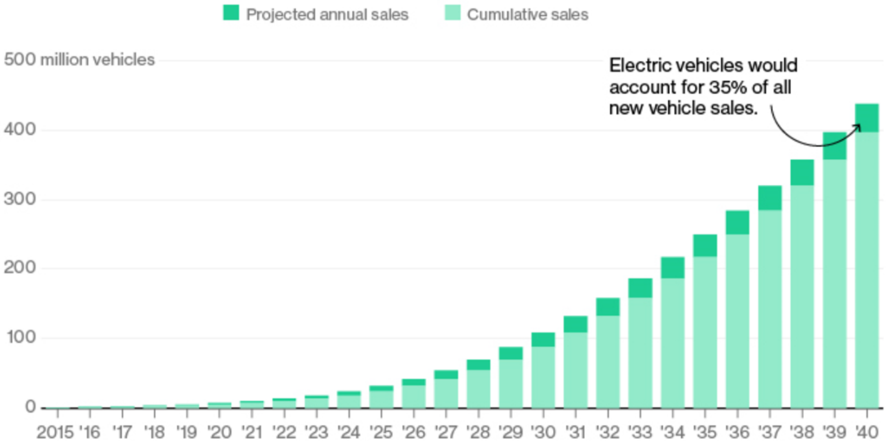

Electric vehicles would account for 35% of all new vehicle sales.

Fig. 1.2: Number of projected EV sales per year. Adopted from Ref. [8].

1.2. Batteries

Batteries are devices that store energy in a chemical form and convert that energy, when required, back into electricity. Battery technology is already evolving for hundreds of years. Some scientists believe that the first batteries were used near Baghdad in the period from 250 BC to 250 AD for electroplating purposes, as archaeologists found objects that could have been identified as batteries [9]. However, for other scientists the origin and purpose of these objects remains unclear [10, 11].

In 1745-1746 Edwald Georg von Kleist and Pieter van Musschenbroek independently invented the so-called Leyden Jar, which can store electric energy analogous to a capacitor [12]. A few years later (1748) Benjamin Franklin constructed different Leyden Jars in series to form a battery [13]. Nevertheless, it has been widely accepted that the Italian pioneers Luigi Galvani and Alessandro Volta made the first electrochemical cell known to humanity [14]. In 1791 Galvani published his hypothesis that the electricity involved in the contraction of a frog's muscle had an animal origin [15]. Alessandro Volta opposed this and claimed that this effect originated from the different metals Galvani used in his frog experiment. Triggered by Galvani, Volta performed extensive experiments, which eventually led to the invention of the battery at the end of 1799. As proof he constructed a 'pile' consisting of an alternating sequence of two metals (zinc and silver) separated by clothes soaked into an electrolyte. Volta sent a description of his invention to the Royal Society of London in 1800 [16, 17]. Based on Volta's work, Michael Faraday established a connection between chemical and electrical energy in the year 1834.

Volta's invention induced a rapid evolution in battery technology. William Sturgeon and John Daniell improved Volta's design in 1830 and 1835, respectively [18]. In 1866, Georges Leclanché invented and patented a new system which was very successful [19]. Leclanché used a positive electrode of a manganese oxide-carbon mixture and a negative electrode of zinc. An aqueous ammonium chloride solution served as the electrolyte. These batteries were used extensively to operate in telegraphy networks. It is interesting to notice that the present non-rechargeable batteries, zinc-carbon or zinc-manganese dioxide (or alkaline) are based upon Leclanché's invention.

Six years earlier (1860) than Leclanché, Gaston Planté invented a battery based on lead-acid chemistry [20]. This was the first rechargeable battery ever and became extremely successful. The so-called lead-acid batteries have been used in many applications, even in EVs more than a century ago, but are nowadays most popular for their usage as starter and auxiliary batteries in conventional vehicles.

In about 1890 the Swedish scientist Waldemar Junger and the American inventor Thomas Edison independently introduced the nickel-cadmium and nickel-iron battery [21]. Nickel-cadmium (NiCd) batteries had the advantage to be extremely robust, both mechanically and electrically. Moreover, like the lead-acid battery, NiCd and nickel-iron batteries are also rechargeable.

Effectively, not much innovation took place in the battery field for decades since the systems based on the technology invented by Planté, Leclanché and Junger were simply satisfactory for the technology at that time [14]. However, this situation changed in the late 1960^s, when the demand for portable (consumer) electronics started to increase. The main problem was that the energy density of conventional batteries was insufficient for the fast-evolving technology of portables. Fig. 1.3 illustrates the energy density of various battery technologies. It is clear that the lead-acid and NiCd batteries offer very low energy densities. A new breakthrough came in the late 1980^s with the commercialization of nickel-metal hydride (NiMH) batteries, although the research efforts already took place in the 1950^s [22, 23]. NiMH batteries offer more storage capacity than their cadmium predecessors and are environmentally friendlier due to the absence of cadmium. In the 1990^s, NiMH batteries emerged as the technology of choice for (H)EVs [24–26].

Not much later after the market introduction of the NiMH battery, rechargeable lithium ion (Li-ion) battery technology made its breakthrough. It was commercialized by the Sony Corporation in 1991 [28]. As can be seen in Fig. 1.3, the energy density of Li-ion batteries is higher than that of lead-acid, NiCd and NiMH. Due to this high energy density the Li-ion battery is nowadays the technology of choice. New Li-based concepts, such as lithium sulfur (Li-S) and lithium air (Li-O_2), are currently being investigated. These technologies have the potential to offer even higher energy densities than Li-ion, as shown in Fig. 1.3. Although challenging key issues still have to be resolved, it is to be expected that Li-S and, later, Li-O_2 technologies will take over Li-ion in the near future [29]. The energy density of these advanced Li-technologies approaches even that of gasoline (Fig. 1.3).

In addition to the battery technologies described so far, a wide variety of both chargeable and non-chargeable battery chemistries have been developed since Volta introduced his initial invention. Examples of commercialized systems are high-temperature sodium-sulfur (Na-S) and sodium-nickel chloride (Na-$NiCl_2$) batteries. These batteries are mainly used for stationary energy storage and mobile niche applications [27, 30]. The energy densities of these systems are also shown in Fig. 1.3.

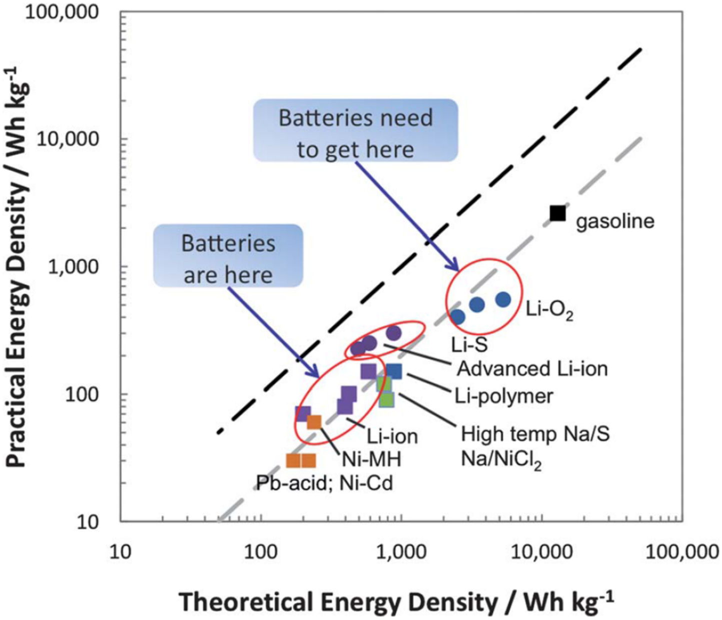

Fig. 1.3: The energy density for various battery chemistries compared with that of gasoline. Note that the (low) efficiency of combustion engines is taken into account for gasoline. Adopted from Ref. [27].

1.3. Scope and outline of this thesis

Due to the high energy density, long cycle life and low self-discharge rate, Li-ion batteries are nowadays the technology of choice to power both stationary and mobile applications [31]. However, challenges are met in monitoring and controlling the states of a Li-ion battery, such as State of Charge (SoC), State of Health (SoH) and temperature [32, 33]. The consequences of poor monitoring and control can lead to a decrease in battery performance, rapid degradation and, even worse, fire or explosion. This would be detrimental for the success of battery-powered devices, especially for (H)EV. Therefore, it is of high importance to keep the battery states within their safe operating range, which is defined by voltage, temperature and current limits. A Battery Management System (BMS), including a Thermal Management System (TMS), is the critical component to monitor and control these states in order to guarantee safe and reliable battery operation.

The main goal of this thesis is to investigate whether impedance-based temperature measurements, sometimes referred to as sensorless temperature measurements, can be applied as method for monitoring the temperature of Li-ion batteries. Impedance-based temperature indication offers some advantages with respect to conventional temperature measurements. For instance, no external or internal hardware temperature sensors are required, thermal measurement delay is short, it measures an average/integral temperature of the active material, and impedance measurements can also be used to determine additional states, such as SoC and SoH [34–37]. In particular, the investigation of the suitability of the intercept frequency as temperature indicator is the central topic in this thesis. Investigations have been performed by both experiments and simulations on Li-ion batteries under various conditions. In the end sensorless temperature measurements facilitate the design of an efficient BMS in terms of safety, performance and reliability.

Chapter 2 explains the working principles of Li-ion batteries. Due to various internal resistances, batteries generate heat during operation. It is explained that heat is generated in the interior and transferred to the environment at the surface. Therefore, it is likely that thermal gradients develop inside batteries during operation. If the developed heat cannot be sufficiently transferred to the environment, the battery temperature continues to increase, which may lead to dangerous situations and in the worst case induce so-called thermal runaway. In these rare thermal situations, a sophisticated BMS should act preventively and shut-down the corresponding battery or battery module. If that is not effective other safety devices should prevent dangerous scenarios becoming worse.

Temperature sensors are required in order to accurately control the battery temperature within a well-defined range. Chapter 3 introduces various existing temperature measurement techniques for Li-ion batteries. It explains both the traditional and novel temperature measurement methods applied to Li-ion batteries. This Chapter also discusses the impedance-based temperature measurements, which are a key topic in this thesis.

In Chapter 4, the as-denoted zero-intercept frequency, a parameter to indicate battery temperature, is introduced and discussed. A simple mathematical model is developed and used to predict the behavior of the intercept frequency as a function of temperature. Laboratory measurements under well-controlled conditions are performed to validate the model. Moreover, the influence of the zero-intercept frequency on SoC and cycling are investigated experimentally.

In Chapter 5, the zero-intercept frequency is applied in order to indicate battery temperature under real driving conditions in EV. The measurement results reveal that the zero-intercept frequency is not suitable for temperature indication in this particular application due to measurement interference from the electric components. Therefore, a non-zero intercept frequency is introduced, which makes it possible to avoid dominating interference and, therefore, making temperature indication in battery-powered applications far more accurate in comparison to zero-intercept-frequency measurements.

Besides interference from the electric components in EV, also so-called crosstalk interference disturbs impedance measurements. Crosstalk interference occurs when impedance measurements are performed simultaneously in battery packs and at the same frequency, resulting in measurement inaccuracies. In Chapter 6, crosstalk interference in battery packs is introduced and discussed comprehensively by means of experiments and modeling on battery packs.

In Chapter 7, three-electrode measurements, with the help of reference electrodes, are reported and discussed. Reference electrodes enable to measure the voltage and impedance of the individual electrodes. However, since impedance measurements with reference electrodes can be heavily subjected to measurement artefacts, measurement results cannot always be accurately analyzed. Therefore, Chapter 7 discusses three-electrode measurement artefacts and describes a new and effective solution to compensate high-frequency artefacts.

Chapter 8 is devoted to the impedance contributions and intercept frequency behavior of the individual electrodes by using reference electrodes. In this chapter, the proposed compensation method described in chapter 7 is used for accurate impedance analysis.

References

[1] U.S. Energy Information Administration (EIA), *International Energy Outlook 2017 Overview*, Tech. Rep. (2017).

[2] M. Höök and X. Tang, *Depletion of fossil fuels and anthropogenic climate change — A review,* Energy Policy **52**, 797 (2013).

[3] N. Abas, A. Kalair, and N. Khan, *Review of fossil fuels and future energy technologies,* Futures **69**, 31 (2015).

[4] P. Poizot and F. Dolhem, *Clean energy new deal for a sustainable world: from non-CO2 generating energy sources to greener electrochemical storage devices,* Energy Environ. Sci. **4**, 2003 (2011).

[5] Z. Rezvani, J. Jansson, and J. Bodin, *Advances in consumer electric vehicle adoption research: A review and research agenda,* Transp. Res. Part D **34**, 122 (2015).

[6] S. Steinhilber, P. Wells, and S. Thankappan, *Socio-technical inertia: Understanding the barriers to electric vehicles,* Energy Policy **60**, 531 (2013).

[7] O. Egbue and S. Long, *Barriers to widespread adoption of electric vehicles: An analysis of consumer attitudes and perceptions,* Energy Policy **48**, 717 (2012).

[8] T. Randall, *Here's How Electric Cars Will Cause the Next Oil Crisis,* (2016).

[9] D. Downs and A. Meyerhoff, *Battery, Baghdad, 250 BCE,* (2000).

[10] *The 10 Most Not-So-Puzzling Ancient Artifacts: The Baghdad Battery,* (2012).

[11] *Riddle of 'Baghdad's batteries',* (2003).

[12] J. Ho, R. Jow, and S. Boggs, *Historical Introduction to Capacitor Technology,* IEEE Electr. Insul. Mag. **26**, 20 (2010).

[13] E. P. Krider, *Benjamin Franklin and Lightning Rods,* Phys. Today **59**, 42 (2006).

[14] B. Scrosati, *History of lithium batteries,* J. Solid State Electrochem. **15**, 1623 (2011).

[15] M. Piccolino, *Animal electricity and the birth of electrophysiology: The legacy of Luigi Galvani,* Hist. Neurosci. **46**, 381 (1998).

[16] M. Piccolino, *The bicentennial of the Voltaic battery (1800 – 2000): the artificial electric organ,* Trends Neurosci. **23**, 147 (2000).

[17] S. Trasatti, *1799 – 1999: Alessandro Volta's 'Electric Pile' Two hundred years, but it doesn't seem like it,* J. Electroanal. Chem. **460**, 1 (1999).

[18] A. Cutter, *The Electricians Green Handbook*, 1st ed. (Cengage Learning US, 2012) pp. 1–288.

[19] D. Linden and B. Thomas, *Handbook of Batteries*, 3rd ed., edited by D. Linden and B. Thomas (McGraw-Hill, 2002).

[20] P. Kurzweil, *Gaston Planté and his invention of the lead–acid battery — The genesis of the first practical rechargeable battery,* J. Power Sources **195**, 4424 (2010).

[21] S. Bergstrom, *Nickel-Cadmium Batteries - Pocket Type,* J. Electrochem. Soc. **99**, 248 (1952).

[22] P. Ruetschi, F. Meli, and J. Desilvestro, *Nickel-metal hydride batteries. The preferred batteries of the future?* J. Power Sources **57**, 85 (1995).

[23] P. Notten, *Rechargeable nickel-metalhydride batteries: a successful new concept,* in *Interstitial Intermet. Alloy.*, edited by F. Grandjean, G. J. Long, and K. H. J. Buschow (Springer Netherlands, Dordrecht, 1995) Chap. 7, pp. 151—-195.

[24] P. Gifford, J. Adams, D. Corrigan, and S. Venkatesan, *Development of advanced nickel/metal hydride batteries for electric and hybrid vehicles,* J. Power Sources **80**, 157 (1999).

[25] S. K. Dhar, S. R. Ovshinsky, P. R. Gifford, D. A. Corrigan, M. A. Fetcenko, and S. Venkatesan, *Nickel/metal hydride technology for consumer and electric vehicle batteries - a review and up-date,* J. Power Sources **65**, 1 (1997).

[26] A. Taniguchi, N. Fujioka, M. Ikoma, and A. Ohta, *Development of nickel/metal-hydride batteries for EVs and HEVs,* J. Power Sources **100**, 117 (2001).

[27] M. Thackeray, C. Wolverton, and E. Isaacs, *Electrical energy storage for transportation—approaching the limits of, and going beyond, lithium-ion batteries,* Energy Environ. Sci. **5**, 7854 (2012).

[28] G. E. Blomgren, *The Development and Future of Lithium Ion Batteries,* J. Electrochem. Soc. **164**, 5019 (2017).

[29] B. Scrosati and J. Garche, *Lithium batteries: Status, prospects and future,* J. Power Sources **195**, 2419 (2010).

[30] B. L. Ellis and L. F. Nazar, *Sodium and sodium-ion energy storage batteries,* Curr. Opin. Solid State Mater. Sci. **16**, 168 (2012).

[31] A. Opitz, P. Badami, L. Shen, K. Vignarooban, and A. Kannan, *Can Li-Ion batteries be the panacea for automotive applications?* Renew. Sustain. Energy Rev. **68**, 685 (2017).

[32] V. Pop, H. Bergveld, P. Notten, and P. Regtien, *State-of-the-art of battery state-of-charge determination,* Meas. Sci. Technol. **16** (2005), 10.1088/0957-0233/16/12/R01.

[33] H. Bergveld, D. Danilov, V. Pop, P. Regtien, and P. Notten, *Adaptive State-of-Charge Determination,* Encycl. Electrochem. Power Sources **1**, 459 (2009).

[34] R. Srinivasan, B. G. Carkhuff, M. H. Butler, and A. C. Baisden, *Instantaneous measurement of the internal temperature in lithium-ion rechargeable cells,* Electrochim. Acta **56**, 6198 (2011).

[35] J. P. Schmidt, S. Arnold, A. Loges, D. Werner, T. Wetzel, and E. Ivers-Tiffée, *Measurement of the internal cell temperature via impedance: Evaluation and application of a new method,* J. Power Sources **243**, 110 (2013).

[36] R. R. Richardson, P. T. Ireland, and D. a. Howey, *Battery internal temperature estimation by combined impedance and surface temperature measurement,* J. Power Sources **265**, 254 (2014).

[37] L. H. J. Raijmakers, D. L. Danilov, J. P. M. Van Lammeren, M. J. G. Lammers, and P. H. L. Notten, *Sensorless battery temperature measurements based on electrochemical impedance spectroscopy,* J. Power Sources **247**, 539 (2014).

2

Working principle of Li-ion batteries

In lithium-ion batteries Li^+ ions shuttle between the positive and negative electrodes upon charging and discharging. Unfavorably, the processes during (dis)charging occur with certain inefficiencies and heat is therefore generated. This heat flows from the electrode materials to the battery surface at which it is dissipated to the environment. Since heat is generated internally, thermal gradients develop, resulting in temperature measurement complications and position-dependent aging. When the heat cannot be sufficiently dissipated, or when the battery is under abusive conditions, thermal runaway may occur, which leads to dangerous situations. In particular, if a battery inside a battery pack induces thermal runaway to adjacent batteries, it can propagate through the complete battery pack. Therefore, careful design considerations need to be taken on single-battery, module, and pack level in order to prevent dangerous situations and to maximize performance and lifetime.

2.1. Introduction

Lithium batteries are able to convert chemical energy into electrical energy by means of electrochemical reduction and oxidation (redox) reactions. In Li-ion batteries, these reactions are reversible, which means that the opposite, *i.e.* conversion of electrical energy into chemical energy, is possible as well, making them so-called secondary batteries. In that respect, secondary batteries are different to primary batteries, in which the stored chemical energy is irreversibly converted to electrical energy. In this overview only Li-ion batteries are considered, whose components and working principles, including thermal considerations, are described in this Chapter.

2.2. Components and working principles

A schematic overview of a Li-ion battery is shown in Fig. 2.1. It shows five main components displayed in different colors. At both outer sides, the current collectors are shown on which the active electrode materials are coated. In commercial Li-ion batteries, aluminum and copper are typical materials for the positive and negative current collectors, respectively [1]. The current collectors serve as a substrate for the electrode materials and for conducting electrons.

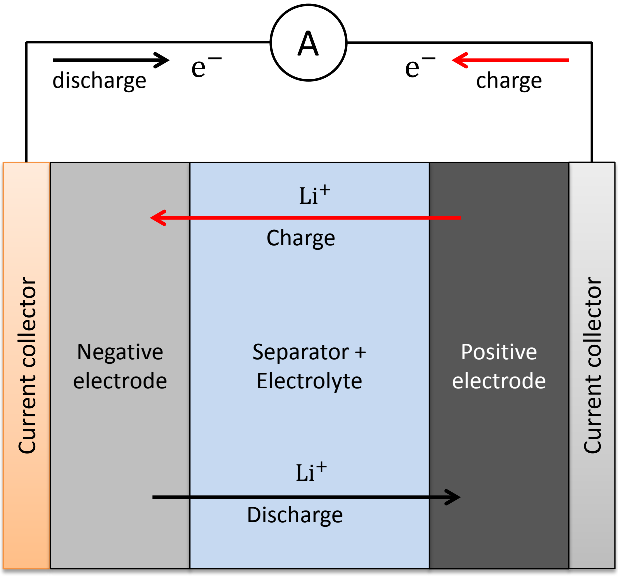

Fig. 2.1: Schematic representation of a Li-ion battery.

The negative and positive electrode materials are intercalation materials that function as a host for lithium ions. An overview of common electrode materials used for Li-ion batteries is shown in Table 2.1. A separator between both electrodes prevents electrical contact but enables ions to pass through. The battery is filled with a lithium-salt-containing non-aqueous electrolyte that facilitates ionic conduction.

Table 2.1: Common battery electrode materials. Modified from Refs. [2, 3].

Materials	Average voltage vs. Li/Li^+ [V]	Theoretical specific capacity [mAh/g]	Advantages	Disadvantages
Positive electrodes				
$LiCoO_2$	3.8	274	Performance, High voltage	Cost and resource limitations of Co, low capacity
$LiNi_{0.8}Co_{0.15}Al_{0.05}O_2$	3.7	279	High capacity, High voltage, excellent rate performance	Safety, cost and resource limitations of Ni and Co
$LiNi_{1/3}Mn_{1/3}Co_{1/3}O_2$	3.7	278	High voltage, moderate safety	Cost and resource limitations of Ni and Co
$LiMn_2O_4$	4.1	148	Low cost and abundance of Mn, high voltage, excellent rate performance	Limited cycle life, low capacity
$LiFePO_4$	3.45	170	Excellent safety, cycling, and rate capability, low cost and abundance of Fe, low toxicity	Low volage, capacity and energy density
Li-S	2.2	1672	Very high capacity, abundance of S	Poor cycle life and rate performance, low voltage
Negative electrodes				
Graphite (C_6)	0.1	372	Long cycle life, abundant	Inefficiencies due to solid electrolyte interface (SEI) growth
$Li_4Ti_5O_{12}$	1.5	175	Good cycling and efficiencies, zero strain material	High voltage, low capacity/energy density
$Li_{22}Si_5$	0.4	4200	Extreme high capacity at low potentials	Rapid degradation due to large electrode expansion, SEI layer growth
Lithium metal	0	3860	High capacity at very low potential, flat potential curve	Dendrite growth, limited Coulombic efficiency

As shown by the red arrow in Fig. 2.1, Li^+ ions leave the positive electrode, enter the electrolyte and intercalate into the negative electrode during charging. At the same time, electrons leave the positive electrode and flow into the negative electrode through the outer electric circuit. Upon charging the positive electrode is being oxidized and the negative electrode reduced. In this case energy is required from an external source and the battery converts electrical energy into chemical energy that is stored inside the electrodes. This process reverses upon discharging, as indicated with the black arrows in Fig. 2.1. The corresponding partial electrochemical reactions for a $C_6/LiMeO_2$ battery are represented by

$$\mathrm{LiMeO_2} \xrightleftharpoons[discharge]{charge} \mathrm{Li_{1\text{-}x}MeO_2} + x\mathrm{Li^+} + x\mathrm{e^-} \qquad (0 \le x \le 0.5) \tag{2.1}$$

and

$$\mathrm{C_6} + y\mathrm{Li^+} + y\mathrm{e^-} \xrightleftharpoons[discharge]{charge} \mathrm{Li_yC_6} \qquad (0 \le y \le 1)\ , \tag{2.2}$$

for the positive and negative electrode, respectively. Note that x is limited to 0.5 to reversibly cycle the positive electrode without causing rapid capacity loss. The overall reaction for the total battery is then given by

$$\mathrm{LiMeO_2} + \mathrm{C_6} \xrightleftharpoons[discharge]{charge} \mathrm{Li_yC_6} + \mathrm{Li_{1\text{-}x}MeO_2}\ , \tag{2.3}$$

where x and y are the stoichiometric coefficients of the positive and negative electrode, respectively. The abbreviation Me stands for a transition metal, which in commercial batteries normally is Cobalt (Co) combined with or without for example Nickel (Ni), Manganese (Mn), or Aluminum (Al) in different ratios [4–6]. Graphite (C_6) is a typical intercalation material that is generally used for negative electrodes in commercial Li-ion batteries [7–9]. More common Li-ion battery electrode materials with their specific electrode characteristics are listed in Table 2.1.

A charged battery experiences a chemical driving force due to the difference in chemical potentials between the two electrodes. This can be expressed as the standard Gibbs free energy change (ΔG). Under equilibrium conditions the chemical driving force is balanced by an electrostatic driving force, that is equal to $-nFV$. The balance between the chemical and electrical forces can then simply be expressed as

$$\Delta G = -nFV\ , \tag{2.4}$$

where n is the number of electrons involved in the charge-transfer reaction (+1 for Li^+), F is the Faraday constant, and V is the voltage difference between the electrodes [10–13]. Eq. 2.4 readily makes it possible to calculate the Electromotive Force (EMF) of the battery if ΔG is known from the overall reaction in Eq. 2.3. The EMF is defined as the battery voltage under equilibrium conditions. Frequently, this voltage is also referred to as the Open-Circuit Voltage (OCV) or Open-Circuit Potential (OCP) [1].

The electrode voltage under equilibrium conditions is dependent on the used host material and the lithium concentration in the active material. These dependencies imply that the voltage can either increase or decrease upon lithium intercalation.

2.3. Thermal considerations

Although Li-ion batteries are very efficient devices [3, 14], lithium (de-) intercalation in both electrodes and all associated processes do not occur with 100% efficiency. These processes results in heat generation when the battery is in operation. The generated heat flows through the materials to the battery surface, at which it is dissipated to the surroundings. The characteristics of these processes are described in this Section.

2.3.1. Heat generation

Due to various reasons the voltage at the battery terminals deviates from the EMF at a given SoC [15, 16]. This voltage difference is better known as the overpotential (η_{bat}) and can be defined as

$$\eta_{bat} = V_{bat} - V_{bat}^{eq} , \tag{2.5}$$

where V_{bat} is the voltage at the terminals and V_{bat}^{eq} is the EMF. The EMF can be experimentally determined by various methods along the complete SoC range. Methods such as (dis)charging at very low currents, interpolation between the charge and discharge voltage curve, voltage relaxation and extrapolation to zero current have been used [17–19]. From Eq. 2.5, it can be seen that η_{bat} is negative during discharging and positive during charging. Similarly, the overpotentials of the individual electrodes (η_{pos} and η_{neg}) can be defined. In this thesis η_{pos} is defined to be positive during charging and negative during discharging. For the negative electrode it is defined to be the opposite.

---

[1] OCV or OCP are popular terms but can occur under non-equilibrium conditions as well, while the EMF is only defined under equilibrium conditions.

The total overpotential is induced by various processes occurring in a battery, such as the charge-transfer reactions at the electrode/electrolyte interfaces (η_{ct}) [20], diffusion and migration of Li-ions across the electrolyte (η_{el}) [21], diffusion and migration of Li-ions in the electrodes (η_d) [22], and the Ohmic losses (η_Ω) [23]. Therefore, the total overpotential can also be expressed as

$$\eta_{bat} = V_{bat} - V_{bat}^{eq} = \eta_{ct} + \eta_{el} + \eta_d + \eta_\Omega \ . \tag{2.6}$$

Note that the charge-transfer processes, diffusion and migration and Ohmic losses occur in both the positive and negative electrodes.

The battery overpotential multiplied with the current results in an irreversible heat power, which is given by [24–27]

$$q_\eta = \eta_{bat} I(t) \ , \tag{2.7}$$

or alternatively

$$q_R = I(t)^2 R \ , \tag{2.8}$$

where I represents the battery current and R the total internal battery resistance. From Eq. 2.8, it can clearly be seen that if the battery current and/or the resistance increases, more irreversible heat is generated. To minimize these thermal losses, it is thus a key issue to keep the battery resistances as low as possible. Generally, these resistances increase during cycling and calendar aging and this consequently leads to more heat generation during the battery life [28–30].

In addition to the irreversible heat source resulting from resistances, a reversible heat source is present due to changes of the reaction entropy [31–33]. Entropic heat generation can be either endothermic or exothermic and depends on the direction of the electrode reactions and SoC. The entropy change (ΔS) can be derived from the enthalpy change (ΔH) and Gibbs free energy change [34, 35]. After further derivations, it is represented by

$$\Delta S = nF \left(\frac{\partial V_{bat}^{eq}}{\partial T} \right)_{\xi, p} \ , \tag{2.9}$$

where T is the battery temperature, ξ is the reaction progress, or more specifically the SoC, and p is the pressure. Generally, the entropy change is experimentally obtained by potentiometric or calorimetric measurements [36]. Since these methods usually require long measurement times, alternatives have been developed, such as electrothermal impedance spectroscopy (ETIS) [37] and an advanced measurement protocol that reduces the measurement time for recording entropy profiles [38]. Once the entropy change is known, the reversible heat generation (q_S) can be calculated, according to

$$q_S = -I\frac{T\Delta S}{nF} \; . \tag{2.10}$$

Although the entropic heat is sometimes neglected [39–41] or adopted as a constant average value [42–44], its contribution can be significant and, therefore, should be considered for thermal modeling purposes [25, 35, 45]. Entropic heat generation or absorption can be present at both electrodes, and its magnitude differs for the various electrode materials. Battery electrodes can be selected such that the entropic contributions of both electrodes cancel each other out [46]. In this perfect electrode match, entropic contributions on the total battery cannot be measured.

Two additional heat generation mechanisms are described in the literature: enthalpy-of-mixing and phase-change terms. Enthalpy-of-mixing represents the heat effect that occurs during the generation or relaxation of concentration gradients. The phase-change term stands for the heat effect due to phase transformations [33, 47]. However, these two terms are often neglected since their contributions are minor to the two previous heat generation terms [45, 48].

2.3.2. Heat conduction

The heat generated by the processes described above flows through the materials of the battery by conduction. This only occurs when temperature differences are present, *i.e.* thermal gradients. The corresponding heat flux ($\vec{q}_{cond}$) in the isotropic materials, that results from thermal conduction can be defined as [49–51]

$$\vec{q}_{cond} = -\kappa \nabla T \; , \tag{2.11}$$

where $\kappa = \kappa(x, y, z)$ is the thermal conductivity and ∇T the temperature gradient. Eq. 2.11 is also called Fourier's Law for heat conduction. It can be seen that κ is a function of location in the battery. Note that Eq. 2.11 contains a minus-sign; therefore, it can be inferred that heat flows from high to low temperatures. Values for κ have been investigated for common battery materials and reported in the literature [44, 52]. These parameter values can be used as input for thermal models.

2.3.3. Heat dissipation

Assuming a battery operating in an environment at a lower temperature than the battery itself, the heat dissipates from the surface to the surroundings. This occurs by both convection and radiation. Convective (q_{conv}) and radiative (q_{rad}) heat exchange are represented by [49–51]

$$q_{conv} = hA(T - T_a) \ , \tag{2.12}$$

and

$$q_{rad} = \sigma \epsilon A(T^4 - T_a^4) \ , \tag{2.13}$$

respectively, where h is the heat-transfer coefficient, A the surface area of the battery, T the battery surface temperature, T_a the ambient temperature, σ the Stefan-Boltzmann constant and ϵ the emissivity ($0 < \epsilon \leq 1$) of the surface material. h depends on factors such as natural or forced convection, location, geometry, surface roughness and the medium that surrounds the battery. In order to increase the heat transfer from the battery surface to the surrounding environment various external cooling methods can be applied. Examples are air cooling [53–55], liquid cooling [56, 57], phase-change materials [58–61], heat pipes [62–64], specially designed heat sinks [65–67], pool-boiling fluids [68], or a combination of these methods.

In addition to external cooling, that only removes heat from the surface of the battery, internal cooling has also been used. For internal cooling either microchannels or small heat pipes are integrated into the battery [69–72]. Internal cooling can be more effective than traditional cooling since undesirable increase in temperature and thermal gradients are easier to control. In addition, internal cooling favorably prolongs battery life and is safer. Despite these advantages, internal cooling is more difficult to apply since the standard internal battery construction must be changed significantly.

2.3.4. Heat balance

Now that heat generation and dissipation principles are known, it is possible to define a simple but convenient heat balance equation in order to calculate the temperature evolution of batteries. Considering a uniform battery temperature, the heat balance equation can be defined as

$$mC_p \frac{dT}{dt} = q_{in} - q_{out} \ , \tag{2.14}$$

where m is the mass and C_p the specific heat capacity of the battery. q_{in}, that includes all heat-generating processes, can be defined based on the theory described above, as

$$q_{in} = q_{\eta} + q_S \, . \tag{2.15}$$

q_{out} represents the heat dissipation from the battery to the environment, which can be defined with the theory above as

$$q_{out} = q_{conv} + q_{rad} \, . \tag{2.16}$$

Substantial research on thermal modeling has been conducted with this general heat equation [35, 73–79]. The main advantage of this model is the simplicity to predict temperature evolutions and to integrate this into a TMS. An example of simulation results using this model is shown in Fig. 2.2. Both experimental (dotted curves) and simulated (dashed and solid curves) temperature evolution are shown for discharging a Li-ion battery at three C-rates. Moreover, the model has been simulated with (solid curves) and without the entropic term (dashed curves). It can be seen that the model without entropic term can only predict the global temperature behavior. Including the entropic term into the model leads to a much better modeling accuracy.

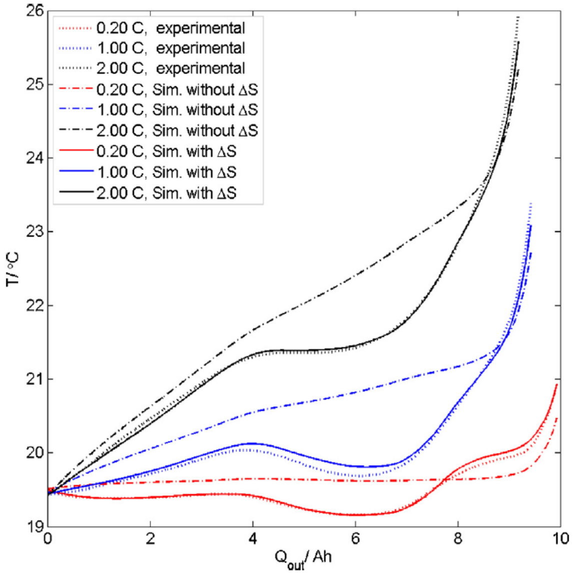

Fig. 2.2: Example of temperature evolution of a 7.5 Ah cylindrical battery during discharge for three C-rates at an ambient temperature of 20°C. Adopted from Ref. [35].

Due to the simplicity of this general thermal model, there are some shortcomings, such as the assumption that the whole battery has a uniform temperature.

In reality, the temperature varies spatially and, therefore, this heat-balance equation must be extended to a two or three-dimensional heat equation. The three-dimensional heat equation is defined as [80]

$$\rho C_p \frac{\partial T}{\partial t} = \nabla \cdot (\kappa \nabla T) + Q_{in} \, , \tag{2.17}$$

where ρ is the material density. The density of the heat-generation power $Q_{in} = Q_{in}(t,x,y,z)$ is now a function of location due to the temperature-dependent entropic term (see Eq. 2.10 and 2.15). Note that the total heat-generation power q_{in} in the heat-balance equation (Eq. 2.14) can be obtained by integration of Q_{in} with respect to the volume (V) of the battery, *i.e.*

$$q_{in}(t) = \int_V Q_{in}(t,x,y,z)dxdydz \, . \tag{2.18}$$

The heat dissipation at each point of the outer surface is written as boundary condition in the form

$$-\vec{n} \cdot (\kappa \nabla T) = h\,(T - T_a) + \sigma \epsilon \left(T^4 - T_a^4\right) \, , \tag{2.19}$$

where at the left-hand side ∇T represents the temperature gradient and $\vec{n}$ the unit (outer) normal vector at the boundary, and the right-hand-side terms describe convection and radiation, accordingly. Using this model, thermal gradients in three dimensions can be simulated and validated with respect to measurements. These models still rely on detailed experiments since the measured overpotentials or resistances are required to calculate the heat generation. Therefore, thermal models have to be coupled to other physical models that are able to simulate all heat losses of all battery processes [40, 81, 82]. However, these multiscale physical models are computationally elaborate and are not very well-suited to integrate into sophisticated BMS and TMS [83].

2.4. Temperature gradients

Temperature gradients develop as a result of internal heat generation, thermal conduction, and heat dissipation in individual batteries, on module, and pack level. The development of temperature gradients in battery packs is a key issue that cannot be underestimated because gradients can lead to serious complications. One of these complications is temperature monitoring of a battery. Under extreme conditions, such as over(dis)charge, high current loads, or short-circuiting, substantial heat is generated internally. Therefore, monitoring the surface temperature underestimates the maximum temperature of batteries. Thermal simulation examples on a cylindrical 7.5 Ah battery at a 6 C-rate discharge are shown in Fig. 2.3. It can be seen that the temperature in the battery core is significantly higher than at the surface. Additional monitoring of the internal temperature therefore provides more accurate information, which can improve the performance, life-time and safety of Li-ion batteries.

Other complications, resulting from temperature gradients, are current density distributions and local SoC differences [84]. Temperature gradients cause spatially varying electrochemical impedances and, therefore, current density distributions. SoC inhomogeneities are a result of both non-uniform current density distributions and the temperature dependence of the EMF. These effects lead to local aging differences and hence to global aging of batteries [85]. Moreover, it was found that batteries perform differently in presence of a temperature gradient in comparison to a uniform temperature which has the same average value [86].

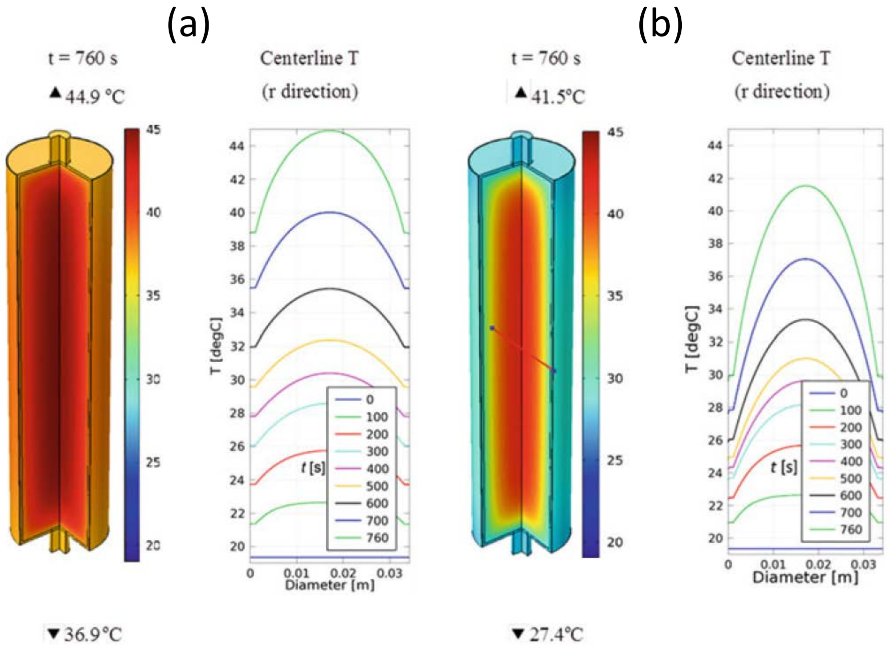

Fig. 2.3: Examples of thermal simulations of a 7.5 Ah cylindrical battery under a 6C-rate discharge; natural convection (a) and forced convection (b). Adopted from Ref. [87].

Apart from temperature gradients inside individual batteries, temperature gradients will also develop in battery packs, in which multiple batteries are connected in series and/or in parallel. Simulation examples of temperature gradients in a battery pack can be seen in Fig. 2.4 for two different types of air cooling. Temperature gradients in battery packs result in unbalanced (dis)charge currents for parallel-connected batteries [88, 89]. In addition, batteries far away from the cooling inlets operate at higher temperatures than batteries close to the cooling inlets, which can be seen in Fig. 2.4a. Using different or modified cooling methods, temperature gradients may be reduced, which is shown in Fig. 2.4b. Both unbalanced (dis)charge currents and different operating temperatures result in unequal aging phenomena among batteries in a pack.

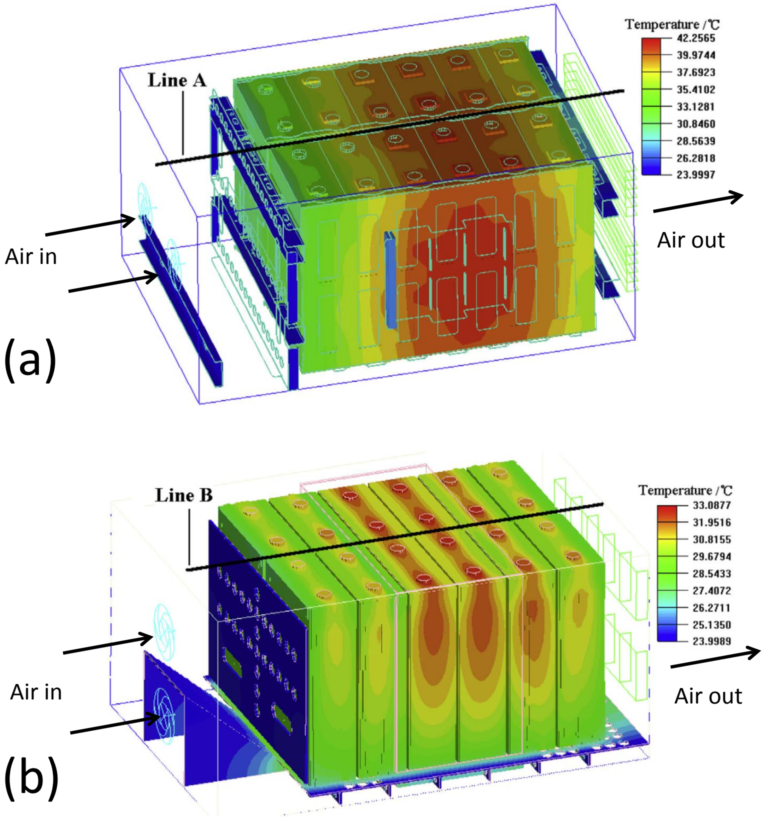

Fig. 2.4: Examples of thermal simulations of a Li-ion battery pack, containing 12 180 Ah batteries, at the end of 1C-rate discharging, using forced convection with one-directional air flow (a) and forced convection with two-directional air flow (b). Modified from Ref. [90].

Generally, high C-rates and low ambient temperatures lead to high temperature rise and large thermal gradients [91]. At high C-rates, stronger cooling is therefore necessary to not exceed the maximum specified temperature. Stronger cooling results in a lower temperature rise; however, larger temperature gradients develop [87, 92, 93]. This effect can clearly be seen in Fig. 2.3. Under natural convection (Fig. 2.3a), the surface temperature is far higher than under forced convection (Fig. 2.3b). However, the thermal gradient in the case of forced convection is much larger than under natural convection. The cooling method has a large influence on this particular behavior. For example, tab cooling leads to a more homogeneous temperature behavior than surface cooling [94]. Therefore, surface cooling can lead to higher capacity losses than tab cooling. In terms of temperature control, internal battery cooling is even more superior to tab cooling [95]. However, internal cooling is much more complicated and increases the mass of the battery and, therefore, decreases the specific energy density.

Because of all above-mentioned reasons, it is highly important to give careful consideration to the design of the TMS. On the one hand, it must be designed such that batteries do not exceed the maximum and minimum specified temperatures and, preferably, operate in the optimal working temperature range. On the other hand, it has to keep the temperature difference between individual batteries and modules inside a pack as low as possible. Literature suggests that the optimal temperature range, *i.e.* an appropriate balance between performance, battery life and safety, lies within approximately 20°C to 40°C with a maximum temperature gradient of 5°C [96–101]. Note that, however, the operating temperature can be in a range between -30°C and 60°C. Furthermore, a TMS should be reliable, low-cost, compact, light-weight and easy to maintain [100].

2.5. Thermal issues and safety devices

In Section 2.3 it is explained that the battery temperature is determined by the heat balance between the generated and dissipated heat. If the generated heat cannot sufficiently be dissipated, the battery temperature continues to increase, which can lead to failures and dangerous situations. Although the relative number of failures associated with Li-ion batteries is limited, some published incidents related to fires and explosions have raised concerns about the overall safety [102]. Moreover, faults and misuse during manufacturing and operation can cause internal and external short-circuits, over(dis)charge or overheating that, if uncontrolled, can lead to thermal runaway, venting, fire and/or explosion of Li-ion batteries [103]. These events result in hazardous situations and obviously are detrimental for the battery market.

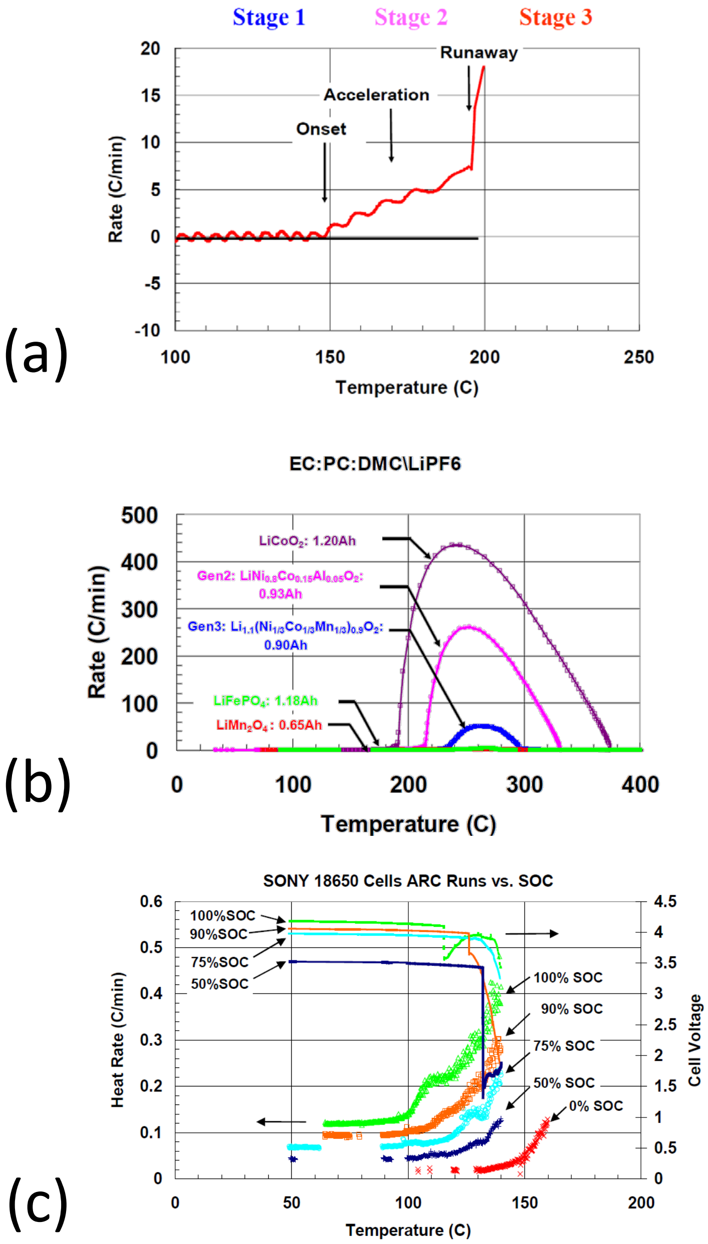

Fig. 2.5: Self-heating rates of Li-ion batteries. Self-heating rate during a forced thermal ramp test (a); Self-heating rate of 18650 batteries measured by Accelerating-Rate-Calorimetry (ARC) for different chemistries (b); Self-heating rate of Sony batteries measured by ARC at different SoC (c). Note that in (c) an offset is shown for easier comparison. For details of this figure see Refs. [104, 105].

The worst-case thermal scenario is that of thermal runaway, which can occur under insufficient cooling or abusive conditions and can easily lead to fire or explosions. Although Feng *et al.* [106] extensively described thermal runaway to occur in six stages, it is more frequently described by a three-stage process [103, 104, 107–112], that can best be explained by Fig. 2.5a [104, 109]. This figure shows experimental results of the self-heating rate of a battery, divided into three stages. In this experiment, an external source adds heat to the battery until the moment the onset temperature is reached. At the onset temperature the self-heating rate is equal or larger than a certain threshold value and no external heat from the source is added to the battery. From this point onwards, reactions inside the battery are exothermic and self-induce an increase in temperature.

It is known that at temperatures around 90°C the Solid Electrolyte Interphase (SEI) starts to decompose exothermically. Consequently, this induces electrolyte reduction at the exposed negative electrode surface. This reaction sequence becomes even more significant at 120°C (stage 1). At stage 1 the separator can also start to melt, leading to a sudden voltage drop, thereby further increasing the heat generation. In stage 2 heat generation increases more rapidly (acceleration) by both electrolyte reduction and oxidation at the negative and positive electrodes, respectively. At this stage gas venting or even release of smoke may occur. Further internal heating brings the process into stage 3 in which high-rate electrode reactions cause the temperature to increase extremely fast, ultimately leading to the as-denoted thermal runaway. This is mainly caused by positive electrode material decomposition, producing oxygen gas which reacts exothermically with the organic materials in the battery [113]. The results of this process are high-rate venting, possible flames and explosions. Any intervention or strong cooling at this stage most probably does not inhibit thermal runaway anymore.

Thermal runaway phenomena are a function of various properties, such as electrode materials, cell design and electrolyte composition [114]. For example, it has been found that the self-heating rate of Li-ion batteries is strongly dependent on the chemistry [104, 105, 115–117]. An example of the self-heating rate for different chemistries is shown in Fig. 2.5b [104]. From this figure it is obvious that batteries with $LiCoO_2$ electrodes are thermally less stable than Li-ion batteries with for example $LiFePO_4$ electrodes. Experiments also revealed that the self-heating rate is dependent on the SoC [104, 105, 118, 119]. Generally, the onset temperature decreases with increasing SoC. An example of this behavior can be seen in Fig. 2.5c [105], which also shows the battery voltage during the experiment. These results indicate that the electrodes become thermally less stable when the SoC increases. Furthermore, the voltage shows a sharp drop at temperatures around 125°C. This voltage drop corresponds to the melting of the separator. In addition, it has been found that the thermal stability of the electrodes is dependent on the particle size because the active surface area with smaller particles is larger and, therefore, has more contact area between the electrode and electrolyte [120, 121].

To prevent dangerous situations such as thermal runaway, the BMS should monitor the voltage, current and temperature. In case of failure the BMS can intervene preventively. However, a BMS cannot always protect batteries against abusive conditions, such as short-circuiting, penetration and external heating. Therefore, safety devices are additionally integrated in or on Li-ion batteries. These devices have to minimize the impact of hazardous situations. Many safety devices have been investigated, ranging from simple safety vents and fuses to shutdown separators, exotic electrolytes and special electrode coatings. A comprehensive review of safety devices is written by Balakrishnan *et al.* [122].

Hazardous situations arise if the BMS or other safety devices cannot prevent a battery from thermal runaway. This situation becomes even worse if this occurs in a battery pack because a single battery can trigger other batteries inside the pack to a runaway incident [123–125]. A simulation example of thermal runaway propagation through a battery module is shown in Fig. 2.6 [125]. In this example, the first battery is penetrated with a nail in order to initiate thermal runaway. This triggers the neighboring battery and then continues to propagate up to the last battery.

To prevent thermal runaway propagation through a complete battery pack, various designs have been investigated. Examples are thermal isolations or conductive heat sinks between batteries, stronger cooling, reducing energy in the battery and spacing between adjacent batteries [125–128]. Moreover, it has been found that cylindrical batteries are less prone to thermal runaway propagation than, for example, pouch-type batteries due to the smaller contact areas and large air gaps between the battery covers [124]. It was also found that for cylindrical batteries the electrical connections become more pronounced [124]. A parallel connection leads to stronger propagation due to heat transfer through the module and an electrical short at the location where thermal runaway is initiated.

Evidently, careful design considerations have to be taken in order to prevent thermal runaway in a single battery and propagation through a complete battery pack. Once the battery pack is being used in an application, it is important that all batteries inside a module or pack are monitored, not only for performance purposes, but more importantly also for safety purpose.

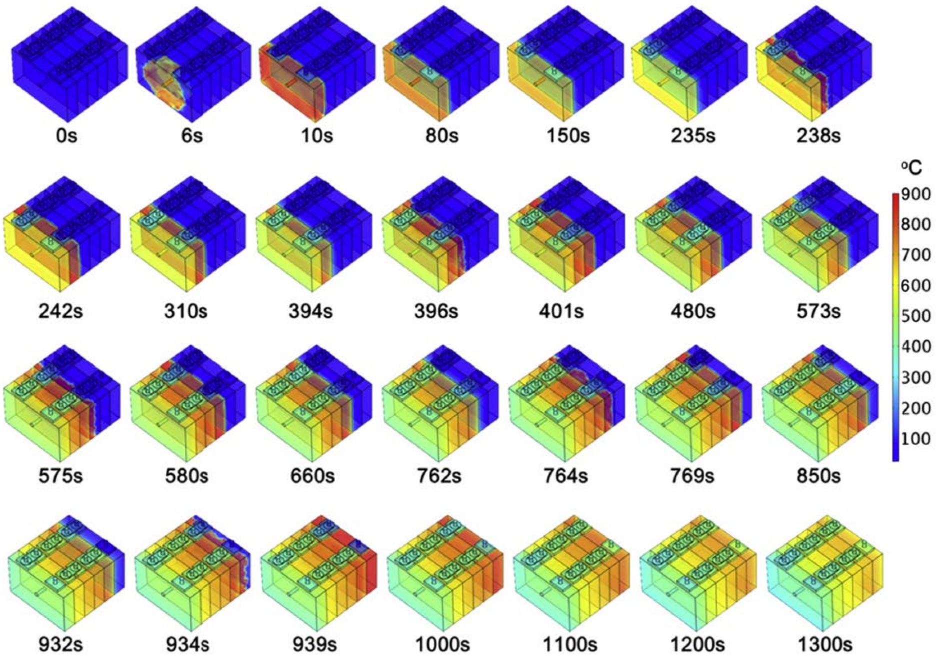

Fig. 2.6: Simulation example of thermal runaway propagation in a battery module, containing six 25 Ah batteries. Adopted from Ref. [125].

References

[1] S.-t. Myung, Y. Hitoshi, and Y.-k. Sun, *Electrochemical behavior and passivation of current collectors in lithium-ion batteries,* J. Mater. Chem. **21**, 9891 (2011).

[2] K. Kam and M. Doeff, *Electrode Materials for Lithium Ion Batteries,* Mater. Matters **7**, 56 (2012).

[3] N. Nitta, F. Wu, J. T. Lee, and G. Yushin, *Li-ion battery materials: present and future,* Mater. Today **18**, 252 (2015).

[4] R. Hausbrand, G. Cherkashinin, H. Ehrenberg, M. Gröting, K. Albe, C. Hess, and W. Jaegermann, *Fundamental degradation mechanisms of layered oxide Li-ion battery cathode materials: Methodology, insights and novel approaches,* Mater. Sci. Eng. B **192**, 3 (2015).

[5] A. Manthiram, B. Song, and W. Li, *A perspective on nickel-rich layered oxide cathodes for lithium-ion batteries,* Energy Storage Mater. **6**, 125 (2017).

[6] Y. Ding, D. Mu, B. Wu, R. Wang, Z. Zhao, and F. Wu, *Recent progresses on nickel-rich layered oxide positive electrode materials used in lithium-ion batteries for electric vehicles,* Appl. Energy **195**, 586 (2017).

[7] M. N. Obrovac and V. L. Chevrier, *Alloy Negative Electrodes for Li-Ion Batteries,* Chem. Rev. **114**, 11444 (2014).

[8] K. Kinoshita and K. Zaghib, *Negative electrodes for Li-ion batteries,* J. Power Sources **110**, 416 (2002).

[9] P. Verma, P. Maire, and P. Novák, *A review of the features and analyses of the solid electrolyte interphase in Li-ion batteries,* Electrochim. Acta **55**, 6332 (2010).

[10] R. Huggins, *Advanced batteries*, 1st ed. (Springer US, 2009) p. 474.

[11] H. Gerischer, F. Decker, and B. Scrosati, *The Electronic and the Ionic Contribution to the Free Energy of Alkali Metals in Intercalation Compounds,* J. Electrochem. Soc. **141**, 2297 (1994).

[12] C. Liu, Z. G. Neale, and G. Cao, *Understanding electrochemical potentials of cathode materials in rechargeable batteries,* Mater. Today **19**, 109 (2016).

[13] K. M. Abraham, *Prospects and Limits of Energy Storage in Batteries,* J. Phys. Chem. Lett. **6**, 830 (2015).

[14] B. Scrosati and J. Garche, *Lithium batteries: Status, prospects and future,* J. Power Sources **195**, 2419 (2010).

[15] J. B. Goodenough and K.-S. Park, *The Li-Ion Rechargeable Battery: A Perspective,* J. Am. Chem. Soc. **135**, 1167 (2013).

[16] J. Kasnatscheew, U. Rodehorst, B. Streipert, S. Wiemers-meyer, R. Jakelski, R. Wagner, C. Laskovic, and M. Winter, *Learning from Overpotentials in Lithium Ion Batteries: A Case Study on the* $LiNi_{1/3}Co_{1/3}Mn_{1/3}O_2$ *(NCM) Cathode,* J. Electrochem. Soc. **163**, 2943 (2016).

[17] H. Bergveld, W. Kruijt, and P. Notten, *Battery management systems: design by modelling* (Kluwer Academic Publishers, Dordrecht, 2002) p. 295.

[18] V. Pop, H. Bergveld, J. Op het Veld, P. Regtien, D. Danilov, and P. Notten, *Modeling Battery Behavior for Accurate State-of-Charge Indication,* J. Electrochem. Soc. **153**, A2013 (2006).

[19] D. Danilov, R. Niessen, and P. Notten, *Modeling All-Solid-State Li-Ion Batteries,* J. Electrochem. Soc. **158**, A215 (2011).

[20] C. Heubner, M. Schneider, and A. Michaelis, *Investigation of charge transfer kinetics of Li-Intercalation in* $LiFePO_4$*,* J. Power Sources **288**, 115 (2015).

[21] D. Danilov and P. H. L. Notten, *Mathematical modelling of ionic transport in the electrolyte of Li-ion batteries,* Electrochim. Acta **53**, 5569 (2008).

[22] D. Grazioli, M. Magri, and A. Salvadori, *Computational modeling of Li-ion batteries,* Comput. Mech. **58**, 889 (2016).

[23] D. Andre, M. Meiler, K. Steiner, C. Wimmer, T. Soczka-Guth, and D. Sauer, *Characterization of high-power lithium-ion batteries by electrochemical impedance spectroscopy. I. Experimental investigation,* J. Power Sources **196**, 5334 (2011).

[24] E. Schuster, C. Ziebert, A. Melcher, M. Rohde, and H. J. Seifert, *Thermal behavior and electrochemical heat generation in a commercial 40 Ah lithium ion pouch cell,* J. Power Sources **286**, 580 (2015).

[25] A. D. Vita, A. Maheshwari, M. Destro, and M. Santarelli, *Transient thermal analysis of a lithium-ion battery pack comparing different cooling solutions for automotive applications,* Appl. Energy **206**, 101 (2017).

[26] R. E. Williford, V. V. Viswanathan, and J.-g. Zhang, *Effects of entropy changes in anodes and cathodes on the thermal behavior of lithium ion batteries,* J. Power Sources **189**, 101 (2009).

[27] X.-g. Yang, G. Zhang, and C.-y. Wang, *Computational design and refinement of self-heating lithium ion batteries,* J. Power Sources **328**, 203 (2016).

[28] M. Ecker, J. B. Gerschler, J. Vogel, S. Käbitz, F. Hust, P. Dechent, and D. U. Sauer, *Development of a lifetime prediction model for lithium-ion batteries based on extended accelerated aging test data,* J. Power Sources **215**, 248 (2012).

[29] A. Eddahech, O. Briat, and J.-m. Vinassa, *Performance comparison of four lithium-ion battery technologies under calendar aging,* Energy **84**, 542 (2015).

[30] J. Schmitt, A. Maheshwari, M. Heck, S. Lux, and M. Vetter, *Impedance change and capacity fade of lithium nickel manganese cobalt oxide-based batteries during calendar aging,* J. Power Sources **353**, 183 (2017).

[31] L. Rao and J. Newman, *Heat-Generation Rate and General Energy Balance for Insertion Battery Systems,* J. Electrochem. Soc. **144**, 2697 (1997).

[32] M. Guo, G. Sikha, and R. E. White, *Single-Particle Model for a Lithium-Ion Cell: Thermal Behavior,* J. Electrochem. Soc. **158**, 122 (2011).

[33] D. Bernardi, E. Pawlikowski, and J. Newman, *A General Energy Balance for Battery Systems,* J. Electrochem. Soc. **132**, 5 (1970).

[34] H. F. Gibbard, *Thermal Properties of Battery Systems,* J. Electrochem. Soc. **125**, 353 (1978).

[35] M. Shadman Rad, D. L. Danilov, M. Baghalha, M. Kazemeini, and P. H. L. Notten, *Adaptive thermal modeling of Li-ion batteries,* Electrochim. Acta **102**, 183 (2013).

[36] X.-f. Zhang, Y. Zhao, Y. Patel, T. Zhang, W.-m. Liu, M. Chen, J. Offer, and Y. Yan, *Potentiometric measurement of entropy change for lithium batteries,* Phys. Chem. Chem. Phys. **19**, 9833 (2017).

[37] J. P. Schmidt, A. Weber, and E. Ivers-tiffée, *A novel and precise measuring method for the entropy of lithium-ion cells:* ΔS *via electrothermal impedance spectroscopy,* Electrochim. Acta **137**, 311 (2014).

[38] P. J. Osswald, M. del Rosario, J. Garche, A. Jossen, and H. E. Hoster, *Fast and Accurate Measurement of Entropy Profiles of Commercial Lithium-Ion Cells,* Electrochim. Acta **177**, 270 (2015).

[39] Z. H. C. Daud, D. Chrenko, F. D. Santos, E.-h. Aglzim, A. Keromnes, and L. L. Moyne, *3D electro-thermal modelling and experimental validation of lithium polymer-based batteries for automotive applications,* Int. J. Energy Res. **40**, 1144 (2016).

[40] M. Guo and R. E. White, *A distributed thermal model for a Li-ion electrode plate pair,* J. Power Sources **221**, 334 (2013).

[41] M. Debert, G. Colin, G. Bloch, and Y. Chamaillard, *An observer looks at the cell temperature in automotive battery packs,* Control Eng. Pract. **21**, 1035 (2013).

[42] Z. Liu and H.-x. Li, *A Spatiotemporal Estimation Method for Temperature Distribution in Lithium-Ion Batteries,* IEEE Trans. Ind. INFORMATICS **10**, 2300 (2014).

[43] L. Song and J. W. Evans, *Electrochemical-Thermal Model of Lithium Polymer Batteries,* J. Electrochem. Soc. **147**, 2086 (2000).

[44] F. Richter, S. Kjelstrup, P. J. S. Vie, and O. S. Burheim, *Thermal conductivity and internal temperature profiles of Li-ion secondary batteries,* J. Power Sources **359**, 592 (2017).

[45] K. E. Thomas and J. Newman, *Thermal Modeling of Porous Insertion Electrodes,* J. Electrochem. Soc. **150**, 176 (2003).

[46] V. V. Viswanathan, D. Choi, D. Wang, W. Xu, S. Towne, R. E. Williford, J.-g. Zhang, J. Liu, and Z. Yang, *Effect of entropy change of lithium intercalation in cathodes and anodes on Li-ion battery thermal management,* J. Power Sources **195**, 3720 (2010).

[47] W. B. Gu and C. Y. Wang, *Thermal-Electrochemical Modeling of Battery Systems,* J. Electrochem. Soc. **147**, 2910 (2000).

[48] C. Forgez, D. Vinh Do, G. Friedrich, M. Morcrette, and C. Delacourt, *Thermal modeling of a cylindrical LiFePO$_4$/graphite lithium-ion battery,* J. Power Sources **195**, 2961 (2010).

[49] J. H. Lienhard, *A Heat Transfer Textbook*, 4th ed. (Phlogiston Press, Cambridge, 2017).

[50] F. P. Incropera, *Fundamentals of heat and mass transfer*, 6th ed. (John Wiley and Sons, Michigan, 2007).

[51] A. Bejan and A. D. Kraus, *Heat Transfer Handbook* (John Wiley and Sons, New Jersey, 2003).

[52] O. S. Burheim, M. A. Onsrud, J. G. Pharoah, F. Vullum-bruer, and P. J. S. Vie, *Thermal Conductivity, Heat Sources and Temperature Profiles of Li-ion Batteries,* J. Electrochem. Soc. **58**, 145 (2014).

[53] T. Wang, K. J. Tseng, J. Zhao, and Z. Wei, *Thermal investigation of lithium-ion battery module with different cell arrangement structures and forced air-cooling strategies,* Appl. Energy **134**, 229 (2014).

[54] H. Park, *A design of air flow configuration for cooling lithium ion battery in hybrid electric vehicles,* J. Power Sources **239**, 30 (2013).

[55] L. Fan, J. M. Khodadadi, and A. A. Pesaran, *A parametric study on thermal management of an air-cooled lithium-ion battery module for plug-in hybrid electric vehicles,* J. Power Sources **238**, 301 (2013).

[56] W. Tong, K. Somasundaram, E. Birgersson, A. S. Mujumdar, and C. Yap, *Numerical investigation of water cooling for a lithium-ion bipolar battery pack,* Int. J. Therm. Sci. **94**, 259 (2015).

[57] L. H. Saw, A. A. O. Tay, and L. W. Zhang, *Thermal Management of Lithium-ion Battery Pack with Liquid Cooling,* in *Therm. Meas. Model. Manag. Symp. (SEMI-THERM), 2015 31st* (IEEE, San Jose, CA, USA, 2015) pp. 298–302.

[58] G.-h. Kim, J. Gonder, J. Lustbader, and A. Pesaran, *Thermal Management of Batteries in Advanced Vehicles Using Phase-Change Materials,* World Electr. Veh. J. **2**, 134 (2008).

[59] Y. Azizi and S. M. Sadrameli, *Thermal management of a LiFePO$_4$ battery pack at high temperature environment using a composite of phase change materials and aluminum wire mesh plates,* Energy Convers. Manag. **128**, 294 (2016).

[60] S. Wilke, B. Schweitzer, S. Khateeb, and S. Al-hallaj, *Preventing thermal runaway propagation in lithium ion battery packs using a phase change composite material: An experimental study,* J. Power Sources **340**, 51 (2017).

[61] Z. Rao, S. Wang, and G. Zhang, *Simulation and experiment of thermal energy management with phase change material for ageing $LiFePO_4$ power battery,* Energy Convers. Manag. **52**, 3408 (2011).

[62] A. Greco, D. Cao, X. Jiang, and H. Yang, *A theoretical and computational study of lithium-ion battery thermal management for electric vehicles using heat pipes,* J. Power Sources **257**, 344 (2014).

[63] T.-h. Tran, S. Harmand, B. Desmet, and S. Filangi, *Experimental investigation on the feasibility of heat pipe cooling for HEV/EV lithium-ion battery,* Appl. Therm. Eng. **63**, 551 (2014).

[64] R. Zhao, J. Gu, and J. Liu, *An experimental study of heat pipe thermal management system with wet cooling method for lithium ion batteries,* J. Power Sources **273**, 1089 (2015).

[65] S. K. Mohammadian and Y. Zhang, *Thermal management optimization of an air-cooled Li-ion battery module using pin-fin heat sinks for hybrid electric vehicles,* J. Power Sources **273**, 431 (2015).

[66] J. Smith, M. Hinterberger, C. Schneider, and J. Koehler, *Energy savings and increased electric vehicle range through improved battery thermal management,* Appl. Therm. Eng. **101**, 647 (2016).

[67] L. H. Saw, Y. Ye, M. C. Yew, W. T. Chong, M. K. Yew, and T. C. Ng, *Computational fluid dynamics simulation on open cell aluminium foams for Li-ion battery cooling system,* Appl. Energy (2017), 10.1016/j.apenergy.2017.04.022.

[68] R. W. Van Gils, D. Danilov, P. H. Notten, M. F. Speetjens, and H. Nijmeijer, *Battery thermal management by boiling heat-transfer,* Energy Convers. Manag. **79**, 9 (2014).

[69] S. K. Mohammadian, Y.-l. He, and Y. Zhang, *Internal cooling of a lithium-ion battery using electrolyte as coolant through microchannels embedded inside the electrodes,* J. Power Sources **293**, 458 (2015).

[70] T. M. Bandhauer and S. Garimella, *Passive, internal thermal management system for batteries using microscale liquid-vapor phase change,* Appl. Therm. Eng. **61**, 756 (2013).

[71] D. Anthony, D. Wong, D. Wetz, and A. Jain, *Improved Thermal Performance of a Li-Ion Cell through Heat Pipe Insertion,* J. Electrochem. Soc. **164**, A961 (2017).

[72] K. Shah, C. Mckee, D. Chalise, and A. Jain, *Experimental and numerical investigation of core cooling of Li-ion cells using heat pipes,* Energy **113**, 852 (2016).

[73] H. Dai, L. Zhu, J. Zhu, X. Wei, and Z. Sun, *Adaptive Kalman filtering based internal temperature estimation with an equivalent electrical network thermal model for hard-cased batteries,* J. Power Sources **293**, 351 (2015).

[74] F. Bahiraei, M. Ghalkhani, A. Fartaj, and G.-A. Nazri, *A pseudo 3D electrochemical-thermal modeling and analysis of a lithium-ion battery for electric vehicle thermal management applications,* Appl. Therm. Eng. **125**, 904 (2017).

[75] Q.-k. Wang, Y.-j. He, J.-n. Shen, Z.-f. Ma, and G.-b. Zhong, *A unified modeling framework for lithium-ion batteries: An artificial neural network based thermal coupled equivalent circuit model approach,* Energy **138**, 118 (2017).

[76] L. Cai and R. E. White, *An Efficient Electrochemical–Thermal Model for a Lithium-Ion Cell by Using the Proper Orthogonal Decomposition Method,* J. Electrochem. Soc. **157**, 1188 (2010).

[77] W. Fang, O. J. Kwon, and C.-y. Wang, *Electrochemical–thermal modeling of automotive Li-ion batteries and experimental validation using a three-electrode cell,* Int. J. Energy Res. **34**, 107 (2010).

[78] S. Panchal, I. Dincer, M. Agelin-chaab, R. Fraser, and M. Fowler, *Experimental and theoretical investigations of heat generation rates for a water cooled $LiFePO_4$ battery,* Int. J. Heat Mass Transf. **101**, 1093 (2016).

[79] B. Schweitzer, S. Wilke, S. Khateeb, and S. Al-hallaj, *Experimental validation of a 0-D numerical model for phase change thermal management systems in lithium-ion batteries,* J. Power Sources **287**, 211 (2015).

[80] D. W. Hahn and M. Özisik, *Heat Conduction*, 3rd ed. (John Wiley and Sons, New Jersey, 2012) pp. 1–744.

[81] K.-j. Lee, K. Smith, A. Pesaran, and G.-h. Kim, *Three dimensional thermal-, electrical-, and electrochemical-coupled model for cylindrical wound large format lithium-ion batteries,* J. Power Sources **241**, 20 (2013).

[82] M. Guo, G.-h. Kim, and R. E. White, *A three-dimensional multi-physics model for a Li-ion battery,* J. Power Sources **240**, 80 (2013).

[83] A. A. Franco, *Multiscale modelling and numerical simulation of rechargeable lithium ion batteries: concepts , methods and challenges,* RSC Adv. **3**, 13027 (2013).

[84] M. Fleckenstein, O. Bohlen, M. A. Roscher, and B. Bäker, *Current density and state of charge inhomogeneities in Li-ion battery cells with $LiFePO_4$ as cathode material due to temperature gradients,* J. Power Sources **196**, 4769 (2011).

[85] T. Waldmann and M. Wohlfahrt-mehrens, *In-Operando Measurement of Temperature Gradients in Cylindrical Lithium-Ion Cells during High-Current Discharge,* ECS Electrochem. Lett. **4**, A1 (2015).

[86] Y. Troxler, B. Wu, M. Marinescu, V. Yufit, Y. Patel, A. J. Marquis, N. P. Brandon, and G. J. Offer, *The effect of thermal gradients on the performance of lithium-ion batteries,* J. Power Sources **247**, 1018 (2014).

[87] O. Veneri, ed., *Technologies and Applications for Smart Charging of Electric and Plug-in Hybrid Vehicles* (Springer International Publishing, Naples, 2017).

[88] N. Yang, X. Zhang, B. Shang, and G. Li, *Unbalanced discharging and aging due to temperature differences among the cells in a lithium-ion battery pack with parallel combination,* J. Power Sources **306**, 733 (2016).

[89] W. Shi, X. Hu, C. Jin, J. Jiang, Y. Zhang, and T. Yip, *Effects of imbalanced currents on large-format* $LiFePO_4$*/graphite batteries systems connected in parallel,* J. Power Sources **313**, 198 (2016).

[90] K. Yu, X. Yang, Y. Cheng, and C. Li, *Thermal analysis and two-directional air flow thermal management for lithium-ion battery pack,* J. Power Sources **270**, 193 (2014).

[91] X. Zhang, *Thermal analysis of a cylindrical lithium-ion battery,* Electrochim. Acta **56**, 1246 (2011).

[92] G. Zhang, L. Cao, S. Ge, C.-y. Wang, C. E. Shaffer, and C. D. Rahn, *In Situ Measurement of Radial Temperature Distributions in Cylindrical Li-Ion Cells,* J. Electrochem. Soc. **161**, 1499 (2014).

[93] R. Kizilel, R. Sabbah, J. R. Selman, and S. Al-Hallaj, *An alternative cooling system to enhance the safety of Li-ion battery packs,* J. Power Sources **194**, 1105 (2009).

[94] I. A. Hunt, Y. Zhao, Y. Patel, and G. J. Offer, *Surface Cooling Causes Accelerated Degradation Compared to Tab Cooling for Lithium-Ion Pouch Cells,* J. Electrochem. Soc. **163**, 1846 (2016).

[95] D. Worwood, Q. Kellner, M. Wojtala, W. D. Widanage, M. Ryan, D. Greenwood, and J. Marco, *A new approach to the internal thermal management of cylindrical battery cells for automotive applications,* J. Power Sources **346**, 151 (2017).

[96] A. A. Pesaran, *Battery thermal models for hybrid vehicle simulations,* J. Power Sources **110**, 377 (2002).

[97] M. R. Khan, M. J. Swierczynski, and S. K. Kær, *Towards an Ultimate Battery Thermal Management System: A Review,* Batteries **3**, 1 (2017).

[98] G. Karimi and X. Li, *Thermal management of lithium-ion batteries for electric vehicles,* Int. J. Energy Res. **37**, 13 (2013).

[99] Q. Wang, B. Jiang, B. Li, and Y. Yan, *A critical review of thermal management models and solutions of lithium-ion batteries for the development of pure electric vehicles,* Renew. Sustain. Energy Rev. **64**, 106 (2016).

[100] Z. Rao and S. Wang, *A review of power battery thermal energy management,* Renew. Sustain. Energy Rev. **15**, 4554 (2011).

[101] H. Liu, Z. Wei, W. He, and J. Zhao, *Thermal issues about Li-ion batteries and recent progress in battery thermal management systems: A review,* Energy Convers. Manag. **150**, 304 (2017).

[102] L. Florence, *Safety Issues for Lithium-Ion Batteries*, Tech. Rep. (UL, 2012).

[103] D. Lisbona and T. Snee, *A review of hazards associated with primary lithium and lithium-ion batteries,* Process Saf. Environ. Prot. **89**, 434 (2011).

[104] D. Doughty and E. P. Roth, *A General Discussion of Li Ion Battery Safety,* Electrochem. Soc. Interface **21**, 37 (2012).

[105] E. P. Roth and D. H. Doughty, *Thermal abuse performance of high-power 18650 Li-ion cells,* J. Power Sources **128**, 308 (2004).

[106] X. Feng, M. Fang, X. He, M. Ouyang, L. Lu, H. Wang, and M. Zhang, *Thermal runaway features of large format prismatic lithium ion battery using extended volume accelerating rate calorimetry,* J. Power Sources **255**, 294 (2014).

[107] J. Wen, Y. Yu, and C. Chen, *A Review of Lithium-Ionn Batteries Safety Issues: Existing Problems and Possible Solutions,* Mater. Express **2**, 197 (2012).

[108] D. P. Abraham, E. P. Roth, R. Kostecki, K. Mccarthy, S. Maclaren, and D. H. Doughty, *Diagnostic examination of thermally abused high-power lithium-ion cells,* J. Power Sources **161**, 648 (2006).

[109] E. Roth, *Abuse Response of 18650 Li-Ion Cells with Different Cathodes Using EC:EMC/LiPF6 and EC:PC:DMC/LiPF6 Electrolytes,* ECS Trans. **11**, 19 (2008).

[110] T. M. Bandhauer, S. Garimella, and T. F. Fuller, *A Critical Review of Thermal Issues in Lithium-Ion Batteries,* J. Electrochem. Soc. **158**, R1 (2011).

[111] R. Spotnitz and J. Franklin, *Abuse behavior of high-power, lithium-ion cells,* J. Power Sources **113**, 81 (2003).

[112] J. R. Dahn and E. W. Fuller, *Thermal stability of* Li_xCoO_2, Li_xNiO_2 *and* λ-MnO_2 *and consequences for the safety of Li-ion cells,* Solid State Ionics **69**, 265 (1994).

[113] H. Arai, M. Tsuda, K. Saito, M. Hayashi, and Y. Sakurai, *Thermal Reactions Between Delithiated Lithium Nickelate and Electrolyte Solutions,* J. Electrochem. Soc. **149**, A401 (2002).

[114] Q. Wang, P. Ping, X. Zhao, G. Chu, J. Sun, and C. Chen, *Thermal runaway caused fire and explosion of lithium ion battery,* J. Power Sources **208**, 210 (2012).

[115] M. Brand, S. Gläser, J. Geder, S. Menacher, S. Obpacher, A. Jossen, and D. Quinger, *Electrical safety of commercial Li-ion cells based on NMC and NCA technology compared to LFP technology,* in *EVS27 Int. Batter. Hybrid Fuel Cell Electr. Veh. Symp.* (IEEE, Barcelona, Spain, 2013) pp. 1–9.

[116] J. Jiang and J. R. Dahn, *ARC studies of the thermal stability of three different cathode materials: $LiCoO_2$; $Li[Ni_0.1Co_0.8Mn_0.1]O_2$; and $LiFePO_4$, in $LiPF_6$ and LiBoB EC/DEC electrolytes,* Electrochem. commun. **6**, 39 (2004).

[117] D. D. Macneil, Z. Lu, Z. Chen, and J. R. Dahn, *A comparison of the electrode/electrolyte reaction at elevated temperatures for various Li-ion battery cathodes,* J. Power Sources **108**, 8 (2002).

[118] S. Al Hallaj, H. Maleki, J. Hong, and J. Selman, *Thermal modeling and design considerations of lithium-ion batteries,* J. Power Sources **83**, 1 (1999).

[119] O. S. Mendoza-hernandez, H. Ishikawa, Y. Nishikawa, Y. Maruyama, and M. Umeda, *Cathode material comparison of thermal runaway behavior of Li-ion cells at different state of charges including over charge,* J. Power Sources **280**, 499 (2015).

[120] S. E. L. Khakani, D. Rochefort, and D. D. Macneil, *ARC Study of $LiFePO_4$ with Different Morphologies Prepared via Three Synthetic Routes,* J. Electrochem. Soc. **163**, A1311 (2016).

[121] J. Jiang and J. R. Dahn, *Effects of particle size and electrolyte salt on the thermal stability of $Li_0.5CoO_2$,* Electrochim. Acta **49**, 2661 (2004).

[122] P. G. Balakrishnan, R. Ramesh, and T. P. Kumar, *Safety mechanisms in lithium-ion batteries,* J. Power Sources **155**, 401 (2006).

[123] R. M. Spotnitz, J. Weaver, G. Yeduvaka, D. H. Doughty, and E. P. Roth, *Simulation of abuse tolerance of lithium-ion battery packs,* J. Power Sources **163**, 1080 (2007).

[124] J. Lamb, C. J. Orendorff, L. A. M. Steele, and S. W. Spangler, *Failure propagation in multi-cell lithium ion batteries,* J. Power Sources **283**, 517 (2015).

[125] X. Feng, L. Lu, M. Ouyang, J. Li, and X. He, *A 3D thermal runaway propagation model for a large format lithium ion battery module,* Energy **115**, 194 (2016).

[126] X. Feng, X. He, M. Ouyang, L. Lu, P. Wu, C. Kulp, and S. Prasser, *Thermal runaway propagation model for designing a safer battery pack with 25 Ah* $LiNi_xCo_yMn_zO_2$ *large format lithium ion battery,* Appl. Energy **154**, 74 (2015).

[127] F. Larsson, J. Anderson, P. Andersson, and B.-e. Mellander, *Thermal Modelling of Cell-to-Cell Fire Propagation and Cascading Thermal Runaway Failure Effects for Lithium-Ion Battery Cells and Modules Using Fire Walls,* J. Electrochem. Soc. **163**, A2854 (2016).

[128] P. T. Coman, E. C. Darcy, C. T. Veje, and R. E. White, *Numerical analysis of heat propagation in a battery pack using a novel technology for triggering thermal runaway,* Appl. Energy **203**, 189 (2017).

3

Temperature indication methods for Li-ion batteries

Temperature measurements for Li-ion batteries are of high importance for control and safety purposes. However, due to thermal gradients, which might quickly develop during operation, fast and accurate temperature measurements can be rather challenging. For a proper temperature measurement method selection, aspects such as measurement range, accuracy, resolution, and costs of the method are important. This Chapter gives a comprehensive overview of the various temperature measurement methods that can be used for temperature indication of Li-ion batteries. At present, traditional temperature measurement methods, such as thermistors and thermocouples, are extensively used. The more recently introduced methods, such as impedance-based temperature indication and fiber Bragg-grating techniques are under investigation in order to determine if those are suitable for large-scale introduction in sophisticated battery-powered applications.

3.1. Introduction

In this Chapter, various battery temperature indication methods are discussed, ranging from the well-known traditional methods to the novel ones, which are currently being investigated. Key characteristics such as measurement range, accuracy, resolution (in temperature, space, time) and costs are important for a proper sensor selection. Moreover, *in situ* temperature measurements are attractive for safety and controlling purposes since temperatures in the battery core are, generally, higher (see Chapter 2). These unequal temperature distributions increase the challenges in developing and selecting temperature sensors for Li-ion batteries.

The literature described in this Chapter is restricted to temperature measurement methods and sensors for Li-ion batteries. The corresponding analogue or digital circuits are not discussed, as well as methods to determine the thermal battery properties, such as thermal conductivity and heat capacity. Thermometers that do not output electrical signals suitable for BMS, such as glass tube or bimetallic thermometers, are also not reported.

3.2. Thermo-resistive devices

Thermo-resistive devices are devices whose resistance changes as a function of temperature. This property makes these devices highly suitable for temperature measurements and are discussed in this Section.

3.2.1. Thermistors

Thermistors, or *therm*ally sensitive res*istors* are solid semiconductor devices of which the electrical resistance changes rapidly as a function of temperature [1]. Thermistors may have positive or negative temperature coefficients; if the thermistor has a negative temperature coefficient (NTC), the resistance decreases when the material temperature increases. This behavior is shown in Fig. 3.1 (curves a, b and c) [2], in which it can be seen that NTC behavior is nonlinear, making temperature indication somewhat challenging. For thermistors that have a positive temperature coefficient (PTC) this behavior is the other way around, *i.e.* the resistance increases with increasing temperature. The thermistors with NTC properties, typically made of transition-metal oxides, are usually used for temperature measurements. Thermistors with PTC properties can also be used for temperature measurements but are also frequently used as protection devices to reduce electric currents when the system reaches too-high temperatures.

Thermistors have the advantages of being inexpensive, highly sensitive to temperature changes (see Fig. 3.1), applicable across a considerable temperature range (-55 to 200°C), available in different forms, and can be very small [2]. Due to the small size, it is possible to respond quickly to temperature changes. In addition, a four-terminal contact is not required since thermistors have a high resistivity, which saves cable space and costs. Although thermistors had a reputation of being unstable, the stability improved over the years by new techniques, reaching good long-term stability [3–7]. Using specific provisions with the measurement instrumentation, errors of < 1 mK can be reached [8], although the accuracy in commercial applications often results in the order of ± 1°C [9].

To measure the temperature by using a thermistor, a small well-defined current can be applied at a level at which no or negligible self-heating appears. A voltage measurement across the thermistor can then be used for temperature indication. Conversion to temperature can be performed with the help of lookup tables or by solving equations that approximate the resistance curve. However, other methods, such as those applying linearization techniques, can also be used.

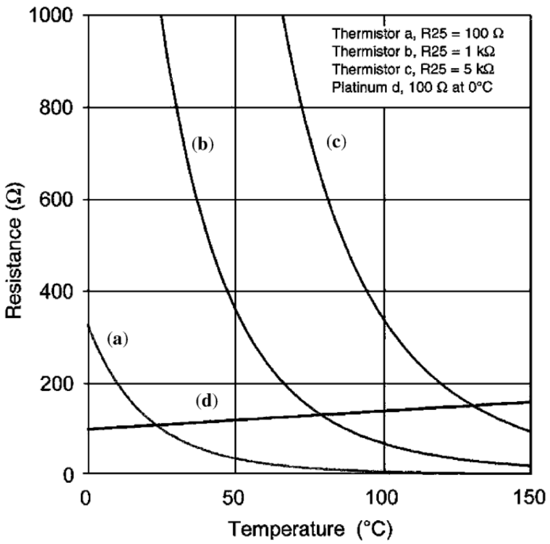

Fig. 3.1: Resistance as a function of temperature of three thermistors (a,b and c), and a Platinum (Pt100) resistance temperature detector (d). Adopted from Ref. [2].

Due to the above-mentioned advantages, thermistors are one of the most-used temperature sensing devices for many applications [10]. For example, the Toyota Prius and Honda Civic Hybrid are using thermistors in order to measure battery temperature [11]. Thermistors are also extensively used to monitor battery temperature in other mobile devices, such as cellphones, laptops and powerbanks [12]. At present, many Li-ion batteries and battery packs can be purchased, including thermistors or protection circuits. Moreover, component and system suppliers frequently deliver products with thermistors as battery temperature sensors.

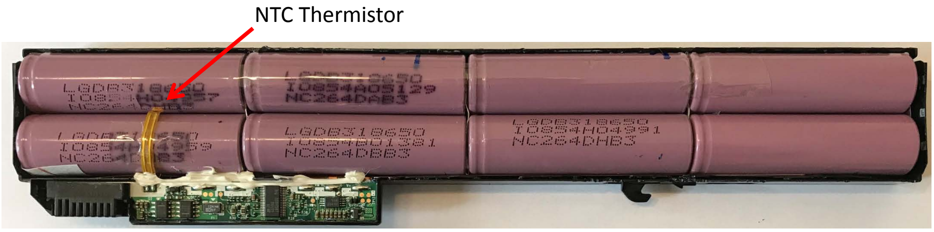

Fig. 3.2: Example of a 73 Wh laptop battery pack with 10 kΩ NTC thermistor. Note that a piece of tape is normally present to fix the thermistor onto the batteries but this was removed for clarity.

For the present practical applications thermistors can be placed on the surface, the terminals, or close to a battery. In the example of Fig. 3.2, a thermistor is placed in the gap between two adjacent cylindrical batteries in such a way that it contacts both batteries. This arrangement only measures the surface temperature of these two batteries, whereas the remaining batteries are not monitored, which can lead to dangerous situations if one of the other batteries becomes overheated. However, for these types of mass-produced applications, costs should be minimized, and thus the number of sensors including wiring, connections and installation should be reduced as much as possible. Through extensive experiments and/or modeling, it is possible to reduce the number of sensors, while still accurate temperature indications can be obtained [13].

Thermal investigations during the design of the battery pack should also reveal hot spots. At the corresponding 'hot' locations, a thermistor can be placed in order to indicate the maximum surface temperature. However, temperature gradients and possible hot spots at other locations on or inside the battery are unlikely to be detected; therefore, the indicated temperature can strongly deviate from the maximum temperature.

Although thermistors are extensively used in practical applications, the use of thermistors for research purposes is limited. NTC thermistors with an accuracy of ± 1°C were used to measure the surface temperature of cylindrical 18650 batteries [14] and on three different pouch-type batteries [15]. To validate a thermal model, non-specified thermistors have been used to monitor the temperature inside the mandrel of cylindrical 28650 batteries [16]. This study indicates that thermistors can be used within the chemical environment of a battery for experimental purposes. Moreover, a mass-produced thermistor was used by Debert *et al.* [17] to measure the temperature of a battery module. The thermistor was placed in an interstice in the module and the data are compared to model simulation results. Grosch *et al.* [18] developed a new low-cost PTC thermistor that can be easily produced with printing techniques. The accuracy of this new thermistor is somewhat lower in comparison to commercially available NTC thermistors and thermocouples. However, it was concluded that the present design can be improved by sensor modifications and more accurate calibrations. Using this new thermistor, either the system cost can be reduced or more thermistors can be used at the same cost.

3.2.2. Resistance Temperature Detectors

Resistance Temperature Detectors (RTD) are devices containing metallic conductors of which the electrical resistance increases as a function of temperature. In essence, any metal could be used for an RTD device, but the choice is limited due to considerations such as cost, temperature coefficient of the resistance, ability to resist oxidation, manufacturing constraints, and stability [9]. Materials used for the metallic conductors in RTD can be copper, silver, nickel, gold, and platinum, of which the last one is the most frequently used, as it offers more advantages than the others. The resistance increase of a platinum RTD is shown in Fig. 3.1 (line d) [2]. This figure shows that a platinum RTD is less sensitive to temperature changes than NTC thermistors. However, unlike thermistors, platinum RTD show a linear dependence on temperature, which makes these very convenient for use in an application. Other advantages of platinum RTD are the excellent stability, accuracy (approaching 1 mK), and wide temperature operating range of -260 to 960°C [19]. RTD can be offered as inner-coiled, outer-wound, or thin-film device. Thin-film RTD have the advantage to be less expensive, more robust, and smaller with respect to the inner-coiled and outer-wound RTD. Due to the small size, thin-film RTD have faster response times.

The type of Platinum RTD is often indicated with the abbreviation 'Pt' followed with a number, *e.g.* Pt100. The number indicates the resistance at 0°C. Hence, a Pt100 is a platinum RTD with a resistance of 100 Ω at 0°C. The most common platinum RTD have a temperature coefficient of resistance (TCR) of 0.00385 Ω/(Ω·°C). The TCR indicates the average resistance change per °C across a temperature range from 0 to 100°C and can be seen as sensitivity parameter. In other words, the resistance of the most common platinum RTD changes 0.38% per °C. Furthermore, there are two performance classes (Class A and Class B) for Pt100 RTD, which indicate accuracy. The accuracy of Class A is approximately twice as high as the accuracy of Class B.

Using RTD, temperature measurements can be performed similarly as with thermistors, *i.e.* a small current of < 1 mA can be applied at a level at which self-heating can be neglected and a voltage drop is measured across the RTD [20]. Subsequently, the voltage can be converted to temperature. However, using an RTD in a branch of a Wheatstone bridge on which a constant voltage is applied is possible as well. Although a four-wire connection is preferred for the most accurate measurements, two- and three-wire connections can also be used. However, the two- and three-wire connections are more prone to measurement errors due to cable resistances.

In comparison to thermistors, RTD are more frequently used for Li-ion battery research purposes. Various authors used one or more commercial Pt100 elements to measure battery surface temperatures during (dis)charging [21–26]. Interestingly, all these measurements were used for thermal model validation purposes. A particular reason why these authors selected Pt100 RTD for their experiments is unknown. Moreover, from these authors only Daud *et al.* [23] indicate that Class A Pt100 RTD were used for surface temperature measurements. Furthermore, Day *et al.* [27] used Pt100 RTD to measure battery temperature and to control a cryostat apparatus for differential thermal analysis.

Pt1000 RTDs with sizes 2.3 mm * 2.0 mm * 0.9 mm were used by Wang *et al.* [28] for temperature measurements inside and at the surface of a coin-type battery. The internal RTD was positioned between both electrodes, separated by two insulation diaphragms. The RTD sensing the internal temperature was connected to copper foil, utilized as measurement leads. Both the sensor and foil were covered by a 50 μm thick polyimide insulation to prevent electrical contact with other parts and also to prevent reactions with the electrolyte. It appeared that the charge capacity reduced tremendously by introducing an internal RTD. This has been attributed to the relative large size of the sensor in comparison to the coin-type battery. It is expected that such a large capacity reduction is absent when the sensor is used in large-scale batteries. However, the used internal RTD provides a more representative temperature than the RTD at the surface of the coin-type battery.

Recently, a self-heating Li-ion battery has been introduced that is able to rapidly self-heat at temperatures below 0°C [29–32]. The principle of self-heating is based on an insulated nickel foil, having an electrical resistance, which is integrated between the electrodes of a battery. When a current is applied under freezing circumstances, the battery current flows through the resistive nickel foil, generating heat internally and heating the battery. The advantage of this construction is that the nickel foil can be used both for heating and as an RTD to measure the internal battery temperature [30, 31]. The authors showed that the nickel foil has a linear resistance increase in a temperature range from -40 to 60°C, making it suitable and convenient for internal battery temperature indication [30, 31]. However, this method requires an extra terminal on the battery and integration of the nickel foil, which increases cost and reduces the specific battery capacity. On the other hand, in comparison to platinum RTD, nickel advantageously has a higher sensitivity and obviously a lower material price.

Flexible thin-film micro RTD for internal battery temperature measurements were developed by Lee *et al.* [33]. The authors claim that these sensors can be easily mass-produced, measure the temperature accurately and have very short response time due to their limited size. The working principle of this sensor is based on a 200 nm thick layer of gold deposited on a substrate of which the resistance changes as a function of temperature. A photograph of this thin-film device is shown in Fig. 3.3. The sensor resistance shows linear behavior in a temperature range between -20 to 90°C over three consecutive cycles. However, the linearity has not been quantified and the stability for more than three cycles, as well as the calendar stability, have not been shown, which is of considerable importance if these sensors are used inside batteries. The authors integrated two thin-film micro-sensors into a pouch-type battery at different positions, including a thermocouple at the surface, and compared the temperature development of the battery. The thin-film micro-sensors showed faster response times and higher temperatures than the thermocouple at the surface. The same research group [34–36] continued this work with adding a voltage and current probe to the same sensor, making it a three-in-one sensor. The authors reported that temperature measurements with this sensor can be performed with an accuracy of better than 0.5°C and a response time less than 1 ms [36].

Using Electrical Resistance Tomography (ERT), the temperature of a battery can be obtained by relating the measured ERT resistivity to temperature. ERT is a technique to measure and visualize cross-sectional conductivity distributions within its sensing region [37, 38]. Hong *et al.* [39, 40] used ERT at the metal surface of Li-ion batteries and were able to map surface- and internal temperature profiles. The temperatures obtained with ERT were, however, not verified against a sufficient number of calibrated surface and internal temperature sensors. Moreover, a metal surface and a large array of properly-attached sense electrodes with corresponding cabling is required in order to measure temperature with this method; this is shown in Fig. 3.4. Furthermore, the battery SoC influences the ERT measurement data, which implies that the ERT temperatures must be compensated. Although this

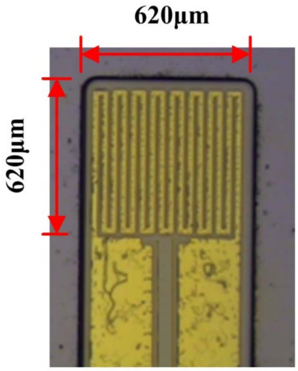

Fig. 3.3: Flexible micro-temperature sensor developed by Lee *et al.* [33].

method is practically somewhat complicated, a three-dimensional temperature map of the battery can favorably be obtained.

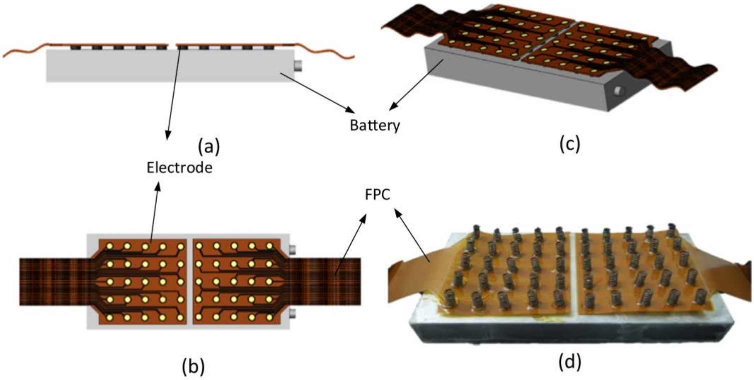

Fig. 3.4: Schematic (a-c) and real (d) representation of a Li-ion battery with ERT sensors shown in various viewing angles. The yellow dots indicate the sense electrodes, which are attached to a so-called flexible printed circuit (FPC), serving as measurement cable. Adopted from Ref. [40].

3.3. Thermocouples

Thermocouples are devices working on the basis of the Seebeck effect, which is called after the inventor Thomas Johann Seebeck [41]. The Seebeck effect is the generation of an electromotive force (EMF) by subjecting two different (semi) conductors to a temperature gradient. In Fig. 3.5, an illustration of the thermocouple measurement principle is shown [42]. It can be seen that two dissimilar metals (Metal A and B) are connected at one end. This is the so-called measurement junction, which is located at the temperature measurement position. At the other end, an EMF can be measured due to a temperature difference across the dissimilar metals. The generated EMF is proportional to the temperature difference between the warm and cold sides. As shown in Fig. 3.5, a measurement device cannot simply be connected to a thermocouple since this introduces another dissimilar metal junction with the measurement cables. To compensate for this effect, a so-called reference junction must be introduced that has a known temperature.

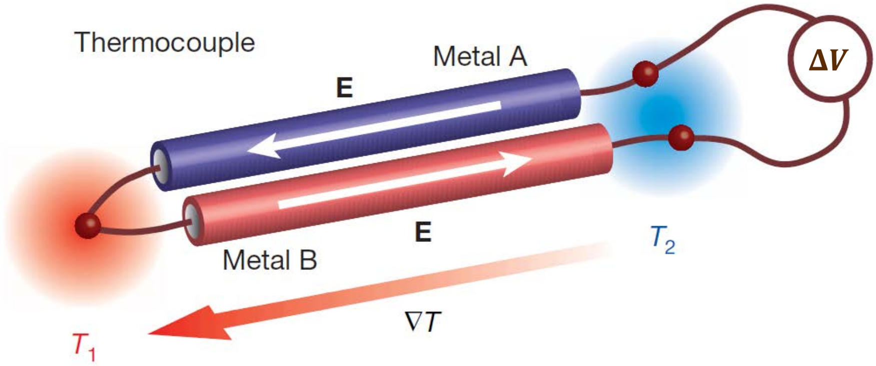

Fig. 3.5: Illustration of the working principle of a thermocouple. Modified from Ref. [42].

Thermocouples have become the industry standard because of the low costs, robustness, size and temperature range [9, 20, 43]. The sensitivity and response time are adequate for most applications as the dimensions can be made very small. Although better accuracy can be reached, it is typically within 1 or 2°C, and is therefore moderate. Small additional drawbacks of thermocouples are the requirement of reference-junction compensation, sensitivity to corrosion, and that the cables cannot simply be extended. Furthermore, the EMF is a nonlinear function of temperature, making it complicated to obtain accurate temperature readings [43]. The sensitivity to corrosion is caused by the dissimilar metal junction. For this reason, thermocouples may need protection and maintenance. These properties make them somewhat unsuitable for long-term battery temperature measurements.

The number of material combinations used for thermocouples is numerous. Each combination has its own temperature and voltage characteristics. However, only eight types are standardized and regularly used, which are listed by for example Childs *et al.* [9] and Tong [20]. The most common types of this selection are the so-called J-, T- and K-types, of which the last one is most popular. Although these three are commonly used, the standardized E-type would be very suitable for battery temperature measurements due to the high EMF output in comparison to the other types. The EMF measured at the cables can be directly converted to temperature with help of a lookup table or by using a mathematical function. No power source is required and, therefore, self-heating is not an issue, such as in the case of thermistors or RTD.

It can be concluded that, among the available literature on battery temperature measurements, commercial thermocouples are numerously used. The reason is, most likely, because scientific measurement devices are often equipped with thermocouple input channels. As expected, the vast majority of authors is using the common K-type or T-type thermocouples in order to measure battery temperature. N-types [44–46], J-types [47, 48] or E-types [49] are used less frequently. About 27% of the scientific contributions using thermocouples for temperature measurements did not precisely indicate what type they used. Therefore, measurement details partly remain unknown, making it impossible to accurately reproduce the measurement results reported in the literature.

As with thermistors and RTD, commercial (micro) thermocouples are also used to measure the internal battery temperature [14, 50–63]. Although these measurements are useful for quantifying the internal temperature, either specially designed batteries with integrated sensors must be made, or a hole must be drilled into an existing (commercial) battery to insert a sensor. This leads to complicated battery designs, and this is therefore less suitable for practical battery-powered applications. In addition, the integrated sensors should be chemically inert and may not react with or dissolve into the electrolyte. For that reason, sensors are sometimes coated with parylene [57, 64] or polyimide [28]. Remarkably, most of the thermocouples used for internal temperature measurements are not coated with a protective layer, or at least the authors did not report that. Therefore, it is expected that these sensors show instabilities or malfunctioning on the long term.

Some specially designed thermocouples for *in situ* temperature measurements are worthwhile to shed some light on. For example, Mutyala *et al.* [65] used flexible thin-film thermocouples integrated into a battery to measure the internal temperature. A K-type thermocouple was sputtered onto a glass substrate and, later, transfered to a thin copper foil. The transferring process and end result are shown in Fig. 3.6. After insulating with polyimide, the thermocouple was integrated into a pouch battery. The measurement results performed with these integrated flexible thin-film thermocouples are promising, but duration experiments are yet to be proven.

For spatial internal battery temperature measurements, a thin-film thermocouple matrix was developed by Martiny *et al.* [67]. Nickel and Copper were used as

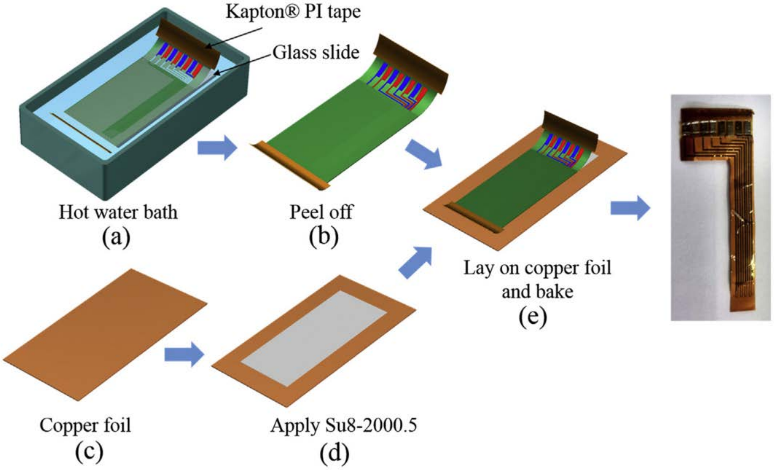

Fig. 3.6: Process used by Mutyala *et al.* [65] to make sputtered K-type thermocouples on a copper strip.

dissimilar materials for the thermocouple matrix and sputtered onto a Kapton® foil. A final coating of parylene C was applied for protection. Fig. 3.7 shows a photograph of a prototype sensor. The resulting sensor had a thickness of less than 27 µm and has been integrated into a laboratory-scale pouch battery. The sensor had no large influence on battery performance at a C/9 cycling rate, but the protective coating damaged during battery assembly and, subsequently, caused instability due to corrosion. Zhang *et al.* [57, 64] and Lee *et al.* [33, 34] also used parylene for their internal sensors. Although Lee *et al.* [35, 36] switched to polyimide in their last reports with an unmentioned reason, they did not report any damage or instability of parylene. Nevertheless, the first thermocouple matrix design was improved by using Kapton® foil as cover instead of parylene C [66]. Although Kapton® increased the sensor thickness to 54 µm, it both improved the thermal stability and created a more homogeneous sensor as the substrate was Kapton® as well. However, the improved version also encountered stability issues, and hence is not suitable for internal battery temperature measurements. The next step is to make stability improvements by using polyimide. In addition to stability issues, this sensor has a relatively large footprint area and, consequently, may reduce the capacity of the battery. However, the sensor has the advantage of measuring internal and spatial-varying temperatures.

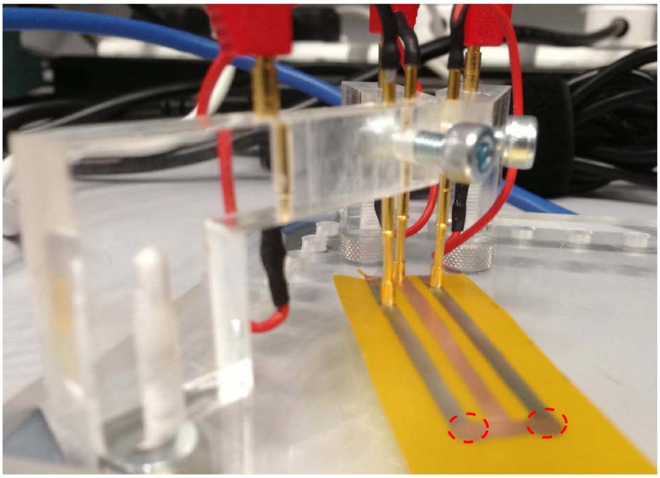

Fig. 3.7: Photograph of a prototype thermocouple matrix on a 2 cm x 6 cm substrate, attached to a measurement setup. The two measurement points for internal battery temperature measurements are circled in red. Adapted from Ref. [66].

3.4. Fiber Bragg-grating sensors

Fiber Bragg Gratings (FBG) are deployed along the length of an optical fiber (see Fig. 3.8) and are used to manipulate the behavior of light. The so-called Bragg gratings are inscribed into the core of an optical fiber by applying UV-light, creating a permanent change in refractive index [68]. These Bragg gratings will act as a wavelength-selective mirror. When a spectrum of light propagates through the fiber core, light with a specific wavelength is reflected back, while the remaining part of the spectrum is transmitted nearly unaffected. This effect is schematically shown in Fig. 3.8a. The wavelength of the reflected signal, which is called the Bragg wavelength (λ_B), has been defined as

$$\lambda_B = 2n_{eff}\Lambda \, , \tag{3.1}$$

where n_{eff} is the effective core index of refraction and Λ the period of index modulation or grating spacing [69]. A change in n_{eff} and/or Λ will result in a shift in the reflected Bragg wavelength. The measurement of this wavelength shift, resulting from external influences, is the basis for FBG sensors [70]. Illustrations of two types of external influences on the Bragg wavelength are shown in Fig. 3.8b-c. When a fiber is compressed or stretched (Fig. 3.8b), the grating spacing changes, which leads to a shift in the Bragg wavelength. A shift in Bragg wavelength can also be observed for temperature changes (Fig. 3.8c). This can be mainly attributed to a temperature-dependent refraction index. The influence of thermal expansion is very small and, thus, grating spacing changes may be neglected; the index changes are by far the most dominant effect [71].

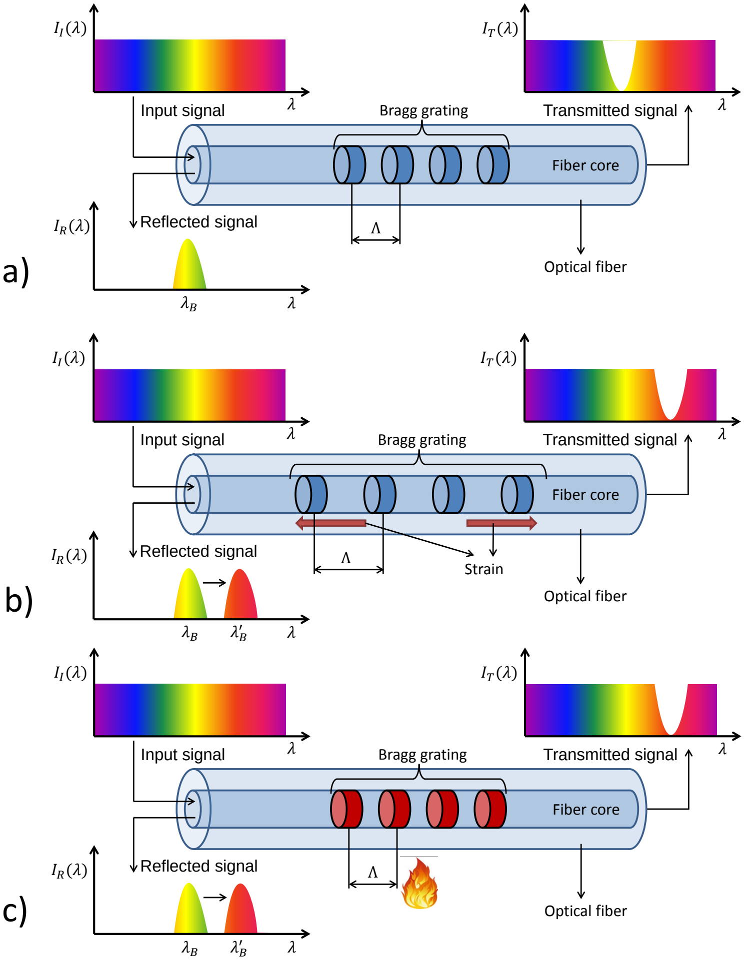

Fig. 3.8: Working principle of a fiber Bragg-grating sensor (a), FBG sensor under influence of strain (b), and FBG sensor under the influence of heat (c).

FBG sensors are becoming increasingly popular due to advantages such as small size, light weight, passive nature, immunity to electromagnetic and radio-frequency interference, high sensitivity, and long-term reliability [72]. In addition, the Bragg wavelength shifts linearly with temperature, and FBG signals can be multiplexed [73]. Multiplexing implies that multiple FBG can be inscribed into a single optical fiber, which makes it possible to perform measurements at different locations along the fiber length.

The temperature range of an optical fiber strongly depends on what materials are used. Black *et al.* [74] listed various optical fiber and coating materials including the corresponding temperature ranges. Silica, the most standard material, can withstand temperatures from -273 up to 1190°C before softening occurs. However, the protective coatings have limitations. For example, acrylate, the standard optical fiber coating, is stable within a temperature range of -40 to 85°C. Polyimide can be used as an alternative, making the temperature range larger (-190 to 385°C). Furthermore, the strong chemical resistivity makes it ideal for internal battery temperature measurements. In a temperature range of approximately 20 to 60°C, measurement accuracies of ± 0.4 to ± 0.2°C have been obtained with FBG sensors [73, 75]. A typical value for temperature sensitivity is a wavelength shift of 10 pm/°C [69, 71].

Although optical FBG sensors already were investigated in electrochemical systems such as PEM fuel cells [76, 77], Yang *et al.* [78] were the first who investigated this type of sensors in Li-ion battery technology. Three coin-type batteries were used at which the temperature was measured with FBG at both flat surfaces. In addition, the temperature was measured on the flat and lateral face of an as-denoted columnar (cylindrical) battery. The calibration of the FBG sensors showed a linear response in the temperature range from 0 to 60°C. Through these calibration measurements, a typical sensitivity of 10 pm/°C was found. It was concluded that FBG temperature sensors show an adequate thermal response in comparison to thermocouples. However, this was not quantified, although the operation of FBG sensors on Li-ion batteries was demonstrated successfully for the first time. After this contribution, research activities with optical FBG sensors in the field of Li-ion batteries increased.

Others followed quickly with temperature and strain measurements on Li-ion batteries using FBG sensors [79–81]. For example, Nascimento and co-workers [81] applied FBG sensors on a cylindrical 18650 Li-ion battery. A single fiber, with two inscribed Bragg gratings (2 cm apart), was used for temperature measurements at two locations on the battery. An additional fiber was attached along the longitudinal axis to monitor variations in strain. The measurement results indicated that temperature and strain evolutions are higher at a high C-rate (1.33 C) in comparison to a low C-rate (0.25 C). In addition, it was found that at the highest C-rate, temperature differences between the two inscribed FBG are marginal (0.5°C).

The same research group [82] continued their work by investigating FBG temperature measurements at Li-ion pouch-type batteries. Two optical fibers, inscribed with two Bragg gratings, were used for internal and external temperature measurements. The silica optical fiber was tested for its chemical resistivity in a $LiPF_6$ salt-containing electrolyte. After two weeks of storage in the electrolyte, it was found that only a very small amount of Si was dissolved, indicating that this fiber type is not sensitive to the electrolyte. Between a temperature range of 10 to 35°C, an average sensitivity of 8.40 and 10.255 pm/°C for the external and internal FBG sensor were obtained, respectively. It was concluded that optical FBG temperature sensors are able to detect temperature changes at multiple locations, both internally and externally, with a superior response rate. However, these FBG sensor measurements were not verified against temperature measurements with other (commercial) sensors. Therefore, the same group [83] compared FBG temperature measurements with that of commercial K-type thermocouples. The corresponding schematic experimental setup is shown in Fig. 3.9 [83]. Fig. 3.9a shows the thermocouple and FBG connections to the battery. It can be seen that only one optical fiber is required for temperature measurements at three different locations (red dashes on blue line) on the battery surface. Fig. 3.9b shows the equipment used and how it is connected. In this particular study, it was found that the response rate of FBG sensors is approximately 1.2 times faster than that of the used thermocouples. Moreover, in the middle measurement position, the difference between the peak temperatures of FBG and thermocouples reaches up to 5.7°C at a C-rate of 8.25. The difference is attributed to the slower response of thermocouples in comparison to FBG sensors. At high C-rates fast thermal evolutions occur which cannot be fully followed by thermocouples. For these reasons, the authors concluded that FBG sensors are a better choice in comparison to thermocouples for real-time monitoring of battery surface temperatures.

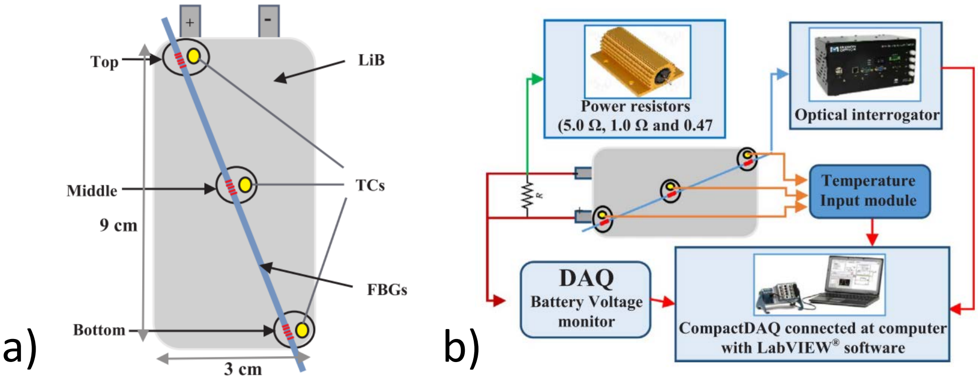

Fig. 3.9: Locations of thermocouples and FBGs on surface of battery (a) and schematic overview of experimental setup (b). Adapted from Ref. [83].

FBG sensors were also used to monitor temperature and strain in battery packs for enhanced safety in a study by Meyer *et al.* [80]. Every single battery in the pack, containing 96 batteries, was monitored with an FBG temperature sensor on a predetermined hot spot. Thermistors were used as default temperature sensors and fixed to the terminal of every fourth battery. Clear differences were found between the thermistors and FBG sensors. During fast charging, a maximum temperature difference of 15°C was reported between the warmest and coldest battery. The relative accuracy of the FBG sensors was determined to be ± 0.05°C, whereas that of the thermistor was only ± 1°C. From the results, it was concluded that the integration of FBG sensors on every single battery considerably improves safety, as the BMS can be provided with far more accurate measurement information.

After using FBG sensors in order to measure diffusion processes [84] and intercalation stages [85] through strain, the team of Raghavan *et al.* [86] embedded FBG sensors for accurate internal monitoring of battery states. The results have been published in a twofold paper [86, 87]. Investigations published in the first version [86] revealed that the seal integrity, capacity retention, and projected cycle life of batteries with embedded FBG sensors are highly comparable to batteries without FBG sensors. It was also shown that batteries with embedded sensors could be integrated into existing modules and that the corresponding system costs are in the range of a few hundreds of U.S. dollars, which is comparable with the conventional system costs. Therefore, this work established the possibility of embedding FBG sensors in large-format Li-ion batteries as a low cost, field-deployable option for internal state monitoring. Their second paper [87] focuses on using the measurements obtained from the embedded FBG sensors for SoC and SoH monitoring at different temperatures. It is shown that the SoC can be estimated with an error of less than 2.5% by using the strain measured by FBG sensors.

Similar work with embedding FBG sensors in coin-type batteries was performed by Fortier and colleagues [88]. During experiments the authors found that the harsh FBG sensor unfortunately cuts through the cathode and separator. This issue has been solved by using extra layers of separator material around the FBG sensors. However, Raghavan *et al.* [86] did not encounter this problem. A possible explanation can be that the used electrode stack was thicker and, therefore, more deformable. Thus, care should be taken with embedding FBG sensors in small electrode stacks.

Recently, an FBG sensor was used by Amietszajew *et al.* [89] to measure the internal temperature of a commercial 18650 high-energy battery. To protect the FBG sensor against electrical, chemical and mechanical stress, it was placed in an aluminum tube. The aluminum tube was then fully sealed with a fluorinated ethylene propylene heat-shrink. The sensor assembly was inserted in the center of the battery. Thermocouples were used to measure the battery surface and ambient temperatures. In addition to the temperature sensors, a lithium metal reference electrode was used. Using the FBG sensor, thermocouple and reference electrode, it was possible to obtain the thermal and electrochemical responses of the battery. From the measurement results, it was found that the battery can be charged with a 6.7 times higher C-rate than specified by the manufacturer, without exceeding the electrochemical and thermal safety limits. Therefore, this study shows the high value of possible performance optimization by integrating internal temperature sensors and the application of reference electrodes.

It is remarkable to see that none of the authors showed calibrations and measurements with FBG temperature sensors for temperatures below 0°C, which is a critical range in Li-ion battery operation. Obviously, the application of FBG sensors in the field of Li-ion batteries is quite recent and still requires thorough investigations, particularly for long-term (*in situ*) measurements and in the application. As FBG sensors offer great advantageous, these can be seriously considered as temperature and strain sensors to measure states in battery-powered applications.

3.5. Differential-voltage technique

Differential-voltage (dV/dQ) analysis is a useful method to investigate Li-ion batteries. The differential voltage can simply be obtained by taking the derivative of the voltage with respect to the capacity. Usually, dV/dQ analysis is used in order to examine phase transitions, (de-)intercalation mechanisms or aging phenomena [90–96]. However, in a recent conference publication of Tripathy *et al.* [97], a method similar to dV/dQ analysis is presented to measure the average internal battery temperature. This temperature is obtained by both measurements and calculations.

At every measured sample, a change in battery voltage (ΔV) is calculated. A so-called effective resistance can then be obtained by dividing ΔV with the current. Subsequently, the generated heat is calculated by multiplying the effective resistance with the current squared. In addition, the conductive and convective heat are obtained by straightforward equations. Finally, if all data are collected, the internal temperature can be calculated.

The authors [97] compared the obtained average internal temperature with surface temperature measurements from K-type thermocouples at various currents and ambient temperatures. Under all conditions, larger internal temperatures were found in comparison to surface temperatures. However, this recently presented method is not yet verified against internal temperature measurements with accurately calibrated sensors. For that reason, measurement accuracies are not given. In addition, the used equations for which thermal parameters are required are somewhat simple and the real temperature evolution can therefore be underestimated.

Hande [98] also developed a method in which a voltage difference is required to estimate the internal battery temperature. The voltage difference is determined after applying a 2 s current pulse. A so-called series resistance can then be calculated by dividing the voltage difference with the applied current. It was shown that the obtained series resistance decreases as a function of temperature; therefore, the series resistance can favorably be used as a measure for internal battery temperature. This is similar to the impedance-based temperature indication methods (Section 3.6). Hande [98] applied this method to measure the internal temperature of lead-acid and NiMH batteries. However, the accuracy of the method has not been validated since the internal battery temperature has not been measured with commercial temperature sensors.

3.6. Impedance-based temperature measurements

Electrochemical Impedance Spectroscopy (EIS) is a non-destructive technique for characterizing the behavior of electrochemical systems [99, 100]. The impedance of a battery can be obtained by voltage or current excitations (typically sinusoidal) and, simultaneously, measuring the response. The ratio between input and output gives the (complex) impedance that can be defined as

$$Z(j\omega) = \frac{V(j\omega)}{I(j\omega)} , \tag{3.2}$$

where Z is the (complex) impedance, V the voltage, I the current, ω the angular frequency and j the imaginary unit satisfying $j^2 = -1$. When these measurements are performed at various frequencies an impedance spectrum of the battery can be obtained. Note that the magnitude of the applied excitation signal should be sufficiently small to guarantee a linear response, but not too small to prevent a poor Signal-to-Noise Ratio (SNR).

EIS is frequently used for extracting kinetic and transport properties of electrode materials, aging studies, modeling purposes and determination of SoC and SoH [101–113]. However, EIS can also be used to measure the internal battery temperature by relating impedance parameters, such as the phase shift, real part, or imaginary part to the temperature. In that case, it is often referred to as impedance-based temperature indication or sensorless temperature indication. In the past five years, investigations on this subject gained substantial interest since impedance-based temperature indication offers significant advantages with respect to conventional temperature measurements. For instance, no external or internal hardware temperature sensors are required, thermal measurement delay is short, it measures an average/integral temperature of the active material, and EIS measurements can also be used to determine additional states, such as SoC and SoH [114–117]. On the other hand, it also has some challenges, such as the possible SoC and aging dependence of the impedance and, moreover, the sensitivity for interference, such as (dis)charge currents and crosstalk signals [118, 119]. These dependencies and the interference can considerably influence EIS-based temperature indications.

A number of impedance-based-related temperature indication methods have been presented. For example, Champlin [120] patented a method to determine internal battery temperature by performing EIS measurements and calculating time constants of RC-circuits, accordingly. These time constants can be readily used to determine the internal battery temperature. Details of the method, such as measurement accuracy and sensitivity to (dis)charge currents are, however, not revealed.

Srinivasan *et al.* [114] reported that a correlation exists between the phase shift of the impedance and the internal temperature at any frequency between 40 and 100 Hz. This correlation is demonstrated at a frequency of 40 Hz for three different batteries in a temperature range of -20 to 66°C. For all batteries, a decreasing phase shift is found with increasing temperature and, moreover, this behavior is essentially SoC independent. In Fig. 3.10a an example of the phase shift is shown as a function of temperature. The authors point out that this unique relationship does not hold for frequencies below 30 Hz since the SoC independence is not guaranteed below these frequencies. In a successive publication of the same group [121], the phase-shift-method was used for real-time temperature monitoring of a 53 Ah Li-ion battery. The phase shift, that was related to the temperature of the negative electrode, was measured under charge and discharge currents below a 1 C-rate. For various conditions, it was demonstrated that the negative electrode temperature deviates from the measured surface temperature.

Schwarz and co-workers [122] also related the phase shift to the internal battery temperature. However, instead of using batteries with common graphite negative electrodes, they used batteries with titanate negative electrodes. In addition, a prototype Printed Circuit Board (PCB) was developed that can directly be connected to the used batteries, enabling online temperature estimation through the phase shift. The PCB was first used for phase-shift calibration measurements at a frequency of 1 kHz in a temperature range between 0 to 40°C. These measurements showed a clear temperature dependence of phase shift and, moreover, a small SoC dependence as well. After calibration, the authors measured the internal battery temperature using the PCB through two approaches. In the first approach, a SoC-specific calibration line, and in the second approach, an averaged calibration line was used to indicate the temperature. An average deviation in temperature of 2.08°C and 2.48°C was found with the first and second approach, respectively. Although these deviations are relatively large, a method for impedance-based temperature indication in battery-powered applications was realized with compact electronics. Furthermore, the authors did not (dis)charge the batteries during phase shift measurements. This implies that the batteries were measured under equilibrium conditions.

Phase shifts under non-equilibrium conditions were measured by Zhu and colleagues [123]. The authors increased the EIS measurement complexity by measuring the impedance during the relaxation time after a sequence of current pulses. The phase shift at a frequency of 10 Hz was favorably selected as temperature indicator for a 30 Ah $LiFePO_4$ battery, since it was found to be SoC independent. Remarkably, Srinivasan *et al.* [114] noted that SoC independence below 30 Hz cannot be guaranteed. This suggests that optimal frequency selection depends on the battery type. The measurement results of Zhu and colleagues [123] revealed that the phase decreases exponentially with increasing relaxation time. Appropriate equations were developed in order to correct the phase shift as a function of relaxation time. Using these expressions, impedance-based temperature measurement errors lower than 1°C can be obtained.

Impedance-based temperature indication can also be performed by relating the real part of the impedance to the internal battery temperature. Schmidt *et al.* [115] were the first who demonstrated this concept and found an intrinsic relationship between real part and the temperature at a frequency of 10.3 kHz for a 2 Ah pouch battery. In Fig. 3.10b, an example of the real part as a function of temperature can be seen, measured at various SoC values. At isothermal conditions this measurement concept can determine temperature within ± 0.17°C and ± 2.5°C for known and unknown SoC, respectively. In addition, it was shown that temperature gradients do not have a considerable influence on the measurement accuracy at the investigated frequency of 10.3 kHz. Therefore, the indicated temperature under gradient conditions reflects the average battery temperature. However, it should be noted that the influence of thermal gradients on impedance spectra in

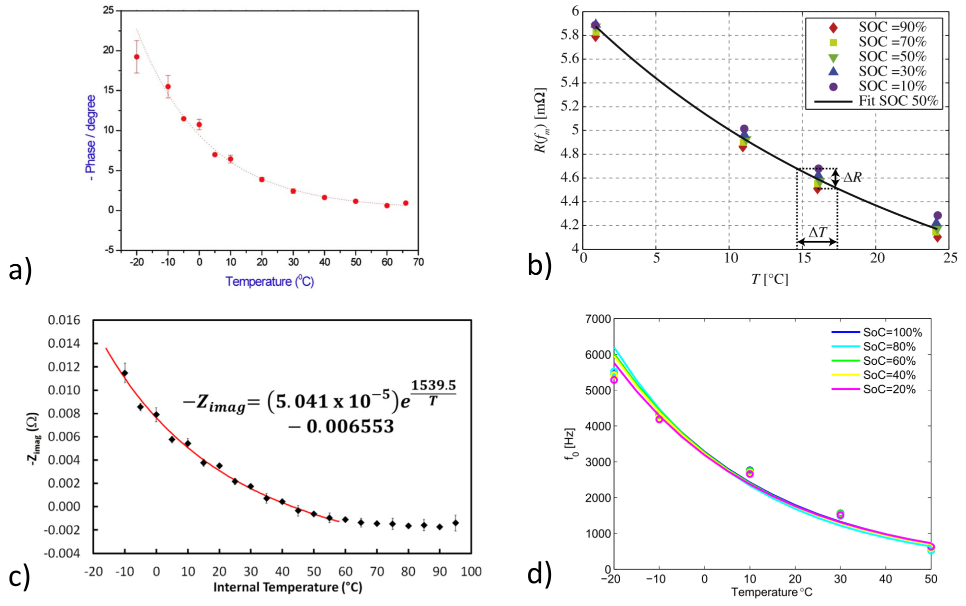

Fig. 3.10: (a) Phase shift (at 40 Hz) as a function of temperature averaged over 20%, 50% and 80% SoC measured on a 4.4 Ah battery [114]; (b) Real part of the impedance (at 10.3 kHz) as a function of temperature, shown for various SoC of a 2 Ah pouch-type battery [115]; (c) Imaginary part of the impedance (at 300 Hz) as a function of temperature, averaged over all measured SoC of a 2.6 Ah cylindrical battery [124]; (d) Intercept frequency as a function of temperature shown for various SoC of a 2.3 Ah cylindrical battery [117].

the low-frequency range can be large [125, 126]. Similar to Zhu and colleagues [123], Schmidt *et al.* [115] performed impedance-based temperature indication during the relaxation time after current pulses. However, no equations were used for corrections. The obtained impedance-based temperature was directly used as indicator for the internal battery temperature. Maximum deviations of 23% between internal and surface temperatures where found, indicating the complexity of measuring temperature gradients.

Richardson an co-workers [116, 127] advantageously used the real part of the impedance at a frequency of 215 Hz as an input parameter for thermal models. In a later contribution [128], the imaginary part, priorly related to the internal temperature by Spinner *et al.* [124], was used since it was found to give superior results in comparison to the real part. An example of the imaginary part as a function of temperature is shown in Fig. 3.10c. The purpose of this unique combination of impedance-based temperature indication and thermal modeling was used for estimating non-uniform internal temperature distributions in cylindrical batteries. Also in these contributions EIS measurements were taken during the relaxation time in order to avoid measurements under DC-currents, providing more accurate results.

A different approach of impedance-based temperature indication was developed by Raijmakers *et al.* [117] and, later, demonstrated again by Ranieri and colleagues [129]. Instead of using a particular frequency to determine, for example, the real part, imaginary part, or phase change, the frequency at zero imaginary value is used for internal battery temperature indication. For several battery chemistries and capacities, it was found that this frequency decreases as a function of temperature and can therefore be used as a temperature indicator. An example of this behavior is shown in Fig. 3.10d at various SoC values. It was found that the intercept frequency is essentially SoC and, moreover, aging independent, which favors on-board battery temperature indication. The method of the intercept frequency has been further developed to a non-zero intercept frequency (NZIF) [118]. Using an NZIF, it is possible to avoid undesirable (current) interference from electric systems in battery-powered applications, such as EV. This offers great potential to increase the SNR and, consequently, to determine temperatures more accurately. In addition to interference from electric systems, EIS measurements can be prone to crosstalk interference in battery packs [119]. This may result in inaccurate EIS measurements and, consequently, inaccurate temperature indications. Therefore, careful design considerations should be taken to develop impedance-based temperature indication methods for battery packs.

Further complications can be met in selecting excitation frequencies and/or *e.g.* real part, imaginary part, phase shift, or intercept frequency to obtain optimal measurement accuracies. In order to investigate these issues, a comparison and accuracy analysis of impedance-based temperature estimation methods was performed by Beelen *et al.* [130, 131]. It was shown that jointly selecting these parameters results in more accurate temperature indications in comparison to all previously discussed individual methods. A detailed study was performed to find a frequency that reveals maximum temperature sensitivity and minimum SoC dependence. In addition, both the real and imaginary part are used with a certain weight to obtain optimal accuracy. This new approach results in an absolute average bias of 0.4°C and average standard deviation of 0.7°C for a 90 Ah battery. However, these investigations were conducted for a battery that resides under equilibrium conditions in a laboratory. Therefore, it would be interesting to perform the same analysis on batteries under non-equilibrium conditions in real applications.

It can be concluded that the presented impedance-based temperature indication methods are valuable tools for temperature monitoring of Li-ion batteries. However, high DC (dis)charge currents, interference from electric components, crosstalk interference, SoC and aging dependencies make it challenging to implement. Most of the research on this subject was performed under laboratory conditions, although applied (dis)charge currents [132–134], and the application in an operating EV [118] also were shown. However, more research efforts on the implementation of impedance-based temperature indication are necessary in order to obtain a clear understanding how accurately and fast impedance-based temperature indication can be performed. (H)EV would be perfect candidates for these investigations as these applications combine all disturbing ingredients, such as high load currents, electric and crosstalk interference, varying SoC, and aging/cycling influences. In addition, the uncertainty of impedance-based temperature indication increases as the battery temperature increases [124, 128]. This limits the measurement range and, therefore, puts challenges on monitoring high temperatures and to guarantee safe operation.

Obviously, the measurement uncertainty is also dependent on the used measurement equipment. Since common electrochemical measurement equipment is not suitable for on-board applications, several authors presented proof-of-concept PCBs that can perform these on-board electrochemical measurements [118, 122, 129, 135–137]. By integrating the PCB functionalities into a small chip, batteries inside a battery pack can be monitored for voltage, impedance and temperature by a single device, enabling accurate SoC, SoH, and temperature measurements at individual battery level.

3.7. Models

Besides direct temperature measurement methods, (thermal) models may be used to perform temperature predictions of Li-ion batteries. By using models, the number of sensors can be reduced, which saves costs, space and possible malfunctioning of hardware sensors. Essentially, models can be divided into two main groups: (*i*) electrochemical/first principle/numerical models [47, 138–140] and (*ii*) equivalent-circuit (EQC) models [59, 62, 141–144]. The numerical models, based on a set of appropriate mathematical equations, have been successfully applied to accurately calculate the thermal behavior of Li-ion batteries. However, numerical models require strong computational power and are therefore less suitable to be integrated into BMS applications for temperature estimation. For that reason, computationally intensive models can be reduced to simplified numerical models that are less accurate but significantly reduce computational times [145–147]. Alternatively, EQC models can be used, which have simple constructions and enable fast calculations. Obviously, due to the simple EQC model construction, thermal simulations are less accurate in comparison to numerical models. Moreover, the accuracy of models does not only depend on the model complexity but also on the underlying parameter values, some of which are difficult to quantify [148, 149].

Thermal models are critically described in various review articles [150–153] and in Section 2.3. An overview and discussion of these models would be redundant and is therefore not given in this Section.

3.8. Thermal imaging and liquid-crystal thermography

Infrared (IR) thermal imaging and liquid-crystal thermography are used to measure and visualize the surface temperature of objects. IR thermal images can be produced with infrared cameras. Infrared cameras are non-contact devices that can detect thermal radiation with special infrared detectors and convert it into an electric signal [154]. The electric signal can then be processed to thermal images or videos. Although surface temperatures advantageously can be obtained, IR thermal imaging is not straightforward in its use. A multitude of factors, such as radiation from objects under investigation, radiation from the atmosphere, and radiation from surrounding objects can influence IR images and therefore its interpretation [155]. For thermal imaging on Li-ion batteries, these issues can be solved to a large extend by *e.g.* coating the surface of the battery with a dull black paint and covering the battery surroundings with black material [15, 24, 156–159]. These measures increase the emissivity of the battery surface and surroundings, effectively eliminating reflections. In addition, the IR camera can be placed at an angle of 45° with respect to the battery in order to eliminate the radiation emitted or reflected by the camera and operator [160]. After accurate calibration within typically 0 to 120°C, thermal sensitivities between 0.03 and 0.09°C can be obtained with 2% accuracy [15, 159]. Depending on the measurement setup, spatial resolutions of 0.1 - 0.3 mm can be achieved [157, 161, 162]. A recent specific review on IR thermal imaging of electrochemical systems, including batteries and fuel cells can be found in Ref. [163].

As with IR thermal imaging, so-called Thermochromic Liquid Crystals (TLC) also make it possible to measure surface temperatures. TLC are organic molecules that change color as a function of temperature in a predictable and repeatable manner [164]. The method of using TLC in order to measure temperature is called liquid-crystal thermography. To measure temperature, surfaces can be coated with TLC material, which is commercially available in the form of adhesive sheets. The color evolution can then be recorded by video cameras, and processed with image-processing software. However, before usage, careful calibration is necessary to determine the color-temperature relationship [165].

TLC operate in a particular bandwidth that can be defined as the range at which light in the visible spectrum actively is reflected back. Beyond both sides of the bandwidth, TLC are transparent. When TLC pass through their bandwidth, they reflect visible light from long wavelengths (red) to short wavelengths (blue) with increasing temperature [166, 167]. This behavior is opposite in comparison to methods such as IR thermal imaging, which typically show high temperatures in red and cold temperatures in blue colors. Various TLC bandwidths are commercially available, ranging from narrowband (typically 0.5 to 4°C) to wideband (typically 5 to 30°C) bandwidths [166]. Measurement uncertainties vary with bandwidth and measurement setup properties, such as lighting and viewing angles, illumination sources, TLC coating thickness and hysteresis effect in TLC [168, 169]. For bandwidths of 5 and 10°C uncertainties of ± 0.1 to 0.3°C and 0.2 to 0.4°C can be achieved, respectively [168].

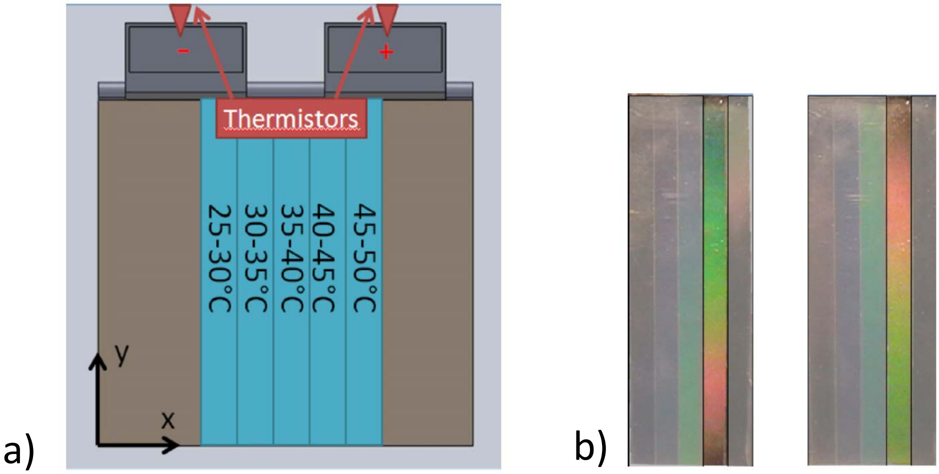

Fig. 3.11: Schematic view of a pouch-type battery surface, with five attached TLC sheets, all having a different range and a bandwidth of 5°C (a) and temperature profiles measured by TLC sheets without cooling (left) and with cooling (right) at a current of 300 A (b). Cooling causes the temperature profile to invert. Note that red colors are low temperatures and green/blue colors high temperatures. Adapted from Ref. [170].

Giuliano and co-workers [170] used liquid-crystal thermography to visualize temperature and temperature gradients of a pouch-type battery that was assembled in a stack. Five TLC sheets with an individual bandwidth of 5°C were attached to the surface of a single battery. All five TLC sheets had a different starting temperature, resulting in a total bandwidth of 25°C. A schematic view of a battery with these five TLC sheets is shown in Fig. 3.11a. Using TLC with individual bandwidths of 5°C leads to higher temperature measurement accuracies. After calibrations, a measurement accuracy of ± 0.5°C was confirmed. The liquid-crystal-thermography results are shown in Fig. 3.11b. The left-hand side is without cooling and right-hand side with cooling conditions. It can be seen that the fourth TLC sheet from the left is the active sheet, indicating that the surface temperature is between 40 and 45°C. The gradient from the top to the bottom of the battery is perfectly visualized by the TLC sheets. Note that in this case red colors indicate low temperatures and green/blue colors high temperatures. Using image-processing software the temperature can be quantitatively obtained.

IR thermal imaging and liquid-crystal thermography provide very useful, accurate, and visual measurements on surface temperatures that cannot be obtained with the previously reviewed measurement techniques, such as thermistors, thermocouples and impedance-based methods. Advantageously, IR thermal imaging and liquid-crystal thermography can be used for qualitatively and quantitatively indicating temperature distributions on battery surfaces and for verifying thermal simulations, making them ideal for research purposes. However, at present these techniques are not suitable for indicating the temperature in commercial battery-powered applications since IR thermal imaging and liquid-crystal thermography are delicate, non-practical and expensive in its use.

3.9. Conclusions and outlook

Accurate temperature measurements must be performed to prevent dangerous situations and to maximize the performance and lifetime of Li-ion batteries. However, due to thermal gradients inside batteries, which might quickly develop during operation, fast and accurate temperature measurements can be rather challenging. Therefore, a proper temperature measurement method should be selected, particularly in terms of measurement range, accuracy, resolution, and cost. In this chapter, various temperature measurement methods for Li-ion batteries have been reviewed. The traditional ones, such as thermistor, RTD, or thermocouple methods, can be used for local surface or local internal temperature measurements. Although these traditional methods can be used for internal measurements as well, it is important that (*i*) the battery cycle life and performance should not be affected; (*ii*) the temperature measurement devices should be insensitive to the chemical environment of the battery materials; and (*iii*) the temperature measurement devices should be compatible with the assembly process, especially in series-produced batteries. Based on the reviewed literature, it can be concluded that not all traditional methods meet these requirements. Recent improvements on the traditional methods have been proposed, and are promising for accurate (internal) temperature measurements. At present, the traditional methods are mature, extensively used for Li-ion battery temperature sensing, and favorable in terms of costs.

Fiber Bragg-grating temperature sensors also measure local temperatures but can easily be multiplexed in one single optical fiber, making temperature measurements possible at multiple locations. By multiplexing, a large number of cables and connections can be saved, especially with respect to traditional methods. However, the method of fiber Bragg-grating temperature sensing applied to Li-ion batteries is still in an early development stage, which also holds for the impedance-based temperature methods. The impedance-based methods have the advantage of measuring the average internal battery temperature without intrusion of hardware temperature sensors and cables. In addition, as the temperature is measured through the impedance, thermal measurement delays are short. Moreover, the impedance can be advantageously used for measuring other states, such as SoC and SoH. Given that both fiber Bragg and impedance-based methods are in a relatively early development stage, they have been proven to be successful only under laboratory conditions. However, there is still room for improvement on the performance outside the laboratory and for the measurement hardware. Therefore, further development on long-term temperature measurements in battery-powered applications is necessary and also expected.

Imaging methods, such as IR thermal imaging and liquid-crystal thermography provide very useful and accurate measurements on surface temperatures that cannot be obtained with measurement techniques such as thermistors, thermocouples and impedance-based methods. IR thermal imaging and liquid crystal thermography are ideal for research purposes, as thermal models can be easily verified. However, at present these techniques are not suitable for indicating the temperature in commercial battery-powered applications, since IR thermal imaging and liquid crystal thermography are delicate, non-practical, and expensive.

References

[1] J. Becker, C. Green, and G. Pearson, *Properties and Uses of Thermistors - Thermally Sensitive Resistors,* Trans. Am. Inst. Electr. Eng. **65**, 711 (1946).

[2] P. Melo de, *Thermistors,* in *Encycl. Med. Devices Instrum.*, edited by J. Webster (John Wiley and Sons, 2006) 2nd ed., pp. 320–340.

[3] E. Boucher, *Theory and Applications of Thermistors,* J. Chem. Educ. **44**, A935 (1967).

[4] S. Wood, B. Mangum, J. Filliben, and S. Tillett, *An investigation of the stability of thermistors,* J. Res. Natl. Bur. Stand. (1934). **83**, 247 (1978).

[5] T. J. Edwards, *Observations on the stability of thermistors,* Rev. Sci. Instrum. **54**, 613 (1983).

[6] K. M. Lawton and S. R. Patterson, *Long-term relative stability of thermistors,* Precis. Eng. **25**, 24 (2001).

[7] K. M. Lawton and S. R. Patterson, *Long-term relative stability of thermistors: Part 2,* Precis. Eng. **26**, 340 (2002).

[8] S. Rudtsch and C. V. Rohden, *Calibration and self-validation of thermistors for high-precision temperature measurements,* Measurement **76**, 1 (2015).

[9] P. R. N. Childs, J. R. Greenwood, and C. A. Long, *Review of temperature measurement,* Rev. Sci. Instrum. **71**, 2959 (2000).

[10] R. K. Kamat and G. M. Naik, *Thermistors - in search of new applications, manufacturers cultivate advanced NTC techniques,* Sens. Rev. **22**, 334 (2002).

[11] J. Cao and A. Emadi, *Batteries Need Electronics,* IEEE Ind. Electron. Mag. **5**, 27 (2011).

[12] S. Dearborn, *Charging Li-ion Batteries for Maximum Run Times,* Power Electroncis Today **31**, 40 (2005).

[13] B. Fleming, *Sensors—A Forecast,* IEEE Veh. Technol. Mag. **8**, 4 (2013).

[14] T. Waldmann, G. Bisle, S. Stumpp, M. A. Danzer, M. Kasper, P. Axmann, and M. Wohlfahrt-mehrens, *Influence of Cell Design on Temperatures and Temperature Gradients in Lithium-Ion Cells: An In Operando Study,* J. Electrochem. Soc. **162**, A921 (2015).

[15] S. Goutam, J.-m. Timmermans, N. Omar, P. V. D. Bossche, and J. V. Mierlo, *Comparative Study of Surface Temperature Behavior of Commercial Li-Ion Pouch Cells of Different Chemistries and Capacities by Infrared Thermography,* Energies **8**, 8175 (2015).

[16] J. Christensen, D. Cook, and P. Albertus, *An Efficient Parallelizable 3D Thermoelectrochemical Model of a Li-Ion Cell,* J. Electrochem. Soc. **160**, A2258 (2013).

[17] M. Debert, G. Colin, G. Bloch, and Y. Chamaillard, *An observer looks at the cell temperature in automotive battery packs,* Control Eng. Pract. **21**, 1035 (2013).

[18] J. Grosch, E. Teuber, M. Jank, V. Lorentz, M. März, and L. Frey, *Device Optimization and Application Study of low cost Printed Temperature Sensor for mobile and stationary battery based Energy Storage Systems,* in *IEEE Int. Conf. Smart Energy Grid Eng.* (IEEE, Oshawa, 2015) pp. 1–7.

[19] Q. Cai, Y.-C. Chen, C. Tsai, and J. F. DeNatale, *Development of a platinum resistance thermometer on the silicon substrate for phase change studies,* J. Micromechanics Microengineering **22**, 1 (2012).

[20] A. Tong, *Improving the accuracy of temperature measurements,* Sens. Rev. **21**, 193 (2001).

[21] S. Tippmann, D. Walper, L. Balboa, B. Spier, and W. G. Bessler, *Low-temperature charging of lithium-ion cells part I: Electrochemical modeling and experimental investigation of degradation behavior,* J. Power Sources **252**, 305 (2014).

[22] D. Chalise, K. Shah, T. Halama, L. Komsiyska, and A. Jain, *An experimentally validated method for temperature prediction during cyclic operation of a Li-ion cell,* Int. J. Heat Mass Transf. **112**, 89 (2017).

[23] Z. H. C. Daud, D. Chrenko, F. D. Santos, E.-h. Aglzim, A. Keromnes, and L. L. Moyne, *3D electro-thermal modelling and experimental validation of lithium polymer-based batteries for automotive applications,* Int. J. Energy Res. **40**, 1144 (2016).

[24] K. Murashko, J. Pyrhonen, and L. Laurila, *Three-dimensional thermal model of a lithium ion battery for hybrid mobile working machines: Determination of the model parameters in a pouch cell,* IEEE Trans. Energy Convers. **28**, 335 (2013).

[25] M. S. Rad, D. L. Danilov, M. Baghalha, M. Kazemeini, and P. H. L. Notten, *Thermal Modeling of Cylindrical LiFePO4 Batteries,* J. Mod. Phys. **04**, 1 (2013).

[26] M. Shadman Rad, D. L. Danilov, M. Baghalha, M. Kazemeini, and P. H. L. Notten, *Adaptive thermal modeling of Li-ion batteries,* Electrochim. Acta **102**, 183 (2013).

[27] R. P. Day, J. Xia, R. Petibon, J. Rucska, H. Wang, A. T. B. Wright, and J. R. Dahn, *Differential Thermal Analysis of Li-Ion Cells as an Effective Probe*

of Liquid Electrolyte Evolution during Aging, J. Electrochem. Soc. **162**, 14 (2015).

[28] P. Wang, X. Zhang, L. Yang, X. Zhang, and M. Yang, *Real-time monitoring of internal temperature evolution of the lithium-ion coin cell battery during the charge and discharge process,* Extrem. Mech. Lett. , 1 (2016).

[29] C.-Y. Wang, G. Zhang, S. Ge, T. Xu, Y. Ji, X.-G. Yang, and Y. Leng, *Lithium-ion battery structure that self-heats at low temperatures,* Nature **529**, 515 (2016).

[30] X.-g. Yang, G. Zhang, and C.-y. Wang, *Computational design and refinement of self-heating lithium ion batteries,* J. Power Sources **328**, 203 (2016).

[31] G. Zhang, S. Ge, T. Xu, X.-G. Yang, H. Tian, and C.-Y. Wang, *Rapid self-heating and internal temperature sensing of lithium-ion batteries at low temperatures,* Electrochim. Acta **218**, 149 (2016).

[32] X.-G. Yang, T. Liu, and C.-Y. Wang, *Innovative heating of large-size automotive Li-ion cells,* J. Power Sources **342**, 598 (2017).

[33] C. Y. Lee, S. J. Lee, M. S. Tang, and P. C. Chen, *In situ monitoring of temperature inside lithium-ion batteries by flexible micro temperature sensors,* Sensors **11**, 9942 (2011).

[34] C.-Y. Lee, S.-J. Lee, Y.-H. Chen, M.-Y. Chung, and K.-C. Han, *In-situ Monitoring of Temperature and Voltage in Lithium-Ion Battery by Embedded Flexible Micro Temperature and Voltage Sensor,* Int. J. Electrochem. Sci. **8**, 2968 (2013).

[35] C.-Y. Lee, H.-C. Peng, S.-J. Lee, I.-M. Hung, C.-T. Hsieh, C.-S. Chiou, Y.-M. Chang, and Y.-P. Huang, *A Flexible Three-in-One Microsensor for Real-Time Monitoring of Internal Temperature, Voltage and Current of Lithium Batteries,* Sensors **15**, 11485 (2015).

[36] C.-Y. Lee, S.-J. Lee, Y.-M. Hung, C.-T. Hsieh, Y.-M. Chang, Y.-T. Huang, and J.-T. Lin, *Integrated microsensor for real-time microscopic monitoring of local temperature, voltage and current inside lithium ion battery,* Sensors Actuators A Phys. **253**, 59 (2017).

[37] M. Sharifi and B. Young, *Chemical Engineering Research and Design Electrical Resistance Tomography (ERT) applications to Chemical Engineering,* Chem. Eng. Res. Des. **91**, 1625 (2013).

[38] S. R. Aw, R. A. Rahim, M. H. F. Rahiman, F. R. M. Yunus, and L. C. Goh, *Electrical resistance tomography: A review of the application of conducting vessel walls,* Powder Technol. **254**, 256 (2014).

[39] X. Hong, N. Li, J. Feng, Q. Kong, and G. Liu, *Multi-Electrode Resistivity Probe for Investigation of Local Temperature Inside Metal Shell Battery Cells via Resistivity: Experiments and Evaluation of Electrical Resistance Tomography,* Energies **8**, 742 (2015).

[40] X. Hong, N. Li, Q. Kong, G. Liu, and M. Ho, *Local cell temperature monitoring for aluminum shell lithium-ion battery based on electrical resistance tomography,* Measurement **86**, 227 (2016).

[41] A. van Herwaarden and P. Sarro, *Thermal sensors based on the Seebeck effect,* Sensors and Actuators **10**, 321 (1986).

[42] K. Uchida, S. Takahashi, K. Harii, J. Ieda, W. Koshibae, K. Ando, S. Maekawa, and E. Saitoh, *Observation of the spin Seebeck effect,* Nat. Lett. **455**, 778 (2008).

[43] B. M. Duff and J. Towey, *Two Ways to Measure Temperature Using Thermocouples Feature Simplicity, Accuracy, and Flexibility,* Analog Dialogue **44**, 1 (2010).

[44] G. Vertiz, M. Oyarbide, H. Macicior, O. Miguel, I. Cantero, P. F. D. Arroiabe, and I. Ulacia, *Thermal characterization of large size lithium-ion pouch cell based on 1d electro-thermal model,* J. Power Sources **272**, 476 (2014).

[45] A. Hofmann, N. Uhlmann, C. Ziebert, O. Wiegand, A. Schmidt, and T. Hanemann, *Preventing Li-ion cell explosion during thermal runaway with reduced pressure,* Appl. Therm. Eng. **124**, 539 (2017).

[46] E. Schuster, C. Ziebert, A. Melcher, M. Rohde, and H. J. Seifert, *Thermal behavior and electrochemical heat generation in a commercial 40 Ah lithium ion pouch cell,* J. Power Sources **286**, 580 (2015).

[47] J. Yi, U. Seong, C. Burm, T. Han, and S. Park, *Modeling the temperature dependence of the discharge behavior of a lithium-ion battery in low environmental temperature,* J. Power Sources **244**, 143 (2013).

[48] Y. Xiao, *Model-Based Virtual Thermal Sensors for Lithium-Ion Battery in EV Applications,* IEEE Trans. Ind. Electron. **62**, 3112 (2015).

[49] S. Al Hallaj, H. Maleki, J. Hong, and J. Selman, *Thermal modeling and design considerations of lithium-ion batteries,* J. Power Sources **83**, 1 (1999).

[50] J. Sun, G. Wei, L. Pei, R. Lu, K. Song, C. Wu, and C. Zhu, *Online Internal Temperature Estimation for Lithium-Ion Batteries Based on Kalman Filter,* Energies **8**, 4400 (2015).

[51] D. Anthony, D. Wong, D. Wetz, and A. Jain, *Non-invasive measurement of internal temperature of a cylindrical Li-ion cell during high-rate discharge,* Int. J. Heat Mass Transf. **111**, 223 (2017).

[52] S. Dey, Z. A. Biron, S. Tatipamula, N. Das, S. Mohon, B. Ayalew, and P. Pisu, *Model-based real-time thermal fault diagnosis of Lithium-ion batteries,* Control Eng. Pract. **56**, 37 (2016).

[53] C. Heubner, M. Schneider, C. Lämmel, and A. Michaelis, *Local Heat Generation in a Single Stack Lithium Ion Battery Cell,* Electrochim. Acta **186**, 404 (2015).

[54] C. Heubner, M. Schneider, C. Lämmel, U. Langklotz, and A. Michaelis, *In-operando temperature measurement across the interfaces of a lithium-ion battery cell,* Electrochim. Acta **113**, 730 (2013).

[55] S. J. Drake, M. Martin, D. A. Wetz, J. K. Ostanek, S. P. Miller, J. M. Heinzel, and A. Jain, *Heat generation rate measurement in a Li-ion cell at large C-rates through temperature and heat flux measurements,* J. Power Sources **285**, 266 (2015).

[56] T. Waldmann and M. Wohlfahrt-mehrens, *In-Operando Measurement of Temperature Gradients in Cylindrical Lithium-Ion Cells during High-Current Discharge,* ECS Electrochem. Lett. **4**, A1 (2015).

[57] G. Zhang, L. Cao, S. Ge, C.-y. Wang, C. E. Shaffer, and C. D. Rahn, *In Situ Measurement of Radial Temperature Distributions in Cylindrical Li-Ion Cells,* J. Electrochem. Soc. **161**, 1499 (2014).

[58] K. Shah, C. Mckee, D. Chalise, and A. Jain, *Experimental and numerical investigation of core cooling of Li-ion cells using heat pipes,* Energy **113**, 852 (2016).

[59] H. Dai, L. Zhu, J. Zhu, X. Wei, and Z. Sun, *Adaptive Kalman filtering based internal temperature estimation with an equivalent electrical network thermal model for hard-cased batteries,* J. Power Sources **293**, 351 (2015).

[60] Z. Li, J. Zhang, B. Wu, J. Huang, Z. Nie, Y. Sun, F. An, and N. Wu, *Examining temporal and spatial variations of internal temperature in large-format laminated battery with embedded thermocouples,* J. Power Sources **241**, 536 (2013).

[61] C. Forgez, D. Vinh Do, G. Friedrich, M. Morcrette, and C. Delacourt, *Thermal modeling of a cylindrical LiFePO$_4$/graphite lithium-ion battery,* J. Power Sources **195**, 2961 (2010).

[62] X. Lin, H. E. Perez, J. B. Siegel, A. G. Stefanopoulou, Y. Li, R. D. Anderson, Y. Ding, and M. P. Castanier, *Online parameterization of lumped thermal dynamics in cylindrical lithium ion batteries for core temperature estimation and health monitoring,* IEEE Trans. Control Syst. Technol. **21**, 1745 (2013).

[63] M. Parhizi, M. B. Ahmed, and A. Jain, *Determination of the core temperature of a Li-ion cell during thermal runaway,* J. Power Sources **370**, 27 (2017).

[64] G. Zhang, L. Cao, S. Ge, C.-Y. Wang, C. E. Shaffer, and C. D. Rahn, *Reaction temperature sensing (RTS)-based control for Li-ion battery safety,* Sci. Rep. **5**, 1 (2015).

[65] M. S. K. Mutyala, J. Zhao, J. Li, H. Pan, C. Yuan, and X. Li, *In-situ temperature measurement in lithium ion battery by transferable flexible thin film thermocouples,* J. Power Sources **260**, 43 (2014).

[66] N. Martiny, A. Rheinfled, J. Geder, Y. Wang, W. Kraus, and A. Jossen, *Development of an all Kapton-based thin-film thermocouple matrix for in-situ temperature measurement in a lithium ion pouch cell,* IEEE Sens. J. **14**, 3377 (2014).

[67] N. Martiny, J. Geder, Y. Wang, W. Kraus, and A. Jossen, *Development of a thin-film thermocouple matrix for in-situ temperature measurement in a lithium ion pouch cell,* in *IEEE Sensors* (IEEE, Baltimore, MD, USA, 2013).

[68] K. O. Hill and G. Meltz, *Fiber Bragg Grating Technology Fundamentals and Overview,* J. Light. Technol. **15**, 1263 (1997).

[69] Y.-J. Rao, *In-fibre Bragg grating sensors,* Meas. Sci. Technol. **8**, 355 (1997).

[70] F. Jülich and J. Roths, *Determination of the Effective Refractive Index of Various Single Mode Fibres for Fibre Bragg Grating Sensor Applications,* in *SENSOR+TEST Conf.* (AMA Conferences, Nürnberg, 2009) pp. 119–124.

[71] A. Othonos, *Fiber Bragg gratings,* Rev. Sci. Instrum. **68**, 4309 (1997).

[72] S. J. Mihailov, *Fiber Bragg Grating Sensors for Harsh Environments,* Sensors **12**, 1898 (2012).

[73] W.-C. Du, X.-M. Tao, and H.-Y. Tam, *Fiber Bragg Grating Cavity Sensor for Simultaneous Measurement of Strain and Temperature,* IEEE Photonics Technol. Lett. **11**, 105 (1999).

[74] R. J. Black and B. Moslehi, *Advanced end-to-end fiber optic sensing system for demanding environments,* Proc. SPIE, Nanophotonics Macrophotonics Sp. Environ. IV **7817**, 78170L1 (2010).

[75] Y.-J. Rao, D. J. Webb, D. A. Jackson, L. Zhang, and I. Bennion, *In-Fiber Bragg-Grating Temperature Sensor System for Medical Applications,* J. Light. Technol. **15**, 779 (1997).

[76] N. A. David, P. M. Wild, J. Hu, and N. Djilali, *In-fibre Bragg grating sensors for distributed temperature measurement in a polymer electrolyte membrane fuel cell,* J. Power Sources **192**, 376 (2009).

[77] N. A. David, P. M. Wild, J. Jensen, T. Navessin, and N. Djilali, *Simultaneous In Situ Measurement of Temperature and Relative Humidity in a PEMFC Using Optical Fiber Sensors,* J. Electrochem. Soc. **157**, B1173 (2010).

[78] G. Yang, C. Leitao, Y. Li, J. Pinto, and X. Jiang, *Real-time temperature measurement with fiber Bragg sensors in lithium batteries for safety usage,* Measurement **46**, 3166 (2013).

[79] L. W. Sommer, A. Raghavan, P. Kiesel, B. Saha, T. Staudt, A. Lochbaum, A. Gunguli, C.-J. Bae, and M. Alamgir, *Embedded fiber optic sensing for accurate state estimation in advanced battery management systems,* in *MRS Spring Meet. Symp. Q* (Cambridge University Press, 2014).

[80] J. Meyer, A. Nedjalkov, A. Doering, M. Angelmahr, and W. Schade, *Fiber optical sensors for enhanced battery safety,* in *SPIE Sens. Technol. Appl.* (Baltimore, Maryland, United States, 2015) pp. 94800Z–1.

[81] M. Nascimento, S. Novais, C. Leitao, F. Domingues, and N. Alberto, *Lithium batteries temperature and strain fiber temperature monitoring,* in *24th Int. Conf. Opt. Fibre Sensors* (Proc. of SPIE, Curitiba, Brazil, 2015) pp. 96347V–1.

[82] S. Novais, M. Nascimento, L. Grande, M. F. Domingues, P. Antunes, N. Alberto, C. Leitao, R. Oliveira, S. Koch, G. T. Kim, S. Passerini, and J. Pinto, *Internal and External Temperature Monitoring of a Li-Ion Battery with Fiber Bragg Grating Sensors,* Sensors **16**, 1394 (2016).

[83] M. Nascimento, M. S. Ferreira, and J. L. Pinto, *Real time thermal monitoring of lithium batteries with fiber sensors and thermocouples: A comparative study,* Measurement **111**, 260 (2017).

[84] L. W. Sommer, P. Kiesel, A. Ganguli, A. Lochbaum, B. Saha, J. Schwartz, C.-J. Bae, M. Alamgir, and A. Raghavan, *Fast and slow ion diffusion processes in lithium ion pouch cells during cycling observed with fiber optic strain sensors,* J. Power Sources **296**, 46 (2015).

[85] L. W. Sommer, A. Raghavan, P. Kiesel, B. Saha, J. Schwartz, A. Lochbaum, A. Ganguli, C.-J. Bae, and M. Alamgir, *Monitoring of Intercalation Stages in Lithium-Ion Cells over Charge-Discharge Cycles with Fiber Optic Sensors,* J. Electrochem. Soc. **162**, A2664 (2015).

[86] A. Raghavan, P. Kiesel, L. W. Sommer, J. Schwartz, A. Lochbaum, A. Hegyi, A. Schuh, K. Arakaki, B. Saha, A. Ganguli, K. H. Kim, C. Kim, H. J. Hah, S. Kim, G.-O. Hwang, G.-C. Chung, B. Choi, and M. Alamgir, *Embedded fiber-optic sensing for accurate internal monitoring of cell state in advanced battery management systems part 1: Cell embedding method and performance,* J. Power Sources **341**, 466 (2017).

[87] A. Ganguli, B. Saha, A. Raghavan, P. Kiesel, K. Arakaki, A. Schuh, J. Schwartz, A. Hegyi, L. W. Sommer, A. Lochbaum, S. Sahu, and M. Alamgir, *Embedded fiber-optic sensing for accurate internal monitoring of cell state in advanced battery management systems part 2: Internal cell signals and utility for state estimation,* J. Power Sources **341**, 474 (2017).

[88] A. Fortier, M. Tsao, N. D. Williard, Y. Xing, and M. G. Pecht, *Preliminary Study on Integration of Fiber Optic Bragg Grating Sensors in Li-Ion Batteries and In Situ Strain and Temperature Monitoring of Battery Cells,* Energies **10**, 838 (2017).

[89] T. Amietszajew, E. McTurk, J. Fleming, and R. Bhagat, *Understanding the limits of rapid charging using instrumented commercial 18650 high-energy Li-ion cells,* Electrochim. Acta **263**, 346 (2018).

[90] I. Bloom, A. N. Jansen, D. P. Abraham, J. Knuth, S. A. Jones, V. S. Battaglia, and G. L. Henriksen, *Differential voltage analyses of high-power, lithium-ion cells 1. Technique and application,* J. Power Sources **139**, 295 (2005).

[91] M. Dubarry, C. Truchot, and B. Y. Liaw, *Synthesize battery degradation modes via a diagnostic and prognostic model,* J. Power Sources **219**, 204 (2012).

[92] M. Ecker, N. Nieto, S. Käbitz, J. Schmalstieg, H. Blanke, A. Warnecke, and D. U. Sauer, *Calendar and cycle life study of Li (NiMnCo) O 2 -based 18650 lithium- ion batteries,* J. Power Sources **248**, 839 (2014).

[93] C. Pastor-Fernández, K. Uddin, G. H. Chouchelamane, W. D. Widanage, and J. Marco, *A Comparison between Electrochemical Impedance Spectroscopy and Incremental Capacity-Differential Voltage as Li-ion Diagnostic Techniques to Identify and Quantify the Effects of Degradation Modes within Battery Management Systems,* J. Power Sources **360**, 301 (2017).

[94] D. Li, D. L. Danilov, J. Xie, L. Raijmakers, L. Gao, Y. Yang, and P. H. Notten, *Degradation Mechanisms of C_6/$LiFePO_4$ Batteries: Experimental Analyses of Calendar Aging,* Electrochim. Acta **190**, 1124 (2016).

[95] D. Li, D. Danilov, L. Gao, Y. Yang, and P. H. Notten, *Degradation Mechanisms of C_6/$LiFePO_4$ Batteries: Experimental Analyses of Cycling-induced Aging,* Electrochim. Acta **210**, 445 (2016).

[96] D. Li, D. L. Danilov, L. Gao, Y. Yang, and P. H. L. Notten, *Degradation Mechanisms of the Graphite Electrode in C_6/$LiFePO_4$ Batteries Unraveled by a Non-Destructive Approach,* J. Electrochem. Soc. **163**, A3016 (2016).

[97] Y. Tripathy, A. Mcgordon, J. Low, and J. Marco, *Internal Temperature Prediction of Lithium-ion Cell Using Differential Voltage Technique,* in *Transp. Electrif. Conf. Expo* (IEEE, Chicago, IL, USA, 2017) pp. 464–467.

[98] A. Hande, *Internal battery temperature estimation using series battery resistance measurements during cold temperatures,* J. Power Sources **158**, 1039 (2006).

[99] M. E. Orazem and B. Tribollet, *Electrochmical Impedance Spectroscopy* (John Wiley and Sons, 2011).

[100] E. Barsoukov and J. R. Macdonald, *Impedance Spectroscopy Theory, Experiment, and Applications*, 2nd ed. (John Wiley and Sons, 2005).

[101] W. Waag, S. Käbitz, and D. U. Sauer, *Experimental investigation of the lithium-ion battery impedance characteristic at various conditions and aging states and its influence on the application,* Appl. Energy **102**, 885 (2013).

[102] K. M. Shaju, G. V. Subba Rao, and B. V. R. Chowdari, *Electrochemical Kinetic Studies of Li-Ion in O2-Structured* $Li_{2/3}(Ni_{1/3}Mn_{2/3})O_2$ *and* $Li_{(2/3)+x}(Ni_{1/3}Mn_{2/3})O_2$ *by EIS and GITT,* J. Electrochem. Soc. **150**, A1 (2003).

[103] J.-H. Lee and W.-J. Choi, *Novel State-of-Charge Estimation Method for Lithium Polymer Batteries Using Electrochemical Impedance Spectroscopy,* J. Power Electron. **11**, 237 (2011).

[104] M.-H. Hung, C.-H. Lin, L.-C. Lee, and C.-M. Wang, *State-of-charge and state-of-health estimation for lithium-ion batteries based on dynamic impedance technique,* J. Power Sources **268**, 861 (2014).

[105] C. T. Love, M. B. V. Virji, R. E. Rocheleau, and K. E. Swider-Lyons, *State-of-health monitoring of 18650 4S packs with a single-point impedance diagnostic,* J. Power Sources **266**, 512 (2014).

[106] Y. Zhang and C.-Y. Wang, *Cycle-Life Characterization of Automotive Lithium-Ion Batteries with* $LiNiO_2$ *Cathode,* J. Electrochem. Soc. **156**, A527 (2009).

[107] X.-Y. Qiu, Q.-C. Zhuang, Q.-Q. Zhang, R. Cao, P.-Z. Ying, Y.-H. Qiang, and S.-G. Sun, *Electrochemical and electronic properties of* $LiCoO_2$ *cathode investigated by galvanostatic cycling and EIS,* Phys. Chem. Chem. Phys. **14**, 2617 (2012).

[108] E. Samadani, S. Farhad, W. Scott, M. Mastali, L. E. Gimenez, M. Fowler, and R. A. Fraser, *Empirical modeling of lithium-ion batteries based on electrochemical impedance spectroscopy tests,* Electrochim. Acta **160**, 169 (2015).

[109] P. Gao, C. Zhang, and G. Wen, *Equivalent circuit model analysis on electrochemical impedance spectroscopy of lithium metal batteries,* J. Power Sources **294**, 67 (2015).

[110] N. Mellgren, S. Brown, M. Vynnycky, and G. Lindbergh, *Impedance as a Tool for Investigating Aging in Lithium-Ion Porous Electrodes,* J. Electrochem. Soc. **155**, A304 (2008).

[111] Y. Xie, J. Li, and C. Yuan, *Mathematical modeling of the electrochemical impedance spectroscopy in lithium ion battery cycling,* Electrochim. Acta **127**, 266 (2014).

[112] L. Gagneur, A. L. Driemeyer-Franco, C. Forgez, and G. Friedrich, *Modeling of the diffusion phenomenon in a lithium-ion cell using frequency or time domain identification,* Microelectron. Reliab. **53**, 784 (2013).

[113] U. Westerhoff, T. Kroker, K. Kurbach, and M. Kurrat, *Electrochemical impedance spectroscopy based estimation of the state of charge of lithium-ion batteries,* J. Energy Storage **8**, 244 (2016).

[114] R. Srinivasan, B. G. Carkhuff, M. H. Butler, and A. C. Baisden, *Instantaneous measurement of the internal temperature in lithium-ion rechargeable cells,* Electrochim. Acta **56**, 6198 (2011).

[115] J. P. Schmidt, S. Arnold, A. Loges, D. Werner, T. Wetzel, and E. Ivers-Tiffée, *Measurement of the internal cell temperature via impedance: Evaluation and application of a new method,* J. Power Sources **243**, 110 (2013).

[116] R. R. Richardson, P. T. Ireland, and D. a. Howey, *Battery internal temperature estimation by combined impedance and surface temperature measurement,* J. Power Sources **265**, 254 (2014).

[117] L. H. J. Raijmakers, D. L. Danilov, J. P. M. Van Lammeren, M. J. G. Lammers, and P. H. L. Notten, *Sensorless battery temperature measurements based on electrochemical impedance spectroscopy,* J. Power Sources **247**, 539 (2014).

[118] L. Raijmakers, D. Danilov, J. van Lammeren, T. Lammers, H. J. Bergveld, and P. Notten, *Non-Zero Intercept Frequency: An Accurate Method to Determine the Integral Temperature of Li-ion Batteries,* IEEE Trans. Ind. Electron. **63**, 3168 (2016).

[119] L. Raijmakers, K. Shivakumar, M. Donkers, M. Lammers, and H. Bergveld, *Crosstalk Interferences on Impedance Measurements in Battery Packs,* IFAC-PapersOnLine **49**, 42 (2016).

[120] K. S. Champlin, *Method and apparatus for electronically evaluating the internal temperature of an electrochemical cell or battery,* (2001).

[121] R. Srinivasan, *Monitoring dynamic thermal behavior of the carbon anode in a lithium-ion cell using a four-probe technique,* J. Power Sources **198**, 351 (2012).

[122] R. Schwarz, K. Semmler, M. Wenger, V. Lorentz, and M. März, *Sensorless Battery Cell Temperature Estimation Circuit for Enhanced Safety in Battery Systems,* in *41st Annu. Conf. IEEE Ind. Electron. Soc.* (IEEE, Yokohama, Japan, 2015).

[123] J. Zhu, Z. Sun, X. Wei, and H. Dai, *Battery Internal Temperature Estimation for $LiFePO_4$ Battery Based on Impedance Phase Shift under Operating Conditions,* Energies **10**, 1 (2017).

[124] N. S. Spinner, C. T. Love, S. L. Rose-Pehrsson, and S. G. Tuttle, *Expanding the Operational Limits of the Single-Point Impedance Diagnostic for Internal Temperature Monitoring of Lithium-ion Batteries,* Electrochim. Acta **174**, 488 (2015).

[125] Y. Troxler, B. Wu, M. Marinescu, V. Yufit, Y. Patel, A. J. Marquis, N. P. Brandon, and G. J. Offer, *The effect of thermal gradients on the performance of lithium-ion batteries,* J. Power Sources **247**, 1018 (2014).

[126] H. Dai, B. Jiang, and X. Wei, *Impedance Characterization and Modeling of Lithium-Ion Batteries Considering the Internal Temperature Gradient,* Energies **11**, 220 (2018).

[127] R. R. Richardson and D. A. Howey, *Sensorless Battery Internal Temperature Estimation using a Kalman Filter with Impedance Measurement,* IEEE Trans. Sustain. Energy **6**, 1190 (2015), arXiv:arXiv:1501.06160v1 .

[128] R. R. Richardson, S. Zhao, and D. A. Howey, *On-board monitoring of 2-D spatially-resolved temperatures in cylindrical lithium-ion batteries: Part II. State estimation via impedance-based temperature sensing,* J. Power Sources **327**, 726 (2016), arXiv:1606.02144 .

[129] M. Ranieri, D. Alberto, H. Piret, and V. Cattin, *Electronic Module for the Thermal Monitoring of a Li-ion Battery Cell through the Electrochemical Impedance Estimation,* in *Therminic 2016 - 22nd Int. Work. Therm. Investig. ICs Syst.* (IEEE, Budapest, Hungary, 2016) pp. 294–297.

[130] H. Beelen, L. Raijmakers, M. Donkers, P. Notten, and H. Bergveld, *An Improved Impedance-Based Temperature Estimation Method for Li-ion Batteries,* IFAC-PapersOnLine **48**, 383 (2015).

[131] H. P. G. J. Beelen, L. H. J. Raijmakers, M. C. F. Donkers, P. H. L. Notten, and H. J. Bergveld, *A comparison and accuracy analysis of impedance-based temperature estimation methods for Li-ion batteries,* Appl. Energy **175**, 128 (2016).

[132] P. Haussmann and J. Melbert, *Internal Cell Temperature Measurement and Thermal Modeling of Lithium Ion Cells for Automotive Applications by Means of Electrochemical Impedance Spectroscopy,* SAE Int. J. Altern. Powertrains **6**, 261 (2017).

[133] S. Socher, C. Jehle, and U. Potthoff, *Improving the functional safety of automotive batteries using in-situ impedance spectroscopy,* Transp. Res. Procedia **14**, 3661 (2016).

[134] R. Koch and A. Jossen, *Temperature Measurement of Large Format Pouch Cells with Impedance Spectroscopy,* in *EVS 28 Int. Electr. Veh. Symp. Exhib.* (Goyang, Korea, 2015) pp. 1–9.

[135] V. Roscher, M. Schneider, P. Durdaut, N. Sassano, S. Pereguda, E. Mense, and K. R. Riemschneider, *Synchronisation using wireless trigger-broadcast for impedance spectroscopy of battery cells,* in *SAS 2015 - 2015 IEEE Sensors Appl. Symp. Proc.* (IEEE, Zadar, Croatia, 2015).

[136] B. G. Carkhuff, P. A. Demirev, and R. Srinivasan, *Impedance-Based Battery Management System for Safety Monitoring of Lithium-Ion Batteries,* IEEE Trans. Ind. Electron. **PP** (2018), 10.1109/TIE.2017.2786199.

[137] X. Wei, X. Wang, and H. Dai, *Practical on-board measurement of lithium ion battery impedance based on distributed voltage and current sampling,* Energies **11**, 64 (2018).

[138] U. S. Kim, J. Yi, C. B. Shin, T. Han, and S. Park, *Modeling the Thermal Behaviors of a Lithium-Ion Battery during Constant-Power Discharge and Charge Operations,* J. Electrochem. Soc. **160**, A990 (2013).

[139] B. Rieger, S. V. Erhard, S. Kosch, M. Venator, A. Rheinfeld, and A. Jossen, *Multi-Dimensional Modeling of the Influence of Cell Design on Temperature, Displacement and Stress Inhomogeneity in Large-Format Lithium-Ion Cells,* J. Electrochem. Soc. **163**, A3099 (2016).

[140] K.-j. Lee, K. Smith, A. Pesaran, and G.-h. Kim, *Three dimensional thermal-, electrical-, and electrochemical-coupled model for cylindrical wound large format lithium-ion batteries,* J. Power Sources **241**, 20 (2013).

[141] Q.-k. Wang, Y.-j. He, J.-n. Shen, Z.-f. Ma, and G.-b. Zhong, *A unified modeling framework for lithium-ion batteries: An artificial neural network based thermal coupled equivalent circuit model approach,* Energy **138**, 118 (2017).

[142] V. Lystianingrum, B. Hredzak, and V. G. Agelidis, *Multiple model estimator based detection of abnormal cell overheating in a Li-ion battery string with minimum number of temperature sensors,* J. Power Sources **273**, 1171 (2015).

[143] I. Arasaratnam, J. Tjong, R. Ahmed, M. El-Sayed, and S. Habibi, *Adaptive temperature monitoring for battery thermal management,* in *IEEE Transp. Electrif. Conf. Expo* (IEEE, Detroit, MI, USA, 2013).

[144] K. S. Hariharan, *A coupled nonlinear equivalent circuit – Thermal model for lithium ion cells,* J. Power Sources **227**, 171 (2013).

[145] M. Guo and R. E. White, *A distributed thermal model for a Li-ion electrode plate pair,* J. Power Sources **221**, 334 (2013).

[146] S. Goutam, A. Nikolian, J. Jaguemont, J. Smekens, N. Omar, P. Van Dan Bossche, and J. Van Mierlo, *Three-dimensional electro-thermal model of li-ion pouch cell: Analysis and comparison of cell design factors and model assumptions,* Appl. Therm. Eng. **126**, 796 (2017).

[147] K. Gopalakrishnan, T. Zhang, and G. J. Offer, *A Fast, Memory-Efficient Discrete-Time Realization Algorithm for Reduced-Order Li-Ion Battery Models,* J. Electrochem. Energy Convers. Storage **14** (2017), 10.1115/1.4035526.

[148] J. Zhang, B. Wu, Z. Li, and J. Huang, *Simultaneous estimation of thermal parameters for large-format laminated lithium-ion batteries,* J. Power Sources **259**, 106 (2014).

[149] K. A. Murashko, A. V. Mityakov, J. Pyrhönen, V. Y. Mityakov, and S. S. Sapozhnikov, *Thermal parameters determination of battery cells by local heat flux measurements,* J. Power Sources **271**, 48 (2014).

[150] Q. Wang, B. Jiang, B. Li, and Y. Yan, *A critical review of thermal management models and solutions of lithium-ion batteries for the development of pure electric vehicles,* Renew. Sustain. Energy Rev. **64**, 106 (2016).

[151] Z. Rao and S. Wang, *A review of power battery thermal energy management,* Renew. Sustain. Energy Rev. **15**, 4554 (2011).

[152] S. Abada, G. Marlair, A. Lecocq, M. Petit, V. Sauvant-Moynot, and F. Huet, *Safety focused modeling of lithium-ion batteries: A review,* J. Power Sources **306**, 178 (2016).

[153] M. B. Effat, C. Wu, and F. Ciucci, *Modeling efforts in the key areas of thermal management and safety of lithium ion battery cells: a mini review,* ASIA-PACIFIC J. Chem. Eng. **11**, 399 (2016).

[154] K.-P. Möllmann and M. Vollmer, *Infrared thermal imaging as a tool in university physics education,* Eur. J. Phys. **28**, S37 (2007).

[155] M. Vollmer and K.-P. Möllmann, *Infrared Thermal Imaging: Fundamentals, Research and Applications*, 2nd ed. (John Wiley and Sons, Weinheim, Germany, 2017).

[156] J. B. Robinson, E. Engebretsen, D. P. Finegan, J. Darr, G. Hinds, P. R. Shearing, and D. J. L. Brett, *Detection of Internal Defects in Lithium-Ion Batteries Using Lock-in Thermography,* ECS Electrochem. Lett. **4**, A106 (2015).

[157] J. B. Robinson, J. a. Darr, D. S. Eastwood, G. Hinds, P. D. Lee, P. R. Shearing, O. O. Taiwo, and D. J. L. Brett, *Non-uniform temperature distribution in Li-ion batteries during discharge - A combined thermal imaging, X-ray micro-tomography and electrochemical impedance approach,* J. Power Sources **252**, 51 (2014).

[158] F. Bahiraei, M. Ghalkhani, A. Fartaj, and G.-A. Nazri, *A pseudo 3D electrochemical-thermal modeling and analysis of a lithium-ion battery for electric vehicle thermal management applications,* Appl. Therm. Eng. **125**, 904 (2017).

[159] S. Kosch, A. Rheinfeld, S. V. Erhard, and A. Jossen, *An extended polarization model to study the influence of current collector geometry of large-format lithium-ion pouch cells,* J. Power Sources **342**, 666 (2017).

[160] S. Panchal, I. Dincer, M. Agelin-chaab, R. Fraser, and M. Fowler, *Experimental and simulated temperature variations in a $LiFePO_4$ -20 Ah battery during discharge process*, Appl. Energy **180**, 504 (2016).

[161] D. J. Cumming and R. H. Elder, *Thermal imaging of solid oxide cells operating under electrolysis conditions*, J. Power Sources **280**, 387 (2015).

[162] M. B. Pomfret, D. A. Steinhurst, D. A. Kidwell, and J. C. Owrutsky, *Thermal imaging of solid oxide fuel cell anode processes*, J. Power Sources **195**, 257 (2010).

[163] J. B. Robinson, P. R. Shearing, and D. J. Brett, *Thermal Imaging of Electrochemical Power Systems: A Review*, J. Imaging **2**, 1 (2016).

[164] K. Toriyama, S. Tada, K. Ichimiya, S. Funatani, and Y. Tomita, *A new method of temperature measurement using thermochromic liquid crystals (extension of measurable range based on spectral intensity in the narrow-band wavelength)*, Int. J. Heat Mass Transf. **92**, 483 (2016).

[165] V. U. Kakade, G. D. Lock, M. Wilson, J. M. Owen, and J. E. Mayhew, *Accurate heat transfer measurements using thermochromic liquid crystal. Part 1: Calibration and characteristics of crystals*, Int. J. Heat Fluid Flow **30**, 939 (2009).

[166] N. Abdullah, A. R. Abu Talib, A. A. Jaafar, M. A. Mohd Salleh, and W. T. Chong, *The basics and issues of Thermochromic Liquid Crystal Calibrations*, Exp. Therm. Fluid Sci. **34**, 1089 (2010).

[167] C. R. Smith, D. R. Sabatino, and T. J. Praisner, *Temperature sensing with thermochromic liquid crystals*, Exp. Fluids **30**, 190 (2001).

[168] Y. Rao and S. Zang, *Calibrations and the measurement uncertainty of wide-band liquid crystal thermography*, Meas. Sci. Technol. **21** (2010), 10.1088/0957-0233/21/1/015105.

[169] D. R. Sabatino, T. J. Praisner, and C. R. Smith, *A high-accuracy calibration technique for thermochromic liquid crystal temperature measurements*, Exp. Fluids **28**, 497 (2000).

[170] M. R. Giuliano, S. G. Advani, and A. K. Prasad, *Thermal analysis and management of lithium – titanate batteries*, J. Power Sources **196**, 6517 (2011).

4

Zero-intercept frequency as temperature indication method

A new method is proposed to measure the internal temperature of (Li-ion) batteries. Based on electrochemical-impedance-spectroscopy measurements, a zero-intercept frequency (ZIF) can be determined, which is exclusively related to the internal battery temperature. The ZIF is defined as the frequency at which the imaginary part of the impedance is zero ($Z_{im} = 0$), i.e. where the phase shift between the battery current and voltage is absent. The advantage of the proposed method is twofold: (i) no hardware temperature sensors are required anymore to monitor the battery temperature and (ii) the method does not suffer from heat transfer delays. Mathematical analysis of an equivalent electrical circuit, representing the battery performance, shows that the ZIF decreases with rising temperatures. Impedance measurements on rechargeable Li-ion batteries of various chemistries were conducted to verify the proposed method. These experiments reveal that the ZIF is clearly dependent on the temperature and, essentially independent of State-of-Charge (SoC) and aging. These impedance-based sensorless temperature measurements are therefore simple and convenient for application in a wide range of stationary, mobile and high-power devices, such as hybrid- and full electric vehicles.

Parts of this chapter have been published in Journal of Power Sources **247**, (2014) 539-544 [1].

4.1. Introduction

Battery temperature measurement methods based on electrochemical impedance spectroscopy (EIS) measure the integral battery temperature without the intrusion of hardware sensors and thermal delay. As already explained in Section 3.6, EIS is a non-destructive technique to characterize electrochemical systems. It applies a harmonic voltage/current signal to the battery and analyzes the respective current/voltage response at various frequencies.

After performing EIS measurements, various diagnostic plots can be made. In particular, the complex plane is very instructive and may reveal a sloping line at low frequencies, a number of (depressed) semicircles at mid frequencies, and a vertical line at high frequencies. Although a lot of research on characterizing Li-ion batteries already has been conducted, the relation of the various processes to the specific parts of the spectrum is not trivial [2–4]. It is generally accepted that the high-frequency semicircle can be attributed to the surface layer on the active electrode material [5–12] and that the mid-frequency semicircle can be attributed to the electrical double layer and electrochemical charge-transfer reaction, occurring at the electrode/electrolyte interface [5, 6, 8–12]. Sloping lines are generally attributed to diffusion processes. It has been reported that the high-frequency semicircle of commercial Li-ion batteries is almost independent of SoC, whereas the temperature has a large influence [3, 6, 8].

In the high-frequency region the impedance of a battery is generally dominated by its inductive behavior. This has been attributed to the porosity of the electrodes [13], the electrode geometry of spirally wound batteries [14], or the conductive path formed by the terminals, connectors and electrodes [15, 16]. As the porosity and electrode geometry hardly change upon cycling, the inductance is expected to remain more or less constant [4]. The inductance of commercial Li-ion batteries was found to be independent of SoC [8] and temperature [3, 8]. The frequency at the intercept with the real axis was also reported to be independent of both SoC and aging of Li-ion batteries [17, 18]. Although it is known from literature that this frequency changes as a function of temperature [3] and is independent of SoC and aging, the relation between these has never been investigated in detail.

In this chapter, earlier work is extended [19], in which the concept of measuring battery temperature through the zero-intercept frequency (ZIF) was introduced. The ZIF is defined as the frequency at which the impedance in the complex plane intersects the real axis, *i.e.* where $Z_{im} = 0$. In other words, the ZIF is the frequency (f_0 [Hz]) or angular frequency ($\omega_0 = 2\pi f_0$ [rad s^{-1}]), at which the phase shift between voltage and current is zero. The ZIF can be measured in a straightforward manner by four-point impedance measurements. The advantage of measuring at relatively high frequencies is that these impedance measurements are less sensitive to variations in battery load currents. This is due to the fact that the ZIF is beyond the frequency range where the main electrochemical storage reactions of batteries take place.

4.2. Theoretical considerations

A schematic representation of a Li-ion battery is shown in Fig. 4.1a. Such a battery consists of two electrodes which are attached to a current collector (Cu and Al in case of Li-ion) and are separated by a separator which is impregnated by a Li-salt-containing electrolyte. It is generally considered that a Solid Electrolyte Interface (SEI) is formed at the surface of the negative electrode and a surface film at the positive electrode. All these layers contribute to the overall battery impedance. A comprehensive equivalent network model can be constructed, as shown in Fig. 4.1b, to simulate the overall impedance where L represents the inductances and R_s the ohmic series resistances of the connections, electrodes, electrolyte, and separator. The outer parallel capacitors and resistors represent the electrical double layer capacitance (C_{dl}), and the charge-transfer resistance (R_{ct}) of the positive and negative electrode, respectively. Two more RC-elements represent the impedance of the (SEI) surface layers. The individual capacitors (C_d) are added to model diffusion in both electrodes. This detailed circuit is rather complicated for an analytical analysis and is, therefore, reduced to the circuit shown in Fig. 4.1c. In this reduced circuit a single RC-chain is combined with an inductance, a series resistance, and a diffusion capacitance. This single RC-chain, comprising R_{kin} and C_{kin}, describes the combined charge-transfer kinetics, double-layer capacitances, and surface-layer behavior of both electrodes.

The impedance of the equivalent circuit shown in Fig. 4.1c can easily be derived from the impedances of the separate elements, according to

$$Z_R = R, \qquad Z_C = \frac{1}{j\omega C}, \qquad Z_L = j\omega L\ . \tag{4.1}$$

The total battery impedance (Z_{Bat}) is then given by

$$Z_{Bat} = j\omega L + R_s + \frac{R_{kin}}{1 + j\omega R_{kin} C_{kin}} + \frac{1}{j\omega C_d}\ . \tag{4.2}$$

The imaginary part of Eq. 4.2 is calculated as

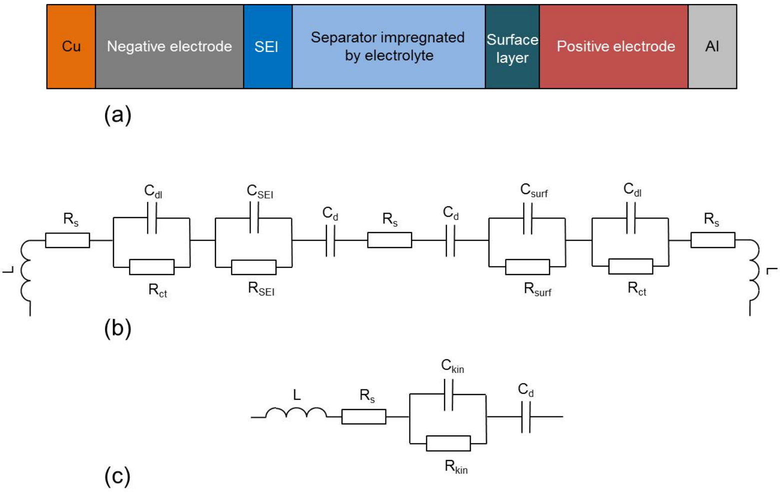

Fig. 4.1: Schematic representation of a Li-ion battery (a), comprehensive equivalent circuit (b), and simplified equivalent circuit (c).

$$Z_{im} = \omega L - \frac{(C_{kin} + C_d)\, C_{kin} R_{kin}^2 \omega^2 + 1}{C_d \omega \left(C_{kin}^2 R_{kin}^2 \omega^2 + 1\right)} \,. \tag{4.3}$$

The ZIF (ω_0) can be calculated by equating Eq. 4.3 to zero. This results in the following bi-quadratic equation

$$\begin{gathered} C_d L \omega_0^2 \left(C_{kin}^2 R_{kin}^2 \omega_0^2 + 1\right) - (C_{kin} + C_d)\, C_{kin} R_{kin}^2 \omega_0^2 - 1 = \\ C_{kin}^2 R_{kin}^2 C_d L \omega_0^4 + \left[C_d L - (C_{kin} + C_d)\, C_{kin} R_{kin}^2\right] \omega_0^2 - 1 = 0 \,. \end{gathered} \tag{4.4}$$

If the parameters of the lumped circuit take finite positive values, then Eq. 4.4, in general, has four (complex) roots. However, since the ZIF cannot be complex and must have a positive value, the only relevant solution of Eq. 4.4 has the following form

$$\omega_0 = \left(\left(\left[\frac{C_d L - (C_{kin} + C_d)\, C_{kin} R_{kin}^2}{2 L C_d C_{kin}^2 R_{kin}^2} \right]^2 + \frac{1}{L C_d C_{kin}^2 R_{kin}^2} \right)^{0.5} - \frac{C_d L - (C_{kin} + C_d)\, C_{kin} R_{kin}^2}{2 L C_d C_{kin}^2 R_{kin}^2} \right)^{0.5} . \tag{4.5}$$

Eq. 4.5 shows that ω_0 is a function of R_{kin}. The ZIF, $f_0 = \omega_0/(2\pi)$, is plotted as a function of R_{kin} in Fig. 4.2. f_0 reveals a sigmoid-shaped curve enclosed between two limiting lines. The lower and upper limit, which are shown as dashed lines in Fig. 4.2 are mathematically derived from Eq. 4.5 when R_{kin} approaches zero and infinity, respectively.

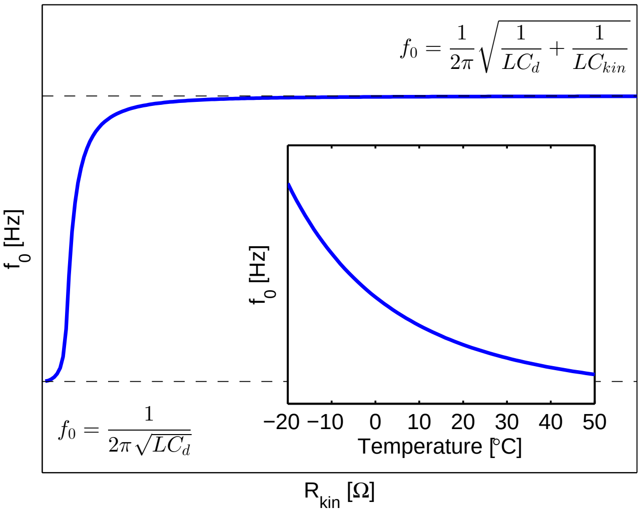

Fig. 4.2: Intercept frequency as a function of R_{kin} with the upper and lower limits (dashed lines) mathematically derived from Eq. 4.5. Inset: theoretical dependence of f_0 as a function of temperature. $C_d = 1$ F, $C_{kin} = 0.01$ F, $L = 7$ nH, $0 \leq R_{kin} \leq 0.02$ Ω, $A_p = 400,000$ Ω^{-1}, $E_a = 10$ kJ mol^{-1}, $R_g = 8.314$ J mol^{-1} K^{-1}, $253 \leq T \leq 323$ K.

It is generally accepted that R_{kin} reveals an Arrhenius behavior [10, 17], which can be given by

$$\frac{1}{R_{kin}} = A_p \exp\left(-\frac{E_a}{R_g T}\right) , \tag{4.6}$$

where A_p is the pre-exponential factor, E_a the activation energy, R_g the gas constant, and T is the absolute temperature. When R_{kin} is substituted in Eq. 4.5, an expression for f_0 is obtained as a function of temperature. The result is plotted in the inset of Fig. 4.2 and reveals that a decreasing ZIF is theoretically expected at higher temperatures. This makes the ZIF suitable for temperature indication of the battery. In the following Sections this theoretical statement will be checked experimentally and ready-to-use algorithms will be developed.

4.3. Experimental details

Three batteries have been investigated experimentally: a pristine high-power 2.3 Ah $LiFePO_4$ ANR26650 cylindrical battery (A123 Systems), pristine and cycled 7.5 Ah cylindrical ultra-high power $Li(NCA)O_2$ batteries (GAIA Akkumulatorenwerke GMBH). All batteries have graphite negative electrodes. All pristine batteries have been activated by (dis)charging these four times according to the specifications of the manufacturers. Charging and discharging is performed using Maccor automated cycling equipment (Model 4200). The impedances were measured in the galvanostatic mode with an Autolab PGSTAT30 (Metrohm Autolab) in the frequency range of 0.01 Hz - 30 kHz, using 50 frequencies logarithmically distributed. The current amplitude was set to 200 mA RMS. During all measurements the batteries were located in climate chambers (Maccor, model MTC-010). Measurements were conducted at -20, -10, +10, +30, and +50°C. Before conducting measurements at a predefined temperature, 3 hours of rest have been applied to reach thermal equilibrium. Five SoC values have been investigated, ranging from 100% to 20% in steps of 20%. The ZIF has been determined by interpolating the imaginary part of the impedance spectrum to $Z_{im} = 0$.

4.4. Results and discussion

Fig. 4.3 shows the impedance spectra of a pristine NCA battery at -10°C and varying SoC in the complex plane. The total impedance varies considerably with SoC, especially the large semicircle in the low-frequency region. On the other hand, the small semicircle and the inductive tail at higher frequencies show only a small dependence on SoC. This becomes more clear in Fig. 4.4, where the same impedance results are plotted in a Bode diagram. Since all phase lines cross 0 at the same frequency, it is evident that the ZIF is the same for all SoC.

Fig. 4.5 shows the impedance spectra of a pristine NCA battery at a SoC of

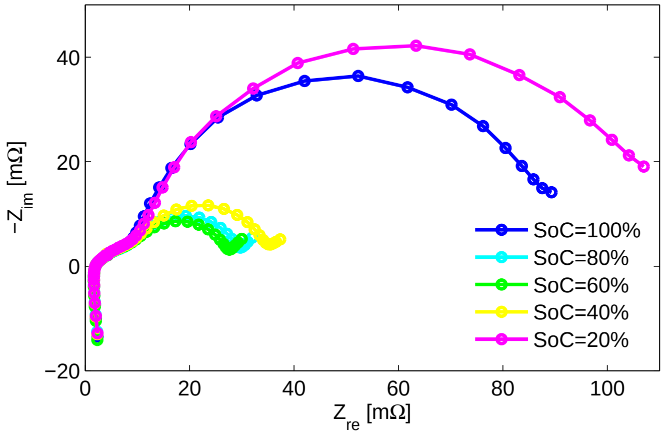

Fig. 4.3: Impedance spectra of a pristine NCA battery measured at -10°C and varying SoC.

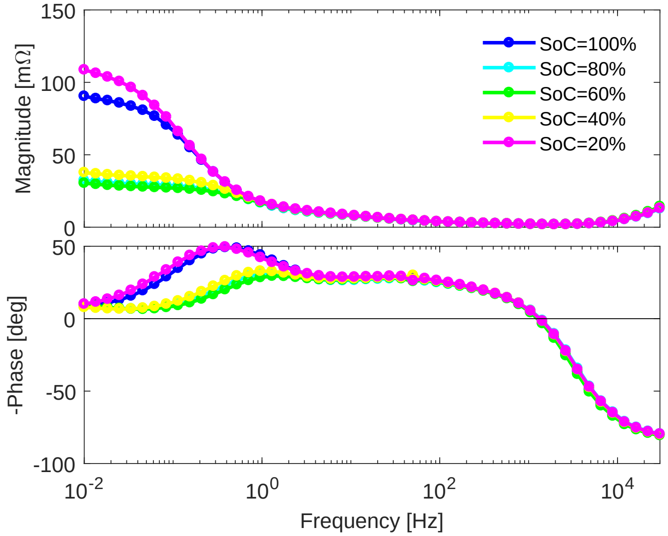

Fig. 4.4: Impedance results of Fig. 4.3 represented in a Bode plot.

60% and five different temperatures. As expected, the large semicircle increases significantly at lower temperatures. It can also be seen that the small semicircle exhibits a similar behavior as the large semicircle and that the whole impedance curve is shifted to the left as the temperature increases, indicating a decreasing ohmic resistance. Furthermore, it can be noticed that the inductive characteristics remain more or less constant. From the phase lines in the Bode plot of Fig. 4.6 it can be seen that the ZIF clearly changes as a function of temperature.

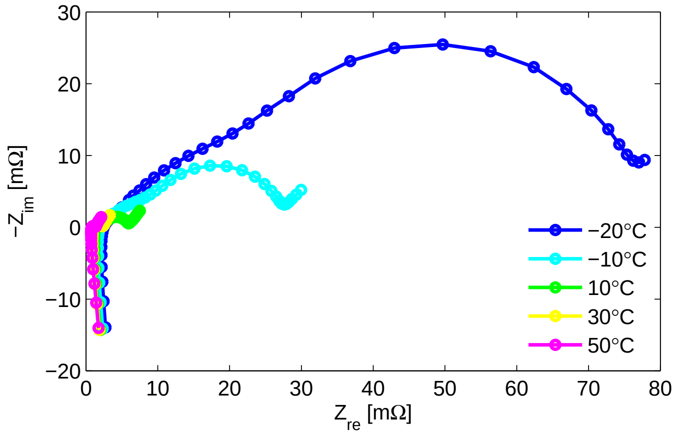

Fig. 4.5: Impedance spectra of a pristine NCA battery measured at 60% SoC for five different temperatures.

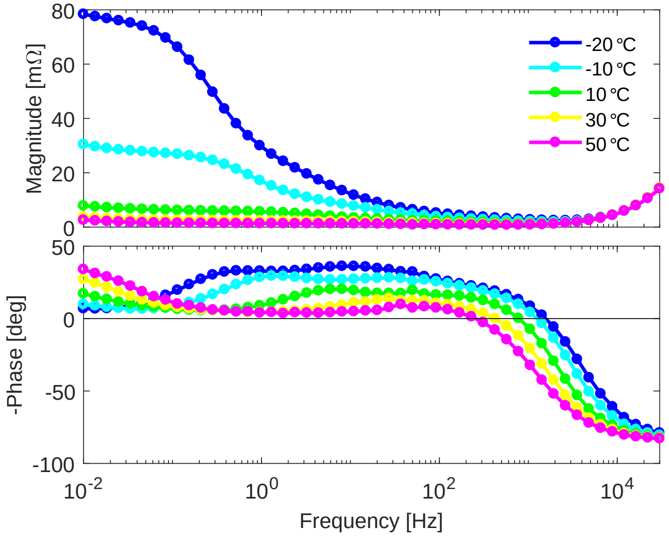

Fig. 4.6: Impedance results of Fig. 4.5 represented in a Bode plot.

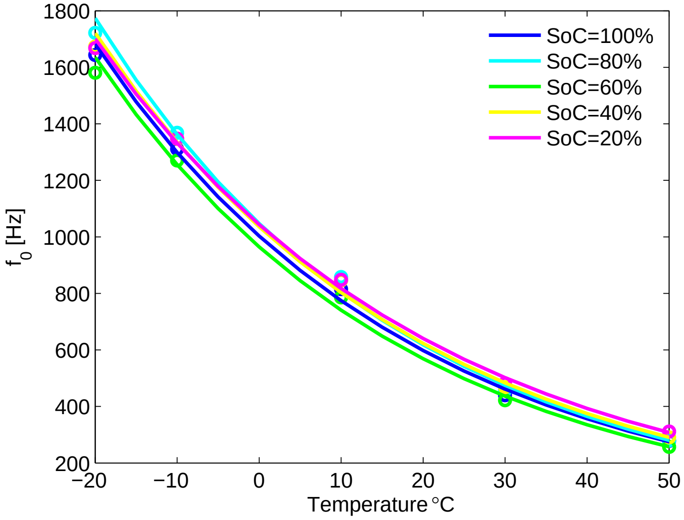

Fig. 4.7: Zero-intercept frequency as a function of temperature for a pristine NCA battery.

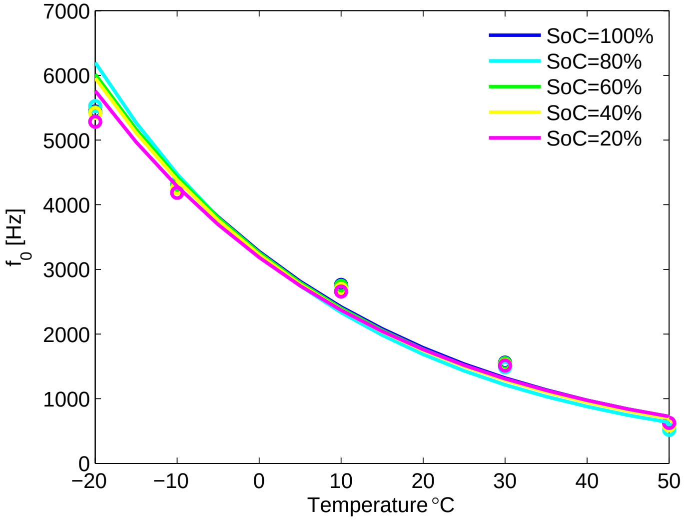

Fig. 4.8: Zero-intercept frequency as a function of temperature for a pristine $LiFePO_4$ battery.

It is evident that the ZIF decreases with increasing temperature. Plotting the ZIF as a function of temperature for a pristine NCA battery (Fig. 4.7) and $LiFePO_4$ battery (Fig. 4.8), an exponential behavior is found for both chemistries, which is essentially independent of SoC. These measurement results confirm the model described in

Section 4.2. The ZIF for the $LiFePO_4$ battery are, however, about five times larger than those of the NCA battery, as can be expected for different sizes and chemistries (see Eq. 4.5). From these results, it can be concluded that a similar ZIF dependence on the temperature is found to be independent of battery chemistry, dimension and storage capacity.

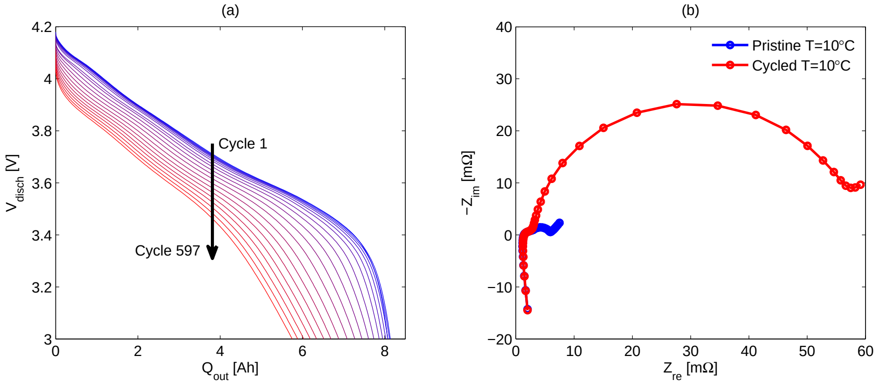

Fig. 4.9: Voltage discharge curves upon cycling an NCA battery (a), and impedance spectra of a pristine and cycled NCA battery at 60% SoC and 10°C.

An interesting question is how battery aging influences the ZIF. In order to investigate this, a 7.5 Ah NCA battery has been cycled for about 600 times. Some of the voltage discharge curves are shown in Fig. 4.9a. About 25% of the storage capacity is lost and the discharge overpotentials are significantly increased after 600 cycles, indicating a major impedance increase. Fig. 4.9b shows, as an example, the impedance of the pristine and cycled NCA battery at 10°C and 60% SoC. In line with the voltage discharge curves (Fig. 4.9a), it can be seen that the impedance of the cycled battery at low frequencies has dramatically increased. In this particular case, there is no significant increase in series resistance, *i.e.* increase in IR drop. According to Eq. 4.5 an increase in series resistance, however, should not influence the ZIF as a function of temperature, because it is not present in this equation and therefore has no influence on the temperature indication. The spectra at high frequencies did not change upon cycling, indicating that the ZIF is independent of aging. This conclusion is confirmed in Fig. 4.10, where the ZIF is plotted as a function of temperature for both the pristine and cycled battery. This figure proves that the ZIF did not change upon cycling.

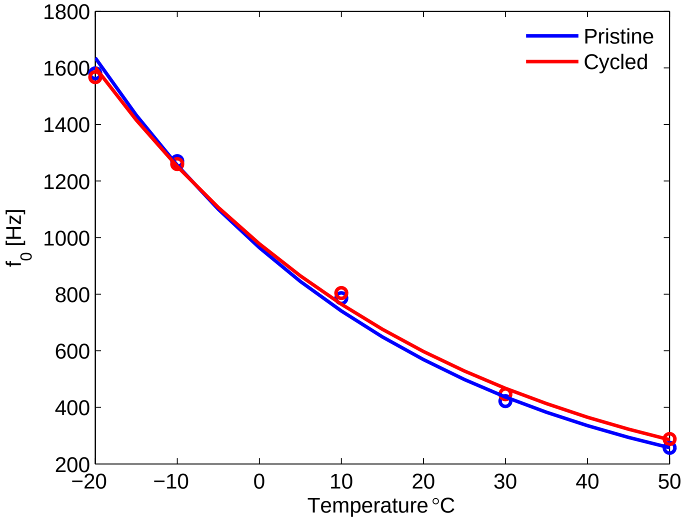

Fig. 4.10: Measured zero-intercept frequency as a function of temperature for a pristine and cycled NCA battery at 60% SoC.

4.5. Conclusions

The ZIF, *i.e.* the frequency at which the phase shift between voltage and current is zero, is extracted from impedance spectra of a Li(NCA)O_2 and a $LiFePO_4$ battery and related to the internal battery temperature. A theoretical analysis based on a simple equivalent electrical network model revealed that the ZIF is expected to decrease with increasing temperature. Experiments confirmed this finding and additionally showed that the ZIF does not depend on SoC. Measurements on a cycled NCA battery showed that the ZIF remains stable during cycling. Additional measurements were conducted on 60 Ah $LiFePO_4$ prismatic batteries. These measurements gave similar results to those of the NCA and $LiFePO_4$ batteries. The proposed temperature indication method is therefore readily applicable to batteries of different chemistries, dimensions and storage capacities. However, the presented measurement results are all measured under equilibrium conditions in the laboratory. Further investigations need to reveal if the proposed temperature indication method is also applicable in battery-powered applications outside the laboratory, such as hybrid- and full electric vehicles.

References

[1] L. H. J. Raijmakers, D. L. Danilov, J. P. M. Van Lammeren, M. J. G. Lammers, and P. H. L. Notten, *Sensorless battery temperature measurements based on electrochemical impedance spectroscopy,* J. Power Sources **247**, 539 (2014).

[2] M. Mohamedi, H. Ishikawa, and I. Uchida, *In situ analysis of high temperature characteristics of prismatic polymer lithium - ion batteries,* J. Appl. Electrochem. **34**, 1103 (2004).

[3] D. Andre, M. Meiler, K. Steiner, C. Wimmer, T. Soczka-Guth, and D. Sauer, *Characterization of high-power lithium-ion batteries by electrochemical impedance spectroscopy. I. Experimental investigation,* J. Power Sources **196**, 5334 (2011).

[4] J. Li, E. Murphy, J. Winnick, and P. A. Kohl, *Studies on the cycle life of commercial lithium ion batteries during rapid charge – discharge cycling,* J. Power Sources **102**, 294 (2001).

[5] M. Levi, K. Gamolsky, D. Aurbach, U. Heider, and R. Oesten, *On electrochemical impedance measurements of* $Li_xCo_{0.2}Ni_{0.8}O_2$ *and* Li_xNiO_2 *intercalation electrodes,* Electrochim. Acta **45**, 1781 (2000).

[6] S. Rodrigues, N. Munichandraiah, and A. K. Shukla, *AC impedance and state-of-charge analysis of a sealed lithium-ion rechargeable battery,* J. Solid State Electrochem. **3**, 397 (1999).

[7] T. Momma, M. Matsunaga, D. Mukoyama, and T. Osaka, *Ac impedance analysis of lithium ion battery under temperature control,* J. Power Sources **216**, 304 (2012).

[8] P. Suresh, A. Shukla, and N. Munichandraiah, *Temperature dependence studies of a.c. impedance of lithium-ion cells,* J. Appl. Electrochem. **32**, 267 (2002).

[9] S. S. Zhang, K. Xu, and T. R. Jow, *Electrochemical impedance study on the low temperature of Li-ion batteries,* Electrochim. Acta **49**, 1057 (2004).

[10] L. Liao, P. Zuo, Y. Ma, X. Chen, Y. An, Y. Gao, and G. Yin, *Effects of temperature on charge/discharge behaviors of* $LiFePO_4$ *cathode for Li-ion batteries,* Electrochim. Acta **60**, 269 (2012).

[11] X.-Y. Qiu, Q.-C. Zhuang, Q.-Q. Zhang, R. Cao, P.-Z. Ying, Y.-H. Qiang, and S.-G. Sun, *Electrochemical and electronic properties of* $LiCoO_2$ *cathode investigated by galvanostatic cycling and EIS,* Phys. Chem. Chem. Phys. **14**, 2617 (2012).

[12] J. Gomez, R. Nelson, E. E. Kalu, M. H. Weatherspoon, and J. P. Zheng, *Equivalent circuit model parameters of a high-power Li-ion battery: Thermal and state of charge effects,* J. Power Sources **196**, 4826 (2011).

[13] N. Hampson, S. Karunathilaka, and R. Leek, *The Impedance of Electrical Storage-Cells,* J. Appl. Electrochem. **10**, 3 (1980).

[14] F. C. Laman, M. W. Matsen, and J. A. R. Stiles, *Inductive Impedance of a Spirally Wound Li/Mos2 Cell,* J. Electrochem. Soc. **133**, 2441 (1986).

[15] J. Y. Song, H. H. Lee, Y. Y. Wang, and C. C. Wan, *Two- and three-electrode impedance spectroscopy of lithium-ion batteries,* J. Power Sources **111**, 255 (2002).

[16] B. Savova-Stoynov and Z. B. Stoynov, *Analysis of the inductance influence on the measured electrochemical impedance,* J. Appl. Electrochem. **17**, 1150 (1987).

[17] W. Waag, S. Käbitz, and D. U. Sauer, *Experimental investigation of the lithium-ion battery impedance characteristic at various conditions and aging states and its influence on the application,* Appl. Energy **102**, 885 (2013).

[18] Y. Zhang and C.-Y. Wang, *Cycle-Life Characterization of Automotive Lithium-Ion Batteries with* $LiNiO_2$ *Cathode,* J. Electrochem. Soc. **156**, A527 (2009).

[19] J. Van Lammeren, M. Lammers, L. Raijmakers, D. Danilov, and P. Notten, *Sensorless battery cell temperature measurement,* in *Fachtagung Kraftw. Batter.* (Aachen, 2013).

5

Non-zero-intercept frequency as temperature indication method

A new impedance-based approach is introduced in which the integral battery temperature is related to other frequencies than the zero-intercept frequency (ZIF). The advantage of the proposed non-zero-intercept frequency (NZIF) method is that measurement interference, resulting from the current flowing through the battery (pack), can be avoided at these frequencies. This gives a higher signal-to-noise ratio (SNR) and, consequently, more accurate temperature measurements. A theoretical analysis, using an equivalent circuit model of a Li-ion battery, shows that NZIFs are temperature dependent in a way similar to the ZIF and can therefore also be used as a battery temperature indicator. To validate the proposed method impedance measurements have been performed with individual $LiFePO_4$ *batteries and with large* $LiFePO_4$ *battery packs tested in a full electric vehicle under driving conditions. The measurement results show that the NZIF is clearly dependent on the integral battery temperature and reveals a similar behavior to that of the ZIF method. However, in contrast to the ZIF method, the NZIF method makes it possible to optimally adjust the measurement frequencies such that the highest SNR can be obtained and therefore accurate temperature measurements.*

Parts of this chapter have been published in IEEE Transactions on Industrial Electronics, **63**, (2016) 3168-3178 [1].

5.1. Introduction

In Chapter 4, a new method is introduced in which a zero-intercept frequency (ZIF) is used to determine the integral battery temperature [2]. This method is designed to determine the temperature under electronically non-disturbing conditions. In applications such as (H)EV, the electric motor and other components draw, however, large currents from the battery (pack) over a wide range of frequencies, which may overlap with the frequencies (ZIF) of interest. In order to avoid dominating interfering currents in an electronically disturbing environment, the ZIF method has been further developed by presenting a temperature measurement method which is based on a non-ZIF (NZIF). The NZIF is defined as the frequency at which the imaginary part of the battery impedance is equal to a non-zero constant, leading to higher or lower frequencies than the ZIF, *i.e.* in either the inductive or capacitive part of the impedance spectrum.

Moving from ZIF toward NZIF determination makes it possible to perform EIS measurements in a frequency range where the external interference is relatively low. This offers great potentials to increase the signal-to-noise ratio (SNR) and, consequently, to determine the temperature much more accurately. In this Chapter, the EIS measurement interference and the NZIF method are addressed in detail and supported by experimental data. To show the strength of the NZIF method, experiments are performed on both individual batteries under laboratory conditions and large battery packs, powering an EV under real driving conditions.

5.2. Theoretical considerations

Equivalent circuit models comprising inductive, resistive, and capacitive elements can be used to simulate the battery impedance [3–5]. A simple, but very convenient equivalent-circuit model for a theoretical analysis is shown in Fig. 4.1c (Section 4.2). Given this circuit, the total battery impedance (Eq. 4.2) and the ZIF (Eq. 4.5) can be derived, as shown in Section 4.2.

For the analytical analysis of the NZIF, Eq. 4.3 (Section 4.2) needs to be rearranged to an algebraic equation of degree 4 in terms of ω. This results in

$$\begin{aligned} C_d L \omega^2 \left(C_{kin}^2 R_{kin}^2 \omega^2 + 1\right) - \left(C_{kin} + C_d\right) C_{kin} R_{kin}^2 \omega^2 - 1 \\ - C_d \omega \left(C_{kin}^2 R_{kin}^2 \omega^2 + 1\right) Z_{im} = 0\ . \end{aligned} \tag{5.1}$$

From Eq. 5.1, it is convenient to define two functions ($\mathscr{h}\left(\omega\right)$ and $\mathscr{g}\left(\omega\right)$) as

$$\mathscr{h}(\omega) = LC_d\omega^2\left(C_{kin}^2R_{kin}^2\omega^2+1\right)-\left(C_{kin}+C_d\right)C_{kin}R_{kin}^2\omega^2-1 \tag{5.2}$$

and

$$\mathscr{g}(\omega) = C_d\omega\left(C_{kin}^2R_{kin}^2\omega^2+1\right)\ , \tag{5.3}$$

accordingly. Given Eqs. 5.2 and 5.3, an implicit function ($\mathcal{H}$) can be defined from Eq. 5.1 as

$$\mathcal{H}\left(\omega, Z_{im}\right) = \mathscr{h}(\omega) - Z_{im}\mathscr{g}(\omega)\ . \tag{5.4}$$

A first-order Maclaurin series approximation can be used to solve the (N)ZIF (ω) as a function of Z_{im}, according to

$$\omega\left(Z_{im}\right) \approx \omega_0 + \left.\frac{d\omega}{dZ_{im}}\right|_{Z_{im}=0} Z_{im}\ , \tag{5.5}$$

where ω_0 is the ZIF defined in Eq. 4.5. The derivative term at the right-hand side of Eq. 5.5 can be determined by differentiating the implicit function in Eq. 5.4, which finally yields [6]

$$\left.\frac{d\omega}{dZ_{im}}\right|_{Z_{im}=0} = \frac{\mathscr{g}(\omega_0)}{\mathscr{h}'\left(\omega_0\right)}\ , \tag{5.6}$$

where

$$\begin{aligned}\mathscr{h}'\left(\omega_0\right) = 2\omega_0LC_d\left(C_{kin}^2R_{kin}^2\omega_0^2+1\right)+2\omega_0^3LC_dC_{kin}^2R_{kin}^2 \\ -2\omega_0\left(C_{kin}+C_d\right)C_{kin}R_{kin}^2\ ,\end{aligned} \tag{5.7}$$

which is the derivative of Eq. 5.2 with respect to ω calculated at ω_0.

When the Arrhenius relationship from Eq. 4.6 is used and substituted for all R_{kin} in the above equations, Eq. 5.5 can be plotted as a function of temperature for various values of Z_{im}. A typical example of such a plot is shown in Fig. 5.1. Since this is only an example to show the NZIF behavior, the y-axis scale is not shown because f_{int} values are dependent on the battery type, where $f_{int} = \omega/(2\pi)$ is the intercept frequency for any value of Z_{im}. It can be seen that the ZIF (f_0) decreases with increasing temperature, which is in line with previous investigations (Chapter 4) [2]. Furthermore the $f_{0.2}$ curve, which is the NZIF calculated at $Z_{im} =$

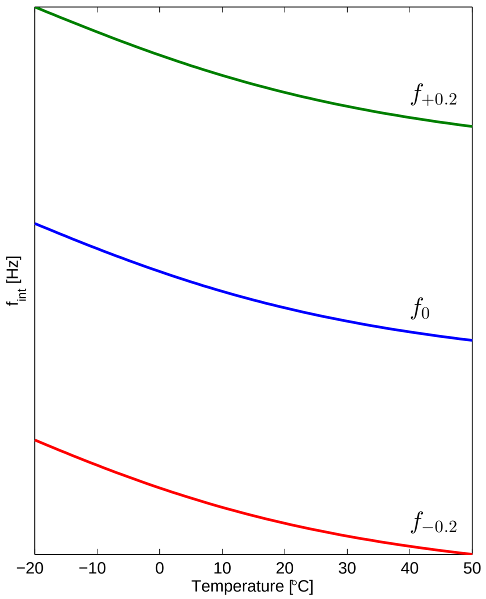

Fig. 5.1: Example of the (N)ZIF behavior as a function of temperature for Z_{im} values 0, +0.2 mΩ and -0.2 mΩ. $C_d = 1$ mF, $C_{kin} = 0.01$ F, $L = 7$ nH, $A_p = 400,000$ Ω^{-1}, $E_a = 10$ kJ mol^{-1}, $R_g = 8.314$ J mol^{-1} K^{-1}, $253 \leq T \leq 323$ K.

$+0.2$ mΩ, shows similar behavior, indicating that the NZIF can also be used as a battery temperature indicator. However, the frequencies for this line are distinctly higher than the frequencies for the ZIF. The $f_{-0.2}$ curve, which is the NZIF calculated at $Z_{im} = -0.2$ mΩ, also shows similar behavior, corresponding to lower frequencies. This theoretical analysis clearly shows that the frequency band, which is used for sensorless temperature indication, can be varied over a wide frequency range, when replacing the ZIF by the NZIF.

5.3. Experimental details

In order to investigate the (N)ZIF as a function of temperature, laboratory experiments have been conducted with prismatic 90 Ah LiFePO$_4$ (Thundersky TS-LFP90AHA) batteries. The impedance spectra were collected in the galvanostatic mode using printed-circuit boards (PCB) developed by NXP Semiconductors. A simplified circuit diagram of the PCB connected in parallel to a battery is shown in Fig. 5.2a. An alternating current is generated through the battery by opening and closing a switch (Fig. 5.2a) with a pulse-density-modulated (PDM) signal of a sine wave (Fig. 5.2b). The AC voltage response of the battery can then be measured through a low-pass filter in order to calculate the complex impedance.

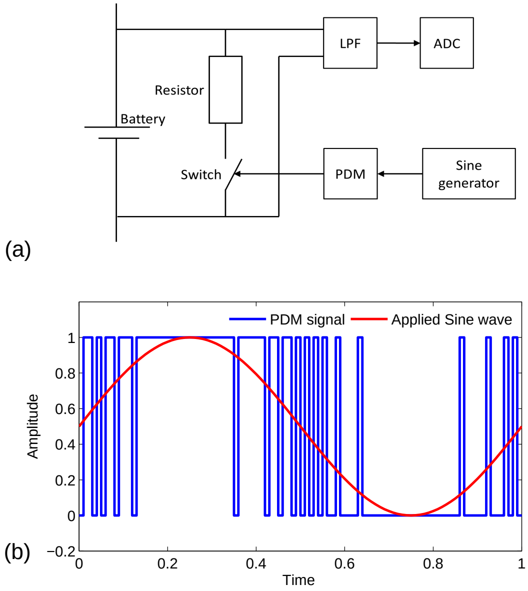

Fig. 5.2: Simplified measurement scheme of a printed-circuit-board assembled in parallel to a battery (a) and a schematic representation of a pulse-density-modulated (PDM) signal (blue line) of a sine wave (red line) (b).

The impedances were measured at twenty five logarithmically distributed frequencies in the range of 10 to 5000 Hz with a sine-wave current of 100 mA RMS. The ZIF and NZIF are determined by interpolating the imaginary part of the impedance to $Z_{im} = 0$ and $Z_{im} > 0$, respectively.

All battery impedance measurements were conducted at a constant temperature of -20, -10, +10, +30 and +50°C using climate chambers (Maccor MTC-010). The State-of-Charge (SoC) has been controlled in all experiments at 20, 40, 60, 80 and 100%. Before the impedance measurements were started the batteries were allowed to equilibrate for 4 hours at the various temperatures. Automatic cycling equipment (Maccor 4200) was used to (dis)charge the batteries.

In order to investigate the (N)ZIF in a full EV under driving conditions [7–9], the EIS spectra for three selected 90 Ah prismatic $LiFePO_4$ batteries were recorded during test drives on a public road. The installed batteries were identical to the individual batteries investigated under the temperature-controlled laboratory conditions described above. During the test drives impedances were measured at predetermined frequencies with a 1 s time interval. In addition to the impedance measurements the current flowing through the battery pack was measured simultaneously.

In order to more accurately analyze and quantify the interfering currents resulting from the electric components in the EV, the battery pack current was recorded at a much higher sampling rate (100 kHz) on a vehicle test bench (dynamometer). A current sensor with a current range of ± 500 A was used to record the pack current.

5.4. Results and discussion

5.4.1. ZIF for LiFePO$_4$ batteries

In Chapter 4, it is shown that the ZIF for small-size Li-ion batteries can be related to the integral battery temperature. Fig. 5.3 shows the ZIF (f_0) as a function of temperature for a large-capacity (90 Ah) LiFePO$_4$ battery measured under laboratory conditions. It can be concluded that f_0 decreases with increasing temperature and that this relationship is essentially independent of SoC, indicating that this specific battery characteristic is generic. Moreover, the measurements presented in Chapter 4 have shown that it also holds for both small and large-capacity Li-ion batteries and that it is aging independent. The only difference is that the present high-capacity LiFePO$_4$ batteries show significantly lower ZIF-values. This is shown in Fig. 5.4, where ZIF (f_0) measurements are plotted as a function of battery capacity. This figure illustrates that the ZIF is lower for high-capacity batteries than for low-capacity batteries.

5.4.2. EV measurement setup

An electric research vehicle has been used to measure the battery impedance and pack current under driving conditions [7–9]. The battery pack of this EV is composed of 91 prismatic LiFePO$_4$ batteries in series. A photograph of one of the three battery modules is shown in Fig. 5.5, which in this case consists of a series assembly of 28 batteries. Each battery is monitored by a conventional cell board (Elithion). These conventional cell boards (see Fig. 5.5a) are all connected to the Battery Management System (BMS) of the EV.

The designed PCBs to measure the impedance are rigidly connected to the terminals of three selected batteries, as indicated in the inset of Fig. 5.5. In order

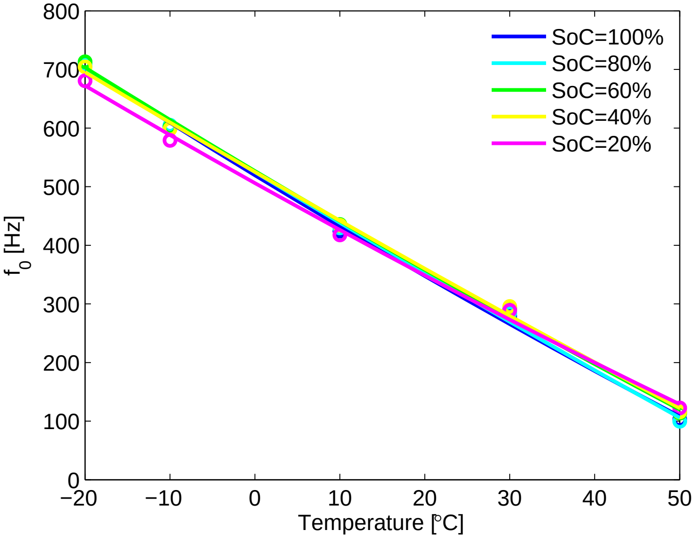

Fig. 5.3: ZIF (f_0) as a function of temperature for a prismatic 90 Ah $LiFePO_4$ battery at various SoC values.

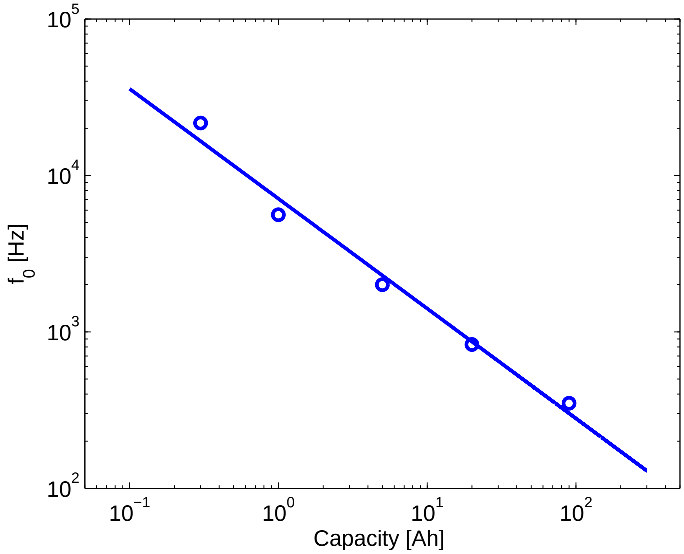

Fig. 5.4: ZIF (f_0) as a function of the battery storage capacity.

to accurately measure the impedance it is very important that the PCB is properly connected to the batteries and that a four-point measurement set-up is applied.

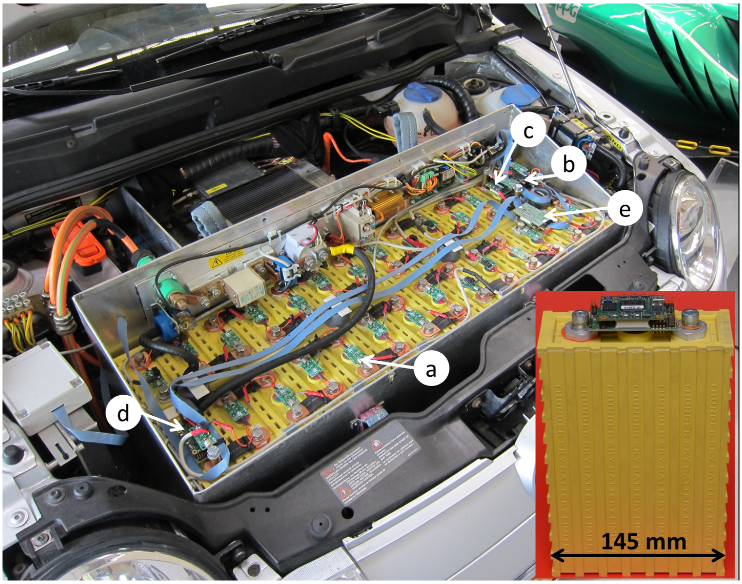

Fig. 5.5: One of the battery pack modules in the EV: example of a conventional monitoring cell board (a), *proof-of-concept* PCB measuring the impedance (b)-(d), and PCB measuring the total pack current across a shunt resistor (e). The inset shows a *proof-of-concept* PCB assembled on the terminals of a 90 Ah $LiFePO_4$ battery to measure the impedance characteristics.

The current flowing through the battery pack is measured by a similar PCB as used for the impedance measurements. This PCB measures the voltage across a shunt resistance of 100 μΩ (Fig. 5.5e). The shunt is connected in series with the battery pack.

5.4.3. ZIF measurements in EV

To demonstrate the concept of measuring the ZIF in a battery-powered application, the impedance is sequentially measured at 300 and 400 Hz with a time interval of 1 s during a test drive on a public road. Since the batteries in the EV were at a temperature of about 20°C during the test drive, it is expected according to Fig. 5.3, that the ZIF is between 300 and 400 Hz. Therefore, these two measurement frequencies were selected in this case. Fig. 5.6 shows the results obtained for a single battery in the battery pack for about 20 min. The pack current is shown in Fig. 5.6a, where a negative current refers to a discharge current upon driving and a positive current to regenerative braking, *i.e.* corresponding to the battery charging process. Fig. 5.6b shows the correspondingly measured imaginary parts of the impedance. The 300 Hz results (red symbols) generally generate negative imaginary values while the 400 Hz results (blue symbols) generally reveal positive imaginary values (note the minus sign in the y-axis label). However, obviously the results at both frequencies are highly scattered when the pack current is high. On the other hand, the impedance results show much less dispersion when the pack current is relatively low. The large spread in these impedance results cannot be attributed to temperature variations as the battery (pack) temperature hardly changes on this time scale, as confirmed by other measurements. These results therefore suggest that the pack current powering the EV significantly interferes with the impedance measurements.

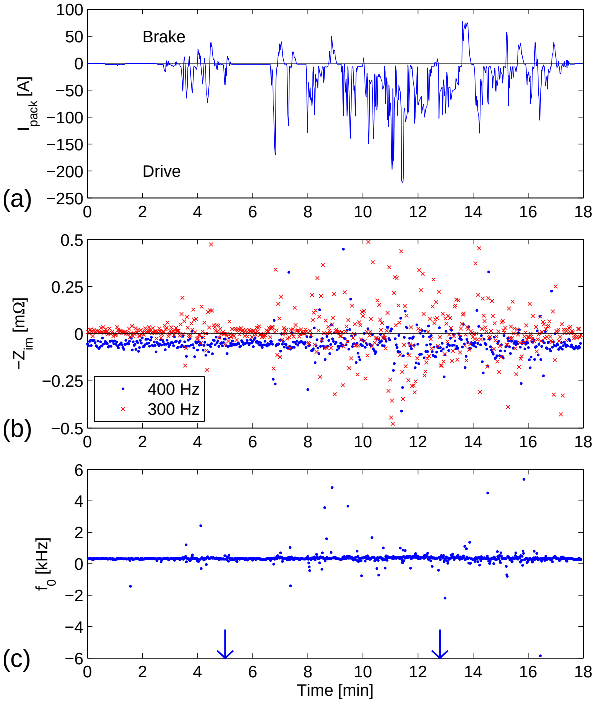

Fig. 5.6: Battery pack current (a), imaginary impedance at 300 Hz (red symbols) and 400 Hz (blue symbols) (b) and interpolated ZIF f_0-values (c) as a function of measurement time during an EV test drive. The two blue arrows indicate the presence of large outliers outside the graph with values (4.80 s, -8884 Hz) and (12.73 s, -23000 Hz).

The dispersion in impedance becomes even more apparent in Fig. 5.7, where the measured values are plotted in the complex plane. Occasionally, large outliers and even unrealistic negative values of the real part of the impedance can be found. The largest outliers are found at 300 Hz and are even outside the scale of the figure, as indicated by the arrow. The extremely deviating values are indicated in the caption of Fig. 5.7.

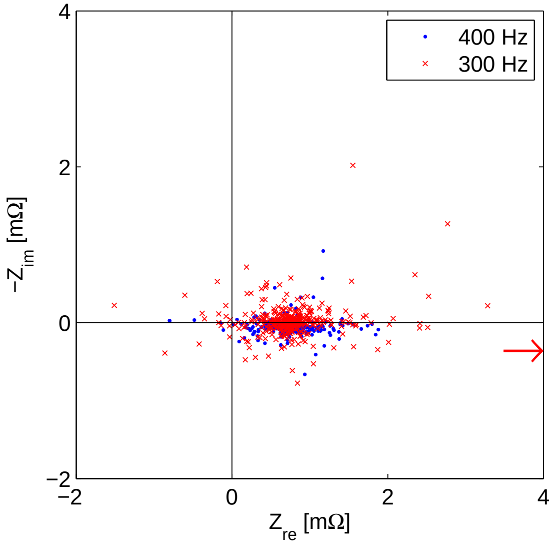

Fig. 5.7: Sequentially measured impedances at 300 Hz (red symbols) and 400 Hz (blue symbols) during a test drive. The red arrow indicates the presence of a 300 Hz outlier outside the graph at $Z_{re} = 7.80$ mΩ and $Z_{im} = 0.35$ mΩ.

The ZIF can be determined by interpolating the imaginary impedances at 300 and 400 Hz to $Z_{im} = 0$. The interpolated f_0-values are shown in Fig. 5.6c and also reveal quite some scatter and large outliers, even at unrealistic negative frequencies. Obviously, using these raw data will lead to inaccurate temperature measurements, unless sophisticated filtering techniques are applied. These results suggest that interference, generated by the electronics of the EV, introduces large errors in the measured impedance and, consequently, also in the ZIF. To investigate the interference source in more detail, the battery pack current in the EV has been investigated at a significantly higher sampling rate.

5.4.4. Battery pack current spectrogram

In order to identify and quantify the battery pack current interference in the EV, test-bench measurements have been performed under laboratory conditions. The tests, mimicking a driving situation, included three cycles of acceleration (to 50 km/h) and deceleration (regenerative braking). Fig. 5.8a shows a typical example of the resulting battery pack current profile measured for 2 min with a sampling frequency of 100 kHz. This sampling frequency is much higher than that reported for the test drive shown in Figs. 5.6 and 5.7. Negative and positive currents in Fig. 5.8a again refer to discharging (driving) and charging (braking), respectively. Discharge currents up to 200 A have been measured, which corresponds to a C-rate of approximately 2.2. The current levels shown in Fig. 5.8a are very similar to those shown in Fig. 5.6.

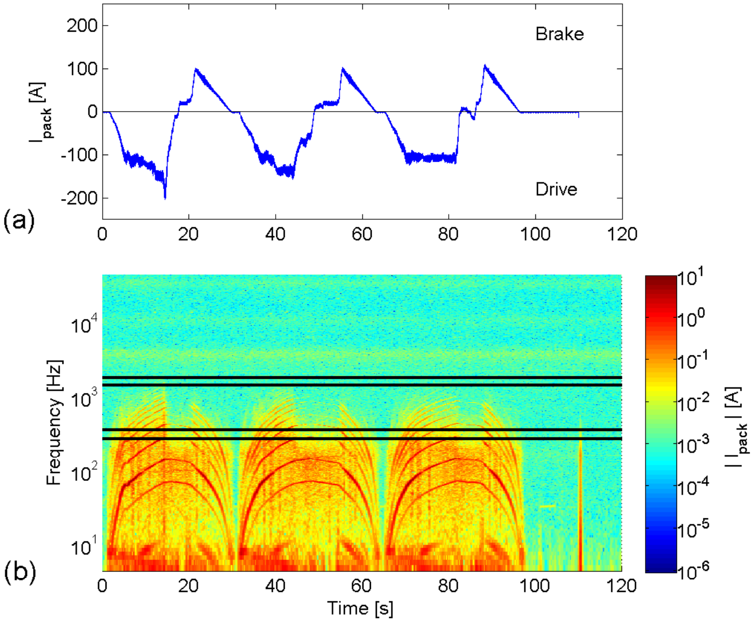

Fig. 5.8: Pack current as a function of measurement time for three accelerating to 50 km/h and regenerative braking cycles of the EV on a test bench (a), pack current spectrogram (b). The paired horizontal lines in (b) indicate the measurement frequencies during the road tests at 300 Hz, 400 Hz, 1600 Hz and 2000 Hz. The colors indicate the amplitude of the current.

A spectrogram was calculated based on these current measurements by taking a Fast Fourier Transform (FFT) with a moving window of 1 s (10^5 samples) and an overlap of 75% (0.75 s). Since the measured data are not periodic, a Hanning window has been used. The spectrogram of Fig. 5.8b shows the current (indicated by colors) flowing through the battery pack as a function of time and frequency. Note that the time axis of Fig. 5.8a and Fig. 5.8b are the same. Obviously, when current starts to flow the current amplitude increases rapidly across a frequency range from 5 Hz up to 1 kHz. Beyond 1 kHz no significant increase is visible. The red semicircles found in Fig. 5.8b represent the electric motor speed, the lowest semicircle is the base frequency and the upper ones are the corresponding harmonics. The spec-

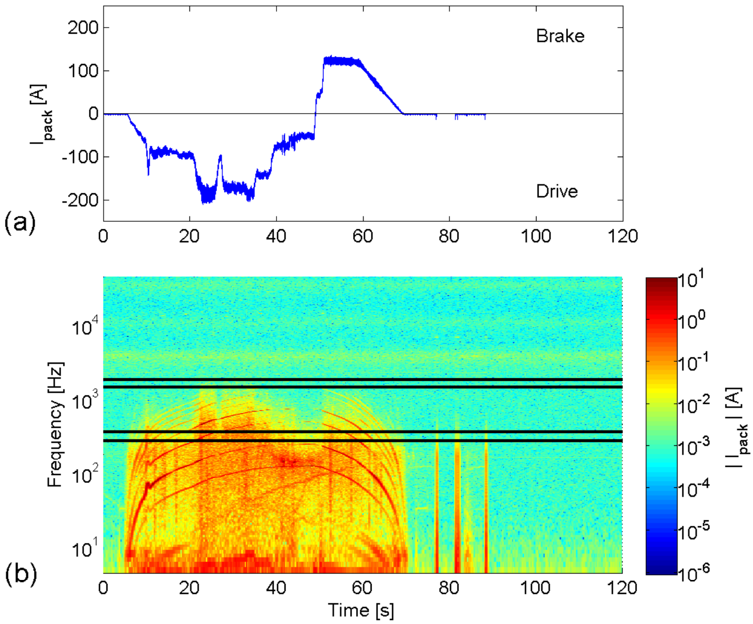

Fig. 5.9: Pack current as a function of measurement time for accelerating to 100 km/h with subsequent regenerative braking of the EV on a test bench (a), pack current spectrogram (b). The paired horizontal lines in (b) indicate the measurement frequencies during the road tests at 300 Hz, 400 Hz, 1600 Hz and 2000 Hz. The colors indicate the amplitude of the current.

trogram shows very similar behavior for acceleration and deceleration, resulting in the characteristic symmetric semi-circles.

Additional measurements without regenerative braking have also been performed. These measurements revealed that the current levels in the low frequencies ($f < 10$ Hz) are lower compared to those found with regenerative braking. At 110 s the power to the electric system of the car has been disconnected which causes a relatively high current for a short period of time up to a frequency of 400 Hz. This event is also visible in the small peak current in Fig. 5.8a. After this moment the current is zero.

In addition to the measurement shown in Fig. 5.8, a similar test-bench run has been performed by accelerating the EV to a speed of 100 km/h with subsequent regenerative braking to standstill. The corresponding pack current is shown in Fig. 5.9a. In this test-bench run the speed is twice as large and the pack current reaches somewhat higher values than in the previous run. In Fig. 5.9b, the calculated spectrogram of the pack current is shown. In this spectrogram one characteristic semicircle is visible during accelerating and decelerating the EV. Despite the high motor speed and current, the amplitude of the pack current does not increase significantly beyond a frequency of 1 kHz. Around 80 s the power to the electric system of the EV was disconnected for 4.5 s and subsequently reconnected again. At 88 s the power has been disconnected permanently. These events are causing three peaks in current amplitude up to 400 Hz, which are clearly visible in Fig. 5.9b.

From the results shown in the spectrograms of Figs. 5.8 and 5.9, it can be concluded that the current extracted from or supplied to the battery pack in an EV is highly dynamic over a wide frequency range, which is caused by both the accelerating and regenerative braking processes. In order to visualize this in more detail, a current spectrum has been taken from Fig. 5.8 in the time interval between 14 and 15 s. The resulting Fig. 5.10 shows that the current decreases about two orders of magnitude between 100 Hz and 1 KHz. The average current hardly changes anymore at frequencies beyond 1 kHz.

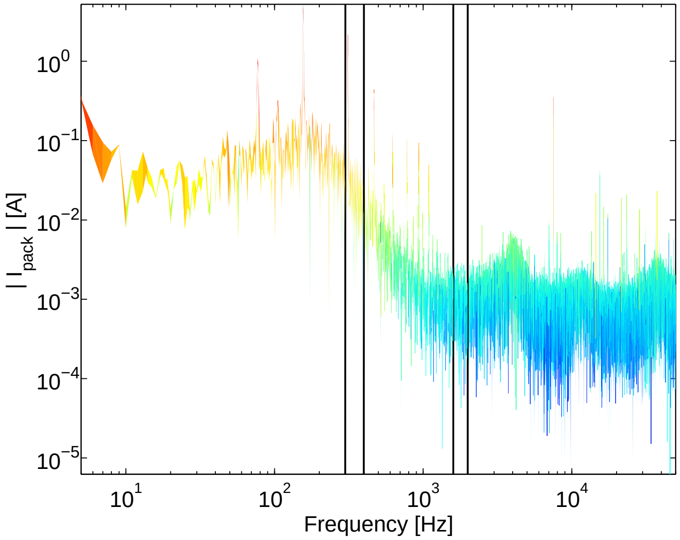

Fig. 5.10: Pack current as a function of frequency taken from the spectrogram shown in Fig. 5.8 between 14 and 15 s. The paired vertical lines indicate the measurement frequencies during the road tests: (300 Hz, 400 Hz, 1600 Hz and 2000 Hz).

The EIS measurements presented in Fig. 5.6 and Fig. 5.7 were taken at 300 and 400 Hz. These frequencies are indicated by two paired horizontal (black) and vertical lines in the spectrogram in Fig. 5.8b and Fig. 5.10, respectively. From these figures it can be concluded that relatively high currents, of the order of 10 mA, are present at these two frequencies, as dictated by the driving process of the EV. If, for example, a 100 mA EIS-excitation signal is applied for the impedance measurements, this 10 mA current will give rise to considerable interference, resulting in the poor SNR found in Fig. 5.6. It is therefore to be expected that much more accurate impedance results can be obtained in a frequency range where the current interference is relatively small. Considering Figs. 5.8b and 5.9b, selecting 1600 and 2000 Hz (see horizontal lines) as measurement frequencies is therefore expected to be much more favorable. The current spectrum of Fig. 5.10 indeed reveals that the interfering current is only about 1 mA under these frequency measurement conditions, which is one order of magnitude lower in comparison to the lower frequency measurements. Fig. 5.9b shows that selecting a set of frequencies lower than 1600 Hz would not result in a complete interference-free region. Therefore, 1600 Hz is the minimum frequency to select in this particular application. At the high frequencies the impedance shows a straight line in the inductive area in the Nyquist plot, which is advantageous for linear interpolation to the NZIF. Therefore, the newly selected frequency window can be larger, *i.e.* 1600-2000 Hz, in comparison to the previous one, which was only 300-400 Hz.

Obviously, measuring the impedance characteristics at higher frequencies will not lead anymore to the ZIF where the imaginary part of the impedance is per definition zero. Therefore, the NZIF method is introduced in this contribution.

5.4.5. NZIF measurements

Fig. 5.11 shows the temperature dependence of the (N)ZIF of a 90 Ah $LiFePO_4$ battery measured in various frequency ranges. The temperature of individual batteries has been accurately controlled. For comparison the f_0 (dark blue) curve, representing the ZIF interpolated at $Z_{im} = 0$, is also included in Fig. 5.11. The NZIF, interpolated at other values (i) of the imaginary part of the impedance, is denoted by f_i. For example, $Z_{im} = 0.2\ \text{m}\Omega$ refers to $f_{0.2}$ (light blue curve) and $Z_{im} = 0.8\ \text{m}\Omega$ to $f_{0.8}$ (magenta curve in Fig. 5.11). Every line shows the average of five different SoC-values. It can be seen that higher interpolation values lead to higher intercept frequencies, as already expected from the theoretical analysis in Section 5.2. The temperature dependencies of all NZIFs are very similar to that of the ZIF method. From this experimental verification, it can be concluded that in case of significant interfering signals, the NZIF method is an excellent alternative to determine battery temperatures at less noisy frequencies.

In line with the investigations presented in Chapter 4, additional EIS measurements have also been conducted with Cobalt-based Li-ion batteries. The (N)ZIF results gave similar dependencies as found with the $LiFePO_4$ system. Other EIS measurements confirmed that this also holds for batteries with smaller storage capacities and for aged batteries.

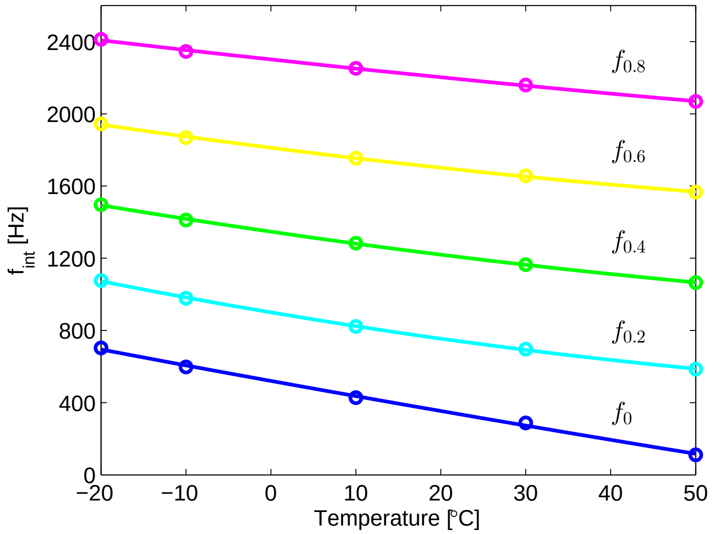

Fig. 5.11: ZIF (f_0) and NZIF (f_i) for a prismatic 90 Ah $LiFePO_4$ battery as a function of temperature.

5.4.6. NZIF measurements in EV

In order to investigate the accuracy of the proposed NZIF-method under real driving conditions, another test drive has been performed on a public road at the preselected optimal frequencies of 1600 and 2000 Hz. The measurements at these two frequencies have been performed in alternating intervals of 1 s. The results are shown in Figs. 5.12 and 5.13. Fig. 5.12a shows that the dynamics in current are of the same order of magnitude as shown in Fig. 5.6a, which indicates that both measurements are comparable. Fig. 5.12b shows that the pack current hardly has an influence on the imaginary values of the impedance. The results are now much more stable and all values measured at 1600 Hz are lower than 0.65 mΩ and at 2000 Hz, the values are all higher than 0.65 mΩ (note the minus sign in the y-axis label). Furthermore no outliers can be detected. This is also demonstrated in Fig. 5.13, where the impedance is plotted in the complex plane. The results indeed show far less spread in real and imaginary part in comparison to the results presented in Fig. 5.7. No negative real impedances and large outliers can be detected, essentially indicating that the interfering currents do not influence these NZIF measurements.

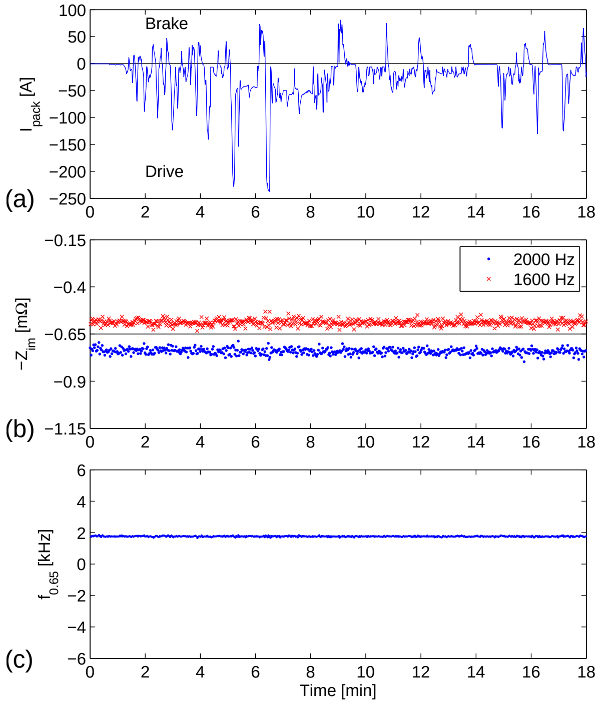

Fig. 5.12: Battery pack current (a), imaginary impedance at 1600 Hz (red symbols) and 2000 Hz (blue symbols) (b), and interpolated NZIF $f_{0.65}$-values (c) as a function of measurement time during an EV test drive.

The NZIF has been determined by interpolating the imaginary values of the impedance between both frequencies to $Z_{im} = 0.65$ mΩ. Fig. 5.12c shows these interpolated NZIF ($f_{0.65}$) results. These results clearly indicate that the NZIF-method generates far more stable and, hence, accurate results and does not show any outliers. From these results, it can be concluded that it is indeed useful to perform EIS measurements at frequencies where the battery pack current amplitudes and, consequently, the interference is relatively low. As a result, the SNR will become higher and the temperature estimation more accurate. Obviously, the accuracy of the final temperature indication is also dependent on the signal processing of the raw data, the measurement device accuracy, and the magnitude of the battery impedance. Without any additional signal processing, a 30-times improvement has been achieved in terms of standard deviation by adopting the NZIF method instead of the ZIF method in this particular application.

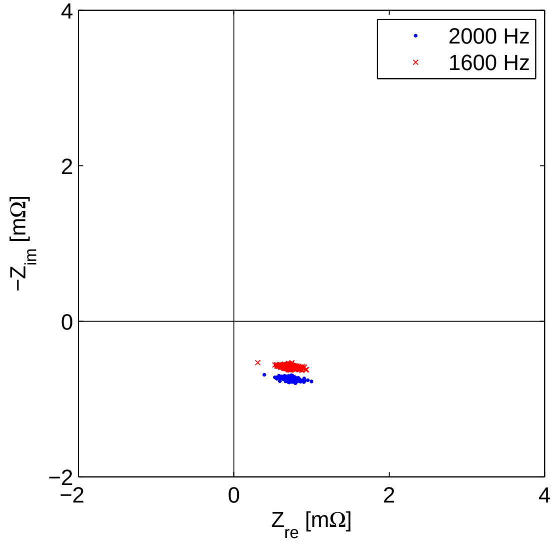

Fig. 5.13: Sequentially measured impedances at 1600 Hz (red symbols) and 2000 Hz (blue symbols) during a test drive.

5.4.7. NZIF measurements in EV under dynamic temperature conditions

In Sections 5.4.3 and 5.4.6, measurement results of the ZIF and NZIF are shown and discussed from test drives with an EV on a public road. Due to the relatively short test periods in which the battery temperature is more or less constant, these results are very well suited to investigate the differences between the ZIF and NZIF. In order to see changes in battery temperature, another test drive was performed of which the duration was 5.5 times longer in comparison to the test drives shown in Figs. 5.6 and 5.12. For a fair comparison, the y-axes in Fig. 5.14 are the same as in Fig. 5.12. In the test drive shown in Fig. 5.14, the same set of optimal frequencies (1600 Hz and 2000 Hz) were used since it was concluded favorably that these are promising for an accurate temperature indication, in contrast to the 300 Hz and 400 Hz frequencies.

In Fig. 5.14a, the drive current is plotted as a function of measurement time. Negative and positive currents represent driving and braking, respectively. At time $t = 0$ driving was started from the garage in which the EV was parked. After approximately 60 min, the EV was parked back in the garage for 6 min. Subsequently, the EV went back on the road again for 20 min of driving. At $t \approx 90$ min, the EV was connected to a power plug in the garage in order to charge the battery pack

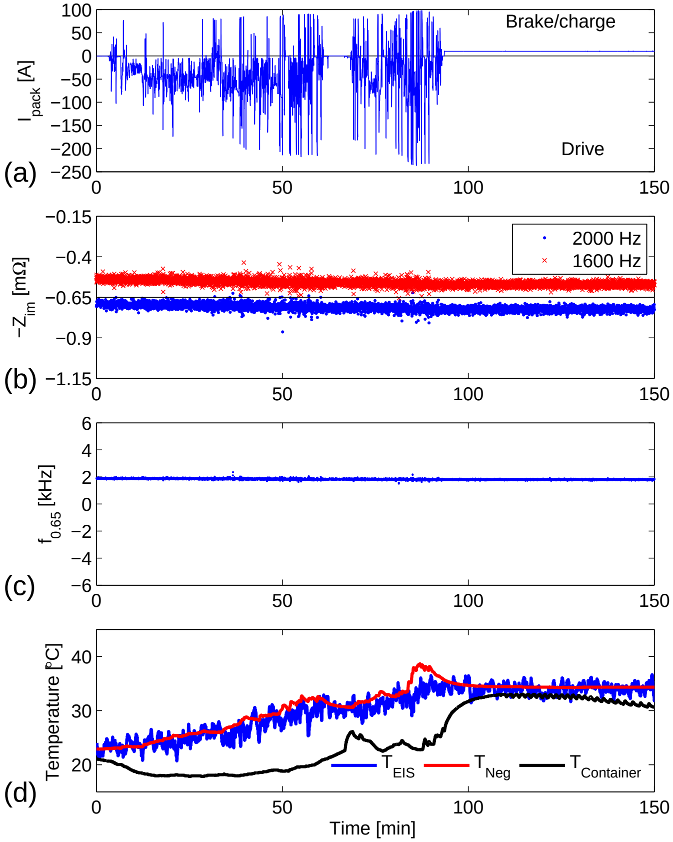

Fig. 5.14: Battery pack current (a), imaginary impedance at 1600 Hz (red symbols) and 2000 Hz (blue symbols) (b), interpolated NZIF $f_{0.65}$-values (c), and temperature (d) as a function of measurement time during an EV test drive.

with a current of 10 A (0.1 C-rate). Fig. 5.14b shows the imaginary impedances measured at 1600 Hz and 2000 Hz. The NZIF, shown in Fig. 5.14c, is interpolated at $Z_{im} = 0.65$ mΩ. As expected, the imaginary impedances and NZIF measurement results are stable and not showing large outliers, in spite of the highly dynamic pack current (Fig. 5.14a) generated by the electric components of the EV.

Fig. 5.14d shows the temperature developments as a function of driving time: (i) the impedance-based temperature (T_{EIS}), which is calculated from $f_{0.65}$, (ii) the temperature on the negative terminal of the battery (T_{Neg}), and (iii) the temperature at the bottom surface of the aluminum container in which the battery pack is assembled ($T_{Container}$). The two latter temperatures were measured by TSP-TH NTC thermistors from Thorlabs. The temperature of all components at $t = 0$ is about 22°C. This is the ambient temperature in the garage where the vehicle was parked. After starting driving, T_{EIS} and T_{Neg} increase due to the heat generated inside the batteries. However, the container temperature decreases since the outdoor temperature was 6°C lower than in the garage. After about 60 min of driving, the container temperature quickly increases because the EV was parked back in the garage for 6 min. After this resting period, the drive was continued. At approximately 90 min, the EV was parked back in the garage. This increased the container temperature rapidly to a level similar to T_{EIS} and T_{Neg}. After parking the EV, no considerable changes in temperature evolution can be seen anymore. That means that the 10 A charge current does not further increase the battery temperature.

It can be concluded that T_{EIS} follows the development of T_{Neg} closely in this experiment. Due to the low average current (0.3 C) and the large thermal mass of the battery pack, the temperature increases slowly and therefore temperature gradients in the battery core are expected to be relatively small. Generally, the integral battery temperature T_{EIS} is somewhat lower than T_{Neg}, which is measured locally at the negative battery terminal. The reason for a lower T_{EIS} is that the relatively cold container cools down the bottom of the battery pack. This cannot be detected by a temperature sensor at the top of the pack where the negative terminal is located. That also explains the local peak in T_{Neg} at 85 min, corresponding to driving with a large current. More heat is developed at the terminals since the current density there is relatively high. Obviously, the final temperature indication is dependent on the post processing of the measurement data. A standard deviation of $\pm$ 1°C in the final indicated temperature has been achieved by using a simple moving average filter with a window length of 36 samples.

5.5. Conclusions

It has been found that the zero-intercept frequency (ZIF) can be considerably influenced by interfering currents flowing through the battery pack under operating conditions of, for example, an electric vehicle (EV). This can make temperature determination based on the proposed ZIF-method inaccurate. The interfering currents may disturb the impedance measurements in such a way that it is complicated to apply the interpolated ZIF-method for temperature determination without sophisticated filtering of the measurement data.

Based on the experiments performed with an EV, it has been concluded that the battery pack current, at frequencies beyond 1 kHz, are about two orders of magnitude smaller than at lower frequencies. This observation opened the way to propose the modified non-zero-intercept frequency (NZIF) method to measure the impedance with significantly higher signal-to-noise ratios. The NZIF-method shows a much more accurate temperature dependence in this application in comparison to the ZIF-method and is therefore a more reliable temperature indication method. Moreover, dependent on the electronic application and conditions, the NZIF-method can be adapted to an optimal frequency range where the battery pack current is low and hence improving the SNR.

Mathematical modeling and experiments with 90 Ah $LiFePO_4$ batteries revealed that the NZIF show similar behavior in comparison to the ZIF as a function of temperature. The proposed NZIF method is therefore very suitable to measure the battery temperature under operating conditions in various electronic applications.

References

[1] L. Raijmakers, D. Danilov, J. van Lammeren, T. Lammers, H. J. Bergveld, and P. Notten, *Non-Zero Intercept Frequency: An Accurate Method to Determine the Integral Temperature of Li-ion Batteries,* IEEE Trans. Ind. Electron. **63**, 3168 (2016).

[2] L. H. J. Raijmakers, D. L. Danilov, J. P. M. Van Lammeren, M. J. G. Lammers, and P. H. L. Notten, *Sensorless battery temperature measurements based on electrochemical impedance spectroscopy,* J. Power Sources **247**, 539 (2014).

[3] M. Petzl and M. a. Danzer, *Advancements in OCV measurement and analysis for lithium-ion batteries,* IEEE Trans. Energy Convers. **28**, 675 (2013).

[4] L. R. Chen, S. L. Wu, D. T. Shieh, and T. R. Chen, *Sinusoidal-ripple-current charging strategy and optimal charging frequency study for Li-ion batteries,* IEEE Trans. Ind. Electron. **60**, 88 (2013).

[5] L. R. Chen, J. J. Chen, C. M. Ho, S. L. Wu, and D. T. Shieh, *Improvement of li-ion battery discharging performance by pulse and sinusoidal current strategies,* IEEE Trans. Ind. Electron. **60**, 5620 (2013).

[6] L. D. Kudryavtsev, *Implicit function,* in *Encycl. Math.*, edited by M. Hazewinkel (Springer, 2001) Chap. Implicit f.

[7] I. J. M. Besselink, P. F. van Oorschot, E. Meinders, and H. Nijmeijer, *Design of an efficient, low weight battery electric vehicle based on a VW Lupo 3L,* in *EVS25* (Shenzhen, China, 2010).

[8] I. J. M. Besselink, J. Wang, and H. Nijmeijer, *Evaluating the TU/e Lupo EL BEV performance,* in *EVS27* (Barcelona, Spain, 2013) pp. 1–12.

[9] P. F. V. Oorschot, I. J. M. Besselink, E. Meinders, and H. Nijmeijer, *Realization and control of the Lupo EL electric vehicle,* in *EVS26* (Los Angeles USA, 2012) pp. 1–10.

6

Crosstalk interference

In order to provide the required power and energy for e.g. automotive applications, a multitude of batteries is assembled into battery packs. For safety and control purposes it is of interest to equip every single battery with an Electrochemical Impedance Spectroscopy (EIS) measurement system. However, performing EIS measurements simultaneously on each battery in a pack at the same frequency introduces crosstalk interference in the surrounding batteries. This causes EIS measurements in battery packs to be inaccurate. Experimental investigations on battery packs showed that crosstalk is a linear phenomenon which is dependent on the measurement frequency, the relative position of the batteries and the inter-battery spacings. However, crosstalk is independent of battery temperature and state of charge (SoC). Furthermore, it has been shown that the (non-)zero-intercept frequency (N)ZIF is clearly dependent on crosstalk interference. Based on the experimental results and a proposed two-coil model with inductive coupling, a transfer-function description has been developed in order to accurately simulate crosstalk behavior. This model can be used as a supporting tool in the development of EIS-based measurement systems in battery packs.

Parts of this chapter have been published in IFAC-PapersOnline, **49**, (2016) 042-047 [1].

6.1. Introduction

In Chapter 5, it has been explained that currents flowing through a battery pack can considerably influence ZIF measurements. Subsequently, it has been shown that NZIF measurements can be applied as an elegant alternative. However, in battery-powered applications in which multiple batteries inside a pack are simultaneously monitored through the impedance, another disturbing phenomenon occurs, which is called crosstalk. This Chapter demonstrates that crosstalk causes considerable interference when performing EIS measurements on batteries within a pack. When not properly dealt with, crosstalk yields inaccurate EIS measurements, leading to inaccurate predictions of SoC, SoH and temperature (*e.g.* through the (N)ZIF). After the demonstration of crosstalk between batteries in a pack, a parameter variation study was performed to determine the dominant parameters influencing crosstalk. For instance, the magnitude of the EIS current excitation, the location of the batteries, and the distance between the batteries was varied. The crosstalk dependence on temperature and SoC was also investigated. In addition, (N)ZIF values were obtained with and without crosstalk interference.

The parameter study allowed to develop a crosstalk model on complete battery packs in the form of a transfer-function matrix. The model and measurements gave in-depth insight into crosstalk interference in battery packs, which can be used to prevent or compensate crosstalk, enabling accurate EIS measurements in battery packs.

6.2. Theoretical considerations

In this Section, the importance of analyzing crosstalk interference in battery packs is discussed. For automotive applications, multiple batteries are typically assembled into a battery pack in order to obtain the required voltages and currents to drive the vehicle. For analyzing crosstalk interference in a battery pack, an impedance transfer-function matrix $Z(s)$ is considered, satisfying

$$\begin{bmatrix} V_1(s) \\ \vdots \\ V_n(s) \end{bmatrix} = \underbrace{\begin{bmatrix} Z_{11}(s) & \dots & Z_{1n}(s) \\ \vdots & & \vdots \\ Z_{n1}(s) & \dots & Z_{nn}(s) \end{bmatrix}}_{=Z(s)} \begin{bmatrix} I_1(s) \\ \vdots \\ I_n(s) \end{bmatrix}, \tag{6.1}$$

where $V_i(s)$ and $I_i(s)$ are the output voltages and input currents, respectively, of battery i and Z_{il} are the transfer functions from battery l to battery i. Furthermore, the Laplace transform variable is given by $s = \sigma + j\omega$, where σ is the real part, ω the imaginary part, and j the imaginary operator satisfying $j^2 = -1$. For $\sigma = 0$ and excitation frequency $\omega = 2\pi f$, the impedances in matrix $Z(s)$ can be interpreted as frequency response functions from (sinusoidal) current input to (sinusoidal) voltage output, which can be experimentally obtained by performing EIS measurements [2, 3]. The diagonal terms in $Z(s)$ represent the battery impedances and the off-diagonal terms the crosstalk impedances from battery to battery.

For a pack that contains two adjacent batteries, a block diagram with corresponding transfer-function matrix elements is shown in Fig. 6.1. To determine $Z_{11}(s)$ and $Z_{22}(s)$, sinusoidal perturbation currents $I_1(s)$ and $I_2(s)$ are applied, respectively, and sinusoidal voltages $V_1(s)$ and $V_2(s)$ are measured. However, since $I_1(s)$ is coupled to $V_2(s)$ through $Z_{21}(s)$, and $I_2(s)$ to $V_1(s)$ through $Z_{12}(s)$, the measured voltages $V_1(s)$ and $V_2(s)$ are influenced. This leads to undesired crosstalk interference and consequently incorrect EIS measurements. From Fig. 6.1, it can therefore be derived that when two adjacent batteries are perturbed with a current of the same frequency $f = \omega/(2\pi)$ simultaneously, an offset appears in the measured impedance, when compared to the impedance of each separate battery. This offset is caused by the fact that the 'obtained impedance' from $I_2(j\omega)$ to $V_2(j\omega)$, *i.e.*, $V_2(j\omega) = Z^{\star}_{22}(j\omega)I_2(j\omega)$, is given by

$$Z^{\star}_{22}(j\omega) = Z_{22}(j\omega) + Z_{21}(j\omega)\frac{I_1(j\omega)}{I_2(j\omega)}\,, \tag{6.2}$$

which is not equal to the actual battery impedance $Z_{22}(j\omega)$.

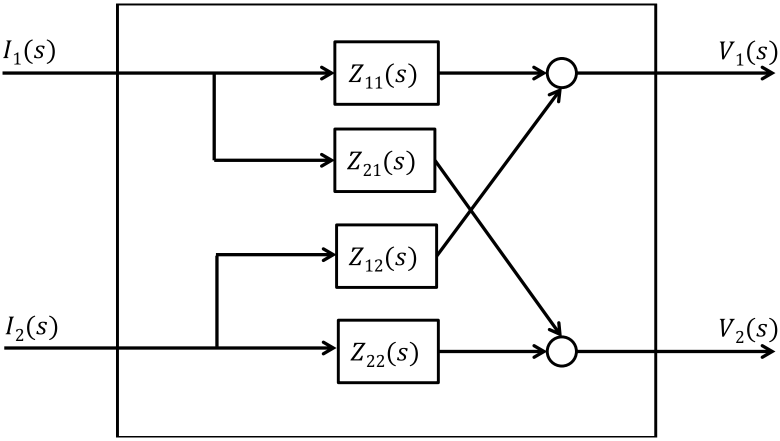

Fig. 6.1: Multiple-input multiple-output block diagram of a battery pack with two adjacent batteries.

The effect of this offset is clearly shown in Fig. 6.2, in which an example of a battery impedance ($f = 2.84$ kHz) is shown without (blue circle) and with crosstalk (red cross) interference. Note that Fig. 6.2 was produced while the batteries were not electrically connected to each other, although the crosstalk would be the same if they were. It should also be noted that there is no minus sign in the y-axis label in this figure, unlike complex planes in the previous Chapters. To compensate for the offset induced in simultaneous EIS measurements at the same frequency in a battery pack, an in-depth experimental analysis and modeling approach is required, which are the topics of the next Sections.

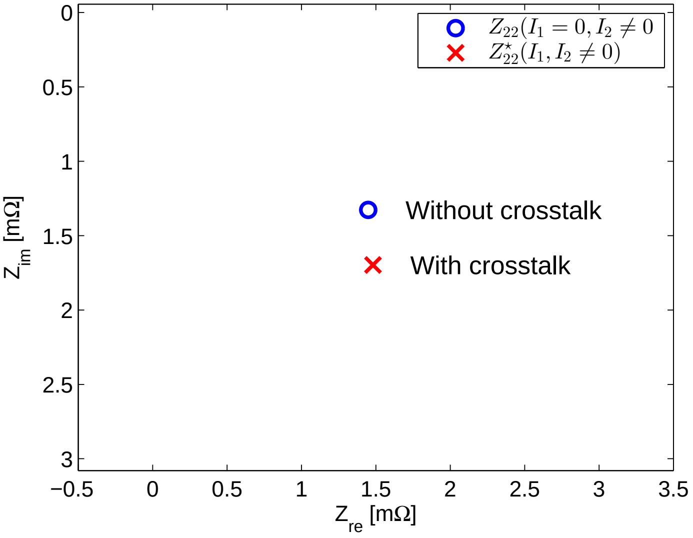

Fig. 6.2: Example of the offset in impedance induced by crosstalk interference at 2.84 kHz. The blue circle represents a measurement without crosstalk interference and the red cross the result with crosstalk interference.

6.3. Experimental details

To experimentally demonstrate that the off-diagonal terms of $Z(s)$ can be nonzero and that crosstalk can interfere with other measurements, a test setup has been assembled, which is shown in Fig. 6.3. The setup contains two 25 Ah rectangular prismatic Nickel-Manganese-Cobalt (NMC) Li-ion batteries that have each been connected to a PCB developed by NXP Semiconductors (see also Sections 5.3 and 5.4). These PCBs are capable of perturbing the batteries with a sinusoidal current with a specified frequency and subsequently measure the induced voltage, from which the impedance of the batteries is obtained. This implies that the PCB of battery 1 will apply current $I_1(s)$ and measure voltage $V_1(s)$, whereas the PCB of battery 2 will apply current $I_2(s)$ and measure voltage $V_2(s)$.

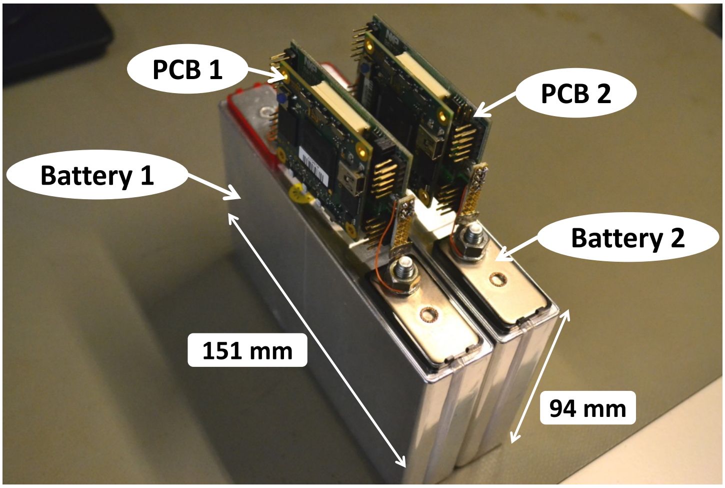

Fig. 6.3: Setup used for crosstalk measurements; two adjacent 25 Ah prismatic Li-ion batteries with connected PCBs.

For investigating the superposition principle, and for battery position and spacing, EIS measurements were performed at room temperature for twelve logarithmically distributed frequencies in the range of 10 to 5000 Hz. For this frequency range, most of the measurements are located in the inductive part of the impedance spectrum, *i.e.* the part were the imaginary values and phase are positive. The batteries have been perturbed with a sine wave current of 165 mA RMS.

In order to validate the temperature and SoC dependence of crosstalk impedances, EIS measurements were performed at temperatures of -20, -10, 10, 30, and 50°C, and at SoC values ranging from 20% to 100% in steps of 20%. For these measurements, a frequency range of 10 to 5000 Hz with 25 logarithmically distributed frequencies was applied. A Vötsch VT4002 temperature chamber was used for temperature control of the battery pack. Furthermore, a Kepco BOP 20-20M bipolar operational power supply and amplifier was used to (dis)charge the batteries. In addition, this power supply was used for AC current excitation to investigate if the system is homogeneous (Section 6.4.1).

Typically, EIS measurements lead to results in complex numbers. Therefore, these measurements are shown in either Bode plots or in the complex plane. In this chapter, the Bode plot shows both the magnitude of the voltage, and the phase between voltage and current as a function of frequency. In the complex plane, the imaginary part of the voltage (V_{im}) is plotted against the real part (V_{re}) for every measured frequency.

6.4. Results and discussion

In order to investigate crosstalk as a function of various parameters, EIS experiments have been conducted with the experimental setup shown in Section 6.3. In particular, it will be investigated if crosstalk is a linear phenomenon and how it behaves as a function of different parameters, such as battery position and inter-battery spacing. Based on these experimental results and on physical knowledge, a crosstalk model will be designed in Section 6.5.

6.4.1. Superposition

To investigate whether crosstalk interference is a linear phenomenon, it is experimentally investigated whether the superposition principle holds. For superposition, both homogeneity, *i.e.*, $F(ax) = aF(x)$, as well as additivity, *i.e.*, $F(x_1 + x_2) = F(x_1) + F(x_2)$ are required. These two properties will therefore be verified experimentally below.

Homogeneity

In Fig. 6.4, the measured voltage amplitude across battery 2 (blue symbols) is shown as a function of the input current in battery 1. Note that an AC current excitation of 2 kHz was applied and an AC voltage response was therefore measured. However, to check the homogeneity property the amplitudes of the AC signals are shown. From Fig. 6.4, it can be observed that a linear approximation, shown by the red line, fits the measurements accurately. The approximation accuracy in terms of Root-Mean-Square-Error (RMSE) is 3 µV. Since the RMSE is extremely low, it can favorably be concluded that the system is homogeneous.

Additivity

In Fig. 6.5, EIS measurement voltages across battery 2 for multiple different (measurement) conditions are shown in the complex plane. The dark blue circles indicate the case where an AC current was applied at $I_2(s)$, while $I_1(s) = 0$, and the resulting voltage $V_2(s)$ was measured. Given the fact that $I_1(s) = 0$, these measurements have not been influenced by crosstalk interference from the EIS measurement in battery 1. The cyan pluses in Fig. 6.5 indicate the case where an AC current at

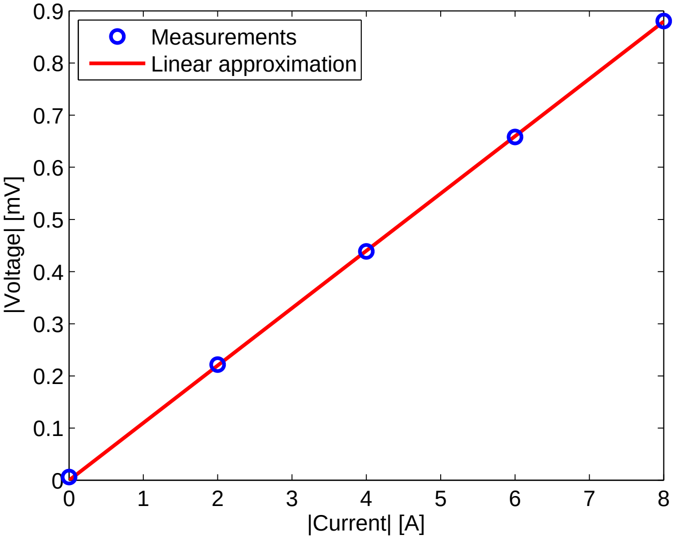

Fig. 6.4: Measured voltage amplitude at $V_2(s)$ as a function of current amplitude excitation in $I_1(s)$ (symbols) at 2 kHz. A linear approximation of the measurements (line) is also shown.

$I_1(s)$ has been applied, while $I_2(s) = 0$ and the resulting voltage $V_2(s)$ was measured. Since the measured voltage $V_2(s)$ is unequal to zero, this clearly indicates that crosstalk between the two batteries is present. Finally, the green squares in Fig. 6.5 indicate the case where both batteries were perturbed with an AC current $(I_1(s), I_2(s) \neq 0)$ and the voltage $V_2(s)$ was measured. These measurements, are clearly influenced by crosstalk and differ considerably from the measurements without crosstalk (dark blue circles), especially at high frequencies.

To verify the additivity property, the cyan pluses in Fig. 6.5 are subtracted from the green squares and the result is shown in red crosses. It can be seen that the corrected signal (red crosses) is in perfect agreement with the measurements without crosstalk. To quantify the error between the voltages without crosstalk and the corrected voltages, the RMSE has been calculated to be 2.3 µV. Evidently, for this system, the response to the sum of its inputs is the same as the summed responses for the individual inputs. Therefore, it can be concluded that the additivity property holds. Since it is experimentally proven that both the homogeneity and additivity properties are valid, it can be concluded that the superposition principle holds. This means that the system in consideration is linear, which is a favorable property for modeling purposes.

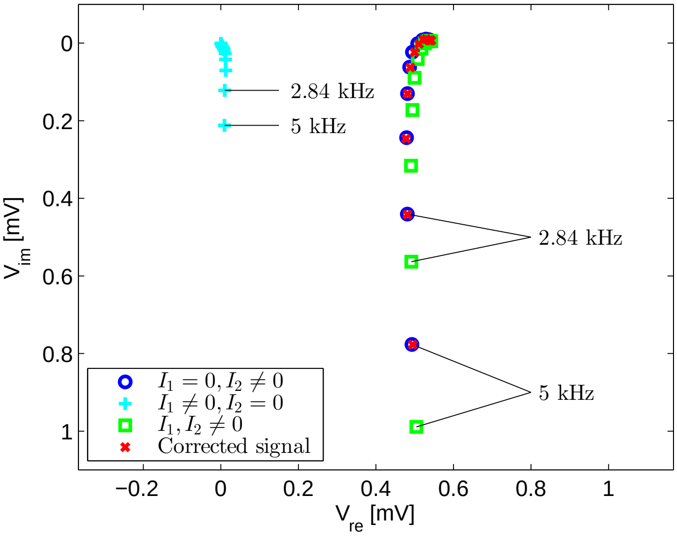

Fig. 6.5: Complex plane showing measured EIS voltages at $V_2(s)$ for different measurement conditions to check the additivity property.

6.4.2. Battery position and spacing

In this Section, an experimental parameter variation study is performed in order to investigate crosstalk interference as a function of battery position and in-between spacing.

Position

In Fig. 6.6a-b, two typical battery positions (position A and B) used for battery packs are shown. The EIS measurement results of positions A and B, under disturbing and non-disturbing conditions are shown in the Bode diagram in Fig. 6.7. In this diagram, it can be seen that the lines start to deviate from each other in the higher frequency range, indicating increasing crosstalk interference. The dark blue solid line with circles shows undisturbed EIS measurements in positions A and B. Current was applied only in battery 2 for this measurement. Obviously, if current would be applied in both batteries simultaneously, crosstalk signals will influence the EIS measurements. However, the direction of influence is determined by the position which is taken (position A or B) to perform the measurements. With respect to the undisturbed measurement, the voltage magnitude and phase in position A ($I_1, I_2 \neq 0$) are larger, whereas the same measurement in position B ($I_1, I_2 \neq 0$) gives smaller results under crosstalk interference.

Although the magnitude and phase between positions A and B are different, the

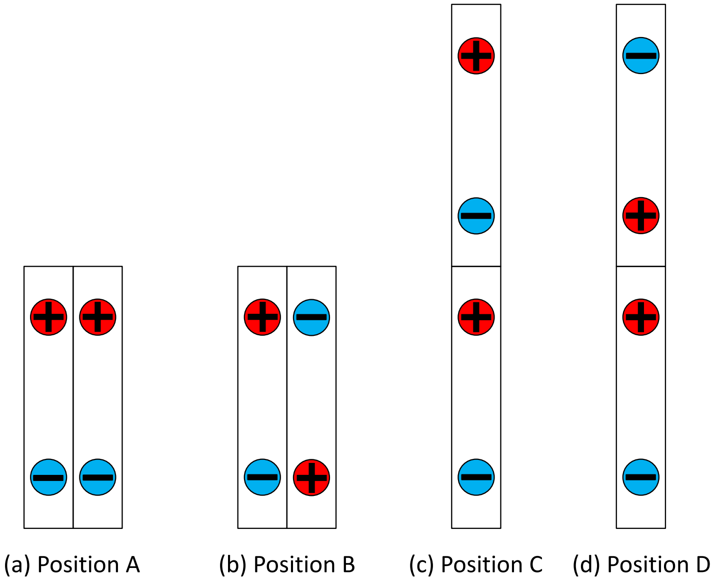
(a) Position A (b) Position B (c) Position C (d) Position D

Fig. 6.6: Four different battery positions inside a battery pack.

deviation with respect to the undisturbed measurement is the same. This implies that the degree of crosstalk interference in both positions is equal, but the sign of the interference changes into the opposite direction. For EIS measurements in position A that means that crosstalk interference adds up to the undisturbed signal and for position B it subtracts. This suggests that crosstalk is caused by inductive/magnetic coupling, as the sign of the interfering signal depends on the direction of the magnetic field. Finally, the fact that the sign of the interfering signal is different for positions A and B allows for averaging out the interfered measurements, which leads to a non-disturbed signal (red crosses), as can be seen in Fig. 6.7.

Two more positions which can be used for battery packs are shown in Fig. 6.6c and d. The EIS measurement results taken on these positions, including positions A and B, are shown in the Bode plot of Fig. 6.8. It can be seen that the measurements in position C and D with current perturbations in both batteries (red crosses) are similar to the undisturbed measurements in position A and B with current perturbation only in one battery (solid blue line with circles). For comparison, an interfered measurement in position A is also shown (solid cyan line with pluses). From this figure, it can be concluded that EIS measurements on batteries in positions C and D are not affected by crosstalk. Hence, in order to avoid crosstalk interference in battery packs, batteries can be ordered in positions C or D, if practically possible.

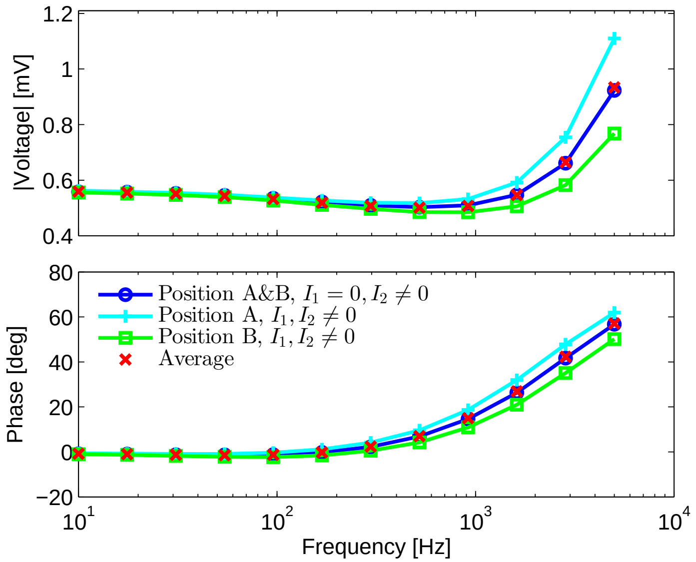

Fig. 6.7: Measured voltage and phase at $V_2(s)$ for battery positions A and B shown in a Bode plot.

Spacing

In this Section, the influence of air spacing between adjacent batteries in positions A and B (Fig. 6.6a and b) on the crosstalk will be discussed. Instead of plotting voltage measurement results, it is more convenient to show the crosstalk impedance for these particular measurements. The crosstalk impedance is given by the $Z_{21}(s)$ and $Z_{12}(s)$ terms in the block diagram in Fig. 6.1. In Fig. 6.9, a Bode plot is shown of the measured transfer function $Z_{21}(s)$ for three different spacings (0 mm, 30 mm, and 60 mm). In general, the impedance magnitude increases with frequency, indicating that interfering crosstalk signals become more dominant at high frequencies, which was also observed in the previous measurements. For frequencies lower than 50 Hz, the measurement noise starts to dominate the measured crosstalk impedance, especially for the 30 mm and 60 mm spacing. The highest impedance magnitudes were found for two adjacent batteries without any distance in-between (0 mm), as the coupling is at maximum then. The phase is approximately 90 degrees across the whole frequency range, which again indicates inductive behavior. That is in agreement with the observation above that the interference might be caused by inductive behavior of the battery. The measured crosstalk impedance in the Bode plot in Fig. 6.9 is of high importance as it can be used for modeling purposes, which will be discussed in Section 6.5.

In addition to measurements with air spacing between two batteries, measure-

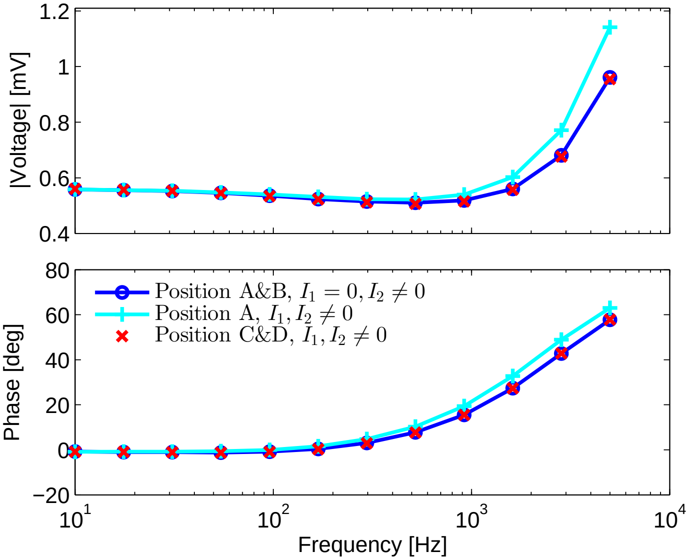

Fig. 6.8: Bode plot of the measured voltage and phase at $V_2(s)$ for battery positions A, B, C and D.

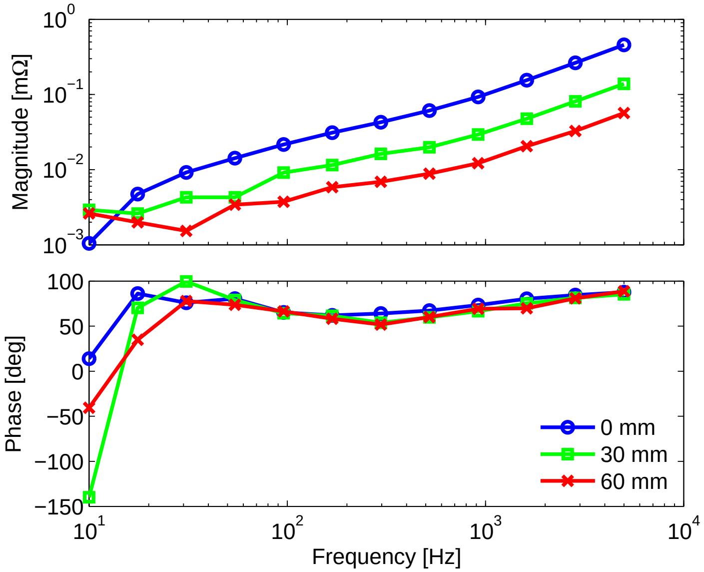

Fig. 6.9: Measured transfer function Z_{21} in a Bode plot for three different spacing's.

ments with dummy batteries in-between were performed. This gave similar results as air spacing, indicating that in this particular situation the magnetic field is not influenced by these batteries. However, that might be different in other experimental setups.

6.4.3. Temperature and SoC dependence

For effective impedance-based state estimation, the crosstalk dependence on temperature and SoC was investigated. Therefore, crosstalk impedance Z_{21} was measured at various temperatures and SoC. The temperature dependence of Z_{21} is shown in Fig. 6.10a and the SoC dependence in Fig. 6.10b. Since all lines are overlapping, it can be concluded that crosstalk impedance Z_{21} is independent of temperature and SoC. The small deviations at high frequencies in Fig. 6.10a can be attributed to PCB measurement inaccuracies. The PCBs were directly connected to the batteries and, thus, also positioned in the temperature chamber. The various temperatures slightly influence the PCB measurement output.

The temperature and SoC independence is another indication that crosstalk is induced by inductive coupling, because the inductance of a battery is independent of temperature and SoC [4, 5]. As the batteries in the pack are identical, it can be assumed that crosstalk impedance Z_{12} is similar to Z_{21}.

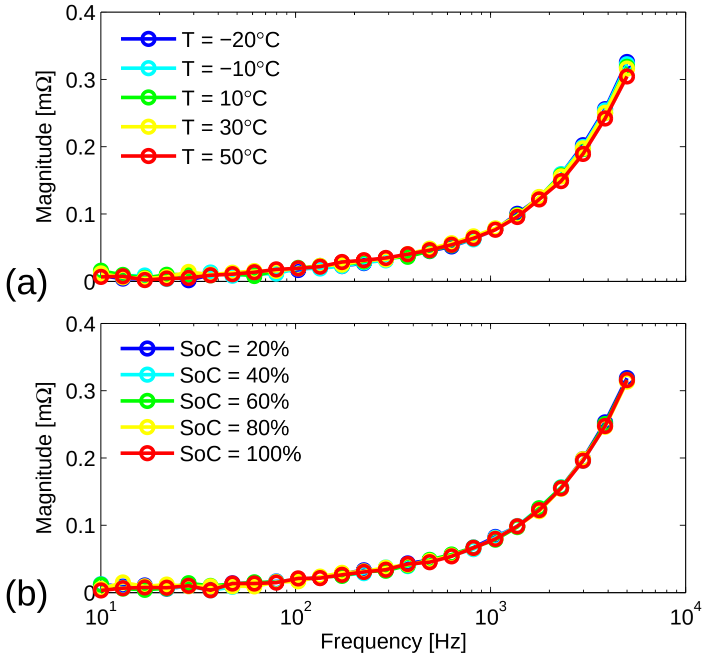

Fig. 6.10: Magnitude of crosstalk impedance Z_{21} at various temperatures (a) and SoC (b).

6.4.4. Intercept frequency

For impedance-based temperature indication through the (N)ZIF, it is interesting to investigate the (N)ZIF without and with the influence of crosstalk. The results are shown in Fig. 6.11, in which NZIF curves are plotted, interpolated to Z_{im} = 0.1, 0.5, and 1.0 mΩ. Due to measurement limitations of the setup, the ZIF (f_0) could not be determined accurately and has therefore been excluded. The results shown in Fig. 6.11 are as expected, because higher interpolation values lead to higher intercept frequencies, as also has been shown in Chapter 5 (Fig. 5.11). Furthermore, NZIF values with crosstalk clearly deviate from NZIF values without crosstalk. Evidently, the deviations between NZIF values without and with crosstalk interference, depend on the interpolation value. High NZIF, interpolated at high Z_{im}, show more deviation than low NZIF. This is in accordance with the investigations above, where it is shown that crosstalk is more dominant at higher frequencies. From these results it is obvious that crosstalk interference influences (N)ZIF values. Therefore, crosstalk should be considered carefully for temperature indication through the (N)ZIF method applied to batteries in a battery pack. Possible solutions to avoid crosstalk interference is to measure EIS sequentially, to measure each battery at different frequencies, position batteries such that crosstalk does not occur, or use models that compensate the offset.

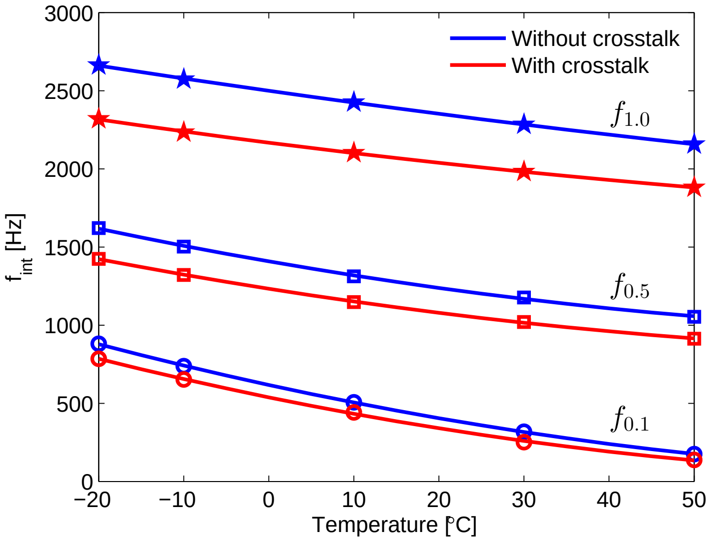

Fig. 6.11: Non-zero-intercept frequencies interpolated to Z_{im} = 0.1, 0.5, and 1.0 mΩ, shown without (blue) and with (red) crosstalk interference.

6.5. Modeling and simulations

As mentioned in Section 6.2, obtaining the transfer-function in Eq. 6.1 requires modeling the impedance of the battery itself, as well as modeling the crosstalk. In this Section, a model for the crosstalk will be provided. Note that crosstalk is only present in batteries that are placed as indicated in Fig. 6.6a and b, meaning that $Z_{il}(s) = 0$ if battery i and battery l are placed as indicated in Fig. 6.6c and d. In this Section, a model for the case that $Z_{il}(s) \neq 0$ will be proposed.

6.5.1. Model description

The measurement results discussed in Section 6.4 suggest that crosstalk interference is induced by inductive coupling. Therefore, it is proposed to model this inductive behavior using a 2-coil model, as shown in Fig. 6.12. In this figure, M_{il} denotes the mutual inductance between the coils i and l, which depends on the coefficient of coupling k_{il} [6–8] that is given by

$$M_{il} = k_{il}\sqrt{L_i L_l}\ , \tag{6.3}$$

where L_i and L_l are the self-inductances of the two coils. The value $0 < k_{il} < 1$ indicates the amount of coupling, where $k_{il} = 1$ indicates a tightly coupled system and $k_{il} = 0$ implies no coupling between L_i and L_l.

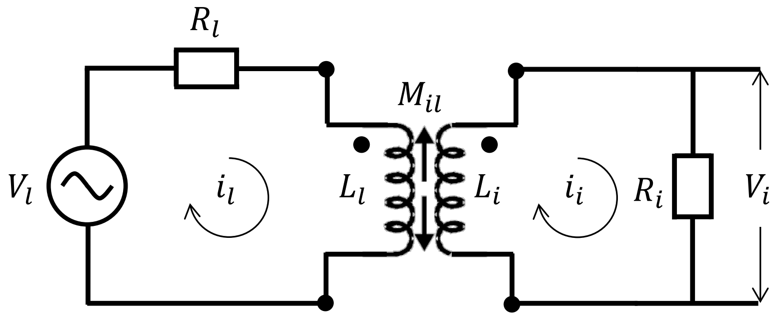

Fig. 6.12: The 2-coil model for modeling crosstalk interference.

The transfer function between current I_l and voltage V_i can be obtained from the application of Kirchoff's voltage laws to the right loop indicated in Fig. 6.12, which yields

$$(R_i + L_i s)I_i(s) - M_{il} s I_l(s) = 0\ , \tag{6.4}$$

while V_i across resistor R_i is given by Ohm's law, *i.e.*, $V_i = R_i I_i$. Solving Eq. 6.4 for I_i and substituting this into Ohm's law leads to a transfer function between V_i and I_l, according to

$$V_i(s) = Z_{il}(s) I_l(s) \qquad \text{with} \qquad Z_{il}(s) = \frac{M_{il} s}{\frac{L_i}{R_i} s + 1} . \tag{6.5}$$

From the measurements described in Section 6.4, the value of k_{il} in Eq. 6.3 only depends on the distance between the batteries and the orientation of the batteries. By assuming that the battery can be modeled as a circular coil, the variation of magnetic field induced by this coil [9] can be described by

$$B = \frac{\mu_0 N a^2 I}{2(z^2 + a^2)^{3/2}} , \tag{6.6}$$

where $\mu_0 = 4\pi \cdot 10^{-7}$ is the vacuum permeability, N is the number of turns of the field coil, a is the radius of the coil in meters, I is the current through the wire in amperes, and z is the axial distance in meters from the center of the coil. Hence, if the coefficient of coupling is considered to be influenced by the magnetic field, it can be modeled by fitting an expression of the form

$$k_{il} = \frac{b}{(d_{il}^2 + a^2)^{3/2}} , \tag{6.7}$$

where a and b are constants to fit the measurement data (where b can be either positive or negative depending on the orientation of the batteries), and d_{il} is the axial distance between the centers of batteries i and l in meters.

6.5.2. Model simulation

From the measurement data obtained from the experimental setup described in Section 6.3, it has been observed that $L_1 = L_2 \approx 20$ nH and $R_1 = R_2 \approx 1.5$ mΩ. The resulting crosstalk model $Z_{21}(s)$ has one zero at the origin and one pole at $s = -R_2/L_2$, which can only be observed in a Bode diagram at higher frequencies than the highest frequency that can be measured with the used experimental setup. This means that the pole is not captured in the measurements and; therefore, the transfer function can be assumed to be $Z_{21}(s) = M_{21} s$. Taking $a = 3.95 \cdot 10^{-2}$ m and $b = 8 \cdot 10^{-5}$ m^3, a fit between the model and the measurements is obtained, as shown in Fig. 6.13 for three different distances between the batteries. Note that b is considered positive since the measurements are performed in position A (Fig. 6.6a).

It can be observed that the model in Eq. 6.5 shows an adequate agreement

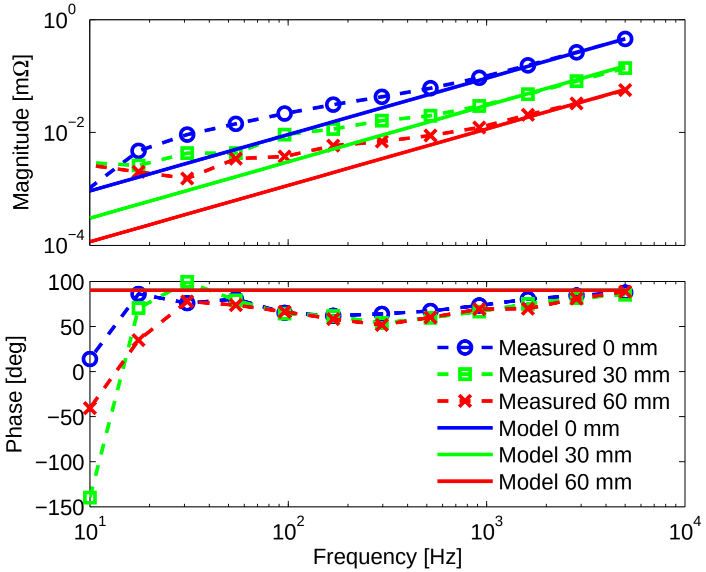

Fig. 6.13: Measured and modeled transfer function Z_{21} in a Bode plot for three different spacings. Note that the indicated spacing in the legend is the in-between spacing; not the center-to-center spacing.

with the measurements in the high-frequency range, but can be further improved for the low-frequency range. Therefore, a phase-lag filter of the form

$$Z_{filter} = k_c \left(\frac{s + 2\pi f_1}{s + 2\pi f_2} \right) , \tag{6.8}$$

is added to the model, where the gain $k_c = 1.1$, $f_1 = 450$ Hz and $f_2 = 150$ Hz provide a good fit with the measurements. This improved model, of which the results are shown in Fig. 6.14, approximates the measurements better at lower frequencies when compared to the simulations shown in Fig. 6.13.

In Fig. 6.15, the measured and simulated coupling coefficient is shown as a function of center-to-center distance. The measured coupling coefficient (*e.g.* k_{21}) can be obtained by substituting Eq. 6.3 into Eq. 6.5 and rewriting for k_{il}. Since Z_{21} is known from measurements (see Fig. 6.9), k_{21} can be calculated, accordingly. This k_{21} is denoted as the 'measured' coupling coefficient and is shown in Fig. 6.15 by the symbols. The simulated coupling coefficient is obtained from Eq. 6.7 and shown in Fig. 6.15 by the line. Both the measured and simulated coupling coefficients are determined at a frequency of 5 kHz, at which crosstalk is most present because it is the highest measured frequency. The measured and simulated coupling coefficients decrease exponentially with increasing distance, meaning that the

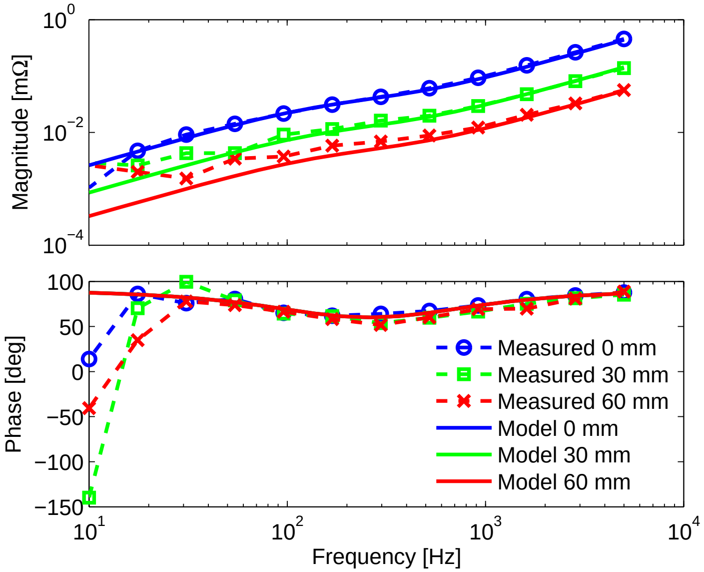

Fig. 6.14: Measurements and simulations of the improved model in a Bode plot for three different spacings. Note that the indicated spacing in the legend corresponds to the in-between spacing and not the center-to-center spacing.

crosstalk impedance also decreases exponentially when the distance between the batteries increases.

6.6. Conclusions

In this Chapter, the influence of crosstalk on EIS measurements in battery packs has been investigated. Crosstalk is a phenomenon which appears when EIS measurements in one battery interfere with the EIS measurements in surrounding batteries. It has been investigated experimentally that crosstalk introduces interference that is homogeneous and additive, meaning that the superposition principle holds and that the particular system in this study is linear, which is advantageous for modeling purposes. Furthermore, a parameter variation study has shown that the battery location and inter-battery spacing influence the amount of crosstalk. This observation, together with the fact that batteries show inductive behavior in the high-frequency range of the impedance spectrum, suggests that crosstalk is induced by magnetic coupling of the batteries. It was found that spacing between batteries attenuates the degree of crosstalk and that crosstalk signals become stronger at increasing frequencies. Furthermore, it has been shown that crosstalk can be

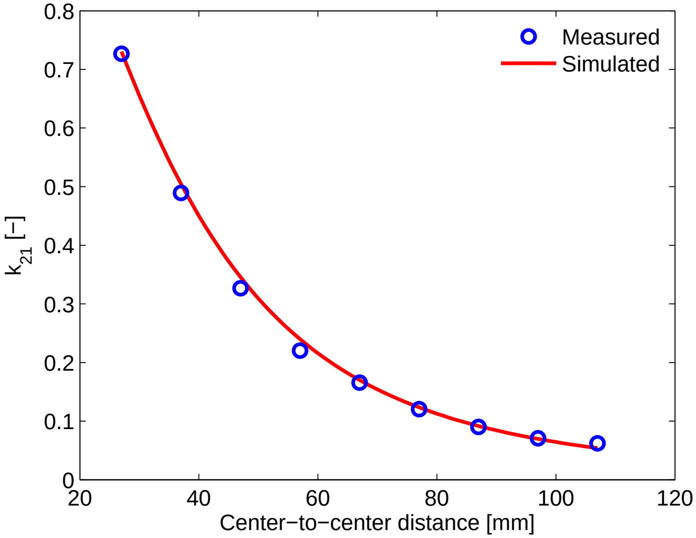

Fig. 6.15: Measured and simulated coupling coefficient at a frequency of 5 kHz as a function of the center-to-center distance between batteries.

prevented if batteries are placed longitudinally with respect to each other.

Besides battery location and spacing, it can be concluded that crosstalk impedances are independent of temperature and SoC, which simplifies temperature indication in the presence of crosstalk. Furthermore, it can be concluded that the (N)ZIF clearly deviates in the presence of crosstalk interference. As crosstalk is more present at higher frequencies, high NZIF values deviate more in comparison to low NZIF values. Therefore, crosstalk should be carefully considered for impedance-based temperature indication systems applied in battery packs.

Based on the presented EIS measurements and a proposed 2-coil model, a transfer-function description has been developed to model crosstalk impedance. It has been shown that the coupling factor between two batteries is proportional to the magnetic field between the 2 coils. This relation is most clearly visible at higher frequencies, where crosstalk interference is strongest. The crosstalk model can favorably be used for the development of EIS-based measurement methods for state-of-charge, state-of-health and temperature indication in automotive battery packs.

This study has shown that crosstalk can be prevented either by designing battery packs in which batteries are positioned in such a way that crosstalk does not occur, or that crosstalk can be compensated by an EIS measurement algorithm.

Two more options to prevent crosstalk are either to measure EIS at different frequencies, or to measure EIS sequentially. However, taking EIS measurements at different frequencies is not always advantageous from an accuracy point of view and sequential measurements require more time to measure all batteries in packs in comparison to simultaneous measurements.

References

[1] L. Raijmakers, K. Shivakumar, M. Donkers, M. Lammers, and H. Bergveld, *Crosstalk Interferences on Impedance Measurements in Battery Packs,* IFAC-PapersOnLine **49**, 42 (2016).

[2] M. E. Orazem and B. Tribollet, *Electrochemical Impedance Spectroscopy* (John Wiley & Sons, 2008).

[3] E. Barsoukov and J. R. Macdonald, *Impedance Spectroscopy Theory, Experiment, and Applications*, 2nd ed. (John Wiley and Sons, 2005).

[4] D. Andre, M. Meiler, K. Steiner, C. Wimmer, T. Soczka-Guth, and D. Sauer, *Characterization of high-power lithium-ion batteries by electrochemical impedance spectroscopy. I. Experimental investigation,* J. Power Sources **196**, 5334 (2011).

[5] P. Suresh, A. Shukla, and N. Munichandraiah, *Temperature dependence studies of a.c. impedance of lithium-ion cells,* J. Appl. Electrochem. **32**, 267 (2002).

[6] C. Patrick Yue and S. Simon Wong, *Physical modeling of spiral inductors on silicon,* IEEE Trans. Electron Devices **47**, 560 (2000).

[7] C. Zierhofer and E. Hochmair, *Geometric approach for coupling enhancement of magnetically coupled coils,* IEEE Trans. Biomed. Eng. **43**, 708 (1996).

[8] C.-S. Wang, O. Stielau, and G. Covic, *Design Considerations for a Contactless Electric Vehicle Battery Charger,* IEEE Trans. Ind. Electron. **52**, 1308 (2005).

[9] H. A. Radi and J. O. Rasmussen, *Principles of physics: for scientists and engineers* (Springer Science & Business Media, 2012).

7

Compensating 3-electrode impedance artefacts

In order to measure the electrochemical characteristics of both electrodes inside Li-ion batteries, micro-reference electrodes (μREF) have turned out to be very useful. However, measuring the electrochemical impedance with respect to μREF can lead to severe measurement artefacts, making a detailed analysis of the impedance spectra complicated. In the work presented in this Chapter, a new method is developed in which high-frequency measurement artefacts can be compensated. A theoretical analysis, using equivalent-circuit models of the measurement setups, shows that if two different impedance measurements are averaged, the impedance contributions from the measurement leads can be completely eliminated. The theoretical analysis is validated using Li-ion batteries with seven integrated μREF, having all different impedances. The measurement results show that artefacts are dominating for high-impedance μREF in the high-frequency range. However, these artefacts can be fully compensated by averaging two separate impedance measurements, as predicted by theory. This makes it easily possible to perform artefact-free impedance measurements, even at high frequencies.

Parts of this chapter have been published in Electrochimica Acta, **259**, (2018) 517-533 [1].

7.1. Introduction

In Chapters 4 and 5, impedance-based temperature indication methods through the (N)ZIF are presented. So far, these methods were only applied to (commercial) Li-ion batteries having two electrodes. For this reason, only the total battery impedance and, hence, (N)ZIF can be measured. However, for research purposes and to develop advanced BMS, it is of interest to distinguish between both electrodes with the use of reference electrodes (REF). Favorably, REF make it possible to measure the electrochemical characteristics and, thus, the (N)ZIF of the individual electrodes.

REF have already been introduced in many studies [2–15]. However, in particular EIS measurements at three-electrode Li-ion battery systems are prone to measurement artefacts [16–27]. These artefacts cause a divergence in impedance spectra and, as a consequence, the analysis of the measurements becomes unreliable and inaccurate. Moreover, underlying physical phenomena can be hidden by artefacts. Therefore, it is important to either prevent or to compensate these artefacts as much as possible.

Many studies on EIS measurement artefacts in the field of Li-ion batteries focus on the battery geometry and/or the position of the REF, since improper three-electrode measurement setups are highly sensitive to artefacts. In general, it can be concluded that EIS measurement artefacts can be prevented to a large extent by using an appropriate cell geometry and REF position. Often these measurement setups are based on Swagelok-type batteries in which perfect electrode alignment can be realized and where the REF can be easily introduced coaxially with respect to the electrodes [17, 19, 22, 23]. Obviously, these setups are suitable for small-scale laboratory experiments. However, perfect electrode alignment and coaxially positioning of REF is more complicated to realize in large-size (commercial) Li-ion batteries, which are used in for example (H)EVs. Therefore, these batteries are often equipped with integrated micro-reference electrodes (µREF) [2, 4, 7, 9, 11, 28].

Not only the cell geometry and electrode positions, but also the REF impedance and measurement equipment, like for instance cables, potentiostats, capillaries, frits, etc. can lead to EIS measurement artefacts [16, 25, 29–35]. Obviously, the input impedance of the measurement device should be selected high and the REF impedance low [32]. Baker *et al.* [36] found by modelling and simulations that artefacts are a function of the REF size, its surface resistance, the resistance of the separator and both the working and counter electrodes. Furthermore, the length of the measurement cables should be reduced as much as possible [25, 29], although this is sometimes difficult due to measurements which have to be performed at remote locations, such as gloveboxes and temperature-controlled climate chambers.

A solution to suppress high-frequency artefacts caused by the measurement equipment and the high-impedance REF, is to use so-called dual REF [30, 33, 34]. This is based on a second reference electrode which is carefully positioned in the measurement setup and connected in series with a conventional REF through a capacitor. Recently, another successful technique has been introduced in which a capacitor bridge between the counter electrode (CE) and the REF is used to suppress high-frequency EIS artefacts of three-electrode geometries [16]. The capacitor bridge balances the leakage current through the REF. However, it is not straightforward to determine the compensating value of the capacitor for systems using dual REF or capacitor bridges. The capacitance must be carefully aligned to the measurement setup under consideration, which can lead to elaborate investigations.

This Chapter presents a new method in which high-frequency EIS measurement artefacts at three-electrode Li-ion batteries can be fully compensated by averaging two individual three-electrode EIS measurements. Strikingly, this results in artefact-free EIS measurements in the high-frequency range of the impedance spectra, which is essential for *e.g.* characterizing the individual electrodes, for modeling purposes, State-of-Health indication and impedance-based temperature measurements [37–40]. The proposed method is similar to the method presented by Hsieh *et al.* [32], in which they correct artefacts arising from a so-called voltage-divider effect. However, their work was performed on solid-state electrochemical devices in which the platinum REF impedance approaches the input impedance of the measurement device. Moreover, Hsieh *et al.* [32] combined one two-point and two three-point measurements in order to correct for the artefacts, which is not required for the method presented in this work.

In this Chapter, models, including all electrode, device input, and lead impedances are systematically developed in order to provide a deeper insight into the measurement artefacts of three-electrode Li-ion battery systems. It will be shown that the lead impedances, which can significantly contribute to artefacts, can be easily compensated by reversing the measurement device connections to the battery. In addition, multiple µREF with various active tip areas are used to investigate the influence of the REF impedance on the artefacts.

In order to experimentally show the artefacts and the strength of the proposed compensation method, EIS measurements are performed with conventional electrochemical measurement equipment on pouch-type Li-ion batteries with seven integrated µREF. The proposed compensation method is compared to the successfully applied capacitor-bridging method, applied by Battistel *et al.* [16]. Finally, it will be shown that the impedance measurements can be accurately simulated by the developed artefact models.

7.2. Theoretical considerations

EIS measurements on three-electrode Li-ion batteries can be prone to artefacts. Fig. 7.1 shows equivalent circuits which are used to derive models for simulating the impedances, including artefacts. Each equivalent circuit shows two (gray) rectangles, which represent the measurement device and the battery. The measurement device is highly simplified and consists of an ideal current source (⊖), two input impedances (Z_{in}), a voltage measurement (ΔV) and a ground (⏚). The connections to the measurement device are indicated with common abbreviations for electrochemical measurement equipment, *i.e.* WE for working electrode, CE for counter electrode, RE for the (µ)REF and S for the sense connection. The CE and WE serve as current-carrying cables and RE and S as voltage-sense cables. This so-called four-point measurement configuration guarantees accurate measurements, although artefacts can still be present. The impedances of all measurement leads (Z_l^i) are shown between the measurement device and the battery. The battery is composed of impedances for the positive electrode (Z_P), the negative electrode (Z_N) and the µREF ($Z_{\mu REF}$).

Using the equivalent circuits in Fig. 7.1, it is possible to derive mathematical models, which make it possible to simulate the measured (^{m}) impedances of the total battery (Z_{Bat}^m), the positive (Z_P^m), and the negative electrode (Z_N^m). It should be emphasized that these measured impedances can deviate from the true impedances for Z_{Bat}, Z_P, and Z_N. This depends on the input impedances (Z_{in}) of the measurement device, the lead impedances (Z_l^i), and the µREF impedance ($Z_{\mu REF}$). Below, all measurement configurations shown in Fig. 7.1 will be discussed and modeled, including the configuration required to compensate for Z_l^i in the three-electrode measurement set-up.

7.2.1. Model assumptions

The equivalent circuits in Fig. 7.1 can easily be modeled by applying Kirchhoff's current and voltage laws. However, this approach makes it rather difficult to analytically investigate what elements are causing the measurement artefacts. Therefore, another approach is adopted in this study. For completeness and for the reader's interest, the Kirchhoff-law approach applied to the circuits in Fig. 7.1 can be found

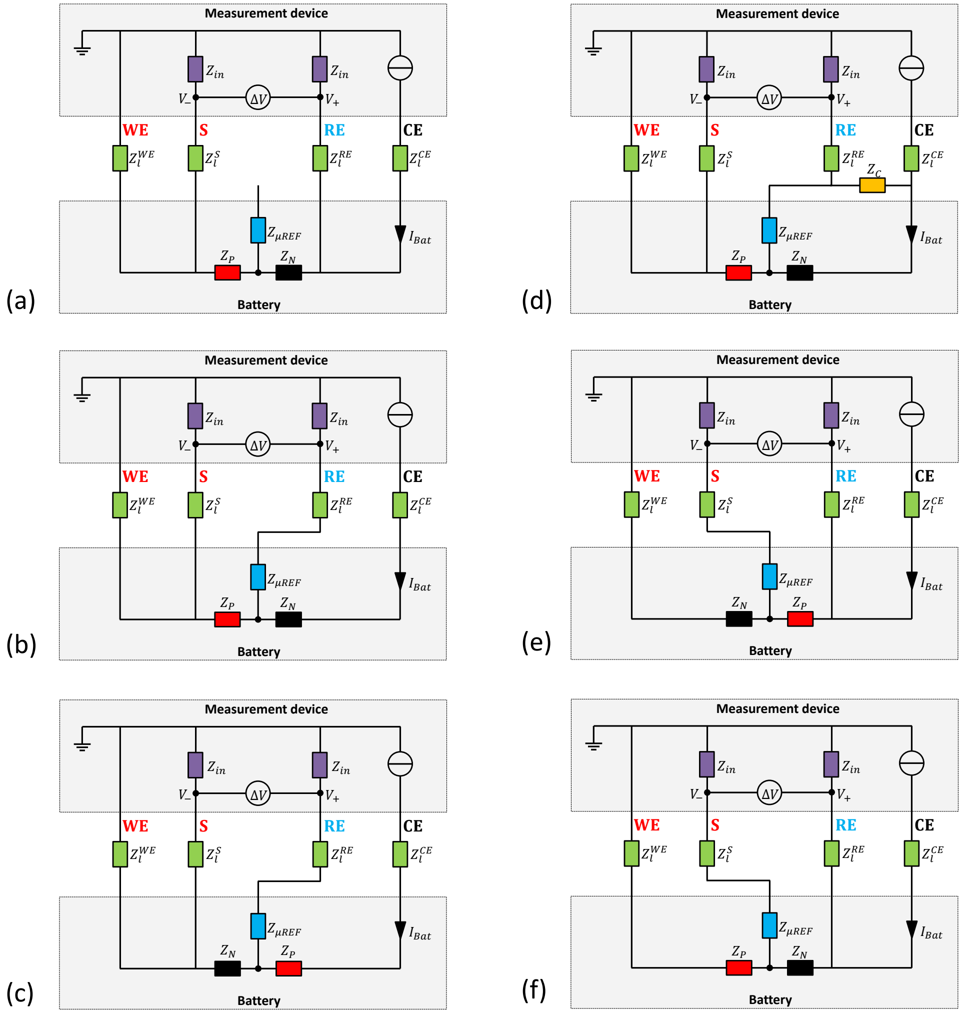

Fig. 7.1: Schematic equivalent circuits for EIS measurements at Bat (a), P (b), N (c), P with capacitor bridge (d), P with reversed connections (e), and N with reversed connections (f).

in appendix A.

Fig. 7.1 shows that the battery excitation current (I_{Bat}) flows between the CE and WE connections of the measurement device and that the WE is connected to ground. The voltage response is measured between the RE and S connections, which are also connected to the ground through the input impedances Z_{in}. Since Z_{in} are input impedances, it is assumed that their magnitudes are relatively large and equal. Therefore, it can be assumed that the currents through the S and RE leads are much smaller than I_{Bat}. For artefact-related modeling purposes it is, however, essential to also consider all lead and connection impedances. For simplicity reasons, the lead and connection impedances of the WE (Z_l^{WE}), CE (Z_l^{CE}), RE (Z_l^{RE}), and S (Z_l^{S}) are considered equal.

7.2.2. Battery impedance

Adopting the simplified equivalent circuit in Fig. 7.1a, it is easy to derive a model for the measured battery impedance (Z_{Bat}^{m}). Therefore, it is first necessary to calculate the voltage response ΔV across the positive electrode (P) and the negative electrode (N), which is measured between the RE and S of the measurement device

$$\Delta V = V_+ - V_- \ , \tag{7.1}$$

where V_+ is the voltage at the RE measured with respect to ground. It can be expressed as

$$V_+ = I_{Bat}\left(Z_N + Z_P + Z_l^{WE}\right)\frac{Z_{in}}{Z_{in} + Z_l^{RE}} \ , \tag{7.2}$$

where $I_{Bat}\left(Z_N + Z_P + Z_l^{WE}\right)$ is the voltage across $\left(Z_N + Z_P + Z_l^{WE}\right)$. However, since V_+ is measured between two impedances (Z_l^{RE} and Z_{in}), a so-called voltage divider is present and, therefore, the first term must be scaled with $Z_{in}/\left(Z_{in} + Z_l^{RE}\right)$. Similarly, V_-, determined at S with respect to ground, can be calculated according to

$$V_- = I_{Bat} Z_l^{WE} \frac{Z_{in}}{Z_{in} + Z_l^{S}} \ . \tag{7.3}$$

Subsequently, Z_{Bat}^{m} can be calculated by

$$Z_{Bat}^{m} = \frac{\Delta V}{I_{Bat}} \ . \tag{7.4}$$

Substituting Eqs. 7.1 - 7.3 into Eq. 7.4 leads to

$$Z_{Bat}^{m} = K_1\left(Z_N + Z_P\right) + Z_l^{WE}\left(K_1 - K_2\right) \ , \tag{7.5}$$

where

$$K_1 = \frac{Z_{in}}{Z_{in} + Z_l^{RE}} \tag{7.6}$$

and

$$K_2 = \frac{Z_{in}}{Z_{in} + Z_l^{S}} \ . \tag{7.7}$$

K_1 and K_2 represent the as-denoted voltage dividers between the lead and input impedances. Obviously, Z_l^{RE} and Z_l^{S} in Eqs. 7.6 and 7.7 are much lower than Z_{in}. Therefore, K_1 and K_2 converge to 1. The total measured battery impedance in Eq. 7.5 can then be simplified to

$$Z_{Bat}^{m} = Z_N + Z_P \ . \tag{7.8}$$

From Eq. 7.8, it is obvious that the measured battery impedance is equal to the summation of the P and N impedances under normal measurement conditions. When the lead impedances Z_l^{RE} and Z_l^{S} are, however, not extremely small, K_1 and K_2 will not converge to 1 anymore, resulting in battery impedances, which will now be influenced by artefacts.

In Fig. 7.2a the connections how to measure the battery impedance are shown, which is experimentally the most conventional measurement configuration. WE and S are connected to the P of the battery, whereas the CE and the RE are connected to the N of the battery.

7.2.3. Positive and negative electrode impedances

The equivalent circuit to measure the positive electrode impedance (Z_P^m) with respect to a reference electrode is shown in Fig. 7.1b. In this configuration, the RE of the measurement device is connected to the µREF. The µREF impedance is now connected in series with Z_l^{RE}. This introduces an unbalance between RE and S (ΔV) because the µREF impedance is only present in the RE branch. Due to this unbalance, artefacts are likely to appear, which can be understood in more detail by the following derivations.

The voltage response across P is measured between the RE and S. Considering $Z_{\mu REF}$, V_+ (Eq. 7.2) has to be modified into

$$V_+ = I_{Bat}\left(Z_P + Z_l^{WE}\right)\frac{Z_{in}}{Z_{in} + Z_l^{RE} + Z_{\mu REF}} \ , \tag{7.9}$$

whereas the expression for V_- (Eq. 7.3) remains the same. Following a similar derivation as for Z_{Bat}^{m} (Eq. 7.5), Z_P^m can be represented by

$$Z_P^m = K_1 Z_P + Z_l^{WE}\left(K_1 - K_2\right) \ , \tag{7.10}$$

where

$$K_1 = \frac{Z_{in}}{Z_{in} + Z_l^{RE} + Z_{\mu REF}} \tag{7.11}$$

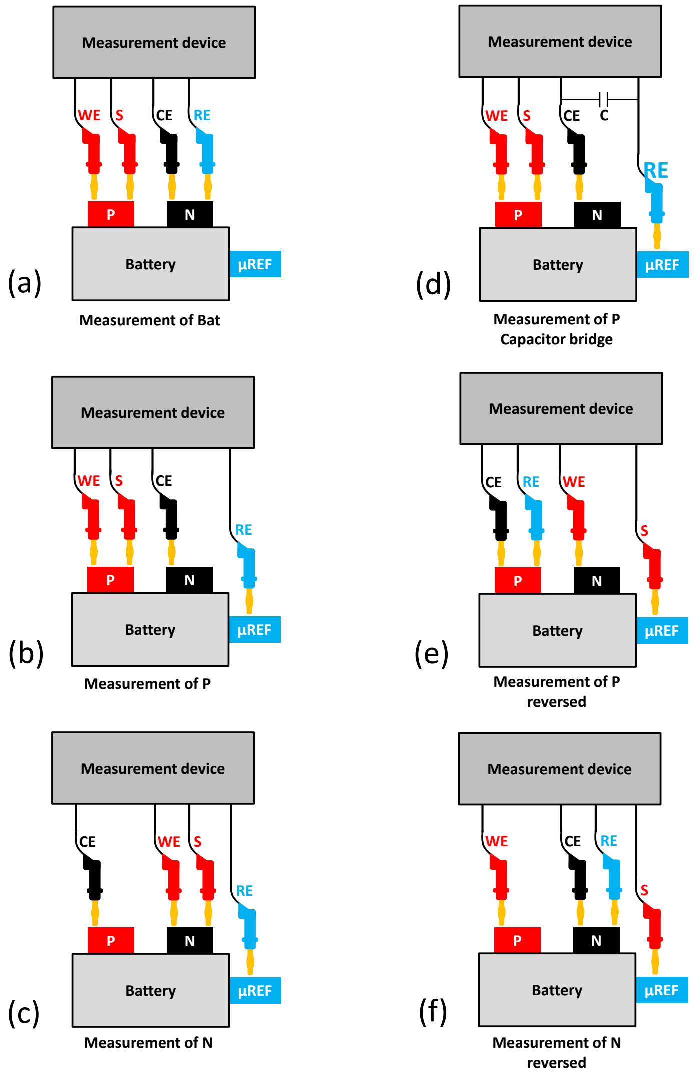

Fig. 7.2: Cable connections to measure EIS at a three-electrode battery. Connections to measure Bat (a), the P (b), the N (c), the P with capacitor bridge (d), the P with reversed connections (e), and the N with reversed connections (f).

and

$$K_2 = \frac{Z_{in}}{Z_{in} + Z_l^S} \; . \tag{7.12}$$

When Z_l^{RE} and Z_l^S are much lower than Z_{in}, K_2 can be considered unity again. However, K_1 in Eq. 7.11 now includes $Z_{\mu REF}$, which can be relatively large for small-sized µREF in Li-ion batteries, as will be shown in Section 7.4, and may even approach Z_{in}. $Z_{\mu REF}$ can therefore not be neglected in this case. However, since K_2 still converges to 1, Eq. 7.10 can be simplified to

$$Z_P^m = K_1 Z_P + Z_l^{WE} (K_1 - 1) \ . \tag{7.13}$$

From Eq. 7.13, it can be concluded that the lead impedance of the WE contributes to Z_P^m if K_1 in Eq. 7.11 does not converge to 1. In other words, the unbalance in the measurement setup caused by the µREF results in contributions from Z_l^{WE}, multiplied with the negative gain $(K_1 - 1)$. Voltage divider K_1 is frequency-dependent and always smaller than 1 (see Eq. 7.11). Especially in the moderate and high-frequency range, this will cause strong deviations in the impedance spectra. Particularly, the impedance spectra in the high-frequency range, which are normally inductive, will bend towards the opposite, capacitive, direction. Obviously, this will lead to unfavorable artefacts in the impedance measurements of P, as will be shown and discussed in detail in Section 7.4. Furthermore, it can be seen that Z_N obviously does not occur in the expression for Z_P^m (Eq. 7.13), indicating that its magnitude is not relevant in this configuration. The measured impedance for the negative electrode (Z_N^m) can be described in a similar way as for P, simply by replacing Z_N for Z_P in Eq. 7.13. The corresponding equivalent circuit is shown in Fig. 7.1c.

To experimentally determine the impedance of P with respect to µREF, RE of the measurement device must be connected to µREF, as indicated in Fig. 7.2b. The other cable connections can be the same as for measuring the total battery impedance in Fig. 7.2a. The cable connections to measure N are shown in Fig. 7.2c.

7.2.4. Capacitor-bridge compensation

Battistel *et al.* [16] investigated the use of a capacitor bridge in order to compensate measurement artefacts in three-electrode geometries. Since Eq. 7.13 shows that artefacts can indeed be present, it seems to be a good solution to apply this bridge method also in the case of three-electrode Li-ion batteries. An ideal capacitor bridge fully compensates the leakage current through µREF. That means that the net current through µREF should be zero for all measurement frequencies. Considering the equivalent circuit in Fig. 7.1d, the measured impedance of P in the presence of a capacitor bridge $(Z_{P,C}^m)$ can be derived. It can be seen that a capacitor (Z_C) is positioned between µREF and N. In this approach we only assume that ideal capacitors are used. Hence, the current through the µREF is zero, making the voltage difference across Z_N equal to the voltage difference across Z_C. The current flowing through the capacitor (I_C) can then be given by

$$I_C = I_{Bat}\frac{Z_N}{Z_C}\ , \tag{7.14}$$

which leads to the following expression for V_+

$$V_+ = I_{Bat}\frac{Z_N Z_{in}}{Z_C}\ . \tag{7.15}$$

Since the current through the µREF is zero, V_+ can also be expressed as

$$V_+ = I_{Bat}\left(Z_P + Z_l^{WE}\right)\frac{Z_{in}}{Z_{in} + Z_l^{RE}}\ . \tag{7.16}$$

Eliminating V_+ from Eq. 7.16 by using Eq. 7.15 this leads, after rearrangement, to an expression for Z_C

$$Z_C = Z_N\frac{Z_{in} + Z_l^{RE}}{Z_P + Z_l^{WE}}\ . \tag{7.17}$$

Using Eq. 7.17 the value of the capacitor bridge can be calculated according to

$$C = \frac{1}{\omega\,|Z_C|}\ . \tag{7.18}$$

where ω is the angular frequency. Strikingly, from Eq. 7.17, it can be seen that the impedance of the capacitor bridge does not depend on the impedance of the µREF in the ideal situation. Furthermore, it can be seen that a large value for Z_{in} is more favorable, as a lower capacitance can be used for compensation. Obviously, when the capacitor bridge is ideal, the measured impedance is equal to the true impedance of the electrodes, *i.e.* $Z_{P,C}^m = Z_P$ and $Z_{N,C}^m = Z_N$.

Fig. 7.2d shows the cable connections for measuring the impedance of P with respect to µREF in the presence of a capacitor bridge. These cable connections are the same as without capacitor bridge (see Fig. 7.2b), except that a capacitor C is now positioned between RE and CE in Fig. 7.2d to compensate for the leakage current through µREF. In case of measuring N, a capacitor should be positioned between RE and CE to fully compensate the artificial impedances.

7.2.5. Reversed-electrode impedances

In order to compensate for high-frequency artefacts arising from the measurement leads, a new measurement concept will be proposed in which the cable connections from the measurement device to the battery are simply reversed with respect to a standard configuration. The schematic equivalent circuit for this reversed connection concept is shown in Fig. 7.1e. It can be seen that this measurement setup reveals the same unbalance with respect to Fig. 7.1b, but now it is reversed. Z_P^m for the reversed configuration ($Z_{P,r}^m$) can be derived similarly as for the standard configuration. The resulting expression for $Z_{P,r}^m$ in the reversed configuration then becomes

$$Z_{P,r}^m = K_2 Z_P + \left(Z_N + Z_l^{WE}\right)(K_2 - K_1) \ , \tag{7.19}$$

where

$$K_1 = \frac{Z_{in}}{Z_{in} + Z_l^S + Z_{\mu REF}} \tag{7.20}$$

and

$$K_2 = \frac{Z_{in}}{Z_{in} + Z_l^{RE}} \ . \tag{7.21}$$

As $Z_l^{RE} = Z_l^S \ll Z_{in}$, it can be seen from Eq. 7.21 that K_2 approaches 1. Eq. 7.19 can then be reduced to

$$Z_{P,r}^m = Z_P + \left(Z_N + Z_l^{WE}\right)(1 - K_1) \ . \tag{7.22}$$

From Eq. 7.22, it can be concluded that both Z_N and Z_l^{WE} contribute to $Z_{P,r}^m$ if K_1 does not converge to 1. This will again result in measurement artefacts. Voltage divider K_1 is frequency-dependent and always smaller than 1. $\left(Z_N + Z_l^{WE}\right)$ is multiplied with a small positive gain $(1 - K_1)$ and this product contributes to $Z_{P,r}^m$, especially at high frequencies. Particularly, the inductive tail will be extended in the same direction. The effect explained in Section 7.2.3, in which impedance spectra deviate to the opposite direction, can therefore be compensated by using the reversed configuration. The measured impedance for the reversed N ($Z_{N,r}^m$) can be calculated similarly as for the reversed P ($Z_{P,r}^m$) by replacing Z_P by Z_N and Z_N by Z_P in Eq. 7.22. The corresponding electronic network scheme is shown in Fig. 7.1f.

Fig. 7.2e shows the cable connections to experimentally determine the impedance of P *vs* µREF in the reversed cable connection set-up. In this configuration, WE changes position with CE and S with RE in comparison to the standard configuration (Fig. 7.2b). The connections to measure the reversed N impedance spectra are shown in Fig. 7.2f.

7.2.6. Lead-impedance compensation

The contribution of Z_l^{WE} (Eqs. 7.13 and 7.22) can now easily be compensated by averaging the standard and reversed configurations. Therefore, the measurement artefacts contributing from the lead impedances can be fully compensated. Obviously, this does not work if the impedance of N is much larger than that of P (see Eq. 7.22). However, in (commercial) Li-ion batteries the impedance of both electrodes are of the same order of magnitude. Taking the average of Eqs. 7.13 and 7.22 leads to

$$\overline{Z_P^m} = \frac{1}{2}\left\{Z_P^m + Z_{P,r}^m\right\} = \frac{1}{2}\left\{Z_P\left(1+K_1\right) + Z_N\left(1-K_1\right)\right\} \ , \tag{7.23}$$

where

$$K_1 = \frac{Z_{in}}{Z_{in} + Z_l^S + Z_{\mu REF}} \tag{7.24}$$

in which $Z_l^S = Z_l^{RE}$. If $Z_l^{RE} = Z_l^S \ll Z_{in}$, K_1 can be reduced to

$$K_1 = \frac{Z_{in}}{Z_{in} + Z_{\mu REF}} \ . \tag{7.25}$$

From Eq. 7.23, it can be concluded that Z_l^{WE} has been canceled out, despite the fact that it is always present in the expressions for the standard and reversed configurations (Eqs. 7.13 and 7.22). This implies that this simple averaging method gives us the opportunity to fully compensate for the lead impedances, which can be a significant source of measurement artefacts, especially for measurements at remote locations using long measurement leads. The compensated impedance for N ($\overline{Z_N^m}$) can be calculated in a similar way as for P ($\overline{Z_P^m}$), by replacing Z_P by Z_N and Z_N by Z_P in Eq. 7.23.

Note that reversing the cable connections (Fig. 7.2e and f) essentially only needs to be done with WE and CE to let this method work. Reversing S and RE is only done in order to get the impedance spectra in the correct complex plane quadrant during the measurements. Obviously, this can also be performed by post-processing the measurement data.

The proposed averaging impedance concept results in five individual impedance measurements, *i.e.* the battery impedance and the impedances of P and N in both the standard and reversed configuration. The impedance measurement at the battery (Fig. 7.2a) only has to be performed once since reversing the cable connections has obviously no influence on the battery result, which can be easily mathematically validated by considering the derivations described in Section 7.2.2

for the reversed configuration. The measurement concept derived above will be experimentally investigated using multi-electrode batteries, of which the results are described in Section 7.4.

7.3. Experimental details

7.3.1. Battery construction

Pouch-type batteries are made with electrode dimensions of 72 x 190 mm (width x length). Each battery consists of six positive and seven negative electrodes, which are separated by Celgard 2400 separators. Each electrode has an external current collector extension of 20 x 20 mm. A schematic representation of such an electrode stack is shown in Fig. 7.3a. The P and N electrodes are stacked in parallel and the complete battery stack is inserted into an Al-polymer pouch which is sealed after the electrolyte has been added. In order to put some pressure on the as-produced batteries, they are clamped between two solid plates connected with bolts.

The positive electrode material used in this study is Lithium Nickel Manganese Cobalt Oxide with composition $LiNi_{0.5}Mn_{0.3}Co_{0.2}O_2$ coated onto aluminum current collectors. Copper current collectors coated with graphite are used as negative electrodes. The pouch is filled with PuriEL battery electrolyte from Soulbrain (Korea) with composition of 1M $LiPF_6$ in 1/1/1 ethylene carbonate/diethyl carbonate/ethyl methyl carbonate + 2 wt.% vinylene carbonate solution.

7.3.2. Preparation of micro-reference electrodes

Insulated (Enamel) copper wires with radius of 100 μm and length of 300 mm are used as μREF. In total seven μREF are inserted into the battery with varying metallic Cu tip-lengths in order to investigate the influence of the μREF impedance on the measurement artefacts. The isolation at both ends is removed by immersing the wires into sulfuric acid, followed by rinsing in ethanol. The unprotected Cu wires, later acting as reference electrodes, are cut into seven different lengths, ranging from 0.5 to 50 mm in a logarithmic order. The other ends are used to make connection with the measurement equipment. Fig. 7.3b shows that the μREF are inserted transversely between four separator sheets (two on both sides) to prevent physical contact with the electrodes. Using this construction, it can be assumed that the distance from the μREF to the positive and negative electrode is equal. The uninsulated ends are positioned in the central part of the battery stack.

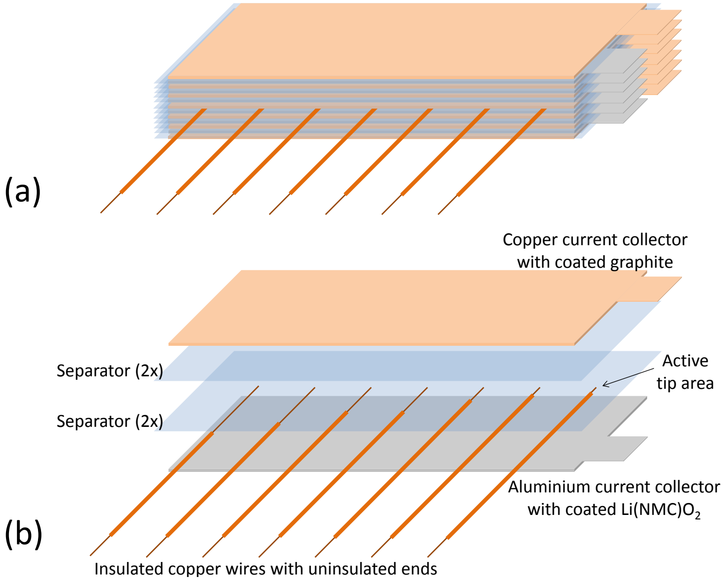

Fig. 7.3: Schematic representation of an electrode stack with seven integrated μREF (a), and enlargement of seven μREF in-between P and N (b). Note that on both sides of the μREF two separator sheets are used to isolate them from the electrodes.

7.3.3. Electrochemical measurements

Automatic battery cycling equipment (Maccor 2300) is used to activate and (dis)-charge the batteries. Initially, all batteries are activated for four cycles using a constant current, constant voltage (CCCV) procedure. CC charging is performed with a current of 0.4 A until the cut-off voltage of 4.2 V is reached. Subsequently, the battery is charged at CV of 4.2 V till a cut-off current of 0.02 A is reached. After charging a resting period of 2 h is applied followed by a 0.4 A discharge with a cut-off voltage of 2.7 V. In addition to these relatively low-current initialization cycles, four cycles with a charge and discharge current of 2 and 4 A are applied, respectively. Finally, the nominal discharge capacity of 3.5 Ah is reached after full activation.

After activation, the batteries are completely charged (CCCV) and metallic lithium is galvanostatically deposited onto the unprotected Cu tips of all μREF in order to get a stable lithium reference electrode potential. A 6 μm deposition layer thickness is chosen for all μREF. The lithium is deposited from both P and N in order to obtain uniform layers around the wires. For a detailed description of the deposition and stability of lithium metal micro-reference electrodes, we refer to the work of Zhou and Notten [11].

Galvanostatic EIS measurements are performed at room temperature and at a voltage of 4.140 V for 50 logarithmically distributed frequencies in the range of 0.1 Hz to 30 kHz with an Autolab PGSTAT302N (Metrohm Autolab) and with an IviumStat (Ivium Technologies). The applied AC current excitation is set to 300 mA. This amplitude gives a good signal-to-noise ratio with optimum linear response. The EIS measurements are performed with complete batteries (Bat) and with P and N measured with respect to all seven µREF.

The impedances of the individual µREF are also measured. However, since the impedances of the µREF are much larger than those of the batteries, the potentiostatic mode is now used. The applied voltage excitation is set to 1 mV for all µREF, except for the 0.5 mm µREF, which is set to 5 mV in order to increase the signal-to-noise ratio.

All measurements are performed in an argon-filled glovebox. The cable length of the measurement cables of the Autolab is 1.5 m and the cable length from the feed-through to the battery inside the glovebox is approximately 2 m.

7.4. Results and discussion

7.4.1. Positive and negative electrode impedances

Fig. 7.4a and b shows the measured impedances for P and N, respectively, measured with respect to six different µREF. Measurement artefacts can clearly be seen, especially in the high-frequency range of the spectra. The artefacts are most dominant for the µREF with the smallest active tip-length of 0.5 mm and they strongly reduce with increasing tip length. It can be seen that the P and N impedance spectra are curling upwards in the high-frequency range. It is obvious that these impedance measurements are highly influenced by the measurement setup configuration. On the other hand, the mid-frequency and low-frequency range are showing the expected characteristic semicircles.

Fig. 7.4c shows the impedance summations (P + N) of the P and N spectra measured according to Figs. 7.1b-c and 7.2b-c together with the measured impedance for the complete battery (Figs. 7.1a and 7.2a). In the high-frequency range, the added spectra clearly show large discrepancies with respect to that of the battery (Bat). This especially holds for the µREF with short tip lengths and strongly reduces for increasing lengths. The µREF with a tip length of 50 mm shows the best results in comparison to Bat and is, therefore, favorable to use in this battery configuration. For the low-frequency range, it can be concluded that the summations of P and N are in perfect agreement with the Bat results.

Evidently, these measurement results reveal that the high-frequency part suffers

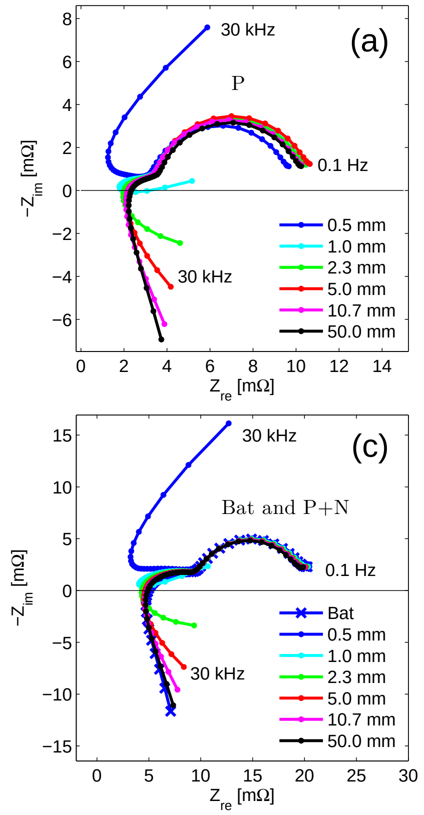

Fig. 7.4: Impedances of P (a) and N electrode (b) measured with respect to µREF with different tip lengths. Comparison of the measured battery impedance (Bat) and the summation of P and N (c). For clarity reasons the results for the 23.2 mm long µREF have been excluded.

from measurement artefacts, especially for µREF with short tip lengths. In order to investigate the µREF characteristics in more detail, their impedances are measured with respect to the low-impedance P. The results are shown in the Bode plots of Fig. 7.5. From these measurements, it can be seen that the µREF with an active tip length of 0.5 mm (blue line) has the highest impedance and that with an active tip length of 50 mm (black line) reveals the lowest impedance. Decreasing impedances with increasing tip lengths are indeed to be expected as the active surface area of the 50 mm tip is about two orders of magnitude larger than that of the 0.5 mm tip.

Following the mathematical analysis in Section 7.2, in particular K_1 (see for example Eqs. 7.11 and 7.20), it is evident that the measured artefacts become more dominant for µREF with smaller tip lengths. The reason is that K_1 will not converge

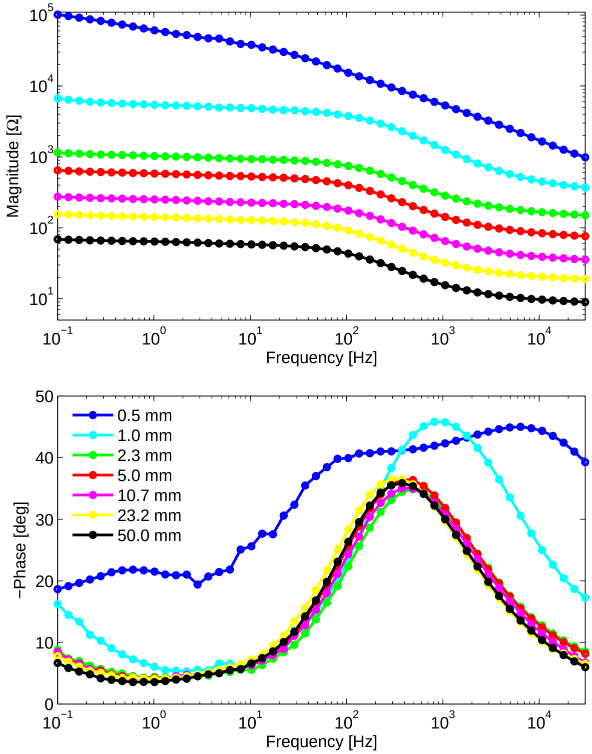

Fig. 7.5: Bode plots of the various µREF measured with respect to the low-impedance P. The tip length of the µREF are indicated in the legend.

to 1 anymore when the µREF impedance becomes too large. For the µREF with the smallest tip length (0.5 mm) this effect is most dominant and the measured electrode impedance starts to deviate. Since the gain $(K_1 - 1)$ in Eq. 7.13 is negative, the high-frequency inductive impedance spectra in Fig. 7.4 bend towards the capacitive region. With increasing tip lengths, K_1 starts to converge to 1 and the gain $(K_1 - 1)$ therefore decreases. This results in a reduction of the artefacts, which now appear clockwise towards the inductive region.

As almost artefact-free impedance spectra can be measured with large-surface-area µREF (see Fig. 7.4), the 0.5 mm µREF is used in the following sections in order to show that the presented compensation method properly operates. Obviously, the compensation method is effective for all µREF, independent on its surface area.

7.4.2. Capacitor-bridge compensation

Fig 7.6a shows the uncompensated EIS measurement results for Bat (dark blue curve) and for P (light blue curve) and N (green curve) measured with respect to a µREF with a tip length of 0.5 mm. As concluded in Section 7.4.1, P and N measurements severely suffer from artefacts in the high-frequency range. Obviously, the summation curve (red curve in Fig. 7.6a) also clearly reveals the presence of these artefacts in the high-frequency range. However, the summation curve agrees perfectly well with the measured Bat curve in the low-frequency range.

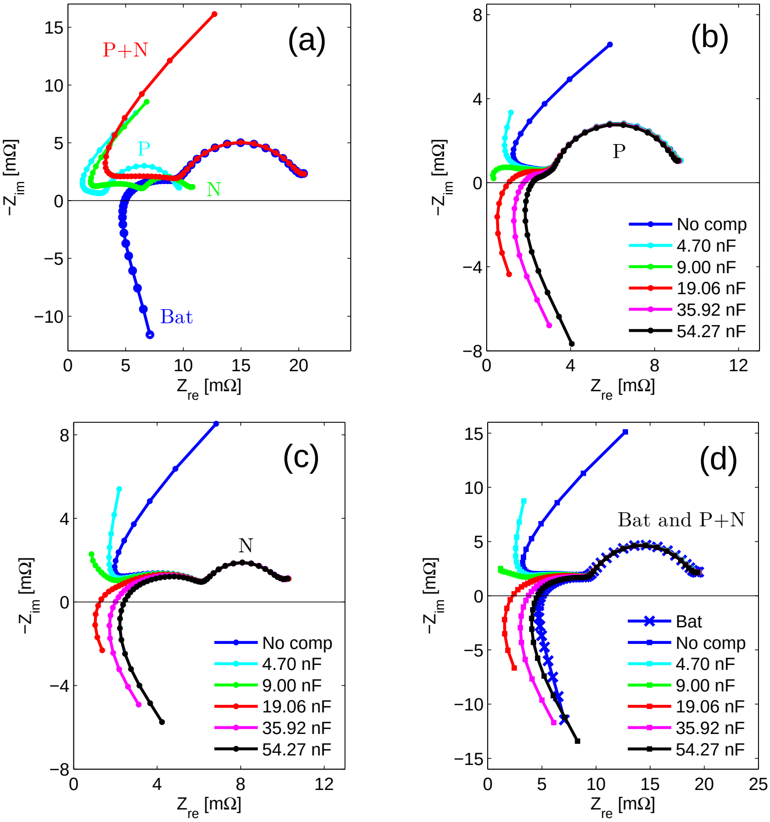

Fig. 7.6: EIS measurements at Bat and both the individual P and N electrode measured with respect to the µREF with active tip length of 0.5 mm and summation (P + N) impedance curve (a). EIS measurements without capacitor compensation (No comp) and with capacitor compensation at P (b) and N (c). Comparison of Bat impedance spectrum and all summation curves of P + N (d).

Fig. 7.6b shows the various compensated EIS measurements of P with respect to the µREF with tip length of 0.5 mm. For these measurements various off-theshelf capacitors have been placed between RE and CE in accordance with Figs. 7.1d and 7.2d to compensate for leakage currents. An EIS measurement without using a capacitor bridge is also shown as reference (dark blue curve). From these results, it can be concluded that the high-frequency artefacts systematically decrease with increasing capacitor values. The same measurements have been performed for N with respect to the μREF with a tip length of 0.5 mm and similar results are found, as shown in Fig. 7.6c.

In order to verify what capacitor value would be the most optimal compensation for the present artefacts, the P and the N impedance are added together for each capacitor and compared to the impedance spectrum of Bat (Fig. 7.6d). These results show that the capacitors with values 35.92 nF (pink curve) and 54.27 nF (black curve) are in close agreement with the Bat result (dark blue curve). These values are comparable to the 100 nF capacitor, which was also favorably selected by Battistel *et al.* [16]. Using higher capacitor values would lead to higher discrepancies between Bat and the summation of P and N.

From these results, it can be concluded that tuning a capacitor bridge to the battery system under consideration is not straightforward and is quite time-consuming. Moreover, relatively large deviations in the high frequencies can still be found between the summation of P and N in comparison to Bat (Fig. 7.6d). Consequently, an accurate EIS analysis of the high-frequency part of the individual electrodes is not possible.

7.4.3. Lead-impedance compensation

In Section 7.2, a new concept has been proposed to compensate for the high-frequency EIS measurement artefacts, simply by reversing the measurement cables. In Fig. 7.7, the measured impedance spectra for all measurement combinations described in Section 7.2 are shown in the complex plane. Both P (light blue curve) and N (green curve) impedances are measured with respect to μREF with an active tip length of 0.5 mm. Also the summations of the P and N impedance spectra (red curve) for both the standard and reversed measurements are shown. The Bat results are represented by the dark blue curve.

Fig. 7.7a shows the measured impedance spectra with the cables in the standard measurement configuration in accordance to the connections shown in Fig. 7.2a, b and c. The same measurement results are also shown in Fig. 7.6a, but are reproduced here in order to properly compare with the results obtained with the reversed cable connections in Fig. 7.7b.

Fig. 7.7b shows the impedance results obtained with the cables in the reversed connections, *i.e.* according to the connections shown in Fig. 7.2a, e and f. For

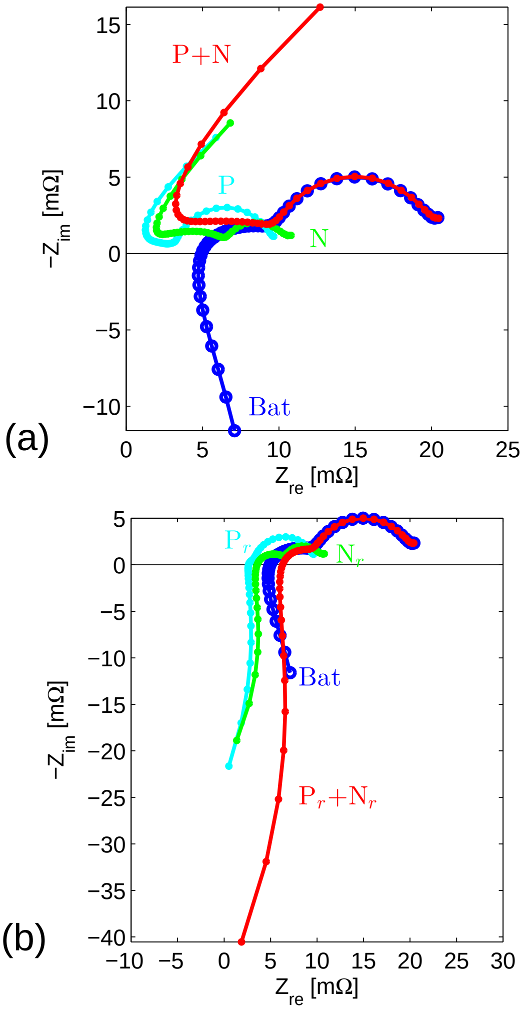

Fig. 7.7: Measurement artefacts in the high-frequency range of the impedance spectra measured with a standard cable connection configuration (a), and with reversed cable connection set-up (b).

the reversed impedance measurements of the positive and negative electrode (P_r and N_r), it can be seen that a high-frequency tail is located in the inductive region (positive imaginary values) of the impedance. However, the tails are reaching relatively far in the inductive area and also bend somewhat to the left, which is atypical for inductive behavior. From the reversed measurements, it can clearly be seen that the artefacts are moving into the opposite direction in comparison to the standard configuration of Fig. 7.7a. These experiments prove the theory, which has been described in Section 7.2.5. The gain $(1 - K_1)$ is positive due to the unbalance in this measurement configuration and, therefore, the inductive tail is extended into the inductive region (see Eq. 7.22). Furthermore, Fig. 7.7b shows that the $P_r + N_r$ curve does not match Bat either in the high-frequency range. Like for the standard measurement configuration (Fig. 7.7a), the summation curves are only in good agreement with the Bat result in the low-frequency range. From these results, it can be concluded that the individual impedance measurements of P, N, P_r, and N_r in the high-frequency range cannot be directly used since measurement artefacts are influencing these significantly.

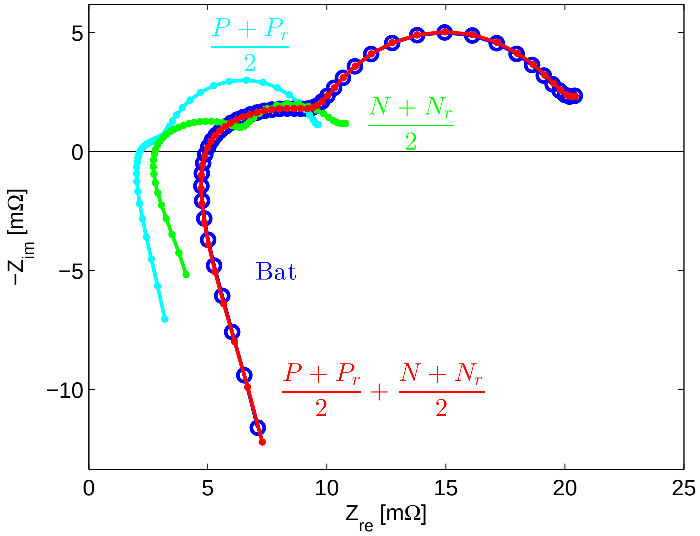

Fig. 7.8: Artefact-compensated impedance spectra. EIS measurements for P and N are performed on a µREF with an active tip length of 0.5 mm.

The result of the new averaging method that is proposed in Section 7.2, is shown in Fig. 7.8. It can be seen that the impedance spectra of P (light-blue curve) and N (green curve) are now close to artefact-free in the high-frequency range. The upward-bending behavior of the summation impedance curve in Fig. 7.7a and the high-frequency inductive tail found with the reversed measurement set-up in Fig. 7.7b have now completely disappeared, as shown by the red curve in Fig. 7.8. Moreover, the summation of the P and N impedance is in very good agreement with the Bat result (dark blue curve) along the whole frequency range. From these results, it can be concluded that the proposed averaging method operates effectively and that the artefacts caused by the lead impedances can indeed be fully compensated. By applying this method the EIS measurements on three-electrode battery systems can be much more accurately analyzed. In comparison to the capacitor-bridge compensation method, the proposed averaging method is also more accurate and easier to apply.

Similar artefacts were measured with other electrochemical measurement equipment (Ivium Technologies) and on smaller-capacity three-electrode batteries, which were made in-house with the Lithylene technology [11, 41]. It was found that high frequency artefacts in all cases can be fully compensated by adopting this new compensation method. Moreover, measuring in the potentiostatic mode, *i.e.* applying an AC voltage and measuring the resulting AC current, resulted in similar artefacts as in the described galvanostatic mode but these can also be fully eliminated by the described compensation method.

7.4.4. Simulations

In order to validate the artefact models developed in Section 7.2, simulations are performed and compared with the impedance measurements. For the model simulations the true values for Z_P and Z_N should be known. However, these values are not known beforehand but can now be easily obtained from the compensated impedance measurements, described in Section 7.4.3. The models also require the input impedances for the measurement device (Z_{in}), the lead impedances (Z_l^i), and the various μREF impedances ($Z_{\mu REF}$). Since the μREF impedances have been determined experimentally (see Section 7.4.1), these values will be used as model input parameters in the simulations. Z_{in} and Z_l^i can then be determined by applying an optimization algorithm.

Figs. 7.9 and 7.10 compare the measured and simulated impedance results for P and N, respectively, measured with respect to the various μREF (0.5, 1.0, 2.3 and 5.0 mm). Since the artefacts are only minor for the longer μREF, these results are therefore not shown. The blue curves show the compensated (averaged) measurements (Section 7.4.3). The green curves show the experimental results including measurement artefacts and the red lines show the simulations of the artefact models.

Fig. 7.9a-d show the simulations for P (conventional configuration), using the model presented in Eq. 7.13. In Fig. 7.10a-d the same simulations are shown for N (note that now Z_P is replaced by Z_N in Eq. 7.13). From these results, it can be concluded that the artefact model is in good agreement with the measurements for all μREF. Fig. 7.9e-h show the simulations for P_r (reversed configuration) using the model presented in Eq. 7.22. Similarly, the same simulations are shown for N_r in Fig. 7.10e-h (note that Z_P is replaced by Z_N and *vice versa* in Eq. 7.22). Again, all

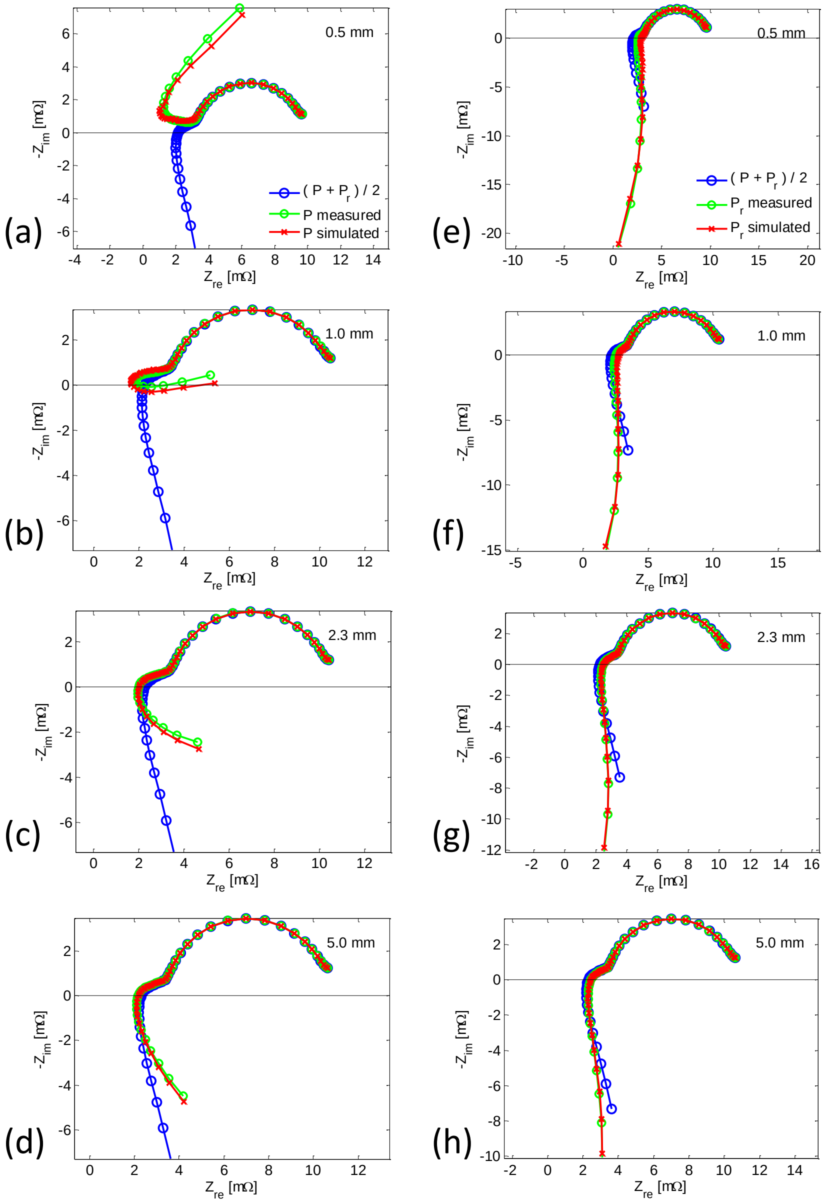

Fig. 7.9: Measured and simulated impedance spectra of P with respect to various μREF with indicated lengths (0.5, 1.0, 2.3 and 5.0 mm) obtained with standard (a-d) and reversed cable connection set-up (e-h). The blue curves show the compensated (averaged) measured impedance of P, the green curves show the measured (uncompensated) P impedance, including artefacts, and the red curves shows the uncompensated simulations.

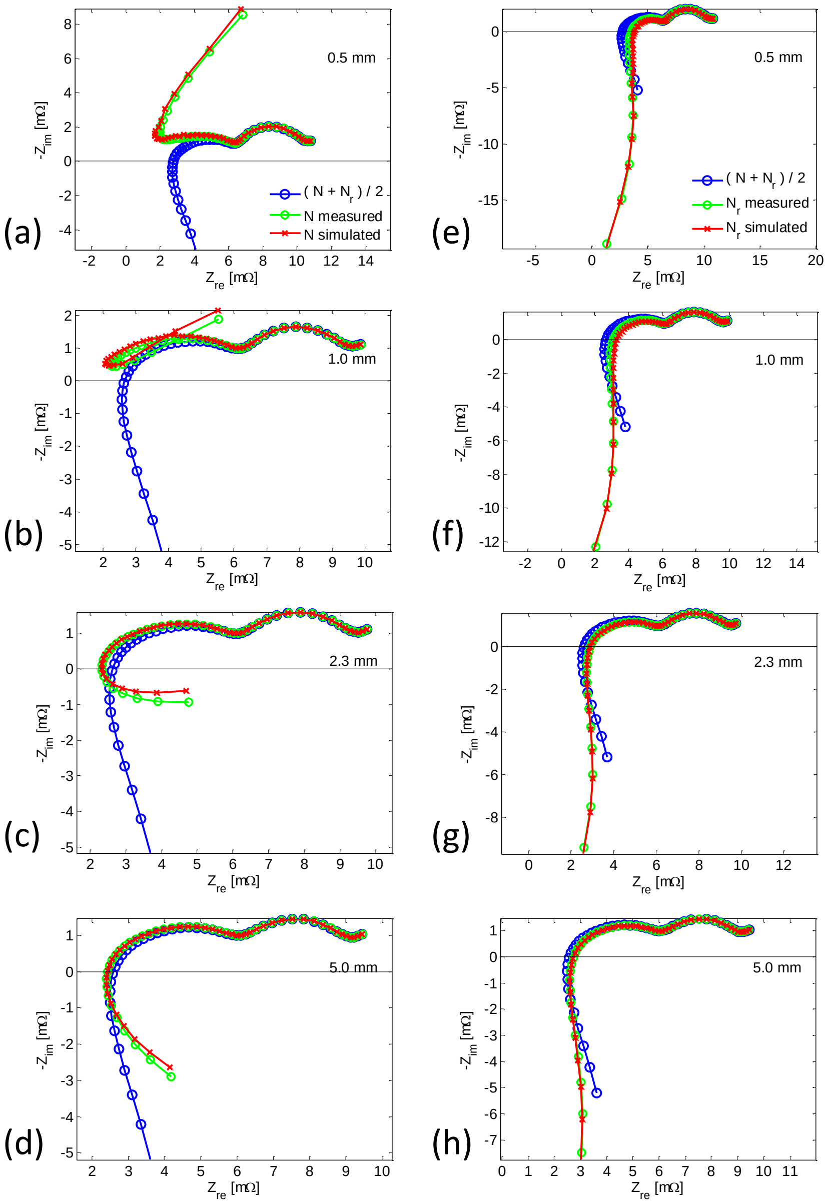

Fig. 7.10: Measured and simulated impedance spectra of N with respect to various µREF with indicated lengths (0.5, 1.0, 2.3 and 5.0 mm) obtained with standard (a-d) and reversed cable connection set-up (e-h). The blue curves show the compensated (averaged) measured impedance of N, the green curves show the measured (uncompensated) N impedance, including artefacts, and the red curves shows the uncompensated simulations.

simulation results are in very good agreement with the measurements.

In Fig. 7.11a and b, the simulations with the ideal capacitor bridge (red line) are shown for P and N, respectively, simulated with respect to the 0.5 mm long µREF. For this simulation the model developed in Appendix A.4 is used in combination with the ideal capacitor bridge described by Eq. 7.17. In Fig. 7.11a and b, it can be seen that the simulations are in perfect agreement with the averaged measurements for both P (a) and N (b) electrodes. Note that the compensated impedances (blue lines) described in Section 7.4.3 are shown for comparison.

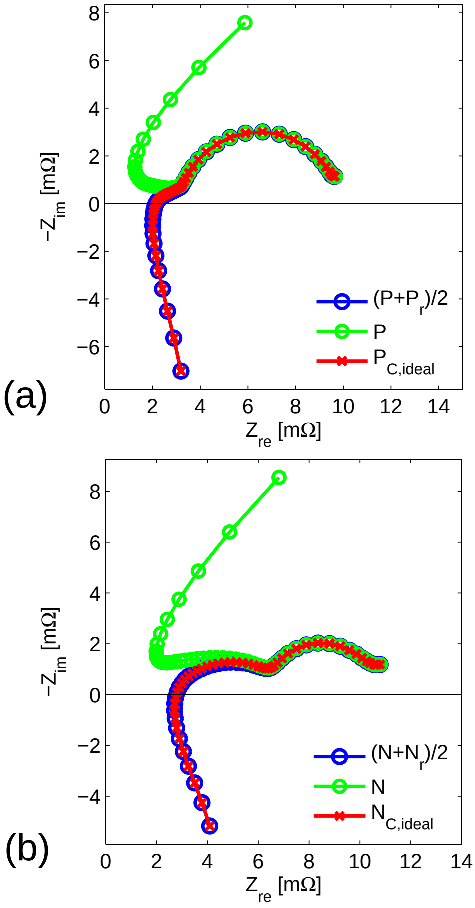

Fig. 7.11: Impedance spectra of P (a) and N (b) measured with respect to the µREF with the smallest tip length of 0.5 mm. Simulations with an ideal capacitor bridge (red) are compared to the proposed compensation method (blue). The measurements with artefacts are shown (green) for convenience.

Although the capacitor-bridge simulations are in perfect agreement with the averaged measurements, it does not imply that the capacitance has a fixed value along the investigated frequency range. Using Eq. 7.18, the capacitance has been calculated for each frequency of which the results are shown in Fig. 7.12 for both P and N. These results clearly show that the capacitance, in the case of ideal compensation, indeed strongly depends on the frequency. This might explain why the capacitor-bridge measurement results (Fig. 7.6), using fixed capacitor values, do not fully converge to the correct impedances. Comparing the simulated capacitances in Fig. 7.12 to the capacitances used in Fig. 7.6, it can be concluded that these are of the same order of magnitude. However, the values found in Fig. 7.12 are somewhat lower. This might be explained by the fact that the used equivalent-circuit models are oversimplified with respect to the real measurement system where stray-capacitances, inductances and other circuitries inside the measurement device might be present. However, from the presented simulation results it can be concluded that the developed models qualitatively show good agreement with the measurements.

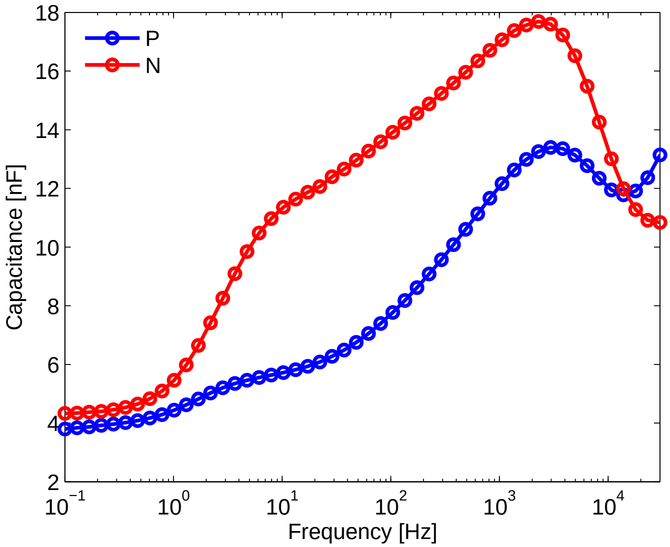

Fig. 7.12: Capacitance as a function of frequency for an ideal capacitor bridge.

7.5. Conclusions

High-frequency three-electrode EIS measurement artefacts are found for Li-ion batteries with integrated lithium µREF. This makes a detailed impedance analysis of the individual electrodes unreliable and inaccurate. It has been found that EIS artefacts are a function of the µREF impedance, more particularly dependent on the active area of the µREF tip. The impedance of µREF should therefore be selected as small as possible in order to reduce these artefacts. However, large-surface-area µREF are not always favorable. Therefore, a method to compensate artefacts for high-impedance µREF has been developed, simply by averaging two individual three-electrode measurements. By using this method the measurement lead impedance, contributing significantly to artefacts, can be fully compensated. The proposed averaging method shows better results than measurements performed with an artefact-compensating capacitor bridge and is easier to apply. The proposed compensation method is therefore readily applicable to three-electrode electrochemical systems with high-impedance µREF, making a detailed impedance analysis and (N)ZIF possible.

Mathematical artefact models based on simplified equivalent circuit models have been developed. These models have been used to simulate the impedance measurements, including artefacts. The model simulations are in good agreement with the measurements.

References

[1] L. Raijmakers, M. Lammers, and P. Notten, *A new method to compensate impedance artefacts for Li-ion batteries with integrated micro-reference electrodes,* Electrochim. Acta **259**, 517 (2018).

[2] M. Dollé, F. Orsini, A. S. Gozdz, and J.-M. Tarascon, *Development of Reliable Three-Electrode Impedance Measurements in Plastic Li-Ion Batteries,* J. Electrochem. Soc. **148**, A851 (2001).

[3] M. Itagaki, K. Honda, Y. Hoshi, and I. Shitanda, *In-situ EIS to determine impedance spectra of lithium-ion rechargeable batteries during charge and discharge cycle,* J. Electroanal. Chem. **737**, 78 (2015).

[4] E. McTurk, C. R. Birkl, M. R. Roberts, D. A. Howey, and P. G. Bruce, *Minimally Invasive Insertion of Reference Electrodes into Commercial Lithium-Ion Pouch Cells,* ECS Electrochem. Lett. **4**, A145 (2015).

[5] G. Nagasubramanian, *Two- and three-electrode impedance studies on 18650 Li-ion cells,* J. Power Sources **87**, 226 (2000).

[6] G. Nagasubramanian and D. H. Doughty, *18650 Li-ion cells with reference electrode and in situ characterization of electrodes,* J. Power Sources **150**, 182 (2005).

[7] T. Osaka, D. Mukoyama, and H. Nara, *Review—Development of Diagnostic Process for Commercially Available Batteries, Especially Lithium Ion Battery, by Electrochemical Impedance Spectroscopy,* J. Electrochem. Soc. **162**, A2529 (2015).

[8] J. Y. Song, H. H. Lee, Y. Y. Wang, and C. C. Wan, *Two- and three-electrode impedance spectroscopy of lithium-ion batteries,* J. Power Sources **111**, 255 (2002).

[9] M.-S. Wu, P.-C. J. Chiang, and J.-C. Lin, *Electrochemical Investigations on Advanced Lithium-Ion Batteries by Three-Electrode Measurements,* J. Electrochem. Soc. **152**, A47 (2005).

[10] Q. Wu, W. Lu, and J. Prakash, *Characterization of a commercial size cylindrical Li-ion cell with a reference electrode,* J. Power Sources **88**, 237 (2000).

[11] J. Zhou and P. H. L. Notten, *Development of Reliable Lithium Microreference Electrodes for Long-Term In Situ Studies of Lithium-Based Battery Systems,* J. Electrochem. Soc. **151**, A2173 (2004).

[12] J. Zhou and P. Notten, *Studies on the degradation of Li-ion batteries by the use of microreference electrodes,* J. Power Sources **177**, 553 (2008).

[13] F. La Mantia, C. D. Wessells, H. D. Deshazer, and Y. Cui, *Reliable reference electrodes for lithium-ion batteries,* Electrochem. commun. **31**, 141 (2013).

[14] S. Solchenbach, D. Pritzl, E. Jia, Y. Kong, J. Landesfeind, and H. A. Gasteiger, *A Gold Micro-Reference Electrode for Impedance and Potential Measurements in Lithium Ion Batteries,* J. Electrochem. Soc. **163**, A2265 (2016).

[15] M. Klett, J. A. Gilbert, S. E. Trask, B. J. Polzin, A. N. Jansen, D. W. Dees, and D. P. Abraham, *Electrode Behavior RE-Visited: Monitoring Potential Windows , Capacity Loss, and Impedance Changes in* $Li_{1.03}(Ni_{0.5}Co_{0.2}Mn_{0.3})_{0.97}O_2$*/Silicon-Graphite Full Cells,* J. Electrochem. Soc. **163**, 875 (2016).

[16] A. Battistel, M. Fan, J. Stojadinović, and F. La Mantia, *Analysis and mitigation of the artefacts in electrochemical impedance spectroscopy due to three-electrode geometry,* Electrochim. Acta **135**, 133 (2014).

[17] C. Bunzli, H. Kaiser, and P. Novak, *Important Aspects for Reliable Electrochemical Impedance Spectroscopy Measurements of Li-Ion Battery Electrodes,* J. Electrochem. Soc. **162**, A218 (2014).

[18] D. W. Dees, A. N. Jansen, and D. P. Abraham, *Theoretical examination of reference electrodes for lithium-ion cells,* J. Power Sources **174**, 1001 (2007).

[19] C. Delacourt, P. L. Ridgway, V. Srinivasan, and V. Battaglia, *Measurements and Simulations of Electrochemical Impedance Spectroscopy of a Three-Electrode Coin Cell Design for Li-Ion Cell Testing,* J. Electrochem. Soc. **161**, A1253 (2014).

[20] M. Ender, A. Weber, and E. Ivers-Tiffée, *Analysis of Three-Electrode Setups for AC-Impedance Measurements on Lithium-Ion Cells by FEM simulations,* J. Electrochem. Soc. **159**, A128 (2012).

[21] Y. Hoshi, Y. Narita, K. Honda, T. Ohtaki, I. Shitanda, and M. Itagaki, *Optimization of reference electrode position in a three-electrode cell for impedance measurements in lithium-ion rechargeable battery by finite element method,* J. Power Sources **288**, 168 (2015).

[22] S. Klink, D. Höche, F. La Mantia, and W. Schuhmann, *FEM modelling of a coaxial three-electrode test cell for electrochemical impedance spectroscopy in lithium ion batteries,* J. Power Sources **240**, 273 (2013).

[23] S. Klink, E. Madej, E. Ventosa, A. Lindner, W. Schuhmann, and F. La Mantia, *The importance of cell geometry for electrochemical impedance spectroscopy in three-electrode lithium ion battery test cells,* Electrochem. commun. **22**, 120 (2012).

[24] M. D. Levi, V. Dargel, Y. Shilina, D. Aurbach, and I. C. Halalay, *Impedance Spectra of Energy-Storage Electrodes Obtained with Commercial Three-Electrode Cells: Some Sources of Measurement Artefacts,* Electrochim. Acta **149**, 126 (2014).

[25] H. Brandstätter, I. Hanzu, and M. Wilkening, *Myth and Reality about the Origin of Inductive Loops in Impedance Spectra of Lithium-Ion Electrodes — A Critical Experimental Approach,* Electrochim. Acta **207**, 218 (2016).

[26] M. Ender, J. Illig, and E. Ivers-Tiffée, *Three-Electrode Setups for Lithium-Ion Batteries I . Fem-Simulation of Different Reference Electrode Designs and Their Implications for Half-Cell Impedance Spectra,* J. Electrochem. Soc. **164**, 71 (2017).

[27] J. Costard, M. Ender, M. Weiss, and E. Ivers-Tiffée, *Three-Electrode Setups for Lithium-Ion Batteries II . Experimental Study of Different Reference Electrode Designs and Their Implications for Half-Cell Impedance Spectra,* J. Electrochem. Soc. **164**, 80 (2017).

[28] I. Jiménez Gordon, S. Grugeon, A. Débart, G. Pascaly, and S. Laruelle, *Electrode contributions to the impedance of a high-energy density Li-ion cell designed for EV applications,* Solid State Ionics **237**, 50 (2013).

[29] D. D. Edwards, J. Hwang, S. J. Ford, and T. O. Mason, *Experimental limitations in impedance spectroscopy: Part V. Apparatus contributions and corrections,* Solid State Ionics **99**, 85 (1997).

[30] Y. Feng, G. Zhou, and S. Cai, *Explanation of high-frequency phase shift in ac impedance measurements for copper in low-conductivity media,* Electrochim. Acta **36**, 1093 (1991).

[31] S. Fletcher, *The two-terminal equivalent network of a three-terminal electrochemical cell,* Electrochem. commun. **3**, 692 (2001).

[32] G. Hsieh, S. J. Ford, T. O. Mason, and L. R. Pederson, *Experimental limitations in impedance spectroscopy: Part I - simulation of reference electrode artifacts in three-point measurements,* Solid State Ionics **91**, 191 (1996).

[33] F. Mansfeld, S. Lin, Y. C. Chen, and H. Shih, *Minimization of High-Frequency Phase Shifts in Impedance Measurements,* J. Electrochem. Soc. **135**, 906 (1988).

[34] A. Tran, F. Huet, K. Ngo, and P. Rousseau, *Artefacts in electrochemical impedance measurement in electrolytic solutions due to the reference electrode,* Electrochim. Acta **56**, 8034 (2011).

[35] C. C. Herrmann, G. G. Perrault, and A. A. Pilla, *Dual Reference Electrode for Electrochemical Pulse Studies,* Anal. Chem. **40**, 1173 (1968).

[36] D. R. Baker, M. W. Verbrugge, and X. X. Hou, *A Simple Formula Describing Impedance Artifacts due to the Size and Surface Resistance of a Reference-Electrode Wire in a Thin-Film Cell,* J. Electrochem. Soc. **164**, A407 (2017).

[37] L. H. J. Raijmakers, D. L. Danilov, J. P. M. Van Lammeren, M. J. G. Lammers, and P. H. L. Notten, *Sensorless battery temperature measurements based on electrochemical impedance spectroscopy,* J. Power Sources **247**, 539 (2014).

[38] J. P. Schmidt, S. Arnold, A. Loges, D. Werner, T. Wetzel, and E. Ivers-Tiffée, *Measurement of the internal cell temperature via impedance: Evaluation and application of a new method,* J. Power Sources **243**, 110 (2013).

[39] H. P. G. J. Beelen, L. H. J. Raijmakers, M. C. F. Donkers, P. H. L. Notten, and H. J. Bergveld, *A comparison and accuracy analysis of impedance-based temperature estimation methods for Li-ion batteries,* Appl. Energy **175**, 128 (2016).

[40] L. H. J. Raijmakers, D. L. Danilov, J. P. M. V. Lammeren, M. J. G. Lammers, H. J. Bergveld, and P. H. L. Notten, *Non-Zero Intercept Frequency: An Accurate Method to Determine the Integral Temperature of Li-Ion Batteries,* IEEE Trans. Ind. Electron. **63**, 3168 (2016).

[41] P. Notten, M. Ouwerkerk, H. van Hal, D. Beelen, W. Keur, J. Zhou, and H. Feil, *High energy density strategies: from hydride-forming materials research to battery integration,* J. Power Sources **129**, 45 (2004).

8

Impedance-based temperature determination unraveled by micro-reference electrodes

In the present work, (N)ZIF values of the complete battery (Bat), the positive electrode (P) and the negative electrode (N) are extracted from the corresponding impedance spectra in order to investigate what electrode is responsible for the (N)ZIF behavior of Bat. It has been found that the impedance of both electrodes is temperature-dependent and that the (N)ZIF of Bat, P, and N all decrease with increasing battery temperature. It also has been found that both individual electrodes contribute to Bat (N)ZIF and are therefore both responsible for its behavior. Since P and N (N)ZIF are temperature-dependent, impedance-based temperature indication through (N)ZIF measurements essentially can also be performed on the individual electrodes. For the investigated batteries, (N)ZIF values of N are more sensitive to temperature changes in comparison to that of P, leading to steeper N (N)ZIF curves than that of P, which is favorable for the temperature indication accuracy. Furthermore, the electrode revealing the highest imaginary value of the impedance in the inductive quadrant of the complex plane is the electrode that dominates the (N)ZIF magnitude of Bat. For the investigated batteries, it was found that P revealed the highest imaginary values in the inductive area and the magnitude of Bat (N)ZIF is therefore dominated by P.

Parts of this chapter have been orally presented at the Advanced Battery Power Conference, Aachen, Germany, 28-30 March 2017.

8.1. Introduction

The (N)ZIF, which can be used to indicate the battery temperature, has been introduced and discussed in Chapters 4 and 5. So far, (N)ZIF values have been determined on the complete battery (Bat) only and it is therefore unknown what electrode is responsible for this effect. In this Chapter, the (N)ZIF behavior is studied for Bat and also for both the positive electrode (P) and the negative electrode (N). In order to measure the individual electrode impedances, µREF were prepared and placed between P and N. From the obtained impedance spectra, (N)ZIF values were determined. This allowed to investigate the (N)ZIF behavior of the individual electrodes in more detail, resulting in a first step towards impedance-based temperature indication at the electrode level and, moreover, investigating the underlying behavior of the Bat (N)ZIF. By investigating the (N)ZIF of the individual electrodes, the responsible electrode for the characteristic (N)ZIF behavior can be revealed.

Since EIS measurements with (µ)REF can introduce measurement artefacts [1–3], a reliable and accurate data analysis might be impossible. Therefore, it is important to either prevent or to compensate for these artefacts as much as possible. An effective method to compensate for high-frequency measurement artefacts for Li-ion batteries with integrated µREF was successfully developed and presented in Chapter 7. This compensation method is advantageously used in the present study to accurately investigate the (N)ZIF behavior of P and N.

8.2. Experimental details

8.2.1. Battery construction

Cylindrical 18650 batteries, having a nominal capacity of 2.0 Ah with $LiCoO_2$ positive and graphite negative electrodes were used. These cylindrical 18650 batteries were delivered unsealed at one end, and did not contain electrolyte. Therefore, it was possible to remove the inner core from the steel casing to introduce µREF(s). An example of a steel casing, core material, and µREF are shown in Fig. 8.1a. The core material contains coiled up electrodes and separator.

In order to introduce the µREF, the inner core was partly unrolled and the µREF was positioned between the two electrodes. A piece of separator material was used to separate the µREF from the electrodes, preventing electrical contact. After introducing the µREF between the electrodes, the inner core was coiled up again and inserted into the steel casing. At the unopened end of the casing, a hole was made to feed-through the negative electrode connection lead. A photo of both the inner

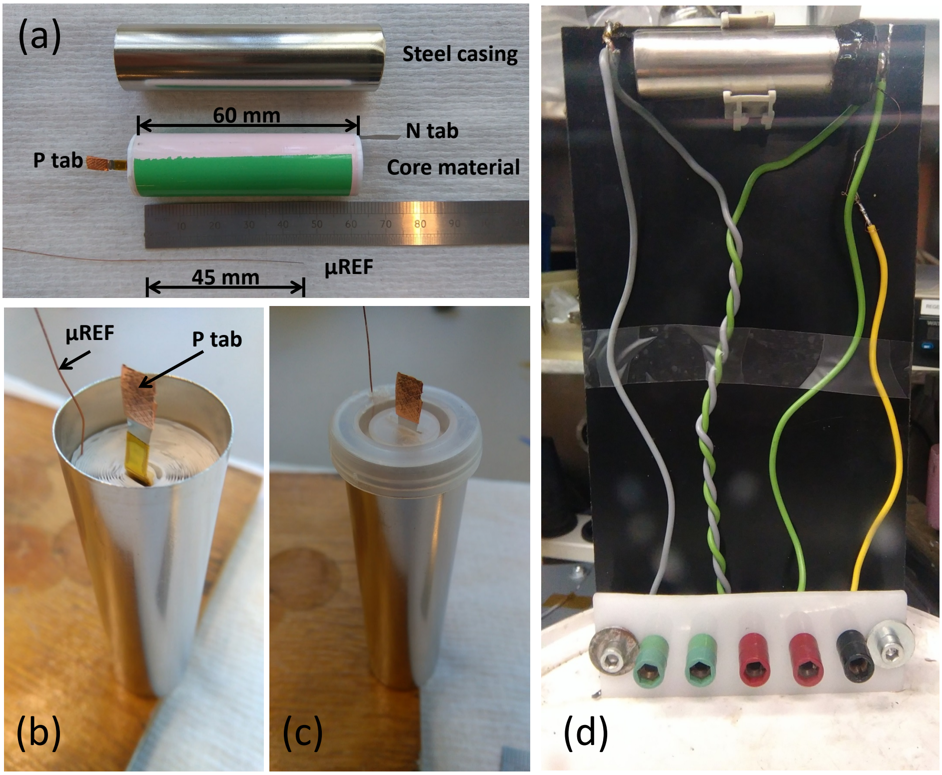

Fig. 8.1: Photographs of an 18650 cylindrical Li-ion battery including µREF (a), unsealed Li-ion battery including µREF (b), closed battery with plastic cap (c), and closed Li-ion battery including µREF in a holder with measurement cables and connections (d).

core and µREF inside the unsealed steel casing is shown in Fig. 8.1b. A plastic cap with two holes (one for the positive connection lead and one for the µREF) was used to close the open end of the steel casing (see Fig. 8.1c). Sealant (Elring, Dirko ProfiPress HT) was used to seal the plastic cap with the steel casing. The gaps around the connection leads and the µREF were not sealed because the batteries had to be vacuum-dried to evaporate moisture. After vacuum drying, the batteries were placed in an Argon-filled glovebox. In the glovebox the batteries were filled with PuriEL battery electrolyte from Soulbrain (Korea) with a composition of 1M $LiPF_6$ in 1/1/1 ethylene carbonate/diethyl carbonate/ethyl methyl carbonate + 2 wt.% vinylene carbonate solution. After filling the batteries with electrolyte, the remaining small gaps around the connection leads and the µREF were sealed with two-component glue. Finally, a plastic holder was used to fix the battery. Measurement cables with connectors were soldered to the electrode connection leads of the battery. The holder including battery, measurement cables, and connectors is shown in Fig. 8.1d.

8.2.2. Preparation of micro-reference electrodes

An insulated (Enamel) copper wire with a radius of 100 μm and a length of 150 mm was used as μREF current collector. The isolation at both ends was removed by immersing the wire into sulfuric acid, followed by rinsing in ethanol. One side of the unprotected Cu wire, later acting as reference electrode, was cut to a length of 45 mm (see Fig. 8.1a). The other unprotected end is used to connect with the measurement cables. Fig. 8.1b shows the location and the orientation of the μREF in the core material.

8.2.3. Electrochemical measurements

Automatic battery cycling equipment (Maccor 2300) was used to activate and (dis)-charge the battery. Initially, the battery was activated for four cycles using a constant current, constant voltage (CCCV) procedure. CC charging was performed with a current of 200 mA until the cut-off voltage of 4.2 V was reached. Subsequently, the battery was charged at a CV level of 4.2 V till a cut-off current of 50 mA was reached. After charging a resting period of 2 h was applied followed by a 200 mA discharge with a cut-off voltage of 2.7 V. In addition to these relatively low-current initialization cycles, ten cycles with a charge and discharge current of 1 and 2 A were applied, respectively. Finally, the nominal discharge capacity of 2.0 Ah was reached after full activation.

After activation, the battery was charged (CCCV) and metallic lithium was galvanostatically deposited onto the unprotected Cu tips of the μREF in order to get a stable lithium reference electrode potential. A 6 μm deposition layer thickness and 0.4 mA/cm^2 current density were chosen for the μREF. The lithium was deposited from both the P and N in order to obtain uniform layers around the wire. For a detailed description of the deposition and stability of lithium metal micro-reference electrodes, the reader is referred to the work of Zhou and Notten [4].

Galvanostatic EIS measurements were performed at temperature-controlled conditions of -10, 0, 10, 20, 30, 40, and 50°C for 50 logarithmically distributed frequencies in the range of 0.1 Hz to 20 kHz with an Autolab PGSTAT302N (Metrohm Autolab). The applied AC current excitation was set such that the voltage response was about 10 mV. This amplitude was chosen to prevent nonlinear responses and to have an adequate signal-to-noise ratio. Five SoC values were investigated, ranging from 100% to 20% in steps of 20%. The EIS measurements were performed with a complete battery (Bat) and with P and N measured with respect to the μREF.

The method described in Chapter 7 was used to compensate for EIS measurement artefacts.

All measurements were performed in a temperature-controlled double-walled chamber that was positioned inside an argon-filled glovebox. A coolant pump (Julabo F32) was used with a high-quality coolant (Julabo Thermal H5) for temperature control. The measurement cable length of the Autolab was 1.5 m and the cable length from the feed-through to the battery inside the glovebox was approximately 2 m.

8.3. Results and discussion

8.3.1. Lithium deposition

After battery activation, metallic lithium was galvanostatically deposited onto the copper µREF according to the method described in Refs. [4, 5]. Before lithium deposition, the battery was charged to an SoC of 100%. A schematic representation of the deposition process is shown in Fig. 8.2. In order to obtain a uniform deposition layer, lithium is first deposited from P (Fig. 8.2a) and, subsequently, from N (Fig. 8.2b). Apparently, this process is essential to prevent shielding effects of the µREF itself, generating a nonuniform layer, which is visualized in Fig. 8.2a [4, 5].

The current and corresponding voltages during the deposition process are shown in Fig. 8.3. The red line in Fig. 8.3a shows the electrode voltage between P and µREF. At the moment the first deposition was initiated, *i.e.* between P and µREF, the voltage was approximately 1.2 V, which corresponds to a voltage between P and the copper substrate of the µREF. However, the voltage rapidly increased to approximately 4.2 V when the current was switched on, indicating that the copper µREF changed into a metallic lithium µREF. The deposition current, shown in Fig. 8.3b, clearly indicates the moment at which deposition starts. After the first deposition, lithium was further deposited from N onto the µREF, of which the voltage is shown by the blue line. As lithium was deposited already from P, the voltage was stable at the moment the lithium deposition from N onto the µREF started. The corresponding currents for both deposition processes are shown in Fig. 8.3b. It can be seen that when the deposition current ends ($\approx$ 93 min), the voltage remains stable.

The deposited capacity was calculated from the deposition current and time. For the applied µREF, a capacity of 0.35 mAh was used, which is 0.017 % of the total battery capacity. Therefore, the amount of charge that was deposited is negligible for the total battery storage capacity.

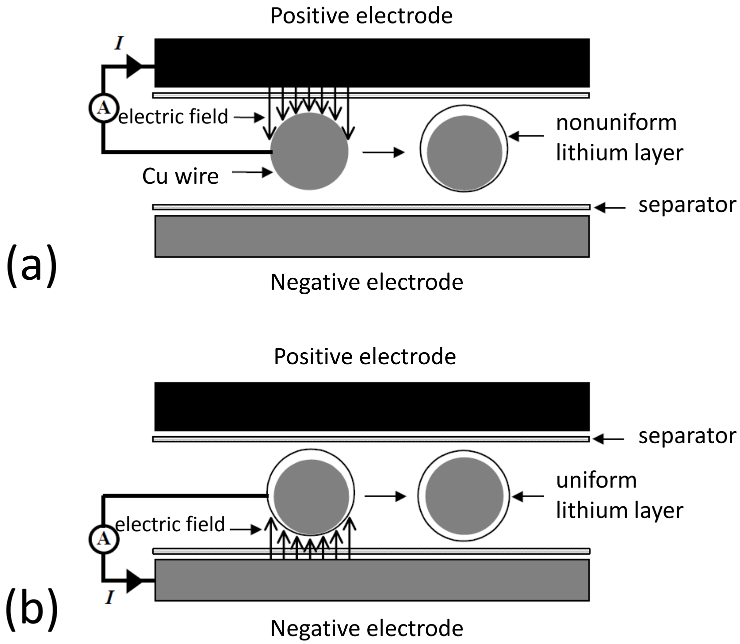

Fig. 8.2: Schematic representation of the lithium deposition process. Deposition from P (a), and deposition from N (b). Adapted from Ref. [5].

8.3.2. Battery and electrode impedances

In Fig. 8.4 P, N, and Bat impedances are shown, measured at various temperatures and at a SoC of 60%. In the left column (Fig. 8.4a-c), all impedances are shown, whereas in the right column (Fig. 8.4d-f) zooms on the impedances measured at higher temperatures are shown. As expected, the impedances for both the individual electrodes and for the battery decrease with increasing temperature, indicating that a temperature-dependent (N)ZIF can be determined for both P and N.

The same results are shown in Fig. 8.5. However, now P, N, Bat, and the summation of P and N are shown in one complex plane for a fixed temperature. For all complex planes (Fig. 8.5a-f), the summations of P and N perfectly agree with Bat measurements, which is an indication that the individual electrode impedances are measured correctly. In addition, the agreement between P + N and Bat at high frequencies is perfect, which implies that high-frequency measurement artefacts are perfectly compensated with the method described in Chapter 7.

From Fig. 8.5, it is interesting to see that N is more sensitive to temperature changes in comparison to P. For example, at a temperature of -10°C (Fig. 8.5a), the impedance of N is larger than that of P. However, at a temperature of 40°C

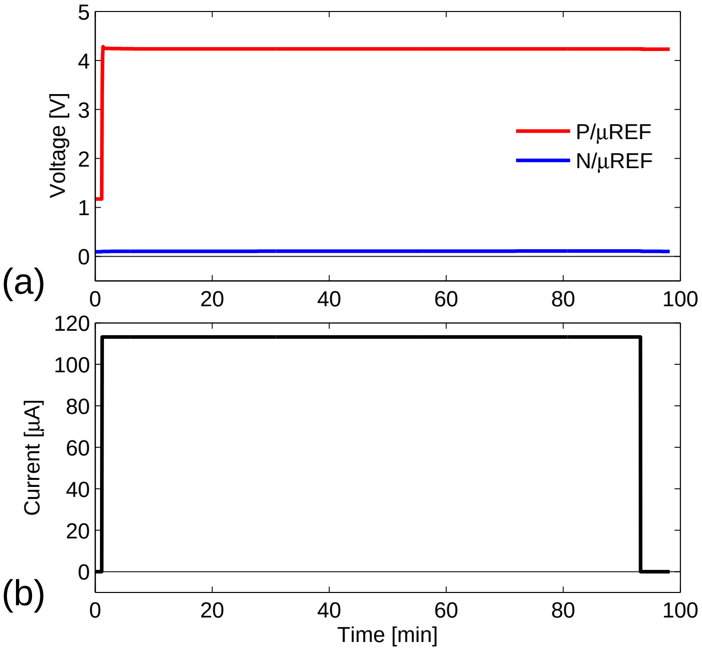

Fig. 8.3: Voltage between P (red line) and N with respect to µREF (blue line) (a), and deposition current (b) during metallic lithium deposition. Note that the depositions were performed sequentially.

(Fig. 8.5f), this is reversed. Hence, the contribution of N to Bat is larger at low temperatures than at high temperatures. Furthermore, the high-frequency part of P always reaches further into the inductive area of the complex plane in comparison to the high-frequency part of N. This behavior might be attributed to the fact that the µREF is positioned more close to the N tab in comparison to the P tab, which is shown in Fig. 8.1b. Consequently, the effective current path between the µREF and the P tab is much longer than the current path between the µREF and the N tab, resulting in more inductance [6]. This asymmetry can be solved by making the length of both current paths the same, *i.e.* placing the µREF in the middle of the electrode windings. However, this was practically impossible since the electrode windings must be unrolled relatively far for introducing the µREF between the electrodes, making it complicated to rewind again such that the core fits into the casing. Because the impedance of P always reaches further into the inductive quadrant, it is to be expected that P (N)ZIF values are lower in magnitude than N (N)ZIF values.

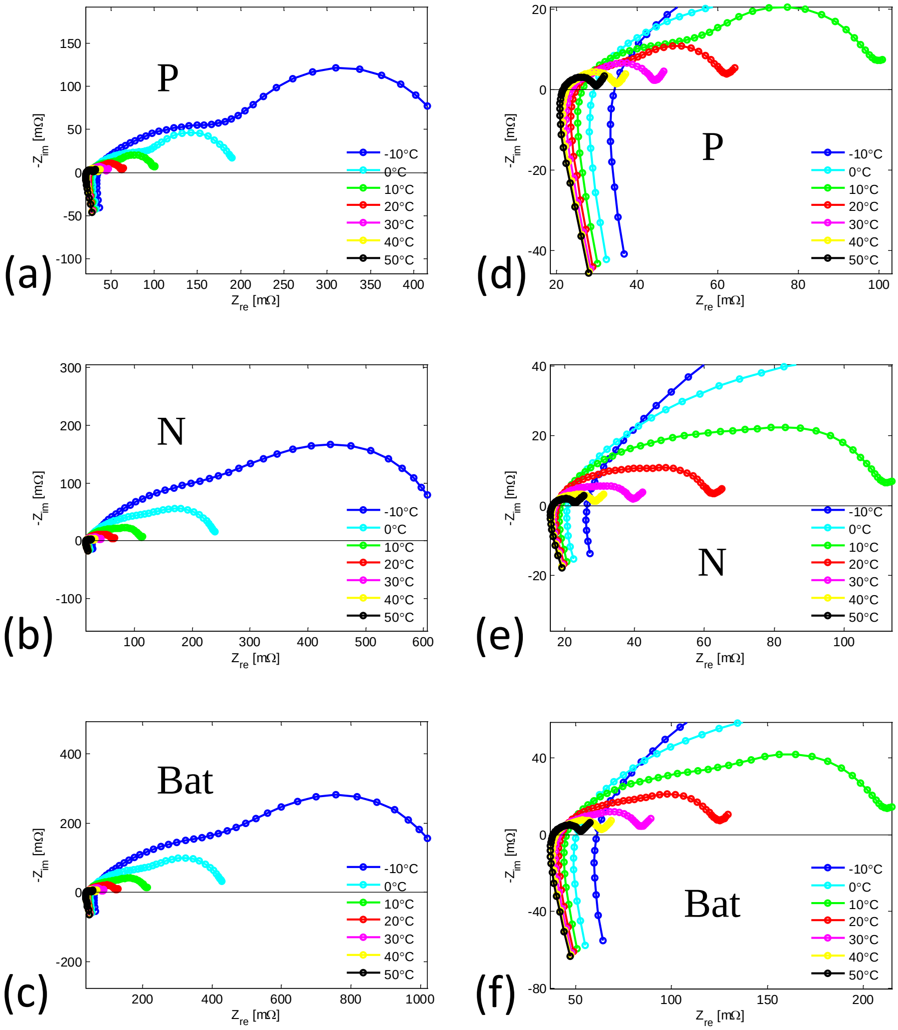

Fig. 8.4: Impedances of P (a) and N (b) measured with respect to the μREF, and impedance of Bat (c) measured at various temperatures at SoC = 60%. A zoom on the impedances of P, N, and Bat is shown in (d-f).

8.3.3. Intercept frequencies

In Fig. 8.6a-c, typical examples of (N)ZIF curves are shown for Bat, P, and N as a function of temperature at 60% SoC. Fig. 8.6a shows the ZIF, interpolated at $Z_{im} = 0$, whereas Fig. 8.6b and c show the NZIF, interpolated at $Z_{im} = 5$ mΩ, and $Z_{im} = 10$ mΩ, respectively. The (N)ZIF curves of P + N have been intentionally left out as these are exactly the same as those of Bat.

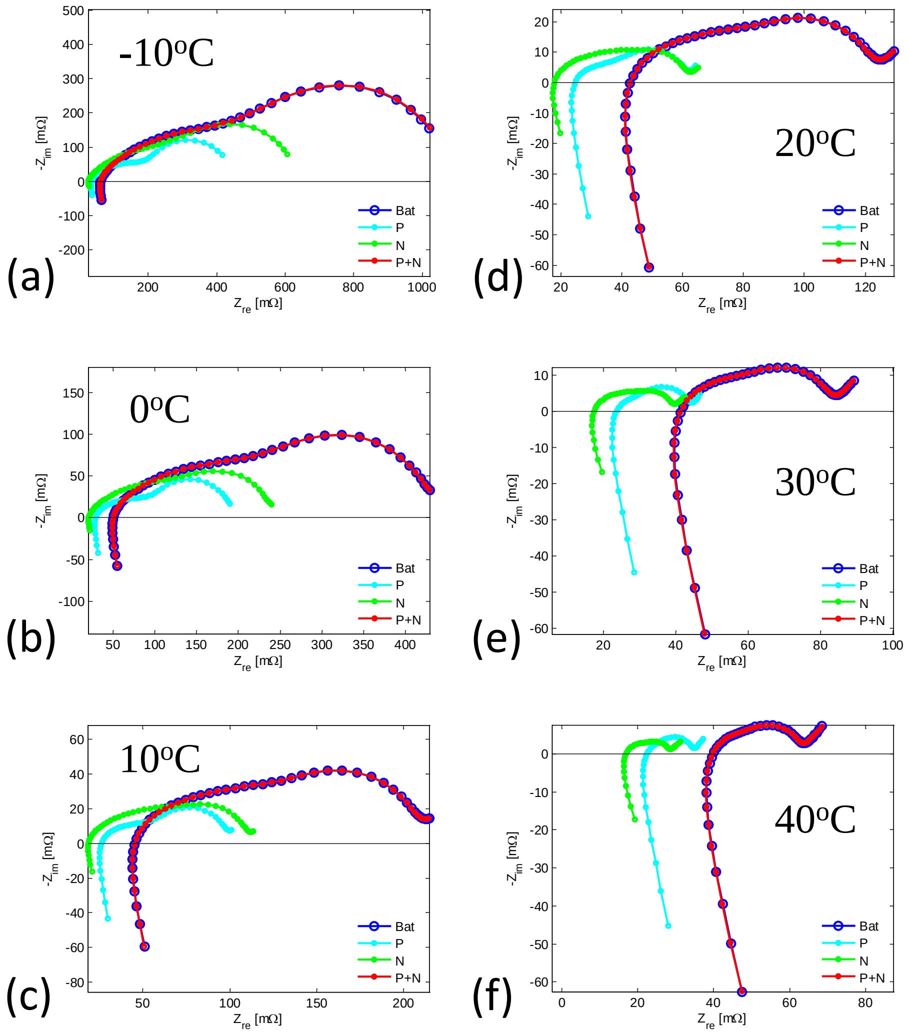

Fig. 8.5: Impedances of P, N, Bat, and P + N shown in complex planes for various temperatures and at SoC = 60%.

From Fig. 8.6a-c, it can be seen that P, N, and Bat (N)ZIF values decrease with increasing temperature. The characteristic (N)ZIF behavior of Bat is already known from the results described in Chapters 4 and 5. However, the results in Fig. 8.6a-c basically show that impedance-based temperature indication through the (N)ZIF also can be performed on both individual electrodes. Furthermore, the (N)ZIF values of N are distinctively higher in magnitude in comparison to the (N)ZIF values of both Bat and P. The reason is that the inductive tail of N reaches less far into the inductive quadrant, which has been discussed in detail in Section 8.3.2.

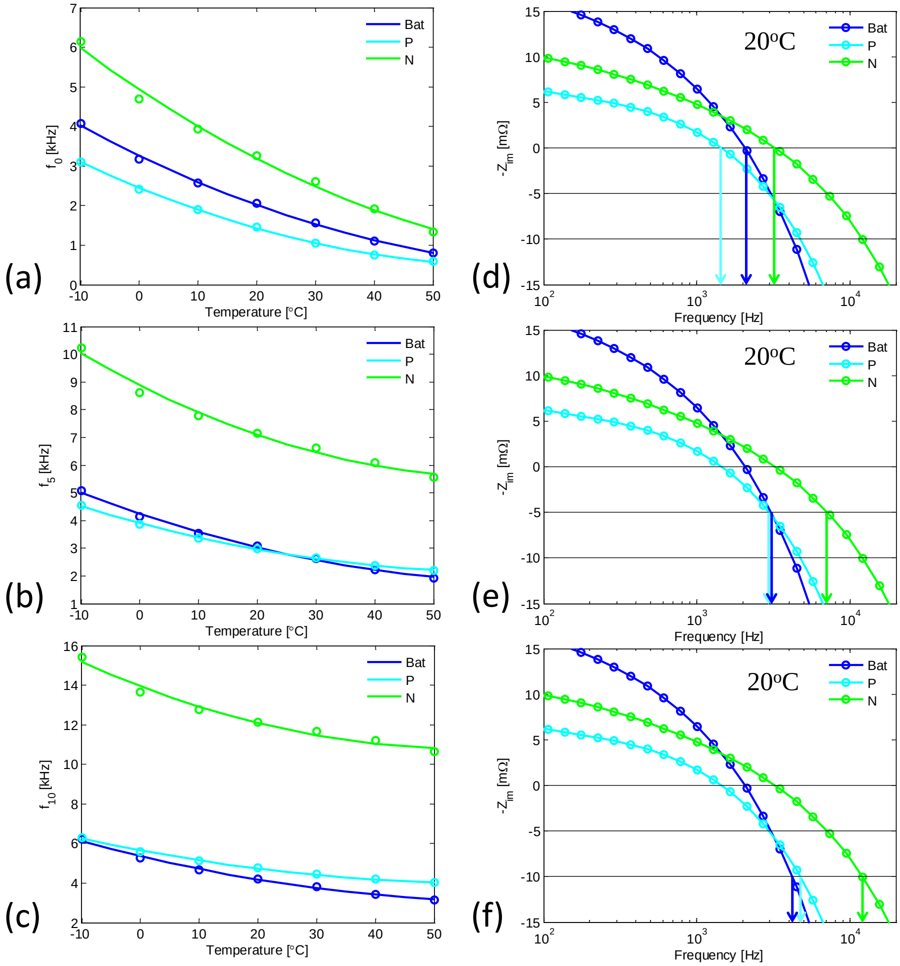

Fig. 8.6: ZIF (a) and NZIF interpolated at Z_{im} = 5 mΩ (b), and Z_{im} = 10 mΩ (c) as a function of temperature for Bat, P, and N at SoC = 60%. Corresponding imaginary impedance (Z_{im}) as a function of frequency for Bat, P, and N at SoC = 60% and T = 20°C (d-f). The (N)ZIF at Z_{im} = 0 mΩ (d), Z_{im} = 5 mΩ (e), and Z_{im} = 10 mΩ (f) are indicated with arrows.

The behavior of the (N)ZIF curves in Fig. 8.6a-c can be further clarified with the help of Fig. 8.6d-f, in which the imaginary part of the impedances (Z_{im}) is shown as a function of frequency (note that $-Z_{im}$ is plotted). Considering the ZIF values interpolated at $Z_{im} = 0$ in Fig. 8.6d, it can be seen that P ZIF is lower in comparison to N ZIF, because it passes the $Z_{im} = 0$ line at a lower frequency than N. It can also be seen that the ZIF of Bat is between that of P and N. The ZIF magnitude of Bat is dictated by the contribution of the imaginary values of both separate electrodes, and therefore both electrodes are responsible for the characteristic ZIF behavior of Bat. For example, in Fig. 8.6d, Z_{im} of P is approximately 2 mΩ at 2 kHz, whereas Z_{im} of N is approximately −2 mΩ at 2 kHz. Adding those two values leads to $Z_{im} \approx 0$ for Bat, at which the ZIF has been determined. Similarly, this also holds for the NZIF values shown in Fig. 8.6e and f. However, the electrode that dominates the (N)ZIF magnitude of Bat, is the electrode with the largest imaginary value. In the example shown in Fig. 8.6, P is found to be the dominating electrode. However, as explained in Section 8.3.2, the asymmetric location of the µREF in the battery core is responsible for the higher imaginary values in the inductive quadrant for P in comparison to N. In reality, it can be assumed that both electrodes have equal inductances and that the imaginary values in the inductive quadrant can be considered equal, leading to equal electrode contributions.

The slope of the (N)ZIF curves is determined by the sensitivity of the electrode impedance with respect to temperature. In Fig. 8.5, it can be clearly seen that the impedance of N is more sensitive to temperature changes than P. For that reason, the slope of N (N)ZIF curves is steeper in comparison to the P (N)ZIF curves (see Fig. 8.6a-c). For high temperature indication accuracy, it would be advantageous when the slopes of (N)ZIF curves are more steep. Steeper slopes of the individual electrodes lead to steeper slopes for Bat. For impedance-based temperature indication, it is sufficient to have only one electrode which is sensitive to temperature changes. Since the graphite N is sensitive to temperature changes (see Fig. 8.5), it is to be expected that the (N)ZIF temperature indication method can be performed on most commercial Li-ion battery systems as the majority of N is based on graphite.

8.4. Conclusions

Both ZIF and NZIF values have been extracted from the impedance spectra measured at cylindrical $C_6/LiCoO_2$ batteries and related to the battery temperature. µREF, *in situ* deposited with a thin metallic lithium layer, allowed to measure the impedance spectra of the individual electrodes. It can be concluded that the (N)ZIF values of P, N, and Bat are all temperature-dependent and, therefore, can be used for impedance-based temperature indication.

For the investigated batteries, it was found that the impedance of N is more sensitive to temperature changes than that of P. For that reason, the slope of N (N)ZIF curves is steeper than the slope of P (N)ZIF curves. The (N)ZIF of Bat is composed of the contribution of the imaginary values of both individual electrodes, indicating that both electrodes are responsible for the characteristic behavior of Bat (N)ZIF. However, the electrode with the highest imaginary value in the inductive quadrant of the complex plane is the electrode that dominates the (N)ZIF magnitude of the complete battery.

The experimental investigations in this work have all been performed under equilibrium laboratory conditions. Future investigations have to reveal if impedance-based temperature indication on the individual electrodes can also be performed under non-equilibrium conditions.

References

[1] H. Brandstätter, I. Hanzu, and M. Wilkening, *Myth and Reality about the Origin of Inductive Loops in Impedance Spectra of Lithium-Ion Electrodes — A Critical Experimental Approach*, Electrochim. Acta **207**, 218 (2016).

[2] C. Bunzli, H. Kaiser, and P. Novak, *Important Aspects for Reliable Electrochemical Impedance Spectroscopy Measurements of Li-Ion Battery Electrodes,* J. Electrochem. Soc. **162**, A218 (2014).

[3] S. Klink, D. Höche, F. La Mantia, and W. Schuhmann, *FEM modelling of a coaxial three-electrode test cell for electrochemical impedance spectroscopy in lithium ion batteries,* J. Power Sources **240**, 273 (2013).

[4] J. Zhou and P. H. L. Notten, *Development of Reliable Lithium Microreference Electrodes for Long-Term In Situ Studies of Lithium-Based Battery Systems,* J. Electrochem. Soc. **151**, A2173 (2004).

[5] J. Zhou, *Lithium Metal Microreference Electrodes and their Applications to Li-ion Batteries*, Ph.D. thesis, Eindhoven University of Technology (2007).

[6] P. J. Osswald, S. V. Erhard, A. Noel, P. Keil, F. M. Kindermann, H. Hoster, and A. Jossen, *Current density distribution in cylindrical Li-Ion cells during impedance measurements,* J. Power Sources **314**, 93 (2016).

A

Appendix A: Kirchhoff's laws applied to electric equivalent circuits

A.1. Introduction

By applying Kirchhoff’s voltage laws to the equivalent circuits in Fig. 7.1 and Fig. A.1, the current flowing through the branches can easily be calculated. In Fig. A.1 the equivalent circuits shown in Fig. 7.1 are reproduced. However, Fig. A.1 also shows the current paths which are used to calculate the various currents flowing through the various circuits. Counterclockwise flowing currents are defined as positive and clockwise currents as negative. When these currents are known, the voltage ΔV and the impedances can be calculated successively.

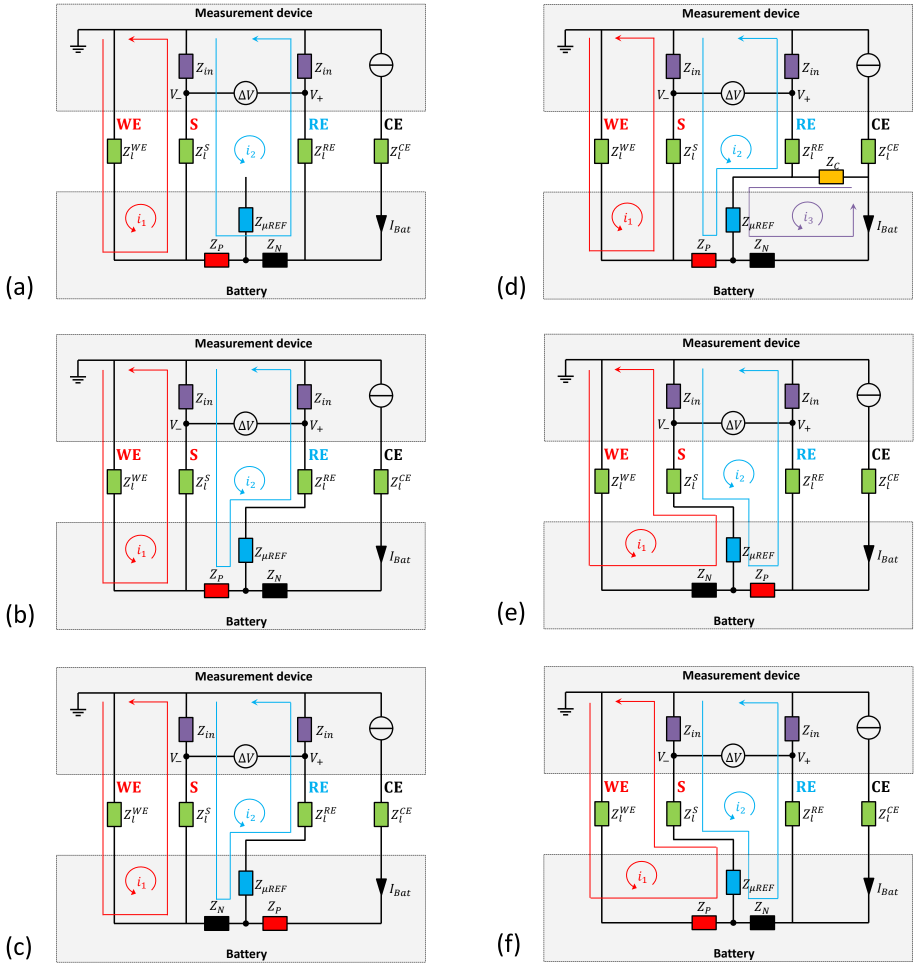

Fig. A.1: Schematic equivalent circuits for EIS measurements at Bat (a), P (b), N (c), P with capacitor bridge (d), P with reversed connections (e), and N with reversed connections (f).

A.2. Battery impedance

In order to calculate the total measured battery impedance (Z^m_{Bat}), two linear equations need to be determined from the circuit shown in Fig. A.1a. Following the current paths i_1 and i_2, we can write

$$(i_1 - I_{Bat})\, Z_l^{WE} + (i_1 - i_2)\left(Z_l^S + Z_{in}\right) = 0 \tag{A.1}$$

and

$$(i_2 - i_1)\left(Z_{in} + Z_l^S\right) + (i_2 - I_{Bat})\,(Z_P + Z_N) + i_2\left(Z_l^{RE} + Z_{in}\right) = 0\ , \tag{A.2}$$

respectively. This system of linear equations can be written in matrix notation to obtain a solution for i_1 and i_2, resulting in

$$MI = I_{Bat}Z\ , \tag{A.3}$$

where

$$M = \begin{bmatrix} Z_{11} & -Z_{12} \\ -Z_{21} & Z_{22} \end{bmatrix}, \qquad I = \begin{bmatrix} i_1 \\ i_2 \end{bmatrix}, \qquad Z = \begin{bmatrix} Z_l^{WE} \\ Z_P + Z_N \end{bmatrix}. \tag{A.4}$$

Note that I is a vector with currents, not an identity matrix. In matrix M,

$$Z_{11} = Z_l^{WE} + Z_l^S + Z_{in} \tag{A.5}$$

$$Z_{12} = Z_{21} = Z_l^S + Z_{in} \tag{A.6}$$

$$Z_{22} = 2Z_{in} + Z_l^S + Z_P + Z_N + Z_l^{RE}\ . \tag{A.7}$$

Solving Eq. A.3 by

$$I = M^{-1} I_{Bat} Z \tag{A.8}$$

for any arbitrary non-zero I_{Bat}, a solution can be obtained for both i_i and i_2. Subsequently, the voltage difference ΔV can be calculated, according to

$$\Delta V = V_+ - V_-\ , \tag{A.9}$$

where

$$V_+ = i_2 Z_{in} \,, \qquad V_- = (i_1 - i_2)\, Z_{in} \tag{A.10}$$

and, therefore,

$$\Delta V = Z_{in}\,(2i_2 - i_1) \ . \tag{A.11}$$

The total measured battery impedance can finally be calculated by

$$Z^m_{Bat} = \frac{\Delta V}{I_{Bat}} = Z_{in}\frac{2i_2 - i_1}{I_{Bat}} \,, \tag{A.12}$$

in which I_{Bat} has the same value as in Eq. A.8. From Eq. A.12 it can be seen that Z^m_{Bat} is dependent on the input impedance of the measurement device multiplied with a current ratio. Obviously, i_1 and i_2 are dependent on the remaining impedances in the circuit.

A.3. Positive and negative electrode impedances

Following the circuit with current paths in Fig. A.1b, the measured impedances for P (Z^m_P) can be derived. The current path i_1 is the same as in Eq. A.1. However, the equation for current path i_2 becomes

$$(i_2 - i_1)\left(Z_{in} + Z^S_l\right) + (i_2 - I_{Bat})\, Z_P + i_2\left(Z_{\mu REF} + Z^{RE}_l + Z_{in}\right) = 0 \ . \tag{A.13}$$

A system of two linear equations can be used in the same matrix notations and derivations as for the battery, shown in Appendix A.2, *i.e.* Eqs. A.3 - A.8. However, Eq. A.7 changes into

$$Z_{22} = 2Z_{in} + Z^S_l + Z_P + Z_{\mu REF} + Z^{RE}_l \,, \tag{A.14}$$

and the second element in vector Z (see Eq. A.4) changes from $(Z_P + Z_N)$ to Z_P.

Solving the system of equations for i_1 and i_2 by Eq. A.8 and using Eqs. A.9 - A.12, Z^m_P can be calculated accordingly. The measured impedances for N (Z^m_N), of which the equivalent circuit is shown in Fig. A.1c, can be obtained with the same approach. In that case, Z_P has to be replaced by Z_N in the corresponding equations.

A.4. Capacitor-bridge compensation

Fig. A.1d shows the circuit in which a capacitor bridge is used to compensate the leakage current through µREF. The capacitor creates one additional current path that must be considered, resulting in three paths in total. In order to calculate the measured P in the presence of a capacitor bridge ($Z^m_{P,C}$), a system of three linear equations must be solved. The equation for the current path i_1 is equal to Eq. A.1. The equations for the current paths i_2 and i_3 become

$$(i_2 - i_1)\left(Z_{in} + Z_l^S\right) + (i_2 - I_{Bat})\,Z_P + (i_2 - i_3)\,Z_{\mu REF} + i_2\left(Z_l^{RE} + Z_{in}\right) = 0 \quad \text{(A.15)}$$

and

$$i_3 Z_C + (i_3 - i_2)\,Z_{\mu REF} + (i_3 - I_{Bat})\,Z_N = 0\,, \quad \text{(A.16)}$$

respectively. In order to work towards a solution for the three currents, Eq. A.3 can be used, in which

$$M = \begin{bmatrix} Z_{11} & -Z_{12} & Z_{13} \\ -Z_{21} & Z_{22} & -Z_{23} \\ Z_{31} & -Z_{32} & Z_{33} \end{bmatrix}, \qquad I = \begin{bmatrix} i_1 \\ i_2 \\ i_3 \end{bmatrix}, \qquad Z = \begin{bmatrix} Z_l^{WE} \\ Z_P \\ Z_N \end{bmatrix}. \quad \text{(A.17)}$$

In Eq. A.17 the elements Z_{11}, Z_{12}, Z_{21}, and Z_{22} are equal to the Eqs. A.5, A.6, A.6, and A.14, respectively. The remaining elements are defined as

$$Z_{13} = Z_{31} = 0 \quad \text{(A.18)}$$

$$Z_{23} = Z_{32} = Z_{\mu REF} \quad \text{(A.19)}$$

$$Z_{33} = Z_C + Z_{\mu REF} + Z_N\,. \quad \text{(A.20)}$$

By using Eq. A.8, the currents i_1, i_2, and i_3 can be obtained. Eqs. A.9 - A.12 can then be used to calculate $Z^m_{P,C}$. In order to calculate the measured impedance of N ($Z^m_{N,C}$), all Z_P must be replaced by Z_N and *vice versa*.

A.5. Reversed-electrode impedances

The circuit in Fig. A.1e shows how P is measured with reversed connections ($Z_{P,r}^{m}$). Following the current paths i_1 and i_2, we can write

$$(i_1 - I_{Bat})\left(Z_l^{WE} + Z_N\right) + (i_1 - i_2)\left(Z_{\mu REF} + Z_l^S + Z_{in}\right) = 0 \tag{A.21}$$

and

$$(i_2 - i_1)\left(Z_{in} + Z_l^S + Z_{\mu REF}\right) + (i_2 - I_{Bat})\, Z_P + i_2\left(Z_l^{RE} + Z_{in}\right) = 0 \tag{A.22}$$

for both paths, respectively. Again, Eq. A.3 can be used to solve this system of two linear equations in which the four elements of matrix M are defined as

$$Z_{11} = Z_l^{WE} + Z_N + Z_{\mu REF} + Z_l^S + Z_{in} \tag{A.23}$$

$$Z_{12} = Z_{21} = Z_{in} + Z_l^S + Z_{\mu REF} \tag{A.24}$$

$$Z_{22} = 2Z_{in} + Z_l^S + Z_{\mu REF} + Z_P + Z_l^{RE}\ . \tag{A.25}$$

Furthermore, vector Z in Eq. A.3 is now defined as

$$Z = \begin{bmatrix} Z_l^{WE} + Z_N \\ Z_l^{RE} \end{bmatrix}\ . \tag{A.26}$$

Solving the currents i_1 and i_2 by Eq. A.8 and subsequently using Eqs. A.9 - A.12, $Z_{P,r}^{m}$ can be obtained. The same approach can also be performed for determining $Z_{N,r}^{m}$, of which the schematic equivalent circuit is shown in Fig. A.1f. However, in all corresponding equations Z_P must be replaced by Z_N and *vice versa*.

Acknowledgments

During my four-year PhD trajectory, I had the opportunity to work on a large variety of research subjects. To my pleasure I, therefore, had the chance to work with a lot of people. In these acknowledgments, I want to thank the people who helped me content wise, and all others who supported me.

First of all, I want to thank Ekkes Brück, Erik Kelder and Peter Notten for offering me a PhD position. Especially, I want to thank Peter; it was a pleasure to work with you, Peter. I highly appreciate your professional guidance, strictness and devotion to scientific research. All those years you gave me the opportunity to develop my own ideas. The professional progress meetings, interesting scientific discussions and your thorough comments were always very much appreciated. Thank you for everything! Ekkes and Erik, although you were not directly involved with all activities, you always supported me in everything. Thank you very much!

Some people were closely involved with the work which is presented in this dissertation. Dmitri Danilov is one of them. Dmitri, your knowledge about mathematics and statistics always impressed me. I always admired your skills to find solutions for many scientific problems. Thank you for helping me! It was a pleasant experience to work with you. This also holds for the collaboration with Henk Jan Bergveld. Henk Jan, the way you always oversee everything is really great. I always admired your pragmatic way of thinking, your speed of working/taking action and giving useful thorough comments. It really was a pleasure to work with you! Thank you as well for reading every letter of this thesis.

I would like to thank the members of my defense committee which I did not mention yet. Rüdicher Eichel, Fokko Mulder, Wouter Serdijn, and chairman Lucas van Vliet, thank you for reading my dissertation and being a committee member.

In my first year I met Tijs Donkers from the Control Systems group in Electrical Engineering (TU/e). Together with Tijs, Henk Jan and Peter we supervised Henrik Beelen on his Master's thesis. This resulted in very nice research output and collaborations, also later during Henrik's PhD work. Henrik and Tijs, I really enjoyed it to work with you, thank you! It gave me the chance to focus and study control-system-related topics as well. The workshop and conference in Sweden we visited are nice things to remember. Unfortunately, time did not allow to collaborate more than we did, but if it did I'm sure we could have done more nice scientific work. In addition, I want to thank Kartik Shivakumar for the nice collaboration we had together with Henk Jan, Tijs and Henrik; it resulted in nice research output.

A lot of support came from Joop van Lammeren, Thieu Lammers and Rabindra Rijal from NXP Semiconductors in Eindhoven. Joop, thank you for arranging meetings with people from the automotive industry, for arranging the electric VW Lupo and for providing useful information. Rabindra, thank you for helping me with measurement software and performing battery measurements. A special acknowledgement to Thieu. We spent hours together on some battery-related measurement issues and thinking about battery measurements and measurement systems/setups in general. I remember we even had our discussions on the afternoon before Christmas eve and on Silvester day. Thieu, your knowledge about electrical systems, measurement setups, and programming were really of great value for this dissertation. We spent a long time on the topic of measurement artefacts. It took a while before we really found the problem, but in the end we solved it. I also highly appreciate the measurements you performed and the technical support you gave.

Dear Chinese colleagues from Eindhoven University of Technology: Dongjiang Li, Jie Xie, Chunguang Chen, Lu Gao, Lei Zhou, and Ming Jiang. Thank you for all support and nice discussions and conversations we had together. You learned me a lot of things about the Chinese life and culture, of which I had no idea beforehand. I always admired your hard way of working far from your home and family; really impressive. A special thanks to my former office mates Dongjiang and Jie, who made my office life somewhat easier. Thank you for all interesting scientific discussions and all general conversations.

I also want to acknowledge my colleagues from Delft University of Technology. Peter Paul (PP) Harks, Tomas Verhallen, Yaolin Xu, Niek de Klerk, Tomas Verhallen, Frans Ooms, Jouke Heringa, Ilse van der Kraaij and Nicole Banga, thank you for everything! In particular PP, thank you for all scientific discussions, nice conversations and assistance in daily activities. A special acknowledgment to Frans. Thank you for assisting me with technical issues and for the provision of equipment! Also the help of Jouke with some LaTeX and computer related issues is very much appreciated. I also would like to thank Ilse and Nicole for arranging all administrative work.

Futhermore, I want to thank all remaining people who helped me during this journey. Thank you Igo Besselink, Joost van Boekel, Paul van Oorschot, Peter Hamels, Erwin Meinders and Henk Nijmeijer from the Department of mechanical Engineering of Eindhoven University of Technology for providing your electric vehicle and test bench. Your assistance during the measurements on the VW Lupo is

highly appreciated. I also want to acknowledge Jiang Zhou, from Tianjin Lishen Battery Co., Ltd. for providing battery materials and useful battery information. The discussions with the gentleman from Ivium Technologies in Eindhoven are also highly appreciated.

Finally, I want to thank my family, who always have been very interested in my work and wellbeing. They always gave me a lot of support during the course of my PhD. This helped me a lot in achieving this dissertation. They always were there for me and took care that I also spent some time to relax, which is sometimes really necessary.

Curriculum Vitæ

Luc Raijmakers was born on 26 August 1985 in Boxmeer, the Netherlands. After finishing secondary school in 2001, he attended a four-year education for mechanic in automotive technology at Gilde Opleidingen in Venlo. In 2005 he started studying Automotive Engineering (Bachelor level) at the Hogeschool Arnhem Nijmegen (HAN), which he successfully finished in 2009. He graduated on the topic of analyzing and optimizing a crank-train mechanism and balancing system of a one-cylinder research engine. After completing the HAN he continued with a Master's study in Automotive Technology at Eindhoven University of Technology (TU/e). In 2013 he graduated with high appreciation on the topic of Sensorless battery temperature measurements based on electrochemical impedance spectroscopy. After completing his Master's degree, he collaborated with NXP Semiconductors in Eindhoven on developing a graphical user interface for Li-ion battery measurement devices. In April 2014 he officially started his PhD at Delft University of Technology. However, most of his work was performed at Eindhoven University of Technology (TU/e) in the group of Prof. dr. Peter H.L. Notten. During his research he intensively collaborated with NXP Semiconductors in Eindhoven and with the Control Systems group in the Electric Engineering department at the TU/e. The research results obtained in his PhD trajectory are presented in this thesis.

List of Publications

Journal publications

1. **L.H.J. Raijmakers**, D.L. Danilov, J.P.M. van Lammeren, M.J.G. Lammers, P.H.L. Notten, *Sensorless battery temperature measurements based on electrochemical impedance spectroscopy*, Journal of Power Sources **247**, (2014) 539-544.
2. **L.H.J. Raijmakers**, D.L. Danilov, J.P.M. van Lammeren, M.J.G. Lammers, H.J. Bergveld, P.H.L. Notten, *Non-Zero Intercept Frequency: An Accurate Method to Determine the Integral Temperature of Li-ion Batteries*, IEEE Transactions on Industrial Electronics **63**, (2016) 3168-3178.
3. H.P.G.J. Beelen, **L.H.J. Raijmakers**, M.C.F. Donkers, P.H.L. Notten, H.J. Bergveld, *A comparison and accuracy analysis of impedance-based temperature estimation methods for Li-ion batteries*, Applied Energy **175**, (2016) 128-140.
4. J. Xie, P.R.M.L. Harks, D. Li, **L.H.J. Raijmakers**, P.H.L. Notten, *Planar and 3D deposition of $Li_4Ti_5O_{12}$ thin film electrodes by MOCVD*, Solid State Ionics **287**, (2016) 83-88.
5. D. Li, D.L. Danilov, J. Xie, **L.H.J. Raijmakers**, L. Gao, Y. Yang, P.H.L. Notten, *Degradation Mechanisms of $C_6/LiFePO_4$ Batteries: Experimental Analyses of Calendar Aging*, Electrochimica Acta **190**, (2016) 1124-1133.
6. **L.H.J. Raijmakers**, M.J.G. Lammers, P.H.L. Notten, *A new method to compensate impedance artefacts for Li-ion batteries with integrated micro-reference electrodes*, Electrochimica Acta **259**, (2018) 517-533.
7. **L.H.J. Raijmakers**, M. Büchel, P.H.L. Notten, *Impedance-based temperature measurement method for Organic Light-Emitting Diodes (OLEDs)*, Measurement **123**, (2018) 26-29.
8. **L.H.J. Raijmakers**, D.L. Danilov, P.H.L. Notten, *A review on various temperature-indication methods for Li-ion batteries*, Submitted to 'Applied Energy' (2018).
9. H.P.G.J. Beelen, K.M. Shivakumar, **L.H.J. Raijmakers**, M.C.F. Donkers, H.J. Bergveld, *Impedance-Based Temperature Estimation for Li-ion Battery Packs*, To be submitted (2018).
10. **L.H.J. Raijmakers**, D.L. Danilov, P.H.L. Notten, *Modeling all-solid-state Li-ion batteries*, To be submitted (2018).

Conference publications (peer reviewed)

1. H.P.G.J. Beelen, **L.H.J. Raijmakers**, M.C.F. Donkers, P.H.L. Notten, H.J. Bergveld, *An Improved Impedance-Based Temperature Estimation Method for Li-ion Batteries*, IFAC-PapersOnLine **48**, (2015) 383-388.
2. **L.H.J. Raijmakers**, K.M. Shivakumar, M.C.F. Donkers, H.J. Bergveld, *Crosstalk Interferences on Impedance Measurements in Battery Packs*, IFAC-PapersOnLine **49**, (2016) 042–047.

Conference contributions

1. H.P.G.J. Beelen, **L.H.J. Raijmakers**, M.C.F. Donkers, P.H.L. Notten, H.J. Bergveld, *An Improved Impedance-Based Temperature Estimation Method for Li-ion Batteries*, 4th IFAC Workshop on Engine and Powertrain Control, Simulation and Modeling E-COSM, Columbus, Ohio, USA, 23-26 August 2015, Oral presentation.
2. **L.H.J. Raijmakers**, D.L. Danilov, J.P.M. van Lammeren, M.J.G. Lammers, H.J. Bergveld, P.H.L. Notten, *An accurate method to determine the integral temperature of Li-ion batteries in electric vehicles*, Advanced Battery Power Conference, Münster, Germany, 25-27 April 2016, Oral presentation.
3. P.H.L. Notten, **L.H.J. Raijmakers**, M.J.G. Lammers, *A New Method to Compensate High-Frequency Impedance Artefacts for Three-Electrode Li-Ion Batteries*, 229th ECS Meeting, San Diego, USA, May 29 - June 3, 2016, Abstract.
4. **L.H.J. Raijmakers**, K.M. Shivakumar, M.C.F. Donkers, H.J. Bergveld, *Crosstalk Interferences on Impedance Measurements in Battery Packs*, 8th IFAC Symposium on Advances in Automotive Control AAC, Norrköping, Sweden, 20-23 June 2016, Oral presentation.
5. **L.H.J. Raijmakers**, P.H.L. Notten, *Impedance-based temperature determination of Li-ion batteries unravelled by microreference electrodes*, Advanced Battery Power Conference, Aachen, Germany, 28-30 March 2017, Oral presentation.